Understanding the Mechanisms of Adhesion Formation with AlSi based Abradables used in the Compressors of Gas Turbines

Aaron Baillieu

A thesis submitted in partial fulfilment of the requirements for the degree of Doctor of Philosophy

The University of Sheffield
Faculty of Engineering
School of Mechanical, Aerospace and Civil Engineering

November 2025

Abstract

AlSi abradables are commonly used in the compressors of jet engines to minimise tip clearances and improve efficiency. Results from abradable testing rigs have shown the abradability of different coatings vary with changing hardness and incursion rates, with Metco 601 (AlSi-Polyester) bonding to the blade (adhesions) at high incursions rates (0.2 – 2µm/pass) but leading to blade wear at low incursion rates (0.02µm/pass). The wear response at high incursion rates is well documented, but the low incursion rate response is not well understood.

In this thesis in-situ tools have been developed for the low-speed spindle test rig at the University of Sheffield to monitor blade profile, temperature and abradable temperature simultaneously. These tools have been applied to rub tests with M601 to show that there is a relationship between abradable temperature and adhesion formation. These tools were applied further in a study targeting rubs at low incursion rates. It was found that the change in behaviour at low incursion rates was a consequence of the ability of the abradable to dissipate thermal energy, with the behaviour changing with changes in the coatings thermal properties.

These findings were applied further through the development of a sample heater block, allowing the bulk temperature of the abradable to be controlled during a test. Analysis of the in-situ data collected at different temperatures allowed the key criteria which influence adhesion formation with M601 to be determined.

To validate if these criteria could be applied to the wider range of AlSi abradables, elevated temperature testing was also completed on M320 (AlSi-hBN) and XPT268 (AlSi-Polyester-hBN). The wear of these materials was also found to follow the criteria proposed, but it was also identified that the addition of hBN had a further impact on the properties of the adhesions formed beyond what could be explained by this work.

Contents

Acknowledgements

The results presented in this thesis would not have been possible without the support and guidance of many people.

I would therefore like to express my gratitude firstly to my supervisor, Professor Matthew Marshall, as well as the other members of the abradables research group. It has been a privilege to work in such a passionate and supportive team, in an environment which has allowed for both personal and professional growth.

I would also like to thank Glen Pattinson, Lloyd Pallett, Matthew Hancock, and Daniel Tejero at Rolls Royce PLC for always going above and beyond to help with our research and ensuring we are kept up to date with the impact that our work is making.

I would like to thank Oliver Cooper and Chris Todd for helping to keep us safe and our rigs running smoothly.

Finally, I would like to thank my family and friends, especially Flo Best, for all their love and support.

List of Tables

List of Figures

Declaration

I, Aaron Baillieu, confirm that the Thesis is my own work. I am aware of the University's Guidance on the Use of Unfair Means (www.sheffield.ac.uk/ssid/unfair-means). This work has not previously been presented for an award at this, or any other, university.

Work completed in this as part of this thesis has been published in two publications:

Baillieu A, Parody A, Rahimov E, Garcia Panizo J, Marshall M. **In situ measurements of thermal-mechanical wear in blade-abradable liner contacts**. *Proceedings of the Institution of Mechanical Engineers, Part C: Journal of Mechanical Engineering Science*. 2023; 238(5). doi: 10.1177/09544062231187204

Baillieu A, Rahimov E, Marshall M. **The role of thermal properties in the wear mechanisms of an AlSi-polyester abradable**. *Wear*. 2025; *562–563*. doi: 10.1016/j.wear.2024.205618

1 Introduction

The increasing popularity, and accessibility, of aviation has seen a significant increase in the number of civil flights per year, with 9.4 billion passengers flying in 2024 alone (1). Although the increased accessibility of aviation can have economic and societal benefits, it also has a severe impact on the environment with more than 2% of global CO_2 emissions coming from civil aviation (2).

To combat this the International Air Transport Association (IATA) has introduced the Carbon Offsetting and Reduction Scheme for International Aviation (CORSIA), aiming to make commercial aviation carbon neutral by 2050 (3). To limit the schemes impact on the accessibility of aviation it has a heavy focus on the efficiency of the Jet Engine, the propulsion system commonly used by civil aircraft. Any improvements in the efficiency and reliability of the Jet Engine will also lead to financial benefits to engine manufactures and operators, for example the improvements enabled by the Abradables Research Group at the University of Sheffield have saved Rolls Royce over £100M in maintenance and servicing costs (4).

To determine methods to improve the efficiency of the Jet Engine a fundamental understanding of its operation is required. Figure 1.1 shows a simplified view of a Jet Engine, with its key components annotated, and the path of air through the engine shown by blue arrows. The engine operates by sucking air into the front (location a in Figure 1.1) and passing it through a compressor, the high-pressure air is then mixed with fuel and ignited in the combustion chamber, producing high temperature air which rapidly expands through a turbine. The turbine is connected to the compressor and extracts some energy from the air, turning the compressor to keep the cycle going, the rest of the energy can leave the back of the engine, providing thrust to the aircraft.

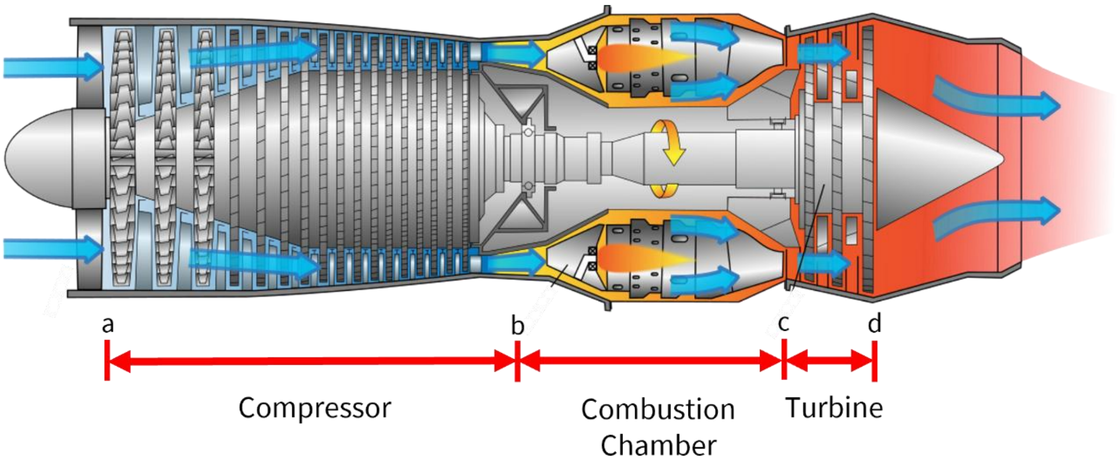

Figure 1.1 – A simplified depiction of a jet engine (5)

This cycle is known as the Brayton Cycle and is visualised in Figure 1.2 as a Pressure – Volume plot. The labels on this plot (a-d) align with the positions marked in Figure 1.1. Visualizing the cycles as a Pressure – Volume plot makes it clearer to see which optimizations will lead to the largest efficiency benefits within the engine.

The area under the curve on a Pressure – Volume plot is equal to the work done on/by the air (6). In Figure 1.2 two areas have been highlighted, A_C (blue) shows the work done by the compressor to compress the air, A_T (red) shows the work done by the air as it expands through the turbine. Some of the work done by the air leaving the engine is used to turn the compressor (equal to A_C), the rest is used to produce thrust. The propulsive efficiency of the engine can therefore be increased by increasing the ratio of A_T to A_C, this can be done by increasing the pressure ratio over the compressor.

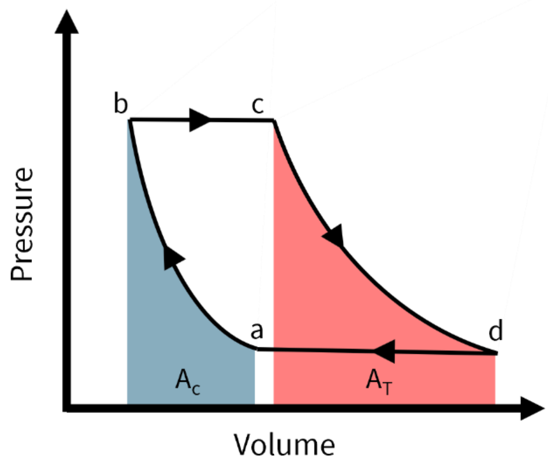

Figure 1.2 – A pressure – volume plot of the Brayton thermodynamic cycle

One theoretically simple way to improve compressor efficiency is to minimise the gap between the blades and the casing, limiting the amount of air which can travel around the outside of the blades. This alone could lead to a 1-5% improvement in compressor efficiency (7).

Due to machining and assembly tolerances, a nominal clearance between the blade and casing must be provided to ensure the blades and casing do not touch in assembly, this allows a path for air to flow around the blades during initial operation (Figure 1.3). As the engine spins up the blades will move outwards due to thermal expansion and centrifugal loads, the engine will also warp during operation as the aircraft manoeuvres and the engine is spooled up and down, these changes can result in blade tip strikes with the engine casing, damaging the blade and increasing airflow around the blades further (8).

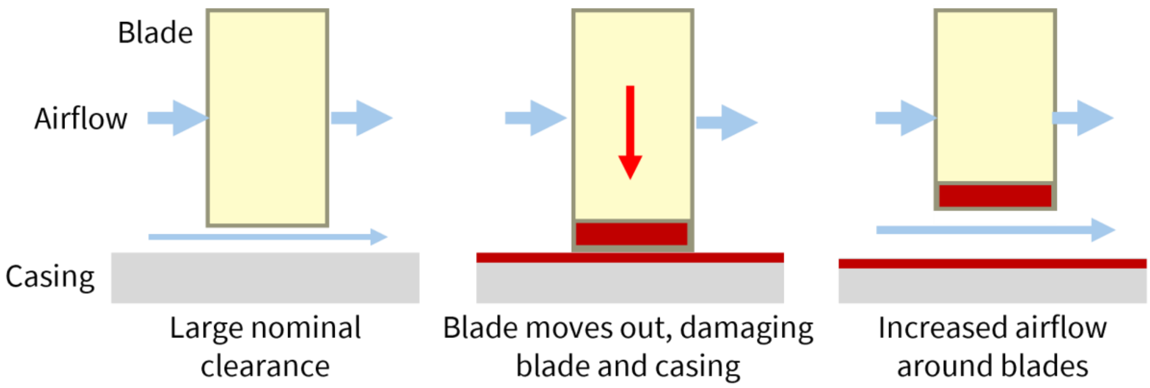

Figure 1.3 – Blade-casing interaction without an abradable

To overcome these limitations an abradable coating is placed between the casing and the blades (Figure 1.4). This coating is designed to provide enough erosion resistance to survive the harsh environment within the jet engine, but also soft enough that the blades can cut into the coating in the event of a blade tip strike without incurring damage.

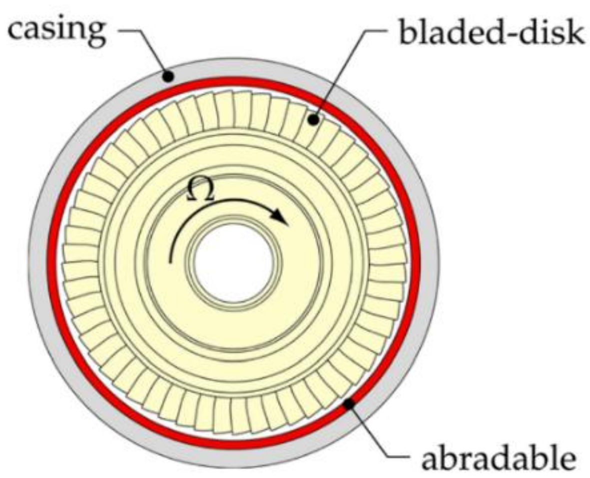

Figure 1.4 – Abradable position within a gas turbine (9)

With the addition of an abradable coating around the casing the nominal clearance can be reduced, with the blade cutting a path through any interference with the abradable during the initial run-in of the engine. Any warping of the engine during operation will result in additional incursions into the abradable but should not result in blade damage. As shown in Figure 1.5 this will result in the blade running inside a groove in the abradable, minimising airflow around the blades.

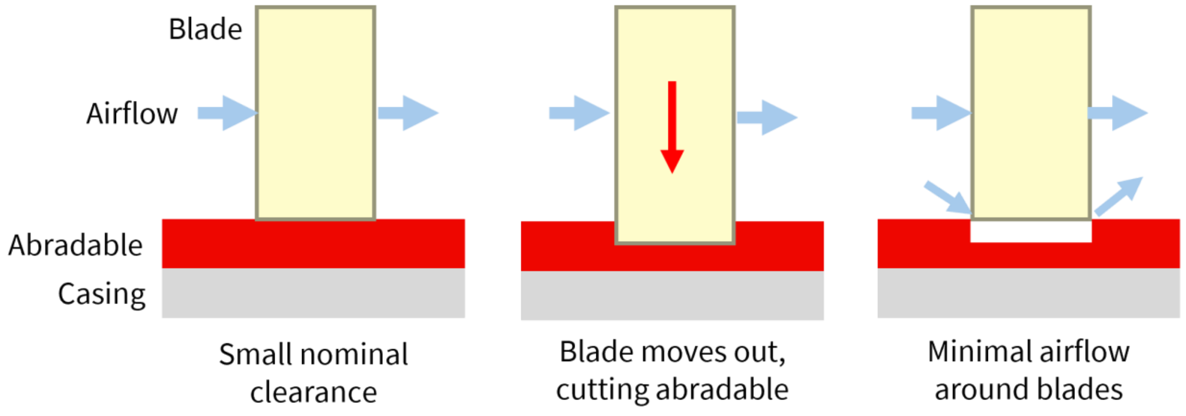

Figure 1.5 – Blade-casing interaction with an abradable

The application of an abradable layer to the casing to prevent air flowing around the blades can lead to significant improvements to the specific fuel consumption of a jet engine, with improvements of as much as 0.6% per compressor stage (10). These benefits are not only limited to jet engines but can also be applied to land-based gas turbines, with trials showing efficiency improvements of 0.3-1% (11).

1.1 Abradable Materials used in Gas Turbines

Abradable coatings are applied in both the compressor and the turbine to reduce tip clearances and improve efficiency. However, as the air is compressed and combustion occurs the temperatures increase significantly, this means that materials which are suitable at the ambient temperatures of the fan would melt if applied in the turbine. This thesis focuses on coatings applied within the Intermediate-Pressure (IP) and early stages of the High-Pressure (HP) compressor, reducing the peak temperatures. However, as shown in Figure 1.6, there is still a significant temperature range.

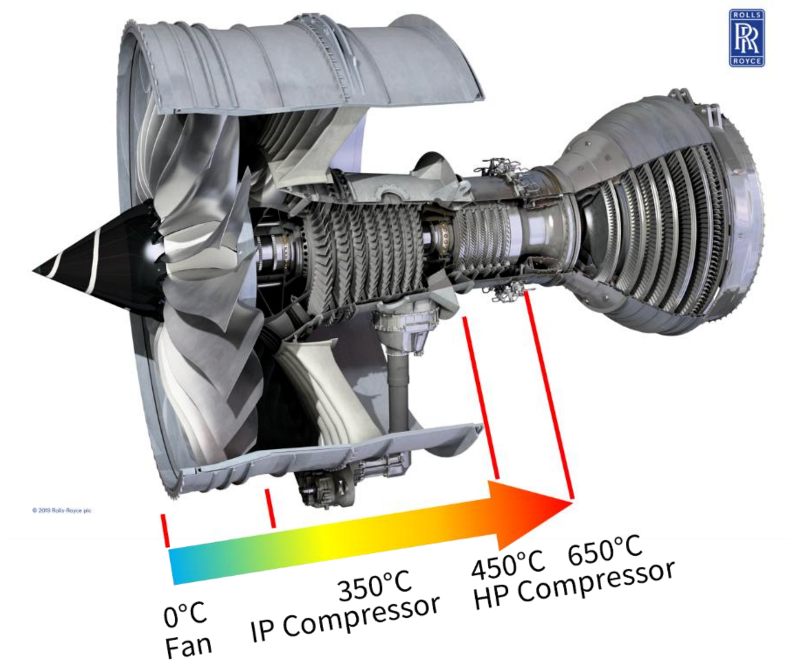

Figure 1.6 – Temperature distribution within an engine (12)

Because of this wide temperature range multiple different coatings are applied within the compressor, the coatings are selected based on the operating temperatures of that stage within the engine. Towards the rear of the High-Pressure Compressor the temperatures reach levels which exceed the operational limits of the Titanium blades, the blade material is also changed at this point to Inconel. Typical abradable and blade combinations used within the compressor are given in Table 1.1.

Table 1.1 – Location of abradable materials within an engine

Engine Location	Fan	Intermediate-Pressure (IP) Compressor		High-Pressure (HP) Compressor	
Abradable Material	Polyester	AlSi – Polyester (M601)	AlSi – Polyester - hBN (XPT268)	AlSi - hBN (M320)	NiCrAl – Bentonite (M314)
Blade Material	Titanium (Grade 5)				Inconel 718

As a further focus to the work the wear mechanics of Aluminium Silicon (AlSi) based abradables are specifically considered, and this study is therefore targeted at the Intermediate-Pressure and beginning of the High-Pressure Compressor.

1.2 Blade Wear Mechanisms due to Blade-Abradable Interactions

Abradable coatings have the potential to introduce large efficiency savings. However, in reality the cutting performance of the abradable is highly variable and can result in adhesions forming on the blades, leading to grooving on the abradable. In more severe cases the blades can wear, melt or even crack (Figure 1.7). These wear mechanisms are not unique to a single blade material but can be observed with both Titanium and Inconel blades, and all have a negative impact on the efficiency and reliability of the engine (13).

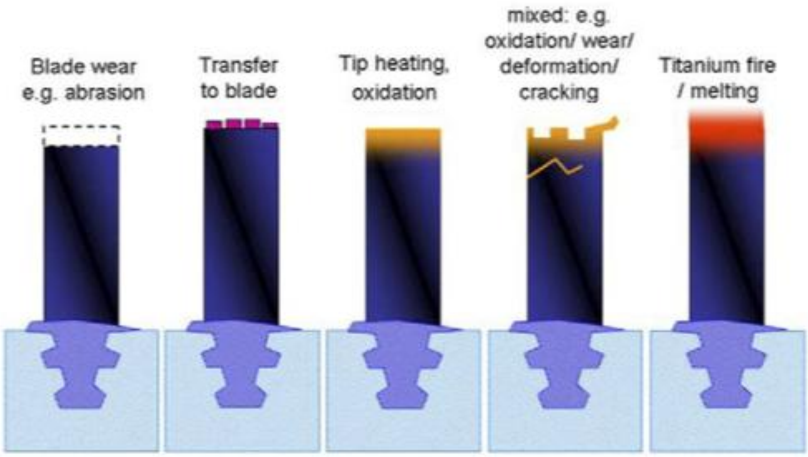

Figure 1.7 – Blade wear mechanics observed during blade-abradable contacts (13)

1.3 Impact of Wear on Gas Turbine Performance

When the blade wear mechanisms outlined above occur within an engine, they can have severe efficiency and safety implications. Due to the variable nature of the wear mechanisms across a blade front it is typical to see a combination of adhesion formation and blade wear. The resulting scored abradable (Figure 1.8A) results not only in air leaking around the blade, but the increased abradable roughness creates turbulent airflow at the casing, introducing further losses. Weakly bonded areas within the abradable can also be pulled out, leading to pitting and further roughness.

If severe adhesion events occur (as shown in Figure 1.8B), the abradable will become scored, but there is the additional risk of large chunks of adhered abradable breaking away from the blade and passing through the engine. These chunks can create clogs within the fuel injectors, leading to combustion instability and potential engine stall or surge events (14).

As temperatures increase the surface layer of the abradable or the blade can locally melt and can therefore be smeared outside of the rub track (Figure 1.8C). This results in an elevated region on the abradable surface, reducing tip clearance and increasing the risk of tip strikes occurring with additional blades.

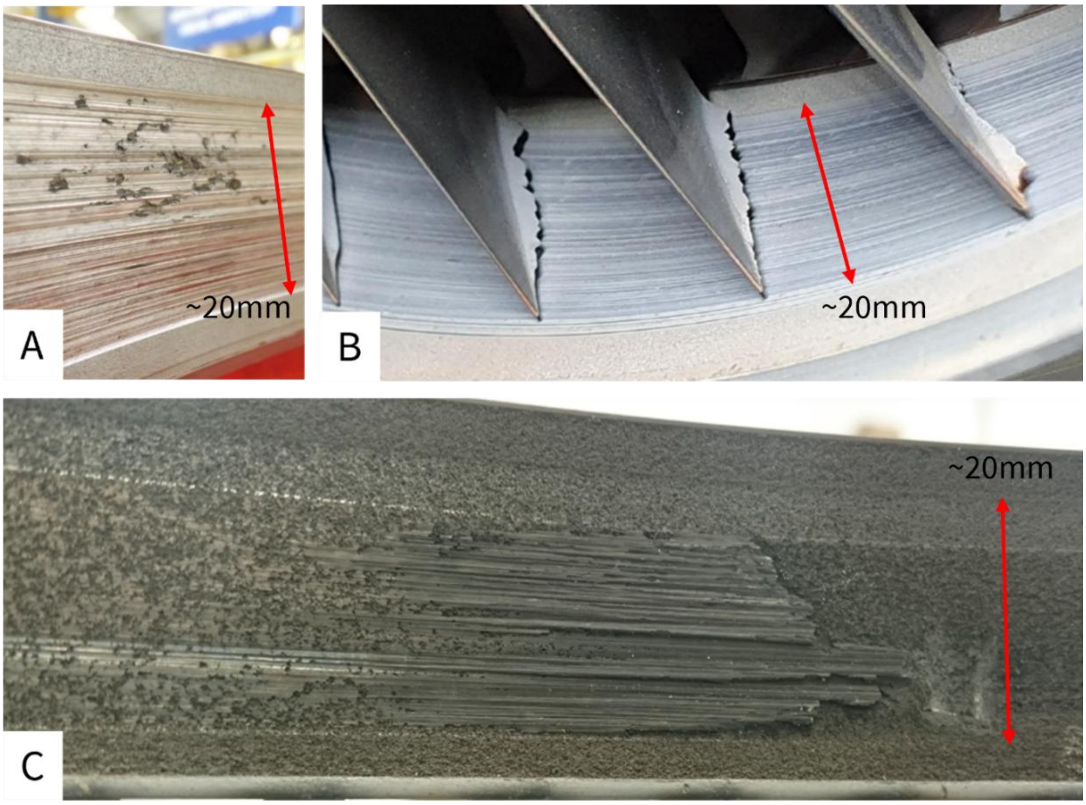

Figure 1.8 – Examples of poor abradable performance within an engine. **A –** Pitting on the abradable surface. **B –** Adhesive pickup on the blades. **C –** Smearing on the abradable surface

During more severe interactions, these tip strikes can produce high temperatures on the blade tips, leading to titanium fires. These fires occur suddenly and are difficult to extinguish, they have contributed to multiple aircraft crashes (15). An example of thermal damage on a blade tip is highlighted in Figure 1.9, with the tip showing decolouration due to high temperatures experienced during a tip-casing interaction.

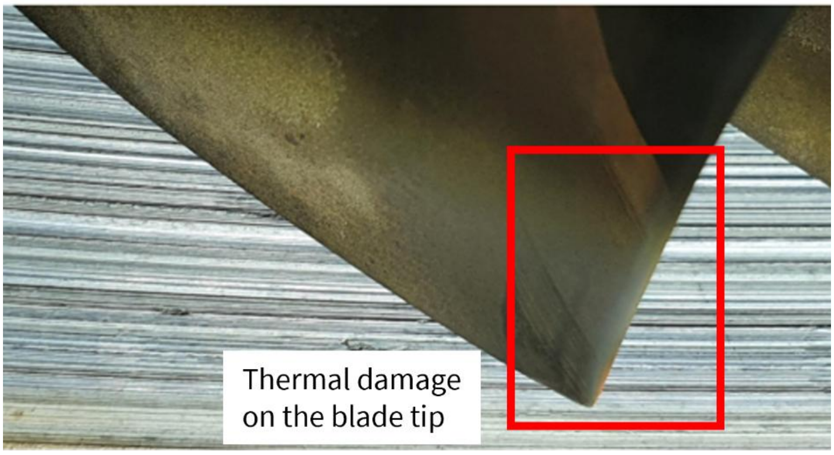

Figure 1.9 – Thermal damage to titanium blades following a tip strike

1.4 Aims and Objectives

The formation of adhesions on the surface of a blade can have significant impacts on the efficiency and reliability of a Jet Engine, with the impact of adhesions in the compressor adding further risks of engine stalls and surges. This has created urgency in the development of a better understanding in how engine conditions impact abradable wear, with wear maps being produced which allow engine manufacturers to target more favourable mechanisms.

Although the wear of AlSi based abradables has been well documented, there is still a limited understanding of why these mechanisms occur. Recent work looking at introducing in-situ monitoring of the wear has produced promising results which show the potential of these tools to provide a better understanding.

This thesis aims to develop novel in-situ measurement tools to apply during abradable rub tests, collecting and processing data which will allow for a better understanding of which material properties and operational parameters impact the wear of AlSi based abradables with a specific focus on adhesion events. With this understanding further testing can be completed, targeting areas which will allow for information on how these parameters can be adjusted to impact wear performance.

The objectives for this study are:

- Develop in-situ measurement tools to capture blade wear and temperatures during a test.
- Identify the key material and test parameters which impact adhesion behaviour.
- Complete testing to determine how modifying these parameters will impact the wear behaviours.
- Determine the impact of the dislocators to AlSi abradables in the commonly used materials: M601, M320, and XPT268.

1.5 Novelty and Impact

The novelty of this work stems from the development of in-situ blade wear and thermal monitoring tools which allow for the visualisation of the relationship between temperature and the wear performance of an AlSi abradable. Through the application of these tools, it will be possible to gain a better understanding of how a materials mechanical and thermal properties, and test conditions affect adhesion behaviours, and how these parameters can be modified to impact wear performance – capabilities not possible on any other abradability testing rig.

The results of this work will be applicable by both engine manufacturers and abradable researchers. A better understanding of the mechanisms which impact abradable performance will allow engine manufacturers to modify their designs to target, or avoid, certain wear mechanisms. While a better understanding of the relationships between temperature, force and wear behaviour will allow researchers to produce more accurate models, or open new avenues of research on how to optimise the blade abradable system based on its thermal performance.

1.6 Thesis Layout

Following the introduction, this thesis has been arranged following the development and application of novel tools to produce a better understanding of the wear mechanisms present with AlSi abradables.

Chapters 2 and 3 detail the starting point for this study as a literature review and methodology respectively. The literature review details the progress made by research groups around the world working to develop the understanding of abradables and their wear properties. Although it is focused on AlSi based abradables, there is further discussion on the different approaches taken when studying abradable systems. This ranges from computational modelling to tribological testing and high-speed spindle test rigs. The methodology then takes this further detailing the test rigs developed by the Abradables Research Group at the University of Sheffield and how they will be used in this study.

Chapter 4 details the development of novel in-situ measurement tools allowing for the blade profile to be measured alongside thermal imaging of blade and abradable, with initial results being analysed to demonstrate how these tools can be applied to develop a better understanding of abradable wear and how it develops throughout a rub.

Chapter 5 applies these tools to explore the previously unexplained behaviour of M601 at low incursion rates, demonstrating how the material does not follow traditional wear relationships at these conditions, and identifying that it is the materials thermal properties which lead to these discrepancies.

Chapter 6 explores how thermal properties can be further exploited by detailing the development of an abradable heater block which allows for control of abradable bulk temperature during a rub. The results of tests with M601 at varying bulk temperatures allow multiple studies of the mechanical properties of M601 to be drawn together to form a more comprehensive understanding of the material.

Chapter 7 repeats the testing completed in Chapter 6, but with two different AlSi based abradables, M320 and XPT268. The results from this chapter allow existing studies into AlSi abradables to be combined with the new understanding of M601, to form a better idea of the impact of each additive within a given material.

Chapter 8 brings together the results of the previous chapters into a general discussion.

Chapter 9 concludes this work, reviewing how well the aims and objectives have been met, and what future work has been unlocked by the findings within this thesis.

1.7 Project Timeline

The need for novel hardware and software tools to meet the objectives for this project dictated that the project timeline was front heavy in the development of new capabilities, before the key research outputs could be delivered towards the end of the work.

Although the development of hardware and software tools was a continuous, iterative process the key milestones within the project, and their completion date from the start of the project, are provided in Table 1.2.

All hardware and software tools developed in this project were designed to not only allow for the research outputs of this work, but also as a long-term solution which can be shared with the rest of the research group for wider application.

Table 1.2 – An overview of the project timeline with hardware, software and research milestones

Completion Date (months)	Hardware	Software	Research Output
6	Initial 3D printed front camera and strobe system. Thermal camera setup using laser tachometer to trigger at both blade and abradable.	Force processing. Align force, front, and side camera footage temporally. Homography tools for warping thermal camera footage. Separate the blade and abradable thermal camera frames. Align thermal and visible camera data spatially.	Feasibility study for the in-situ tools.
12	Permanent metal camera mount. Metal strobe mounts with dust and electromagnetic interference (EMI) shielding. Light gate triggers for the thermal camera to improve reliability.	Edge detection code for blade profile extraction. Introduce standard output data structure with common time and position arrays for ease of analysis. Align thermal and visible cameras temporally.	Chapter 4
18	EMI sealed enclosures for all electrical connections and for light gate signal processing hardware. Replace all cables with EMI shielded alternates to improve signal reliability within the camera triggering systems.	Area-based wear measurement tools. Abradable profile prediction from blade profile. Pyrometer processing.	Chapter 5
24	Design, manufacture and balance new disk.	Combine data into videos.	
30	Design and manufacture heating block.		
36		Pixel-based wear measurement tools.	Chapter 6
42			Chapter 7

2 Literature Review

This literature review aims to provide an overview of the current state of research into abradable coatings, with a focus on AlSi based abradable systems. Starting with a general overview of abradable systems and the demands that they are put under in operation, detailing the tests and standards used to ensure they are safe for flight. Building on this a review of different abradability testing solutions is included, highlighting the benefits and drawbacks of each approach. With the final section, following an overview of the AlSi based abradables, being a focused review of the current level of understanding of M601 wear mechanisms. The objective of this review is to gain an understanding of where there are gaps in the understanding of M601 wear mechanisms, and what tools could be developed to fill these gaps.

2.1 Introduction to Abradables

Abradable coatings have long been in the spotlight as a key technology in the pursuit of efficient jet engines, with a 1979 report by NASA predicting a potential 1.5% specific fuel consumption saving through their application. However, they did also acknowledge that these coatings can introduce addition risk to the engine and that to be safely used any debris must be limited in size to 0.254mm and coatings must be able to survive erosion for 10^4 hours of operation (16).

The need for an abradable coating to be both soft enough for a blade to cut without damage or creating large debris, while also being able to resist the stresses of the tip strikes and erosion damage means a solid material is not feasible. Instead abradable materials take the form of a composite material, typically formed with an interlinked metal frame to resist stresses and a softer dislocator phase to soften, and to increase the friability of the material (Figure 2.1B)(16,17).

However, as an added complication these materials are often used on the inside of engine casings, or within labyrinth seals, and thus are applied to complex geometries in confined spaces. The coatings are therefore provided by the manufacturer in the form of a powder (Figure 2.1A) which is then sprayed onto the component using methods such as atmospheric plasma spraying and combustion spraying (18). These application methods work by heating the powder to a molten state and then accelerating the molten droplets towards the substrate. Upon contact with the substrate the high energy droplets cool rapidly and flatten to form a coating which gains it cohesion strength from mechanical interlocking of the splats. To ensure good adhesion to the substrate a thin bond coat is typically applied to the substrate before the coating is applied.

Although these methods do allow the coatings to be applied, and through control of the spray parameters the global material properties can be reproduced consistently, the microstructure is inherently random with the distribution of the different phases, porosity and cracks differing between samples.

The nonuniformity within the microstructure results in some nonlinearities within the mechanical properties, with Ma and Matthews (19) observing progressive failure occurring during tensile testing of various abradable samples (Figure 2.2). When testing with M601 they were able to observe plastic deformation occurring at loads as low as 1.88N.

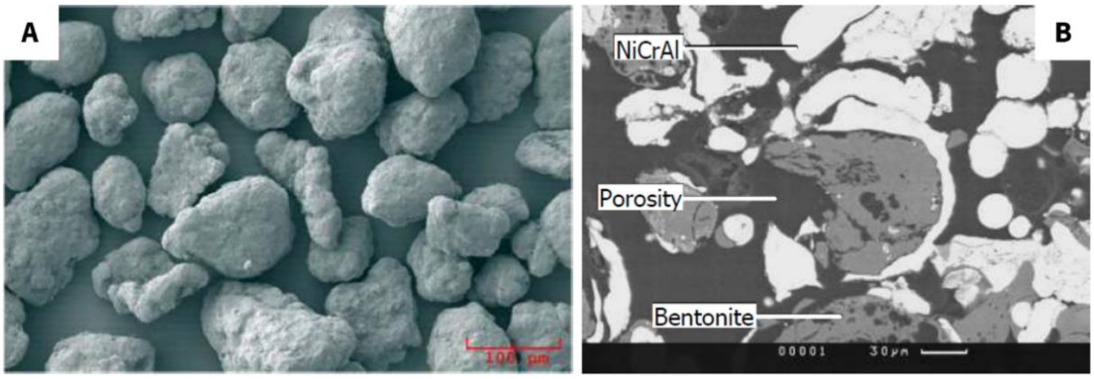

Figure 2.1 – The powder (A) and as sprayed microstructure (B) for a NiCrAl Bentonite abradable (20)

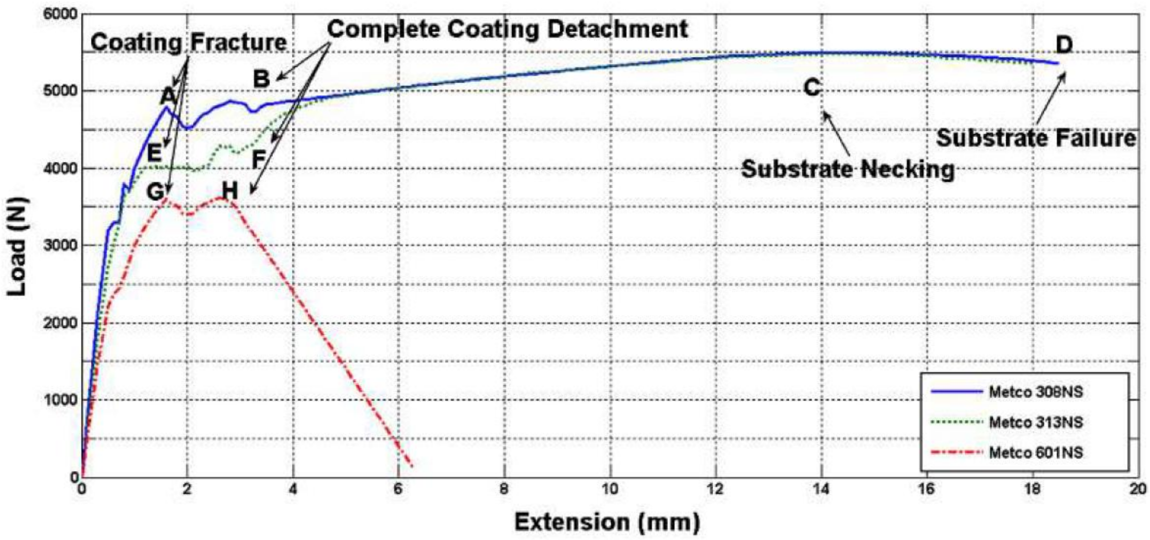

Figure 2.2 – The stress strain curves measured during tensile tests for a range of abradable coatings (19)

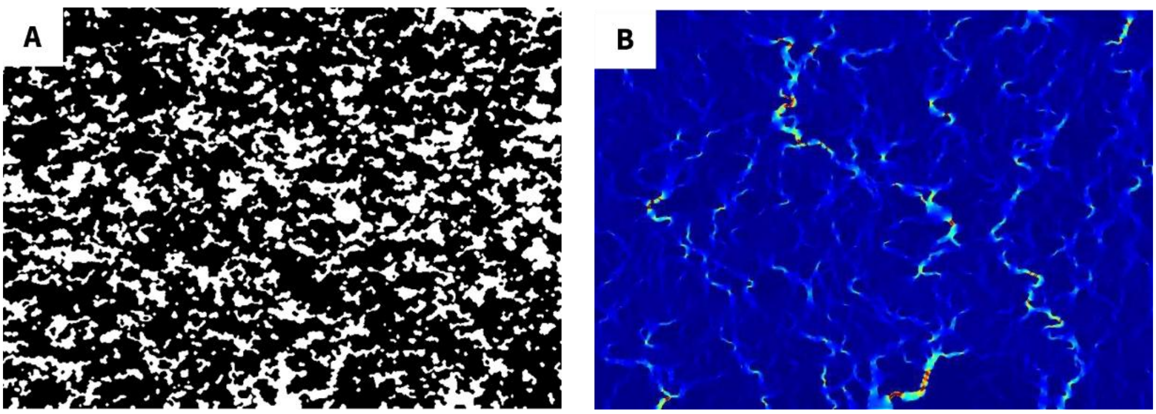

Figure 2.3 – A – A normalised image of a Durablade 1605 abradable, with the metallic phase in white. **B –** The modelled heat flux through the material (21)

Watson et al. was also able to determine that for M601 and M320 the metallic and dislocator phases did not bond well together thermally (22), this restricts the flow of heat through the abradable to the connected metallic chains. Thermal models, such as that created by Bolot et al. (21) allow this to be visualised, with the output shown in Figure 2.3.

The impact of the variability of abradable coatings was observed by Borel et al. during a detailed investigation into the wear within operational engines fitted with these coatings (23). Findings highlighted that not only were the coatings producing large scale debris but were also leading to significant blade damage and were introducing inefficiencies into the engines. This study prompted researchers such as Novinski (24) and Wilson (13) to develop a more detailed set of criteria with which to evaluate the performance of abradable systems. The key criteria for a successful abradable are, in order of priority:

- Abradables must have sufficient bond strength that they do not delaminate during operation.
- Abradables must resist erosion from debris ingested by, or created within, the jet engine.
- Abradables must possess good abradability, limiting wear of the blade.

With a set of criteria in place work could be completed to both quantify, and understand, how different coatings perform.

2.2 Demands on an Abradable Coating within a Gas Turbine

The need to understand and quantify the erosion resistance of abradable coatings led to the parallel development of bespoke erosion test rigs. Each of these rigs approached the problem differently, with varying impingent angles, particle sizes, and temperatures (25–27). They did however allow for an improved understanding of the mechanisms of erosion wear within abradables.

A strong theory of the mechanisms of erosion wear was presented by Maozhong et al. (28) using results collected on a bespoke erosion test rig capable of testing at varying impingement angles. They found that at an impingement angle of 90° material removal was primarily due to extrusion and work hardening of the metallic phase, but at lower impingement angles this mechanism shifted to ploughing and tunnelling under the metallic phase through channels of the softer dislocator (Figure 2.4).

The data collected from these rigs allowed for the formation of a robust understanding of the erosion mechanisms, but their differences prevented the direct comparison of the performance of different coatings. In response General Electric proposed a standard erosion test for use with abradables (29,30), this standard is now commonly used within the field.

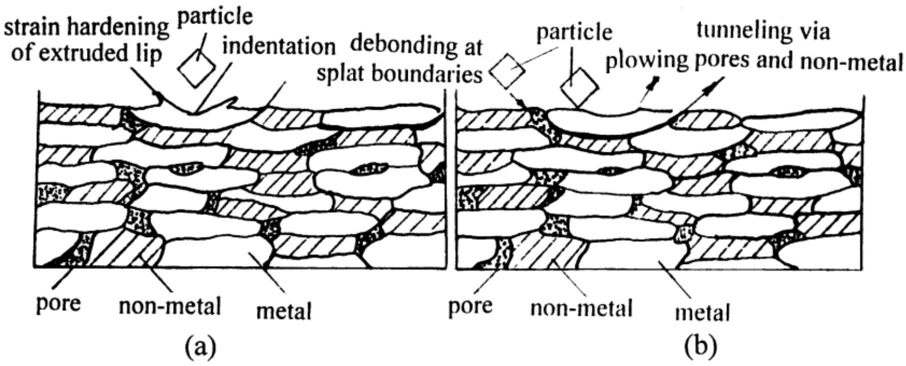

Figure 2.4 – Erosion wear mechanisms for abradables under 90° (a) and 30° (b) impingement angles (28)

The General Electric erosion test standard (E50TF121CL-A) makes use of a simplified set-up shown in Figure 2.5. The abradable sample is placed 100mm from a blast gun with an impingement angle of 20°, 600g of 50µm Al_2O_3 particles are then fired at the sample with a gas pressure of between 0.19-0.24MPa. Following the test, the test duration is divided by maximum depth of erosion into the sample, measured in thousandths of an inch (mil), this produces the ‘‘GE erosivity number” $E^{\#}$ in s/mil.

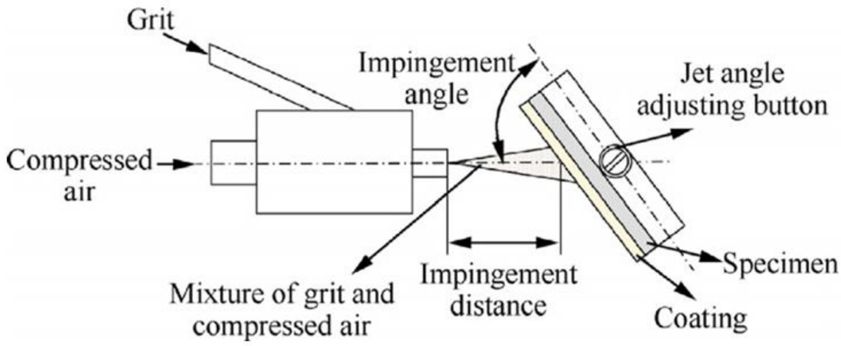

Figure 2.5 – Schematic for the standard GE erosion test rig (30)

With a standard in place to allow for direct comparison between different abradable coatings Schmid et al. was able to complete a comprehensive review of abradable erosion performance within the compressor. They were able to determine that for an abradable installed in the compressor the minimum erosion resistance required was an $E^{\#}$ value of 1 s/mil (17).

The work completed by Schmid et al. provided a hard limit for erosion resistance, a limit which could be applied to work completed by Wilson, who investigated the impact of hardness on erosion resistance (Figure 2.6), to provide a lower limit on the hardness of abradables (13). By applying abradables harder than these lower limits engine manufacturers can ensure that the coatings will meet the criteria of resisting erosion within the engine.

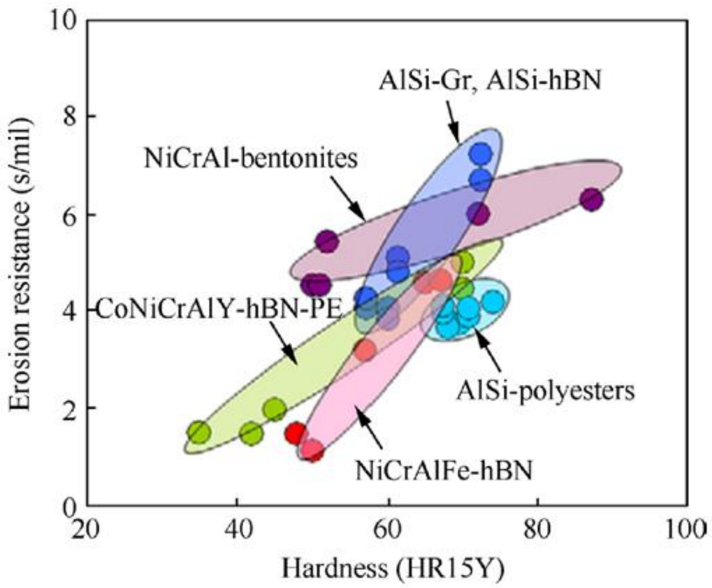

Figure 2.6 – Relationship between erosion resistance and hardness for a range of abradable coatings (13)

To determine the minimum abradable bond strength, as with erosion resistance, a standard test was required (31). A standard was put forward by the American Society for Testing and Materials (ASTM C633) and takes the form of a tensile test on a coated sample between two cylinders (32). When preparing samples for the test the abradable material is sprayed onto one cylinder, which has had its surface prepared and a bond coat added in the same manner as the casing is prepared in the engine. The second cylinder is bonded to the abradable coating using an adhesive, ensuring the abradable sample is thick enough for the adhesive to form a strong bond. During the tensile test the resulting bond strength is either a measure of the adhesive strength between the coating and the substrate if the coating fails at the bond, or the cohesive strength of the abradable if the coating fails within the abradable itself. If the sample fails at the adhesive, the result is not a valid representation of the abradable strength and must be repeated.

The results from testing done to this standard allowed for trends between the hardness and the bonding strength of an abradable, with Dorfman et al. showing that these two properties are proportional to each other (33). However, higher hardnesses often lead to poorer abradability (16), making it difficult to set a minimum hardness for bond strength without also considering the abradablity of the sample.

As the stresses within the coating are often highest during a tip rub, instead of setting a hardness limit based on bonding strength, it is better to consider this alongside abradability. The hardness of the coating should be maximised, to improve bond strength, while ensuring the coating performs well during a tip rub (34).

To investigate the abradability of different coatings it is first important to understand the conditions during the rub, with a key parameter being the incursion rate. Unfortunately, testing and monitoring within a real engine is technically challenging and cost prohibitive meaning there is very little published work. One work package completed on real engine hardware was completed by Batailly et al. (35,36) who monitored the incursions of a blade in a single compressor stage, the incursion rates were however normalized for confidentiality.

Although no values for incursion rates were presented, this work did lead to the development of a numerical model for the interaction between the blade and the casing over multiple rotations (37). This model demonstrated how a single blade-abradable contact could lead to vibrations within the blade, these vibrations will then lead to further tip rubs as the blade rotates. As the blade is twisting during this process the rub depth can vary at different positions on the blade (Figure 2.7) (38). Nyssen et al. then developed this further to show how temperature distributions and initial tip clearances could impact the incursion profiles (39).

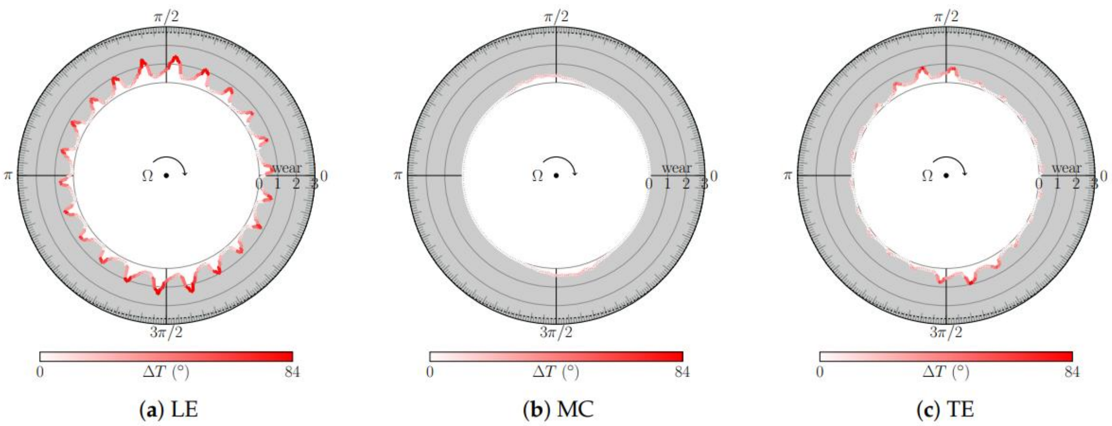

Figure 2.7 – Prediction of abradable wear at the leading edge (a), mid chord (b) and trailing edge (c) of the blade (39)

While the results which were published highlight the importance of the dynamics between the blade and the casing, the lack of incursion rate values limit its applicability in the research of abradability. Instead, incursion rate values have been provided by engine manufacturers based off numerical models and inspection of test engines. Rolls Royce have stated that incursion rates due to blade growth are between 0.01 – 0.2µm/pass (40), and that they can target higher incursion rates, in the order of 2µm/pass, during run in by varying the number of cutting blades and the engine spool rates.

2.3 Determining the Abradability of a Coating

Outputs from real engine studies and information provided by engine manufacturers provided an understanding of the wear problem, including rub conditions and examples of the post rub wear. This understanding could then be used as a baseline when developing lab-based methods to determine the abradability of different coatings.

2.3.1 Tribological Studies of Abradability

One approach to the problem is to test coatings using simplified rub test set-ups. These tests do not aim to replicate the rubs which occur within the engine but instead to create repeatable conditions which produce a wear response analogous to that seen within the engine.

An example of this type of testing would be the scratch testing rig developed by Liang et al. which was applied to quantify the abradability of different coatings and aligned well with wear seen within engines (41). These studies were then developed further by Ma et al. to create the 'Progressive Abradablity Hardness' metric, which looked to create a standard test which could be applied to compare different abradable coatings (19).

To measure the Progressive Abradability Hardness (PAH) a diamond cone indenter is scratched across the sample with an increasing normal load, a PAH value can be calculated from the measured forces. They showed that the results allowed for comparisons between materials and predicted abradability which aligned with results seen from within industry but could not replicate or predict the wear mechanisms within engines (42).

While PAH allows for comparison between coatings, all scratches are completed using a diamond indenter, removing the interaction between the blade material and coating. An alternate test is the Ball on Disk (43) or Ball on Flat (44) test. These tests are completed using balls of the same material as the blades which leads to adhesion formation on the ball, wear mechanisms closer to those seen within the engine. Examples of the wear scars which can be produced in these tests are shown in Figure 2.8.

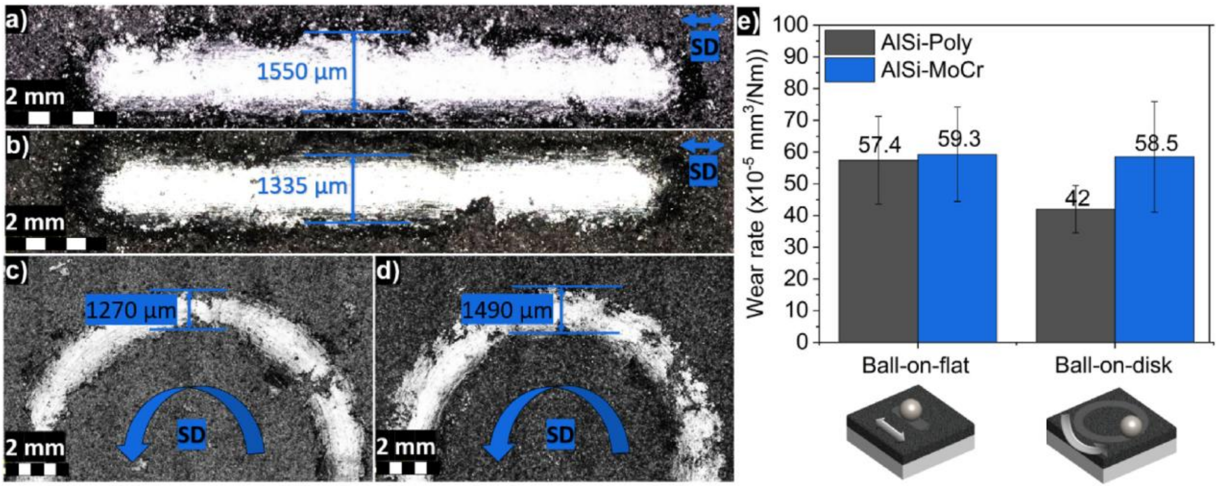

Figure 2.8 – Standardized results from ball-on-flat (a, b) and ball-on-disk tests (c, d) for AlSi-Polyester and AlSi-MoCr Abradables and a comparison of the wear seen for each material (e) (45)

Further work, such as that completed by Pellegrino et al. (46,47), has taken a more fundamental approach to measure the mechanical properties of different coatings. These properties were measured at a range of strain rates using both universal testing machines and the Split-Hopkinson Bar. While it has been shown that it is not possible to predict abradablity from trends in mechanical properties alone (42), they can form the foundation for wear models.

2.3.2 The use of Modelling to Predict Abradability

Material testing of abradables can allow for comparison between coatings but does not predict how the blade and coating with respond during a tip strike. However, with the measured material properties it is possible to make models which can attempt to predict this.

An example of these models was created by Wang, who modelled the temperature of the blade and abradable over successive rubs and then, based on the changing material modulus, predicted wear based on a purely abrasive model (Figure 2.9)(48). These results provided a novel insight into the conditions at the contact point but due to the simplistic wear model did not produce results which aligned with observed wear in the engines.

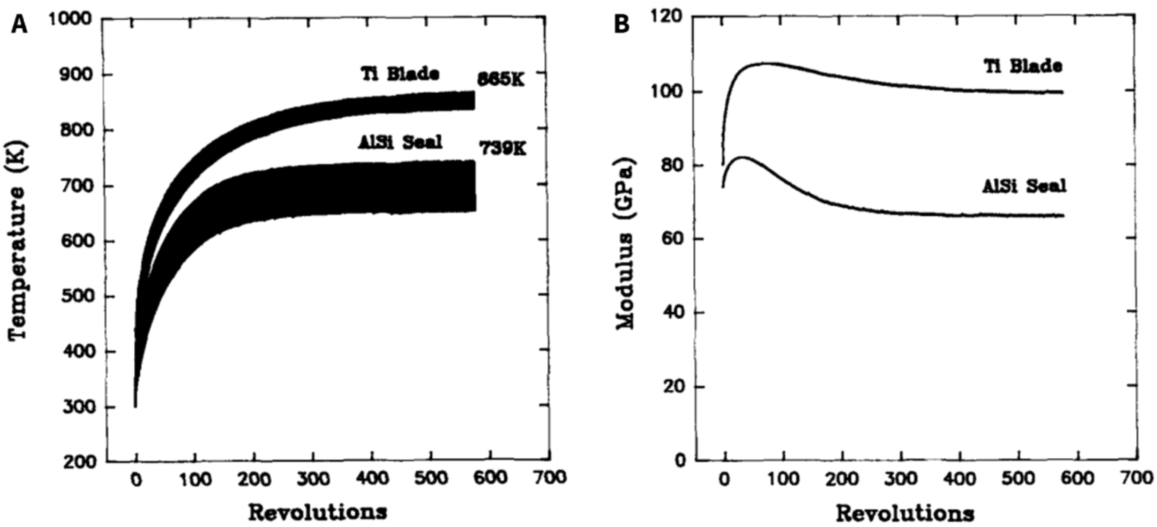

Figure 2.9 – Predicting the temperature (A) and modulus (B) for the blade and abradable during a rub from a numerical model (48)

Attempting to build on these models, Berthoul et al. created a more complex wear model based on the observations made by Borel et al. (23). By combining this wear model with the rotor dynamics model created Legrand et al. (37) they were able to produce results which aligned with wear seen within an engine. However, to achieve these results the model parameters had to be finely tuned, with these parameters being unique to the coating. To allow these models to be more versatile, more experimental work is required which will enable models to be tuned to a wider range of materials (49).

While models for the wear and blade-abradable interaction are still in their infancy, models predicting the mechanical and thermal properties of coatings are becoming increasingly mature.

Applying models created by Bolot et al. (50,51) and Watson et al. (22) it is possible to predict the thermal properties and the density of two-phase abradable coatings based off SEM or optical images of the abradable microstructure. These models have all aligned well with experimental results.

Similar models developed by Faraoun et al. (52,53) attempted to predict the mechanical properties of coatings based on SEM images but could not validate the results. These models have since been developed further by Cheng et al. (54) who created a Finite Element Analysis model and applied it to a 3D model of a 2 phase abradable captured using X-Ray Computed Tomography (xCT). This model produced results which aligned well with experimental results and allowed for predictions to be made on the impact of temperature or changes in the microstructure.

While modelling methods now allow for the prediction of material properties, the ability to relate these properties to the wear which occurs within an engine is limited to only a few conditions and materials. To better predict the wear which will occur within an engine therefore requires more representative testing.

2.3.3 Rub Testing of Abradables

The need for more representative testing has led to the development of multiple abradable testing rigs, with each design focusing on different applications or rig capabilities. A selection of test rigs and their focusses are shown in Table 2.1.

Table 2.1 – List of abradable testing rigs

Design Focus	Rig	Blade Tip Speed (m/s)	References
Labrinth Seals	Karlsruhe Institute of Technology	-	(55)
	Université de Toulouse	-	(56,57)
Projectile	Université de Lorraine	120	(58–60)
Engine Representative Blades	Technische Universität Dresden	Not Stated	(61,62)
	The French Aerospace Lab	95	(63–65)
Engine Representative Speeds	Oerlikon Metco	500	(13,18,66)
	NRC Institute for Aerospace Research of Canada	425	(31,67)
	Beijing General Research Institute of Mining and Metallurgy and Zhejiang University	520	(68–71)
Reduced Scale	The University of Washington	100	(72)
	The University of Sheffield	200	(73–81)
		330	(40,82)
	IMR of Chinese Academy of Sciences	150	(83,84)
	Praxair Surface Technologies	150	(85)
	AVIC Beijing Precision Engineering Institute for Aircraft Industry	350	(86)
	Concordia University	50	(44,45)

Within the engine, abradables are not only applied between the blades and casing but can also be found within the labyrinth seals used to protect components on the shaft, such as bearings, from the high-pressure air. The conditions within a labyrinth seal differ from those seen at a blade tip, therefore bespoke test rigs have been developed. Examples of labyrinth seal test rigs are shown in Figure 2.10.

More commonly the abradable test rigs focus on the blade-liner interaction, building on the limitations of the scratch testing by bringing test conditions closer to those seen within the engine. One such approach is to make use of a projectile test rig, as done at the Université de Lorraine, to fire a test blade at an abradable sample to generate a high-speed scratch with representative materials (Figure 2.11). This set-up can reach higher speeds than a standard scratch test, and by using samples with materials like those within the engine is able to produce more engine representative wear. However, by only completing a single pass the impact of abradable compaction over successive rubs is not included, limiting the ability of this rig design to simulate the wear which occurs within the engine (58).

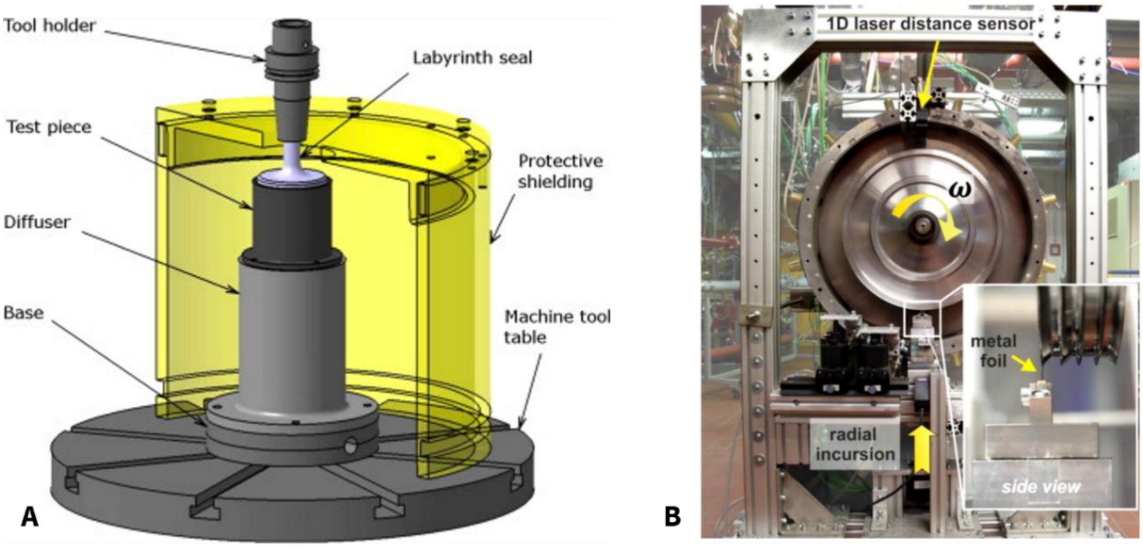

Figure 2.10 – Rigs to test abradable performance within labyrinth seals at **A -** Universite de Toulouse (56) and **B -** Karlsruhe Institute of Technology (55)

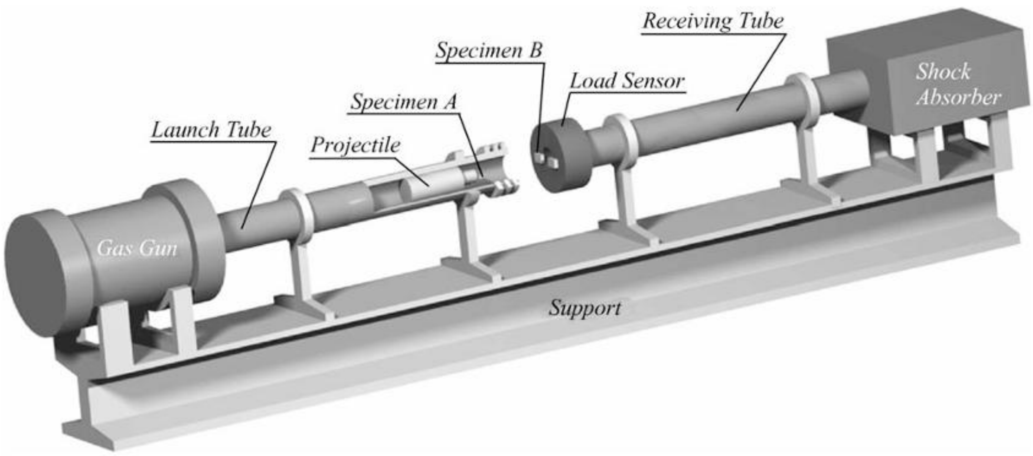

Figure 2.11 – The projectile test rig at the Universite de Lorraine (58)

An alternative approach is to use a rotating test rig which takes a blade and abradable sample, fixes one to a rotating disk, and then pushes the other into it at a set incursion rate. Rigs of this design can better replicate the rub within an engine by simulation the repetitive impacts which occur but can quickly become complicated when trying to accurately replicate the exact conditions within an engine.

To fully replicate the conditions at the blade-liner interface the blade speeds and the sample temperatures will need to be the same as those in the engine, the incursion rate of the blade into the sample will also need to be controlled. However, as shown in the numerical models created by

Legrand et al. (37), the incursion rate is not uniform and instead varies around the casing due to vibrations within the blade. These vibrations can be included into tests by using blades of the same geometry as those used in the engine or, in the case of the rig at the French Aerospace Lab, blades with a geometry designed to mimic the stiffness of real engine blades. Examples of this style test rig are shown in Figure 2.12.

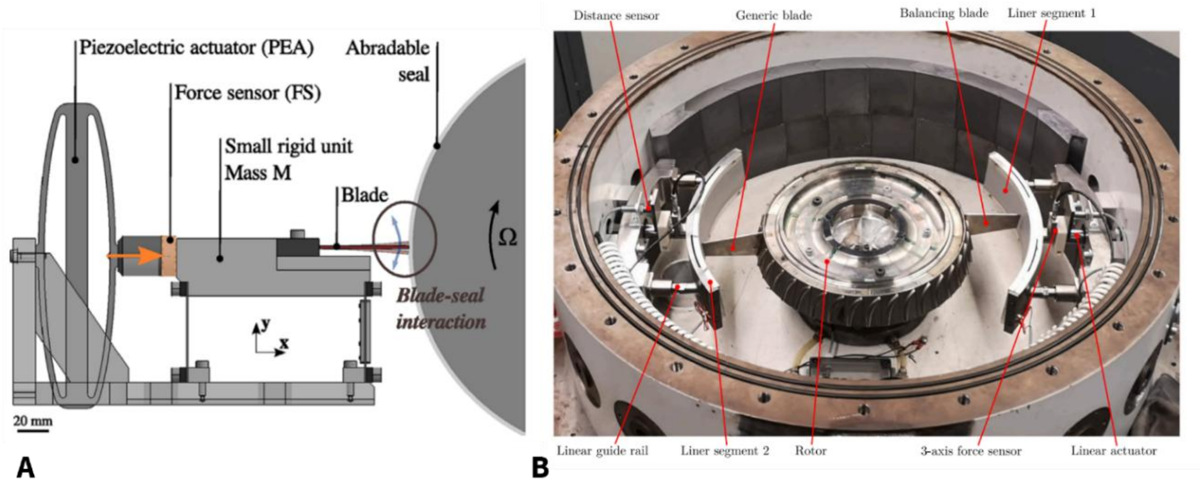

Figure 2.12 – Test rigs with engine representative blades at **A –** The French Aerospace Lab (63) and **B –** Technische Universität Dresden (61)

These rigs can produce engine representative wear, and the outputs of these tests can be used to measure forces and vibrations imparted by the tip rubs onto the rest of the engine. However, the additional complexity in trying to mimic the real engine stiffness increases the complexity of the samples and setup, leading to increased test costs and setup time. The additional impact of the varying incursion rate due to vibration is that the data is difficult to abstract, making it hard to extract relationships between incursion rate and wear mechanisms.

Due to the additional challenges involved in rigs with engine representative stiffness the most common design of abradable test rigs make use of samples with simplified geometries. An example of this rig style is shown in Figure 2.13.

These test rigs function by fixing the test blade into a disk which is spun by a spindle motor or an air turbine, the sample is then pushed into the path of the blade using a motorised stage. Although the rigs all follow a similar base design, they differ in their capabilities and instrumentation.

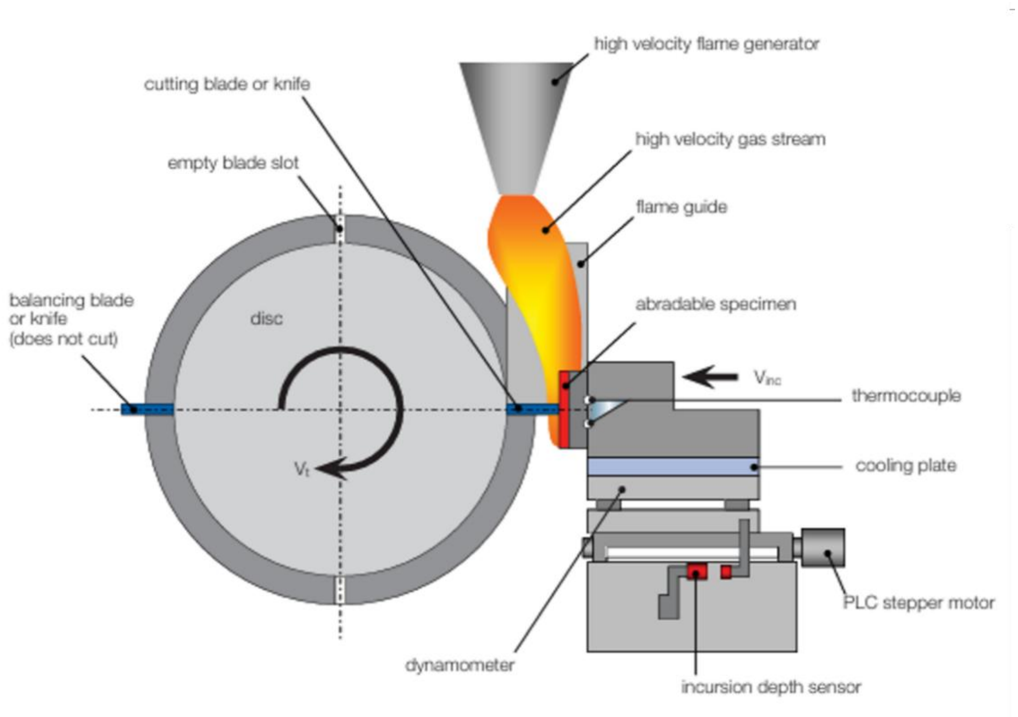

Figure 2.13 – The high-speed spindle test rig developed by Oerlikon Metco (13)

One avenue of rig design focuses on replicating real engine speeds, with the rig developed by Oerlikon Metco going further to replicate engine temperatures with an Oxy-acetylene torch to heat blades up to 1100°C. This rig has been used extensively by Borel et al. (23) and Bounazef et al. (87) to test a range of abradables at varying conditions. The blades and abradable samples were analysed before and after testing allowing for the different wear mechanisms to be identified and linked to different test conditions. This knowledge is vital when evaluating which abradables should be used in different parts of the engine but is not able to provide sufficient information to understand what causes the different wear mechanisms observed. Although these rigs can produce engine representative wear, their complexity increases test setup time and makes data collection during a rub challenging.

A second approach looks to remove complexity from the problem by moving away from replicating exact engine conditions and instead designing small scale rigs which operate a lower speeds and temperatures. With rigs of this design, it is possible to simplify the test process, reducing test time and cost. This allows for rapid testing of different abradables at varying test conditions, the results from these tests allow for more data to be extracted on how test conditions impact the wear of different abradables. Although the forces measured on these rigs will not the same as those experienced by a real engine, the wear results are consistent with those seen in the engine (85). This provides sufficient information to map how abradable performance varies with test conditions, information which can be applied directly by engine manufacturers when running in their engines (77).

The understanding of how test conditions effect wear mechanics was developed further through the introduction of in-situ measurement techniques. An example of this is shown in the work by Fois et al. (77) and Rahimov et al. (79) where stroboscopic imaging was used to capture a side on and front on view of the blade. Using this tool, the profile of the blade can be measured during a test, providing further knowledge not only on what wear has occurred, but also how that wear develops during a test.

These methods have been vital in identifying how different conditions affect abradability, and which operating regions lead to unacceptable outputs. The results from these rigs also allow for the knowledge gained from the more fundamental tribological testing to be applied to create theories on why the abradables exhibit certain behaviours.

2.4 Material Studies Completed on AlSi Abradables

In the low and intermediate compressor of a gas turbine titanium blades are typically used, this has resulted in the creation of a range of 'titanium safe' abradable coatings. Most of these are based on an AlSi metal matrix which has been selected for its low shear strength (88).

However, AlSi alone has been found to perform poorly, with dense coatings producing large amounts of blade wear as well as adhesive transfer (70). To improve the performance of these coatings, secondary phases (known as dislocators) have been added. Commonly used dislocators are polyester, graphite, and hexagonal Boron Nitride (hBN).

Coatings which are typically found in modern gas turbines are Metco 601 (AlSi-Polyester), Metco 320 (AlSi-hBN), and XPT268 (AlSi-Polyester-hBN), these coatings are therefore the focus of this thesis. While all three of the coatings are predominantly formed of AlSi, they each exhibit unique wear properties and as a result have become the subject of many material studies.

2.4.1 Material Studies on Metco 601

Metco 601 (M601) improves on the performance of AlSi alone through the addition of polyester as a dislocator. M601 is purchased as a blended powder with the composition and particle sizes given in Table 2.2 and is then applied as a coating using an atmospheric plasma spraying process (89), the resulting microstructure is shown in Figure 2.14. By adjusting the spray parameters, the ratio of AlSi to Polyester and voids can be adjusted, with higher polyester fractions producing a coating with a lower hardness (22).

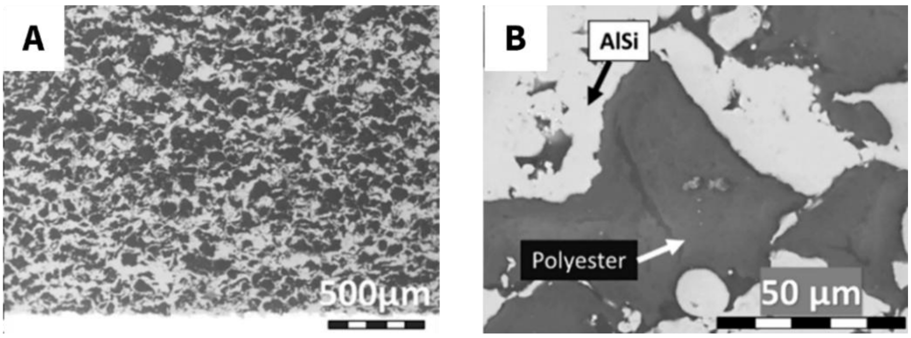

Figure 2.14 – An example of the Microstructure of M601 captured optically (A) and with an SEM (B) (44)

The hardness of the sample has been seen to impact the abradability of the coating, with lower hardness coatings producing lower cutting forces and temperatures which then leads to a reduction in adhesion formation on the blade. Ghasripoor et al. showed that increasing the ratio of polyester does however reduce the bond strength and erosion resistance of the coating, limiting the minimum hardness level suitable for use within an engine (90).

Table 2.2 – Manufacturer supplied properties for M601 (89)

Powder Composition	Al (Balance) Si (7%) Polyester (40%)
Powder Particle Size (µm)	125 – 136
Maximum Operating Temperature (°C)	325
Typical Hardness Range (HR15y)	60 – 75
Bond Strength (MPa)	8 – 11.5
Erosion Resistance (s/mil)	4 – 5

Testing completed on high-speed spindle test rigs, such as that completed by Borel et al. (23), have shown that the wear mechanisms which occur during a blade-liner interaction vary significantly with changes in incursion rate and tip speed. This information is typically presented in the form of wear maps, examples of these are shown in Figure 2.15.

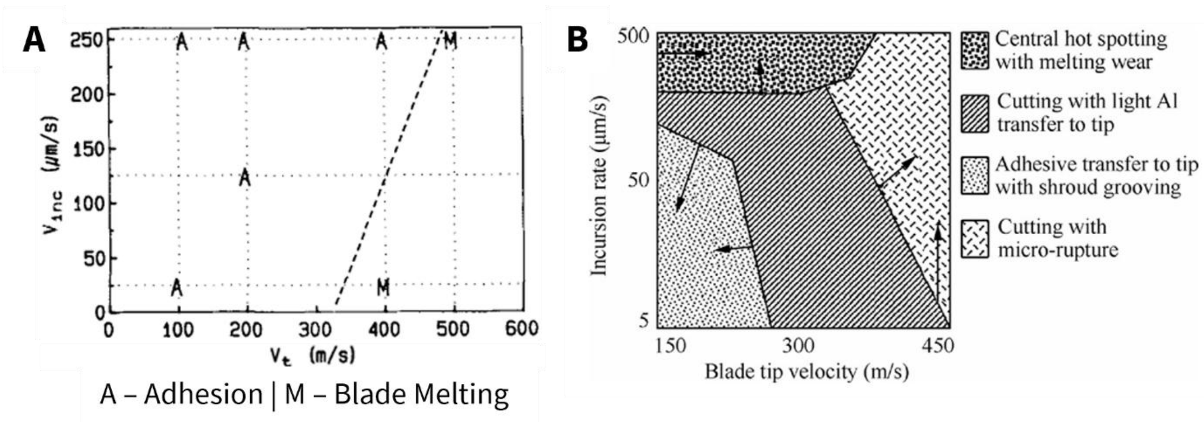

Figure 2.15 – Wear maps for an AlSi-Polyester abradable created by Borel et al. (A)(23) and Chupp et al. (B)(91)

Borel et al. observed that tip rubs against M601 will lead to adhesion formation at low blade tip speeds with a transition to blade wear as speeds increase (Figure 2.15A) (23). This work was taken further by Chupp et al. who created a wear map with a higher resolution, showing a region of good cutting when blade tip speeds reach ~300m/s. They also trialled alternative polymers to replace the polyester phase, and found that with a stiffer polymer the transition boundaries on the wear map would move in the direction of the arrows in Figure 2.15B, resulting in a larger region of good cutting (91).

Although these wear maps allow for the impact of rub conditions on wear to be visualised, it can be seen in Figure 2.15 that these maps do not align in their predictions. This is likely due to them being completed at different, undisclosed, hardnesses. However, they were also completed using different test rigs but have presented the incursion rates in μm/s. As the disk diameter changes between rigs a set tip speed will result in different angular speeds, this will lead to the rig with the smaller disk producing more rubs per second. By recording the incursion rate in μm/s a rig with a smaller disk will be making smaller incursions per pass than a larger disk at the same tip speed. A more comparable measurement is μm of incursion per pass of the blade (μm/pass).

A large investigation into the impact of material properties and test conditions, building on the previously completed wear maps, was completed by Rahimov (82). Rahimov tested M601 samples at a range of hardnesses at tip speeds varying from 100 – 320m/s and incursion rates from 0.02 – 2μm/pass. He found that, while tip speeds did have some effect on wear, the behaviour of M601 is mostly driven by changes in hardness and incursion rate.

The impact of hardness was seen to align with earlier work by Ghasripoor et al. (90), with softer samples producing fewer adhesions, resulting in smoother rub surfaces. However, a more significant change in the wear performance could be seen with varying incursion rates. At low incursion rates (0.02μm/pass) there was little adhesion on the final blade, instead there was significant amounts of blade wear. As the incursion rates increased to 0.2μm/pass the amount of blade wear reduced and adhesions could be seen on the blade, at 2μm/pass the volume of adhesions increased further with very little blade wear visible. Examples of the resulting wear tracks from these tests are shown in Figure 2.16.

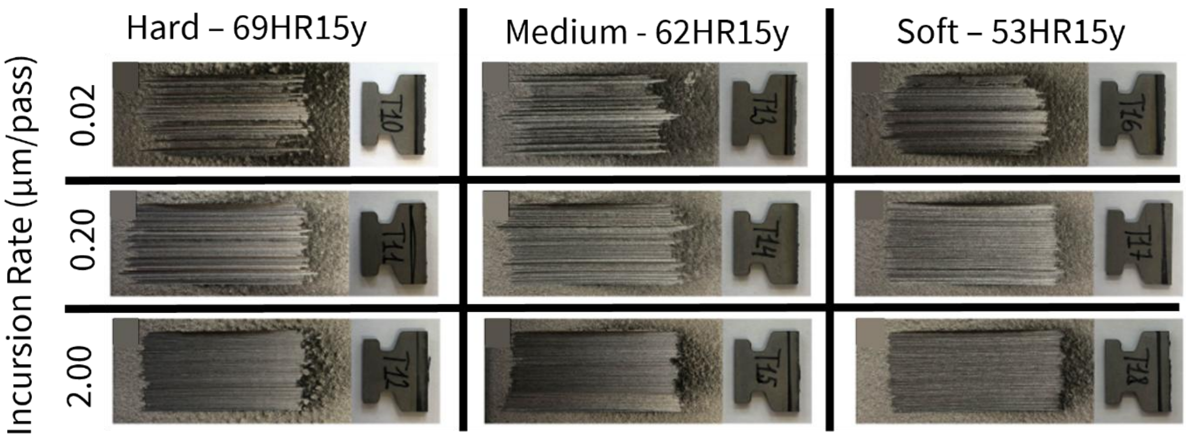

Figure 2.16 – Wear scars created during 200m/s M601 tests at varying incursion rates and hardnesses (82)

To explain the change in wear behaviour with incursion rate statistical models, such as the one created by Watson and Marshall, were developed based off the results of testing completed at varying incursion rates. The model was founded on a theory that the mechanism for material removal changes with incursion rate. At low incursion rates (0.02μm/pass) the abradable is compacted, adhesions from on the blade and then the material is released from the trailing edge of the blade. At higher incursion rates (0.2 – 2μm/pass) the blade can cut the abradable more efficiently, leading to material being ejected from the front of the blade (74).

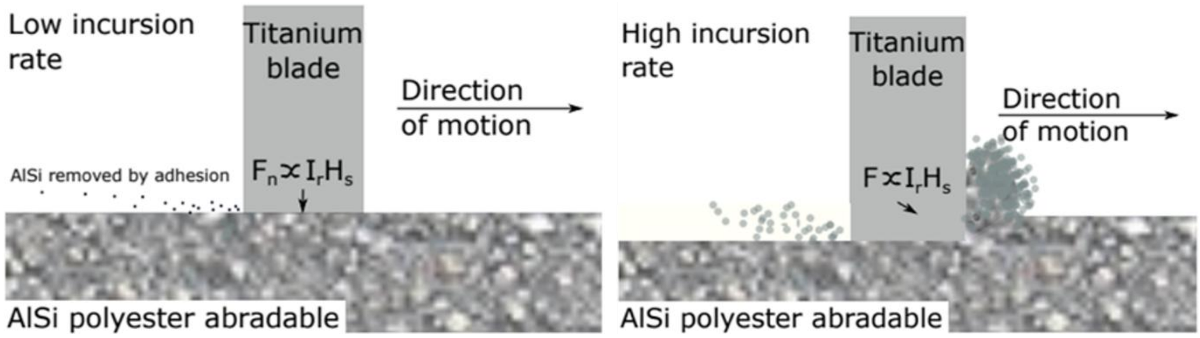

Figure 2.17 – Differences in the material releases mechanisms at low and high incursion rates for M601 (40)

This theory was confirmed by Hadjisoteriou who applied stroboscopic imaging tools to monitor the wear debris ejection during tests with varying incursion rates. He was able to observe an increase in material being ejected from the front of the blade as incursion rates increased, aligning with the theory proposed by Watson and Marshall (92). It was also observed that this trend was dependant on the material hardness, with harder materials producing more constant debris distributions across the range of incursion rates.

Although the theory of changing release mechanism was proved to be correct, the statistical model was only able to predict forces, temperatures, and wear rates for tests at 0.2μm/pass. With the data collected during these tests it could not be determined why tests at higher and lower incursion rates did not follow the model.

To build on this Rahimov et al. installed an in-situ front on camera to the spindle test rig allowing for the blade profile to be monitored during a test. They showed that the wear which occurs during a rub is more complex than a single mode, with both adhesion formation and wear occurring simultaneously (79). They were able to measure adhesion growth rates for tests with varying tip speeds and incursion rates and proposed that the adhesion rates were influenced by the abradable temperature but could not validate these theories with the data available.

2.4.2 Material Studies on Metco 320

As the temperature requirements of the coating increase, the polyester phase must be replaced with a material which can withstand the higher temperatures. Graphite was initially selected to fulfil this role, providing a soft phase within the microstructure, increasing the coatings friability, and acting as a solid lubricator (93). However, the graphite phase suffered debonding at high humidity levels and was therefore replaced by the more inert hexagonal Boron Nitride (hBN), producing Metco 320 (M320).

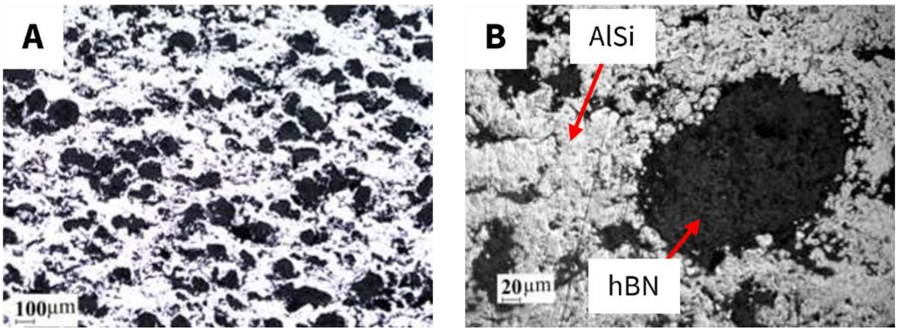

Figure 2.18 – An example of the Microstructure of M320 captured optically (A) and with an SEM (B) (94)

M320 is purchased as a mechanically clad powder and, like M601, is formed into a coating through plasma spraying, resulting in a microstructure as shown in Figure 2.18. By adjusting the spray parameters, the hardness of the coating can be controlled, with softer samples having a higher ratio of hBN to AlSi (22), but also a lower bond strength and erosion resistance (95), setting a limit of the minimum viable hardness (Table 2.3).

Table 2.3 – Manufacturer supplied properties for M320 (96)

Powder Composition	Al (Balance) Si (8%) hBN (20%)
Powder Particle Size (µm)	212 – 234
Maximum Operating Temperature (°C)	450
Typical Hardness Range (HR15y)	45 - 70
Bond Strength (MPa)	10 – 17
Erosion Resistance (s/mil)	3 – 5

Attempting to understand the impact of rub conditions on the wear mechanisms, multiple work packages have been completed testing abradable samples on high-speed abradable testing rigs, producing wear maps as shown in Figure 2.19. The results of these studies show that M320 differs in its response to incursion rate when compared with M601. Where M601 transitions from blade wear to increasing adhesion formation at higher incursion rates, M320 has a trend of adhesion formation reducing with increasing incursion rates, transitioning to an efficient cutting (71).

As with M601, the change in force with incursion rate is due to change in debris release mechanism, with compaction and release at lower incursion rates and cutting at higher incursion rates (78). Debris ejection monitoring by Hadjisoteriou shows that this shift is consistent across the hardness range (92).

Each of these wear maps were however limited to a single hardness. Fois et al. built on this by testing samples at a range of incursion rates and hardnesses (Figure 2.20). They found that, while hardness did not have a significant impact had high incursion rates (0.2 – 2µm/pass), at low incursion rates (0.02µm/pass) the wear mechanisms vary significantly. Samples with a low hardness produce high levels of blade wear, while samples of a high hardness result in adhesion formation (76).

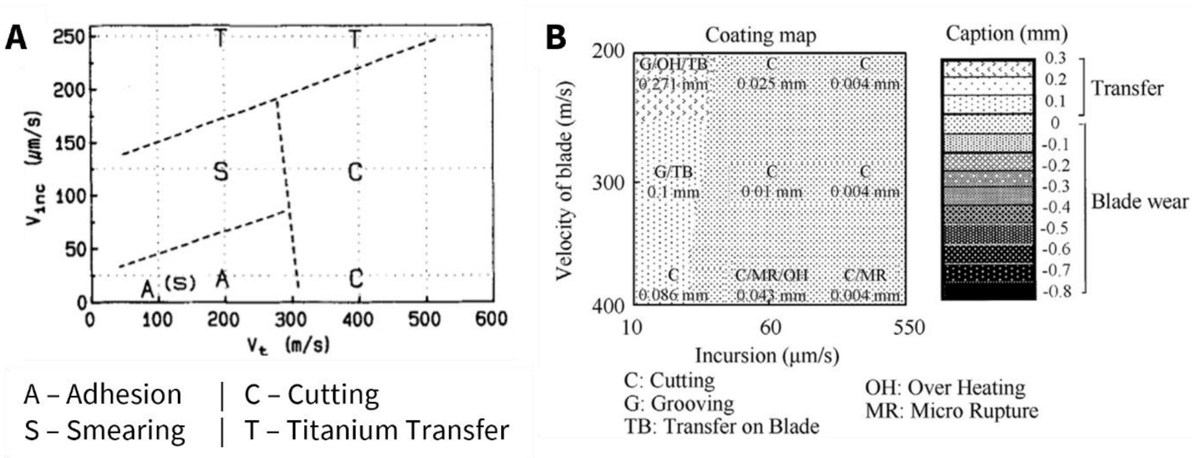

Figure 2.19 – Wear maps for an AlSi-hBN abradable created by Borel et al. (A)(23) and Bounazef et al. (B)(87)

To produce a wear map which includes all the test conditions, including hardness, Fois defined a set of nondimensional terms which can include the contribution of hardness, tip speed, incursion rate and the diameter of the test disk, making the result test rig independent. They also aimed to remove the subjectivity in wear mechanism by quantifying the rate of wear. This was done using stroboscopic imaging to monitor the side profile of the blade, recording the rate of adhesion formation and blade wear(94). This led to the creation of the wear map shown in Figure 2.21.

While this wear map can be applied by engine manufacturers to predict what wear will occur based on the conditions within the engine, it does not explain the mechanisms behind the variable wear performance at low incursion rates.

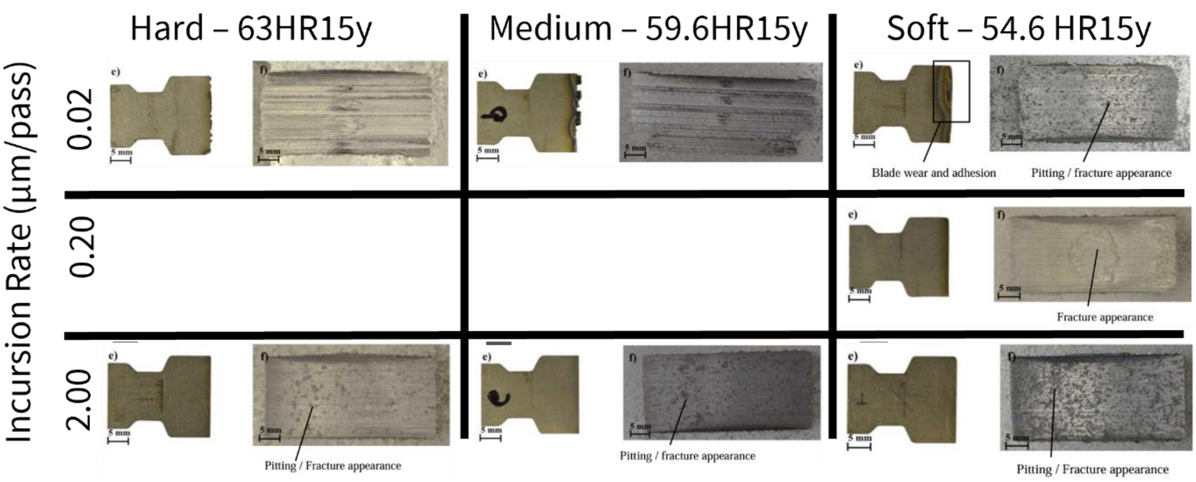

Figure 2.20 – Wear scars created during 200m/s M320 tests at varying incursion rates and hardnesses (94)

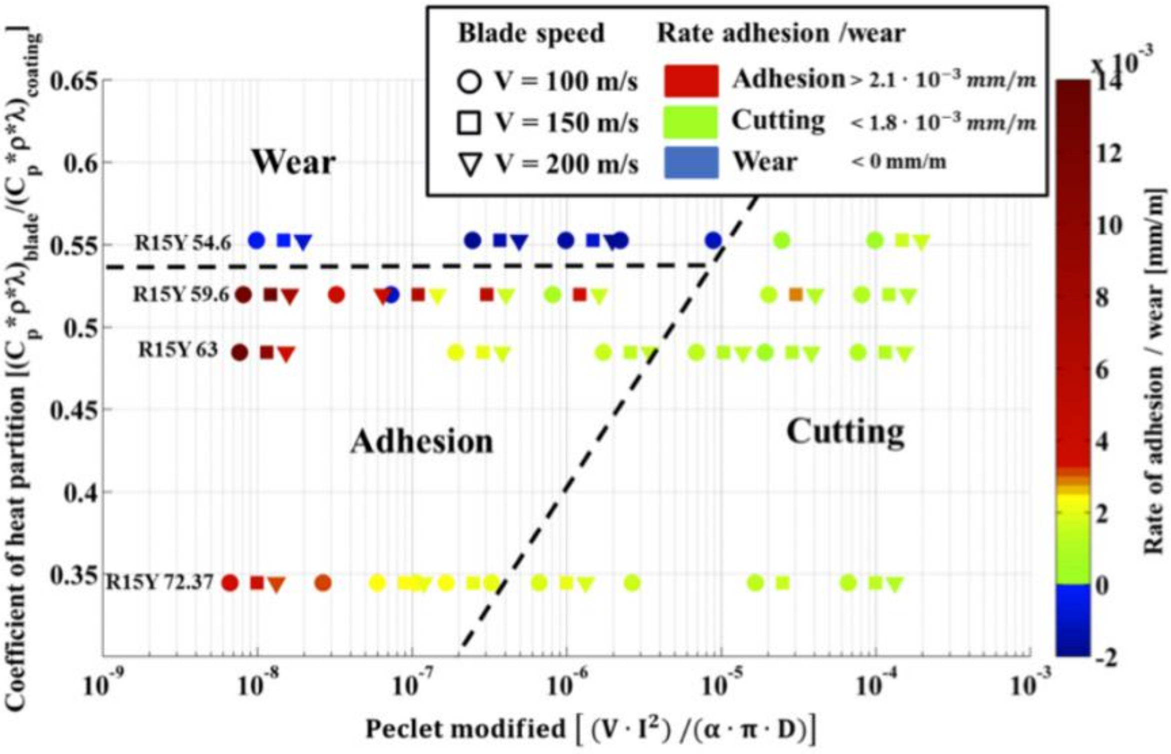

Figure 2.21 – Wear map for M320 based on nondimensional terms (94)

From inspection of the microstructure of M320 (Figure 2.18) the hBN can be seen to form large clumps, which Watson and Marshall showed to be poorly thermally bonded to the AlSi matrix (22). By applying a thermal model to the microstructure images of hard and soft abradables Fois et al. proposed that the change in performance at varying hardnesses was due to the hBN blocking the heat flow through the coating, leading to surface hotspots and blade wear (76).

These theories have not yet been confirmed experimentally, additionally Stringer and Marshall observed from stroboscopic imaging that the adhesions grew at rates faster than the incursion rate. This highlights that substantial phases are being plucked from the surface rather than just cutting (73), and demonstrates that there is still further research to be carried out to fully understand the wear of M320.

2.4.3 Material Studies on XPT268

XPT268 is a more recent addition to the range of AlSi based abradables, including both polyester and hBN as dislocators. This coating was designed to improve on M601 with the additional friability that the hBN provides to M320, improving its performance at high incursion rates. Instead, initial reports from engine manufacturers have stated that this material produces significant amount of blade wear against titanium blades and leads to large adhesion formation against Inconel blades.

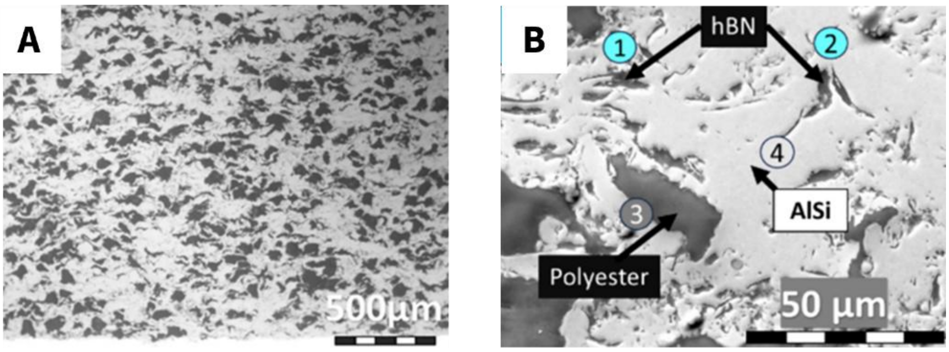

Figure 2.22 – An example of the Microstructure of XPT268 captured optically (A) and with an SEM (B) (89)

This material is purchased as a mechanically clad and blended powder which, as with M601 and M320, is sprayed with an atmospheric plasma spray process to form a coating with the microstructure shown in Figure 2.22. A key difference between this powder and M320 is the powder particle size (89,96), this results in hBN clumps which are smaller and more uniformly distributed throughout the material. The impact of microstructure on hardness and corrosion resistance is not currently well documented for this material, the available data from the supplier is provided in Table 2.4.

Table 2.4 – Manufacturer supplied properties for XPT268 (89)

Powder Composition	Al (Balance) Si (9%) hBN (6%) Polyester (20%)
Powder Particle Size (µm)	125 – 136
Maximum Operating Temperature (°C)	345
Typical Hardness Range (HR15y)	70*
Bond Strength (MPa)	23.4*

*Data only provided for a single hardness

As this material is relatively new there has been very little work published on its abradability. One recent study completed by Bertuol et al., compared XPT268 to M601 using ball on plate, ball on disk and abradability tests on a spindle test rig (44).

The testing was completed with samples of M601 with a hardness of 74.7HR15Y and XPT268 at 83.8HR15Y, the large difference in hardness does therefore make it difficult to separate the impact of hBN from the impact of the higher hardness.

From the ball on disk testing there was a noticeable difference in the wear scar created between the two materials, with XPT268 producing a smoother more uniform scar (Figure 2.23). This potentially highlights the benefits of the hBN acting as a solid lubricant during the rub.

They also were able to observe differences in the wear produced during the abradability test with the spindle test rig, with an increased roughness of the wear track produced for the XPT268 (Figure 2.24). The increase in roughness is due to the increased height of the adhesions formed during the rub. However, the XPT268 sample was harder than the M601 sample. As the hardness of M601 increases the rate of adhesions is also expected to rise (90), so it cannot be determined if the increased roughness is due to the hBN or the hardness.

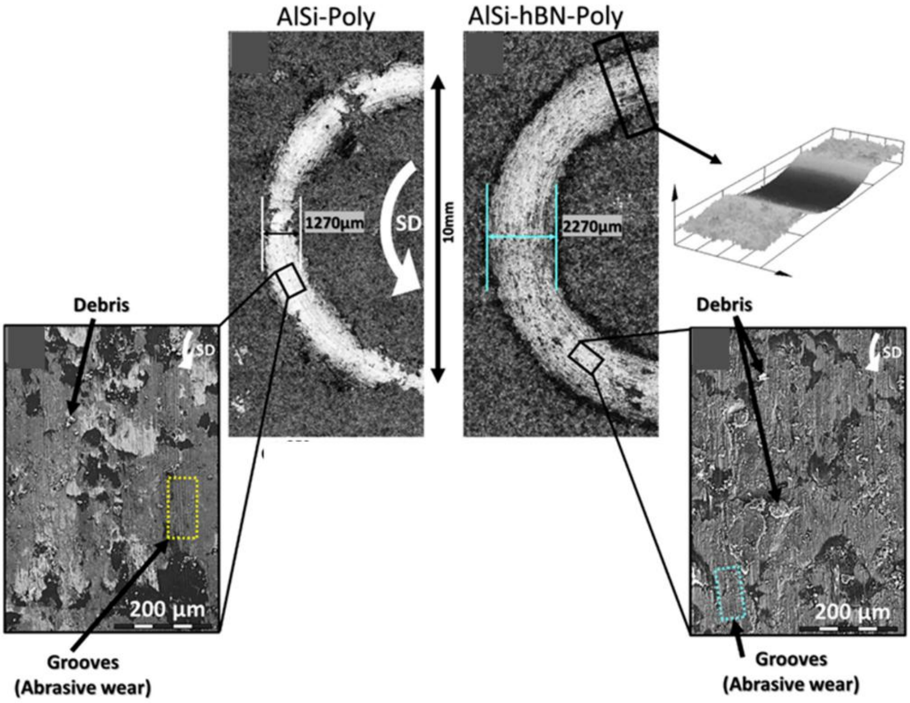

Figure 2.23 – Wear scars produced by ball on disk testing for M601 and XPT268 (44)

Although this testing was completed on samples of different hardnesses, it does highlight the potential for a significant difference in the wear behaviour of XPT268 when compared with M601. This, alongside the reports from engine manufacturers, confirms the need for further work to be done to document the wear behaviour of XPT268 and to understand the impact of the addition of hBN.

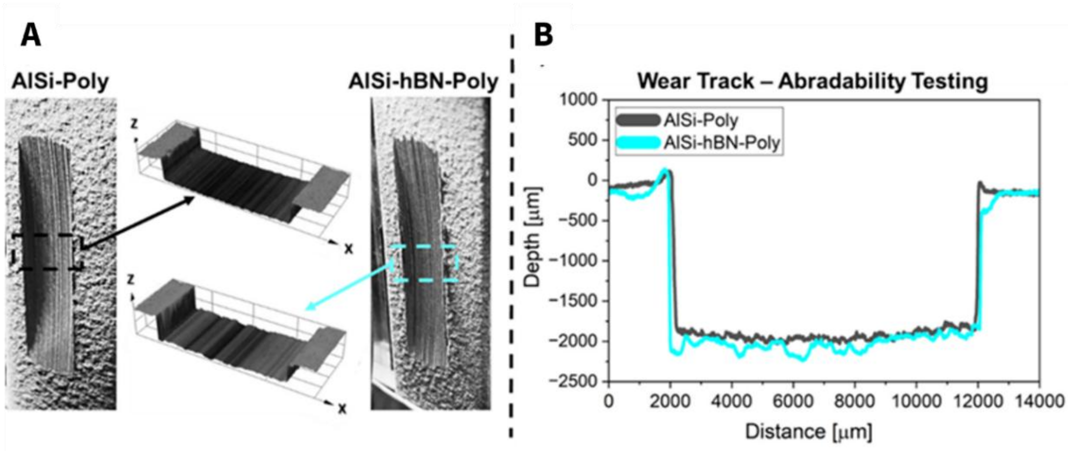

Figure 2.24 – The wear scars (A) and extracted profiles (B) for M601 and XPT268 samples tested with a spindle test rig (44)

2.5 Research into the Wear Mechanisms of M601

Work by Borel et al. on AlSi-Polymer Abradables found that the incursion rate was a significant factor in determining the performance of the abradable. With an Aluminium-Polyester abradable the primary wear mechanisms observed were adhesive wear and blade melting, with adhesions being more prevalent at the higher incursion rates (23).

Alongside the increasing rate of adhesions, Watson et al. showed a trend of increasing forces with increasing incursion rates from 0.2 to 2µm per pass of the blade (74), this aligns with well-established laws of adhesive wear put forward by Archard, stating that the volume of adhesive wear is proportional to the normal load (97). However, this relationship did not hold at the lower incursion rate of 0.02µm/pass.

Watson et al. showed that, although adhesion rates fell, the peak forces present at 0.02µm/pass did not differ significantly to those seen at 0.2µm/pass (74). Beyond this the forces and temperatures observed during the test followed a cyclic pattern, something unique to tests at these low incursion rates.

The impact of material temperature on the rate of adhesive wear is not included in the original relationship proposed by Archard (97). However, recent work by Gåård et al. has shown that severe adhesive wear can occur more readily at increased temperatures (98), with this result aligning with Atomic Force Measurements which show adhesive forces at the atomic level increasing with temperature for titanium, stainless steel and low alloyed steel (99).

Looking to understand the relationship further it is important to understand how energy within a blade-abradable contact is dissipated. Experimental and analytical work by Agrapart et al. has shown that during a rub event between a titanium blade and an AlSi-Polyester abradable most of the energy of the rub is dissipated as heat, with a heat partition ratio of 95% in the abradable coating and 5% in the blade (100). With a large proportion of the heat flowing into the abradable, its ability to manage this energy will have a significant impact on the temperature of the rub event.

Considering the nature of the heat transfer further, work looking into the thermal properties of AlSi-Polyester by Bolot et al. has shown that the microstructure of the abradable has a significant bearing on its thermal properties. AlSi-Polyester coatings are manufactured using a plasma spray process, this results in a bulk of AlSi with clumps of polyester dispersed throughout. During the spray process voids can form within the substructure, this results in a microstructure such as that shown in Figure 2.25. When there is a thermal gradient across the abradable the majority of the heat flow flows through connected chains of AlSi (21). As the hardness of a sample reduces, the ratio of voids and polyester to AlSi increases, which breaks up the connected chains of AlSi and therefore reduces thermal conductivity of the sample. Watson et al. was in turn able to develop this work further, showing how the inherent randomness of the plasma spray manufacture process used for Metco 601 leads to significant variation in thermal properties at different locations within a single sample (22).

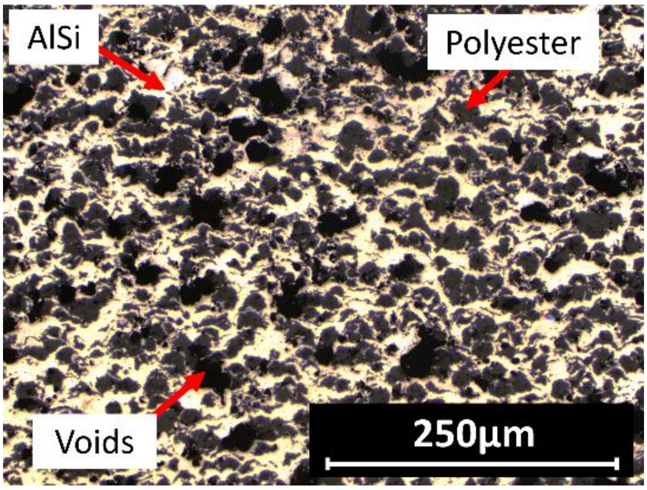

Figure 2.25 – An optical microscope image showing the microstructure of Metco 601

Any impacts of temperature on the wear of M601 will be further compounded in operation, where M601 is used in environments with ambient temperatures reaching 325°C (89), with the casing onto which they have been sprayed also being held at these elevated temperatures. In these conditions the abradable will not be able to conduct heat to the backplate as efficiently, the increase in abradable bulk temperature will also lead to changes in its mechanical properties which will further impact the wear.

The range of operational temperatures for M601 has prompted many studies looking to determine the impact of temperature on mechanical properties. Work by Skiba et al. (101) was able to show how the Youngs modulus of M601 reduces with increasing temperature through compressive testing. This was taken further by Pellegrino et al. (46) who undertook both quasi-static and dynamic experiments at elevated temperatures to review the impact on mechanical properties at a range of strain rates. Their findings show how M601 undergoes brittle fracture at room temperature, but as the temperature increases it becomes increasingly ductile, with an increasing strain to failure and a reduction in yield stress, these results can be seen in Figure 2.26.

These studies have all been completed within the operational limits of M601. However, some studies have taken this further, with Liu et al. (102) holding M601 samples at 350°C for 24 hours. This led to a reduction in the sample hardness from 53.3 to 23.6HR15y with the polyester content within the sample dropping from 56 to 46%. This study not only highlights the importance of the polyester phase within the sample but also demonstrates why care must be taken to stay within the temperature limits provided by Metco.

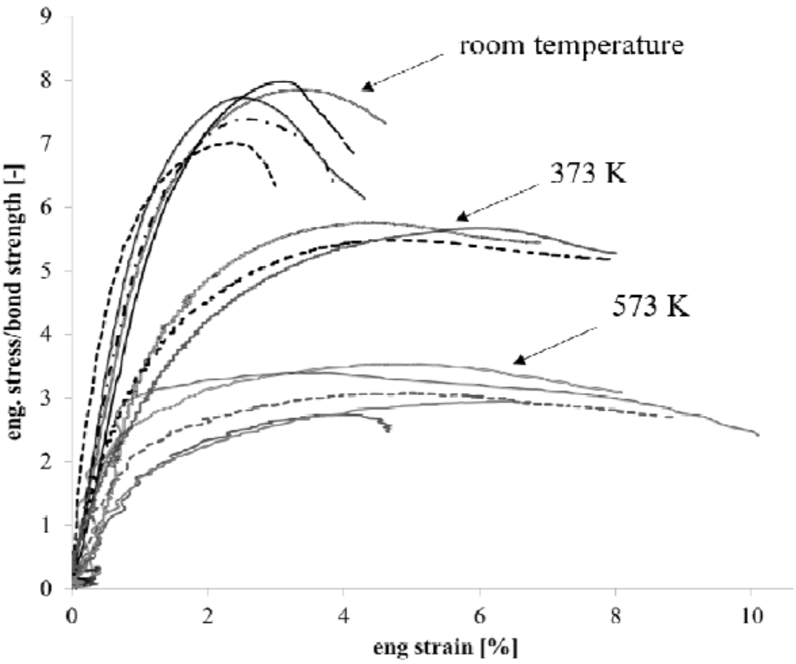

Figure 2.26 – Compressive quasi static mechanical response of Metco 601 abradable coating at different temperatures (46)

Standard mechanical testing of M601 is useful when attempting to develop a fundamental understanding of how the material responds to changes in temperature. However, when applied within an engine the blade – liner interaction is more complex and requires more specialised testing.

Although most of the specialised abradable testing approaches developed do not include any mechanisms for abradable sample heating, there have been some studies which have chosen to include these features. The abradable testing rigs developed by Zhang et al. and Gao et al. (68,83) both make use of a rotating blade and an abradable sample on a stage which moves into the path of the blade but heat the sample using a high temperature flame and irradiation concentrated heating respectively. Both samples are heated on the surface of the abradable with the aim to reach engine representative temperatures. Although these rigs have been able to produce engine representative wear scars, all tests have been completed at the same temperature and the backplate temperature has not been controlled.

One study which did look to investigate the impact of temperature during a blade – liner interaction was completed by Martinet et al. (60), who varied the bulk temperature of an abradable sample which was mounted to a ballistic bench. The high temperature sample was then fired towards a titanium blade at 120m/s with sample temperatures ranging from room temperature to 270°C. Their results showed that although normal forces did not vary significantly at different temperatures, the wear depth increased. This was explained to be due to the increased ductility of the samples at higher temperatures, aligning with the standalone mechanical testing completed by Pellegrino et al. (46) and Skiba et al. (101). These tests however only show the results of a single rub and will not show the impact of thermal energy being added to the system or material compaction over multiple strikes.

Testing with specialized abradable testing rigs can produce engine representative wear scars but are expensive to develop and operate. This has resulted in work looking to develop computational models of abradable systems which can be used model the blade – liner interaction.

Models developed by Cheng et al. have made use of X-Ray Computed Tomography (xCT) to create a 3D model of M601, separating the material phases (Figure 2.27) (54). They have found that in order to build a material model which aligns with experimental data they had to not only include models describing the impact on temperature on Aluminium alloys (103), but also the behaviour of the polyester phase, including the glassy transition and crystallisation of the polymer.

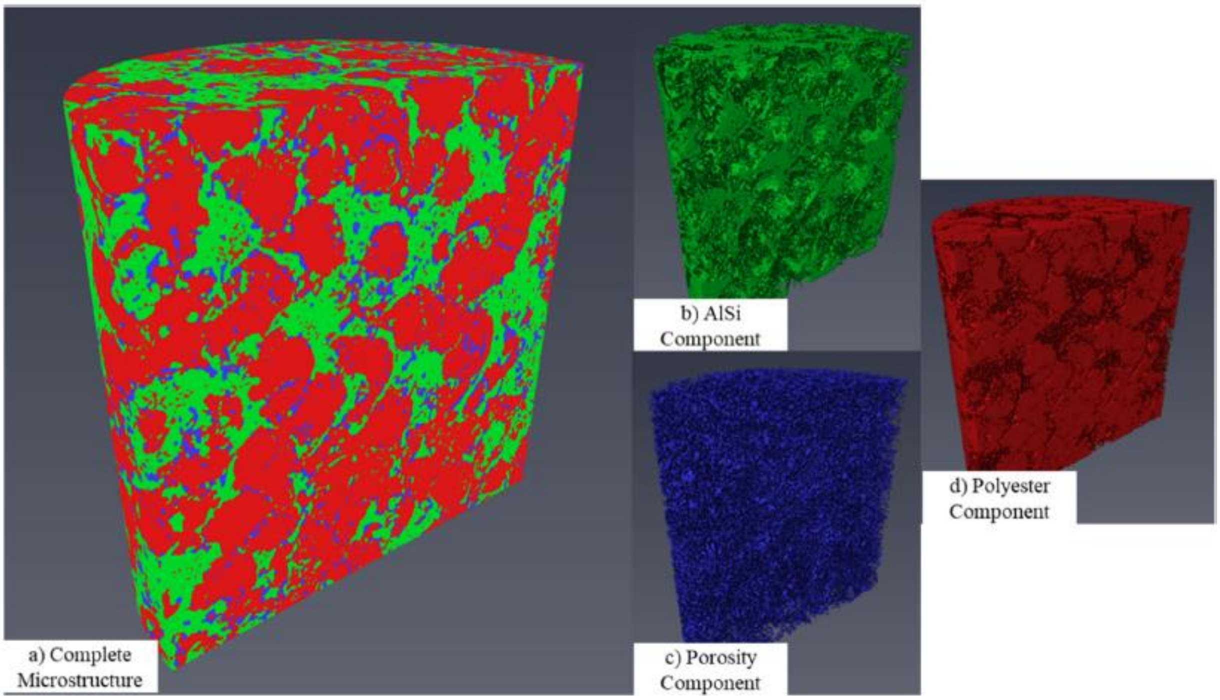

Figure 2.27 – Cross section of M601 xCT results showing the microstructure of an as sprayed sample (54)

With both experimental and modelling work showing the importance of both the AlSi and Polyester phases within M601 to its mechanical properties and response to temperature it is likely that M601 samples of differing hardnesses will respond differently to bulk temperature changes. Watson et al. was able to measure the change in composition of different hardness M601 samples through image segmentation (22). The results of this, shown in Figure 2.28, demonstrate how the ratio of AlSi to Polyester changes as the hardness increases, with the material being predominantly polyester at low hardnesses and mostly AlSi at high hardnesses.

Although previous studies have highlighted the importance of the polyester phase in the material properties of M601 at temperature, these studies did not vary the hardness of the samples to vary how much polyester is present.

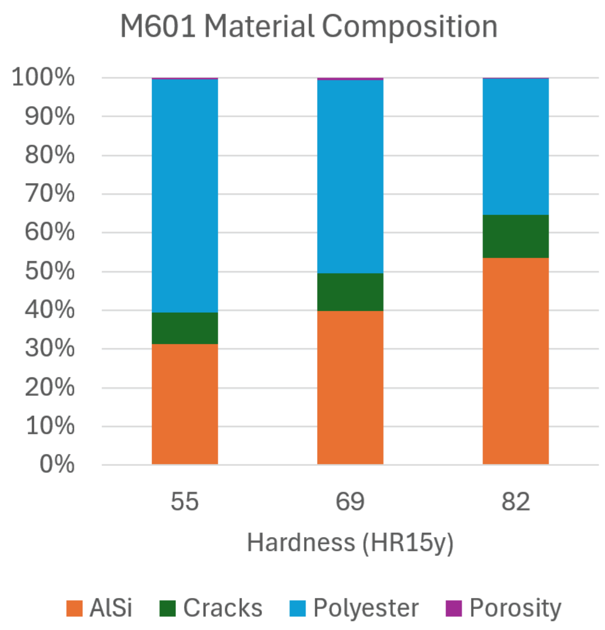

Figure 2.28 – M601 material composition at varying hardnesses (22)

2.6 Conclusion

While the benefits of abradable liners within the compressor can be significant, the conditions which they witness within the engine can produce large volumes of wear, leading to further complications within the engine.

Standard tribology tests and modelling of these coatings have allowed for comparison between different coatings, and a better understanding of the conditions within the engine, but at present the only way to produce engine representative wear is with dedicated abradable testing rigs. These vary in complexity, but the most common design is a reduced scale rig which can produce engine representative wear but does not reach engine speeds.

Within the low and intermediate compressor AlSi based abradables are typically applied, to improve on the performance of the AlSi matrix a dislocator phase is added.

M601 is made of AlSi and polyester. Its wear response is primarily a result of incursion rate and hardness. Increasing incursion rate and hardness leads to increasing adhesions, at low incursion rates (0.02µm/pass) the blade will wear.

M320 replaces the polyester with hBN resulting in a different wear response. M320 produces an efficient cut at high incursion rates (2µm/pass), as incursion rates decrease adhesions will start to form on the blade. At low incursion rates (0.02µm/pass) the blade will either wear with a low hardness abradable, or adhesions will form with a high hardness abradable.

XPT268 contains both polyester and hBN and is a new product. Initial reports from engine manufacturers have described significant wear (both blade wear and adhesion formation) which is dependent on blade material. There is limited academic work looking into this material, but an initial publication has identified some differences in the wear of XPT268 compared with M601 but is not conclusive.

The wear behaviour of M601 has been the subject of many research papers, as a result the spectrum of behaviours has been well documented and is predicable for high incursion rates. However, there is a gap in the understanding when explaining the wear behaviour at low incursion rates – conditions which occur uncontrollably within the engine. Links to the thermal properties of the abradable have been proposed, with standalone material testing supporting these claims, but there has been no work which looks to relate the thermal properties to the wear behaviour during repeated interactions between a blade and an abradable.

The Low-Speed rig at the University of Sheffield is uniquely situated to investigate this relationship due to its simplicity, allowing for the development of in-situ measurement tools and for rapid testing at a range of test conditions. However, to fully investigate this relationship additional capability will need to be added to the rig:

- To monitor the blade wear which occurs during a rub an in-situ front camera system must be developed for the rig.
- To relate this wear to the thermal behaviours the triggering system for existing thermal camera will need to be replaced to allow for capture of both blade and abradable.
- Novel data processing tools will need to be developed to align all data spatially and temporally.
- An abradable sample heater is needed to investigate the impact of bulk temperature on wear.

3 Materials and Methodology

As discussed in section 2.3.3, physical testing of abradables typically follows one of two paths, it either attempts to replicate the conditions within a real engine or simplifies the problem to reduce the testing complexity and provide better control of selected test variables.

This thesis builds on the work completed by the Abradables Research Group, further developing the capabilities of the spindle test rigs developed by previous researchers (40,73,94). These rigs take the approach of removing complexity form the blade-abradable interaction by using simplified blade and abradable geometries. Instead focussing on collecting more, high quality, data through in-situ measurement techniques and repeats.

While these tests have been simplified, the results are still representative of wear which is seen within a real engine. This was demonstrated by work completed by Fois who completing large numbers of tests to produce engine representative wear at varying rub conditions, creating wear maps which allowed engine manufacturers to target more favourable conditions within the engine (78,94).

This method details the base methodology which is common to all chapters in this thesis. The more specialized equipment and analysis tools, which are developed incrementally throughout this thesis, are described in more detail in the relevant chapters.

3.1 Abradability Test Rigs

There are three spindle test rigs in operation within the Abradables Research Group, each rig functions in a similar way but has been specialized to provide unique benefits.

The Low-Speed spindle test rig is limited in its peak blade tip speed to 200ms^{-1}, but its simple design and accessible enclosure allow for easy access to instrumentation. The High-Speed spindle test rig can reach blade tip speed of 330ms^{-1}, closer to those seen within an engine. However, due to the more demanding requirements on the enclosure there is limited access for instrumentation. The High-Temperature is limited to 200ms^{-1} but includes an induction coil which can heat the blade tips during a test.

In this thesis tests have been completed on the Low-Speed rig. The Low-Speed rig was chosen for this work as it allows for the required hardware modifications identified in section 2.6. The accessible enclosure allows for the development of a front camera solution and an abradable heater, and the existing thermal camera could be developed further to facilitate in-situ temperature monitoring. Further data collected by Rahimov (82) on the High-Speed spindle test rig, has been reprocessed for this thesis. Both rigs are therefore described here.

An overview of the status of instrumentation on the two rigs prior to this work, along with details of the improvements completed during this work have been listed in Table 3.1.

Table 3.1 – Features of the test rigs with details of changes made during this work

Test Rig	Feature	Initial Status	Final Status	Section
Low Speed Rig	Spindle Control	Analogue System	Digital system, integrated with safety systems	3.1.3.1
	Disk	2-part assembly, balanced to within 0.2g	Single part, balanced to within 0.05g	3.1.1
	Side Camera	Side camera with 3D printed strobe mount	Strobe replaced with dust and electromagnetic interference sealed assembly	3.1.6
	Front Camera	-	Camera and strobe system installed with permanent metal assembly	4.3.1
	Pyrometer	Pyrometer fitted	Improved noise detection algorithm developed	3.1.5
	Force Measurement	3-axis dynamometer fitted	-	3.1.4
	Thermal Camera	Camera triggered with laser pyro to capture images of blade *or* abradable. No post processing tools	Light gate based triggering solution produces stable output and allows for images to be captured of both blade *and* abradable in the same test. Processing tools developed to warp abradable footage and to spatially align footage with the front camera	4.3.2
	Sample Heater	-	A heater block has been installed onto the test stage which can heat the backplate of the abradable up to 300°C during a test	6.2.1
High Speed Rig	Spindle Control	Analogue System	Digital system, integrated with safety systems	3.1.3.1
	Pyrometer	Pyrometer fitted	Improved noise detection algorithm developed	3.1.5
	Force Measurement	3-axis dynamometer fitted	-	3.1.4
	Front Camera	Front camera with 3D printed strobe mount	-	(79)

3.1.1 Low-Speed Spindle Test Rig

This work builds on the 200ms^{-1} spindle test rig developed by Stringer et al. (73) (Figure 3.1). Tests on this rig make use of a simplified blade and abradable geometry as shown in Figure 3.27. The test blade is clamped into a disk which has a dummy blade positioned 180° from the test blade to provide balance during rotation (Figure 3.2). This disk is then mounted to a spindle motor (GMN

HSP120g- 21000/9) and rotated. In turn, the abradable sample is mounted on top of a motorised stage (SIGMA KOKI SGSP80-20ZF) positioned below the disk.

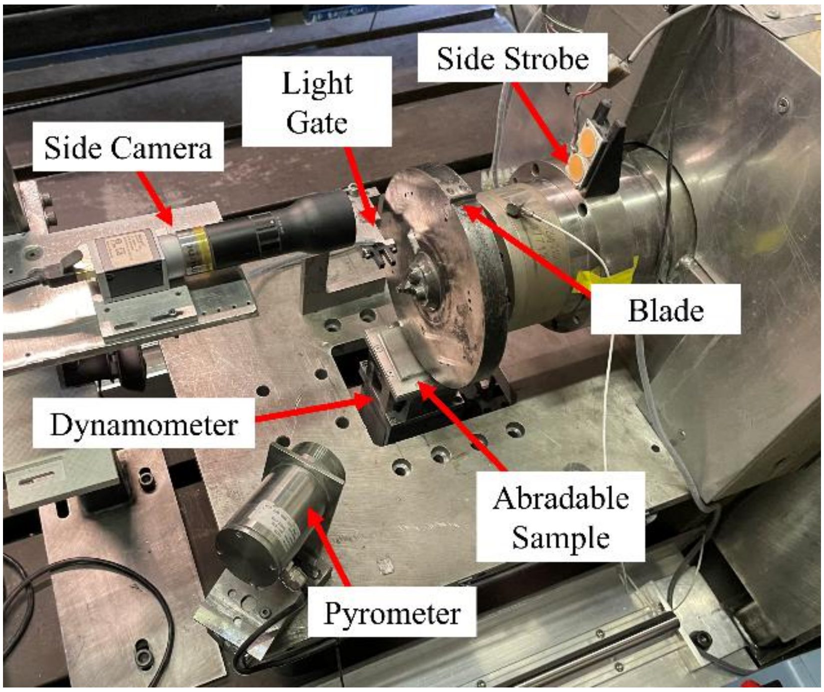

Figure 3.1 – Image of Low-speed test rig prior to this work package

During the test, the speed of the disk can be set at any velocity up to a tip speed of $200ms^{-1}$. When the disk has reached a steady speed, the abradable sample will be pushed upwards by the stage at incursion rates as low as 0.02 µm for each pass of the blade (µm/pass). The stage will then continue to move upwards until a predefined incursion depth has been reached.

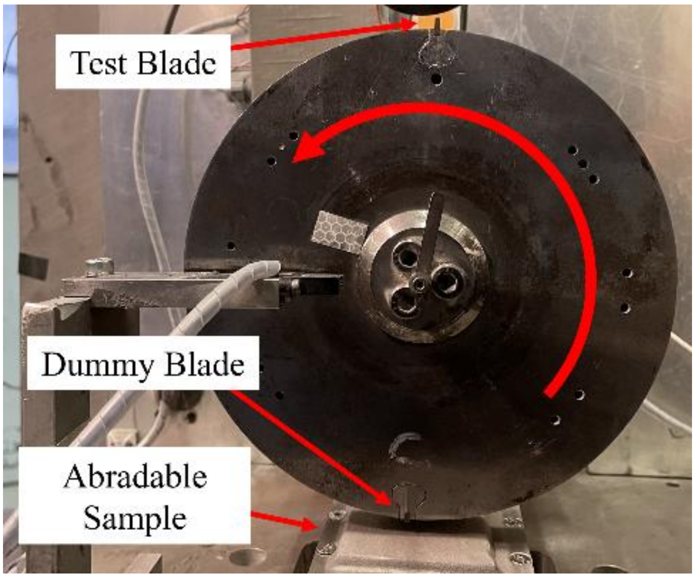

Figure 3.2 – The location of the test blade and abradable sample on the Low-Speed Rig

As a novel contribution completed as part of this work a new disk was designed and fitted to the rig, this was completed as part of scheduled maintenance to the rig. The new disk design (Figure 3.3) took advantage of advances in the machining capabilities of our suppliers to move to a single piece design, improving the balance of the disk.

The disk is made of 17-4PH H900 Stainless Steel and has been designed so that peak stresses seen during a test at 200m/s tip speed (331Hz) will be below the fatigue limit of this material.

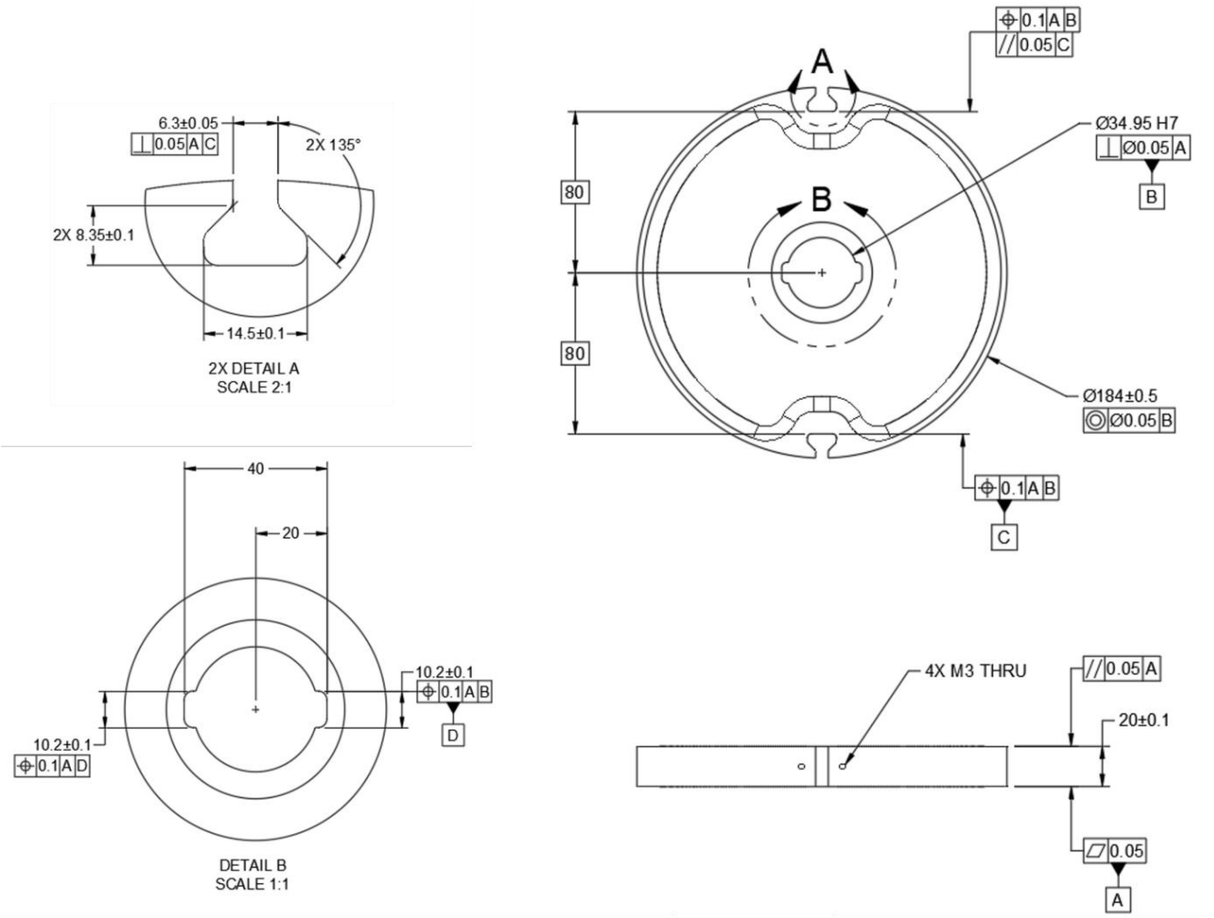

Figure 3.3 – New design for the Low-Speed rig disk

The blade holders work in a clam shell design, with the two-part holder forming a sandwich assembly with the test blade in the centre (Figure 3.4). This assembly then fits into a dovetail slot in the disk (Figure 3.5). The blade holder shape was designed such that it could be measured accurately to ensure blades would always fit. To allow for test blades of differing masses to be balanced 6 individual holder parts have been manufactured, each with a different amount of mass removed. By combining the holders in different combinations, the total mass of the test blade and holders can be balanced to the mass of the dummy blade and holders to within 0.05g.

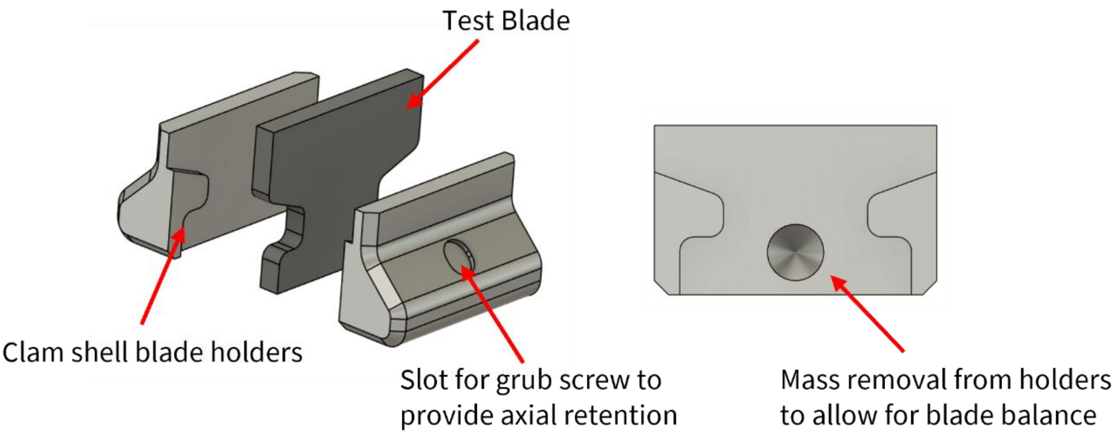

Figure 3.4 – Schematic of blade holder design with detail on mass removal

To ensure the new disk has minimal impact on the test results, the new disk was designed to have the same mass as the old disk (2.3kg) and the same spindle coupling was used (Figure 3.5).

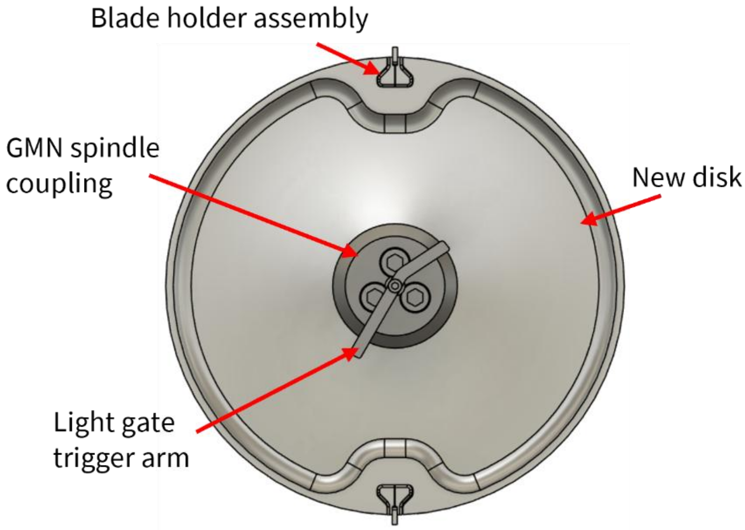

Figure 3.5 – Model of the new disk assembly

During a test data can be collected using tools such as a camera to record the side of the blade, a dynamometer to measure forces, and a pyrometer to measure the temperature at the surface of the abradable.

3.1.2 High Speed Spindle Test Rig

The High-Speed spindle test rig (developed by Watson (40)), follows the same principles as the Low-Speed spindle test rig but on a larger scale to allow for higher tip speeds.

The test and dummy blades are clamped within a larger test disk which, unlike the Low-Speed rig, is permanently mounted to the spindle (GMN HSP170s- 30000/19) via two bearing uprights. The abradable sample is fitted to a high precision ball screw driven linear actuator (HD30406-MF-M-U2-20-C20B).

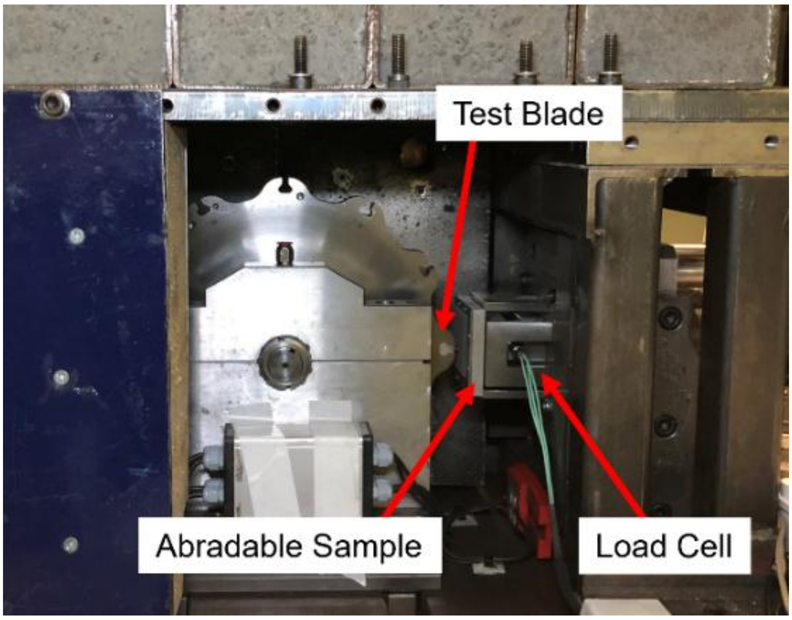

Figure 3.6 – Image of the high-speed spindle test rig (82)

While the Low-Speed rig is contained within a composite aluminium-wood enclosure which can slide away from the rig to provide full access, the High-Speed rig requires a steel and concrete enclosure. This design is far heavier, and therefore only a small access window is available for changing of samples.

3.1.3 Rig Operation

When operating the rigs the data collection and spindle control systems are independent and isolated. This ensures that in the event of a failure within the data acquisition system safe operation of the spindle is still possible.

3.1.3.1 Spindle Control

As part of this project the control of all three spindles were brought under the control of a single Programmable Logic Controller (PLC). This system manages all communication with the spindle invertors, requesting speeds based off user inputs and returning the spindle speed measured by the invertor. This system also monitors and controls the safety systems within the lab, which include the test cell door interlocks and magnetic locks. The schematic of this system is given in Figure 3.7.

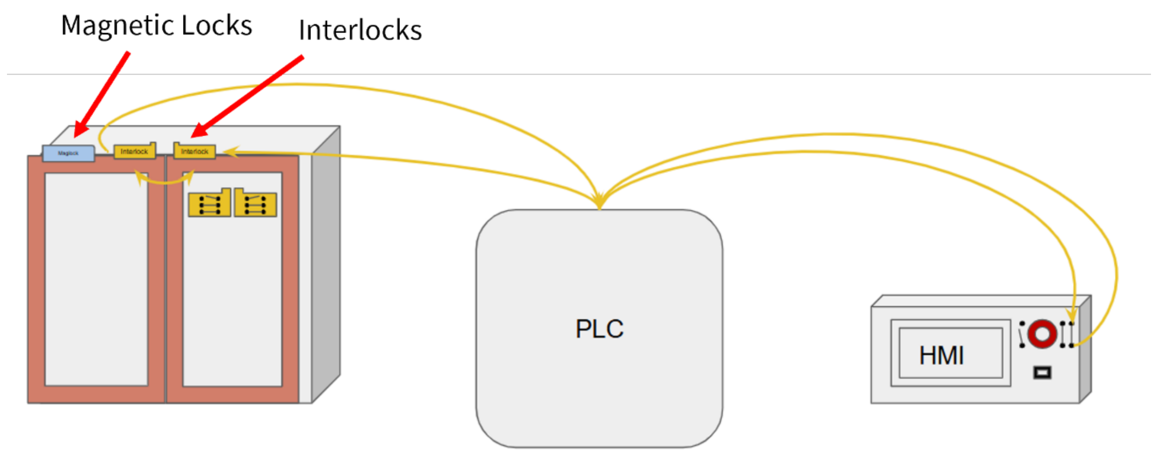

Figure 3.7 – Schematic of the PLC system

The status of the spindle, interlocks, magnetic locks and the physical E-Stop button are constantly monitored by the PLC. The system will not allow the spindle to be activated if the doors are unlocked or open and likewise will not allow the doors to be unlocked if the spindle is spinning. The system has been setup that in the event of signal loss between any components the spindle will be stopped.

All the information gathered by the PLC is displayed to the user via a touchscreen control pad, with an interface shown in Figure 3.8. This system ensures that the spindles can be controlled safely, removing risk of human error by clearly displaying all vital information and preventing access to the spindle when it is in operation.

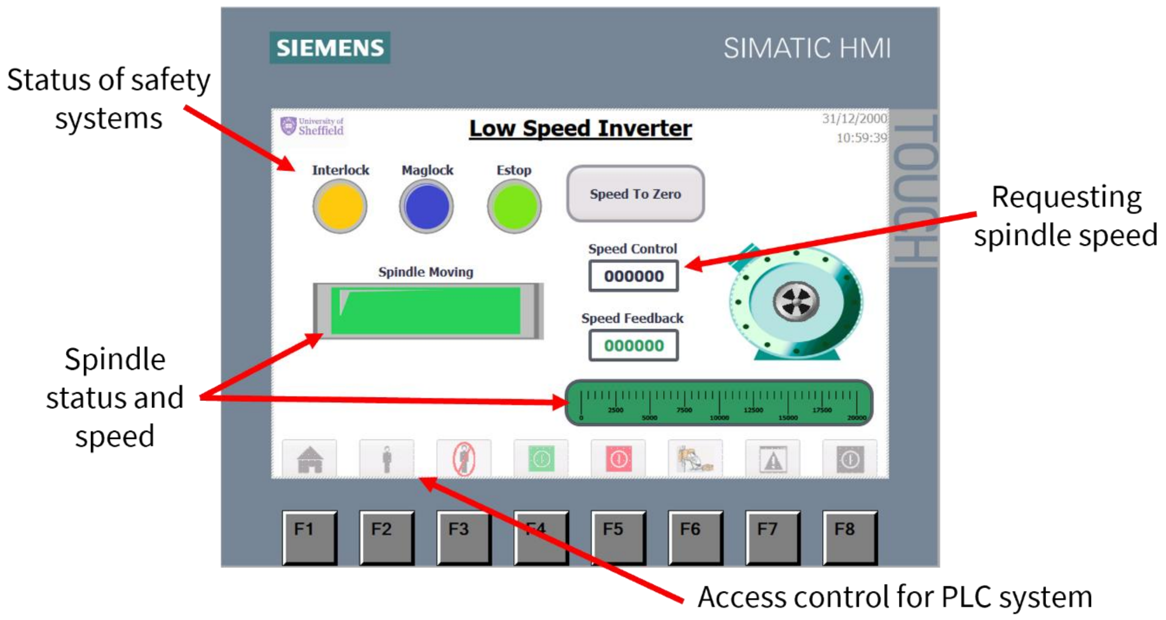

Figure 3.8 – Spindle control PLC interface

3.1.3.2 Data Acquisition

When running a test, the instrumentation and stage are controlled by a LabView script (104), the interface for this is shown in Figure 3.9. This script will take inputs of the test parameters, and which instrumentation are connected and will then communicate with the stage and collate the data from the selected sources, storing them in a test folder.

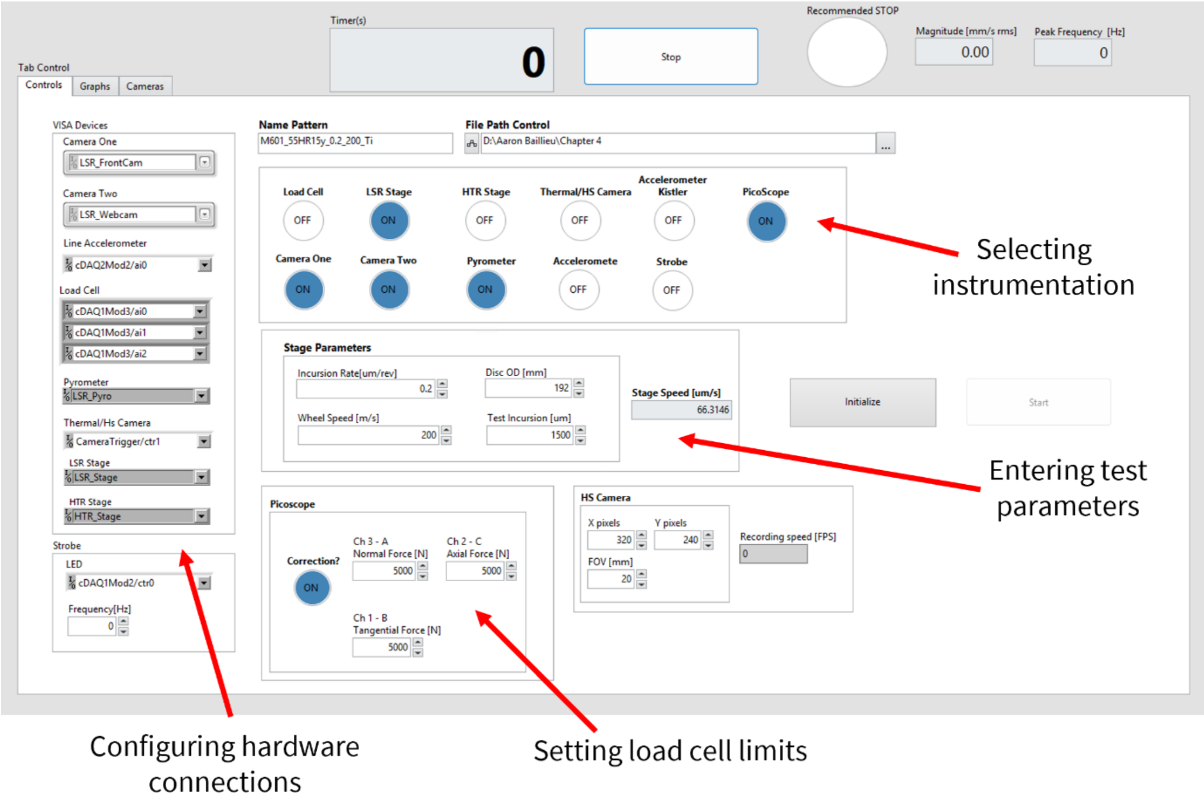

Figure 3.9 – LabView interface for data acquisition

3.1.4 Force Measurement

Forces are measured on both rigs using a 3-axis dynamometer (Kistler Type 9347C) which is positioned directly below the abradable sample (Figure 3.10). As the dynamometer is not designed to resist any torques it is fitted within a steel cage which limits rotation, acting as a mechanical stop to any excessive torques. The signal from the dynamometer is passed through a charge amplifier (Kistler Type 5070A) before the data is recorded by a PicoScope 5000 series at a sample rate of 100kHz.

As the loads are applied to the dynamometer in the form of successive impacts the loadcell responds as damped harmonic oscillator, this can be seen clearly in Figure 3.11 which shows the force peaks and oscillations over 6 successive impacts. The raw data must therefore be processed to extract only the peaks resulting from the impacts, this processing is completed in MATLAB.

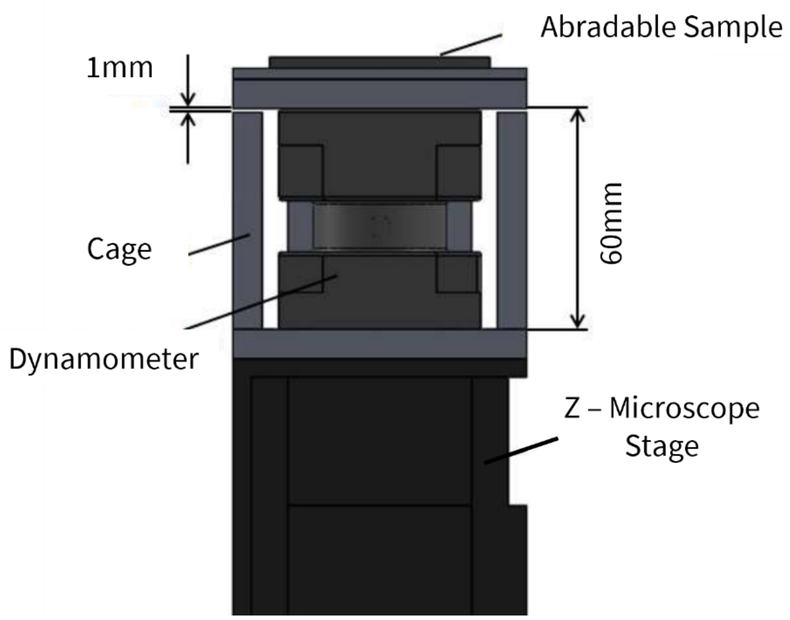

Figure 3.10 – Schematic of the dynamometer and microscope stage arrangement (94)

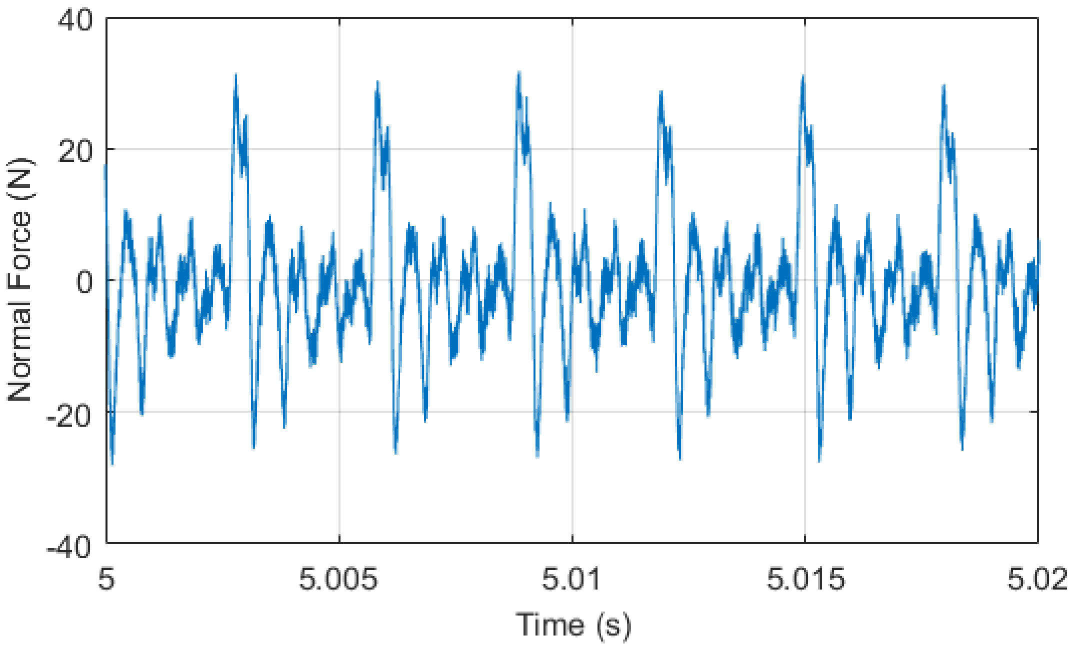

Figure 3.11 – Unprocessed normal force data collected during 6 tip strikes

Alongside peak extraction, the MATLAB code must also correct for any drift in the force which occurs during a test. This drift is due to the dynamometer being piezoelectric and is therefore sensitive to the changes in temperature which occur during the rub.

As can be seen in Figure 3.12 the zero offset changes gradually during a test. With the force values oscillating about the zero point, the centreline can be found by applying a moving average with a timestep large enough to highlight only the long-term trend in zero offset. For this application a timestep of 0.1s was chosen, much larger than the 3ms period between blade strikes.

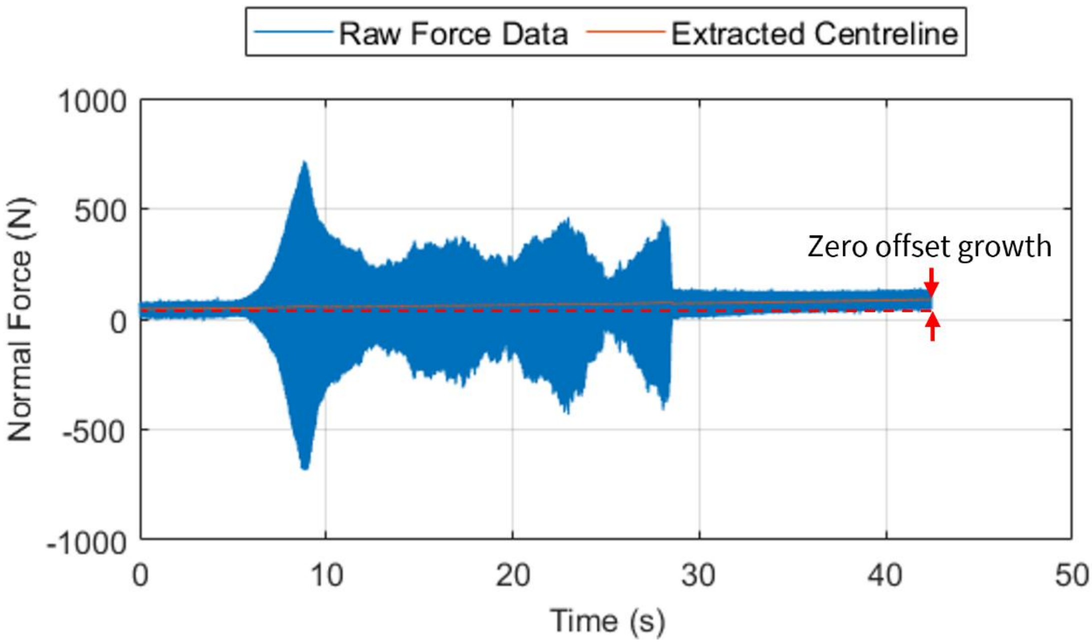

Figure 3.12 – Raw force data collected during a 0.2µm/pass test with the offset extracted

With the zero offset corrected the negative values can be omitted as the loadcell is oriented so that compressive loads are recorded as positive. The peaks can then be extracted. Peaks are extracted by splitting the data into times windows 1.5 times the period between blade strikes and finding the maximum value in each window. This ensures that there will be at least 1 blade strike in each window. The result of this is shown in Figure 3.13.

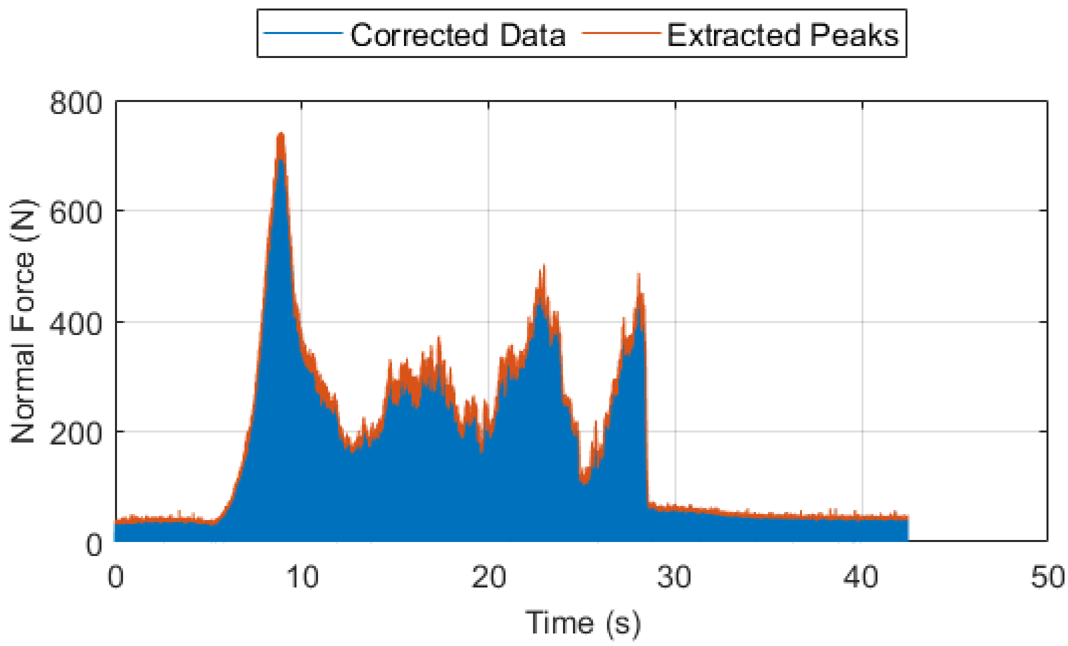

Figure 3.13 – Peaks extracted from the corrected normal force data shown in Figure 3.12

The extracted peaks can then have the signal noise, which is introduced by vibrations in the rig, removed by subtracting the average force value measured before the blade first contacted the sample. The resulting force plot is shown in Figure 3.14.

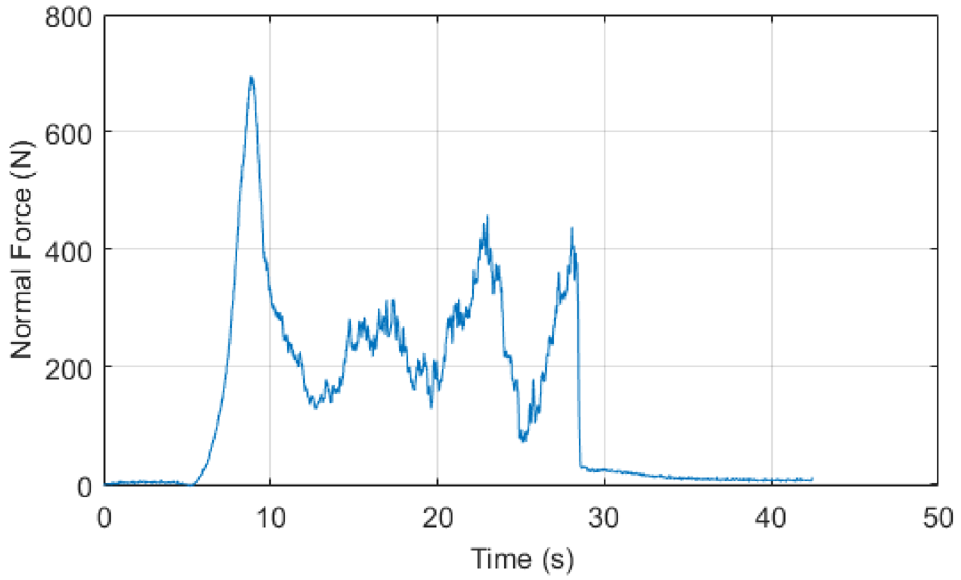

Figure 3.14 – The final output of the normal force processing completed on the data shown in Figure 3.12

3.1.5 Pyrometer

Each rig is fitted with an infrared pyrometer (Micro Epsilon CTLM-3H1CF3) targeted at the centre of the rub track. The pyrometer can measure temperatures between 150 – 1000°C at a sampling frequency of 50Hz. However, during a test sparks and dust are generated resulting in noise in the output data.

The temperature of the sample during the periods of noise cannot be determined from the pyrometer, but processing of the data to remove as much noise as possible will reduce the risk of false peaks in temperature. To remove the noise a novel two-step algorithm has been developed and implemented in MATLAB as part of this project.

As the pyrometer can only measure between 150 and 1000°C any values outside this range must be noise and can be removed. The result (shown in Figure 3.15) can capture most of the noise but still leaves some false peak temperature values.

To identify any further false peak values all temperature values are sorted numerically. As the abradable surface is heated gradually during a test the sorted temperature values should follow a steady relationship, a step change would signify an instantaneous jump in temperature.

To identify a step change in the peak temperatures a second order polynomial is fitted to the lower 85% of the data (Figure 3.16). If any peak values above this deviate from the trend by more than 20°C (equivalent to a heating rate of 1000°C/s) they are considered noise and removed. The result of this process can be seen in Figure 3.17.

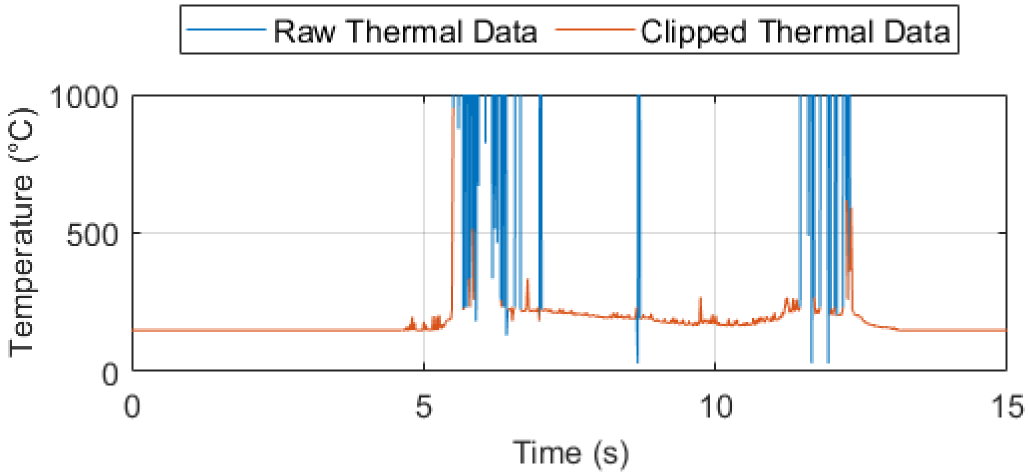

Figure 3.15 – Raw Pyro data and data clipped to measurable limits for a 1µm/pass test

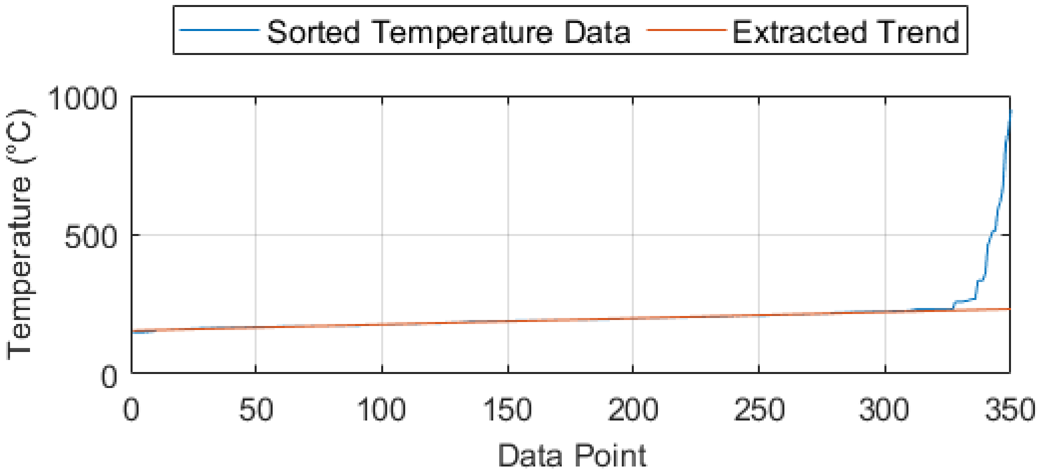

Figure 3.16 – The Clipped thermal data from Figure 3.15, sorted with trend line extracted

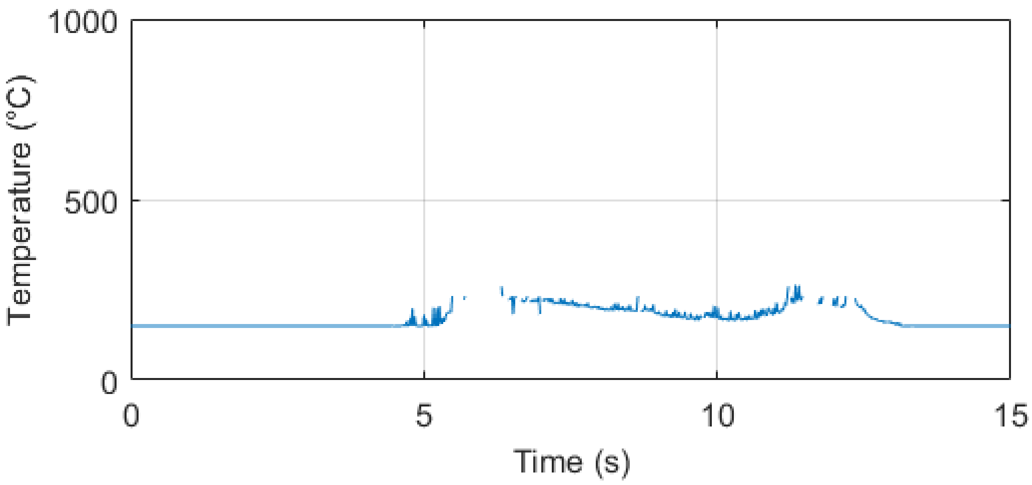

Figure 3.17 – The final output of the pyrometer data processing applied to the data shown in Figure 3.15

3.1.6 Side Camera

A camera has been fitted to the Low-Speed rig which makes use of stroboscopic imaging techniques to capture images of the side of the blade during a rub. For this task an LED has been placed on top of the spindle aiming towards the disk, a camera (Basler Ace acA1600-60gm) fitted with a telecentric lens (Edmund Optics 1X SilverTL) is placed on the other side of the disk facing the LED. As the blade passes between the camera and the LED a strobe controller (Gardasoft RT200F-20), triggered by a light gate (Optek OPB916B) will pulse the LED. The strobing LED illuminates a silhouette of the blade on each revolution, allowing the camera to capture the side profile. A schematic of this process is shown in Figure 3.18.

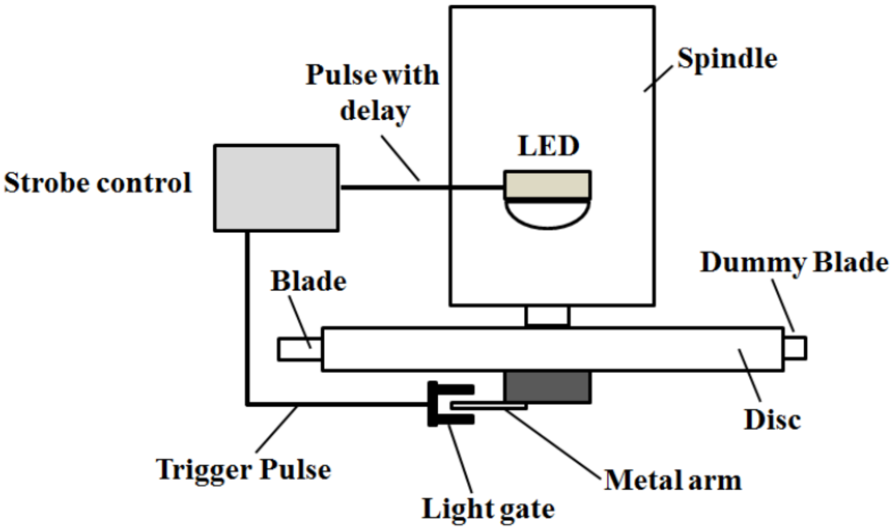

Figure 3.18 – Schematic for side camera strobe trigger system (94)

The resulting image (Figure 3.19) allows for the peak height of the blade to be extracted and monitored during a rub. Further development of a front camera system to replace the side camera is detailed in Chapter 4.

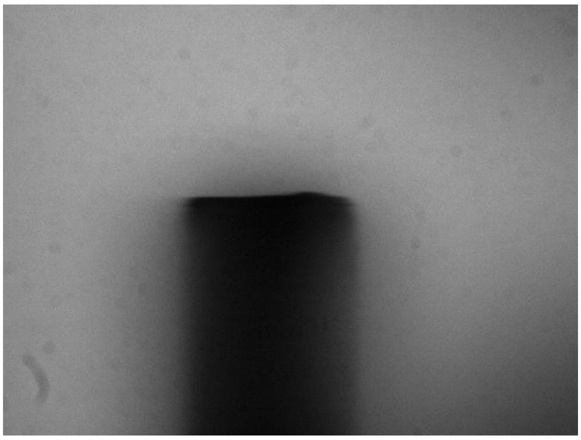

Figure 3.19 – Example image from the side camera

3.1.7 Abradable Heater Block

To allow for the control of abradable bulk temperature during a test, a heater block has been developed which can be fitted to the stage of the Low-Speed rig.

Implementations of heater units to abradable spindle test rigs by other research groups have applied heat, and measured temperature, on the surface of the abradable sample. This has the benefit of moving the heater hardware out of the load path of the blade-abradable contact but means the bulk temperature of the abradable is not controlled while also allowing for conduction of heat through the sample.

For this investigation a novel heating solution has been developed which sits below the abradable sample to apply heat to the sample backplate. By applying heat to the backplate and measuring at the surface it is possible to ensure that the bulk temperature of the sample is being controlled and thermal conduction through the sample is being limited as it is in an engine. However, this implementation leads to additional complexity in the heater design, ensuring that the heater can survive the stress of impact, and that heat does not flow into the load cell.

The design of this heater block is shown in Figure 3.20 and revolves around a steel sample interface plate. This plate contains the threads to mount a standard abradable sample as described in Section 3.2 as well as a pair of 300W resistive cartridge heaters (RS: 860-6921) and a k-type thermocouple (RS: 334-2622). The heating elements are controlled by a PID thermal controller designed by Elmatic, employing the Ascon Tecnologic K39 temperature regulator**.** The piezo dynamometer installed on the LSR has a maximum operating temperature of 120°C and therefore requires some thermal insulation. For an insulative material the fibre filled cement, Syndanyo H91, has been used. This material was selected due to its low thermal conductivity of 0.5 W/mK, its high operating limit of 700°C, and its high compressive strength.

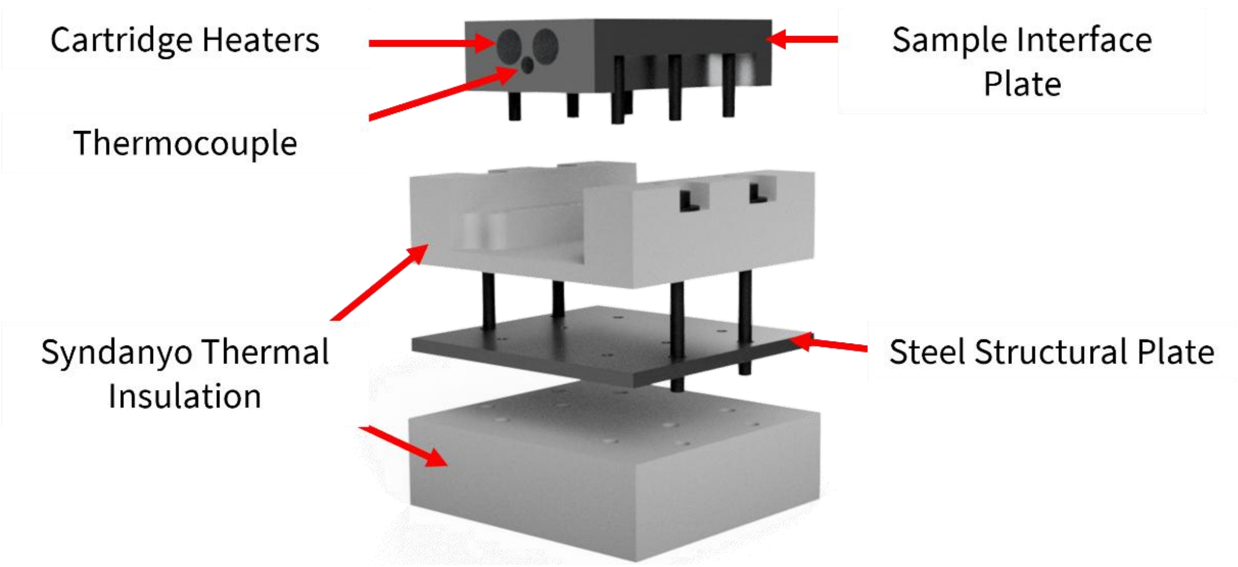

Figure 3.20 – An exploded view of the design of the abradable heater block

Each impact between blade and the abradable induces vibrations within the load cell and stage (78), these vibrations are measured as a period of tensile and compressive forces within the load cell with an initial peak equal to the contact force. These inertial loads will also be experienced by the heater block and although strong in compression, Syndanyo performs poorly in tension, meaning additional structural support is required.

This heater block is designed to support the tensile loads through high tensile strength bolts, and compressive loads through the Syndanyo. To do this a structural steel plate has been placed in the centre of two Syndanyo blocks. This plate contains the threads which the sample interface plate is mounted to and acts to spread any compressive stresses within the block across the full area of the Syndanyo.

Figure 3.21 shows how the stress flows through the block. During impact the blade pushes down on the sample interface plate, which then pushes on the Syndanyo below resulting in compressive loads. As the blade moves away and the inertial loads from the oscillations begin, the sample interface plate will pull up on the structural plate through tension in the screws, this will then apply a compressive load to the top piece of Syndanyo, which is held in place by a set of mounting screws with oversized washers to distribute the stress under the screw head.

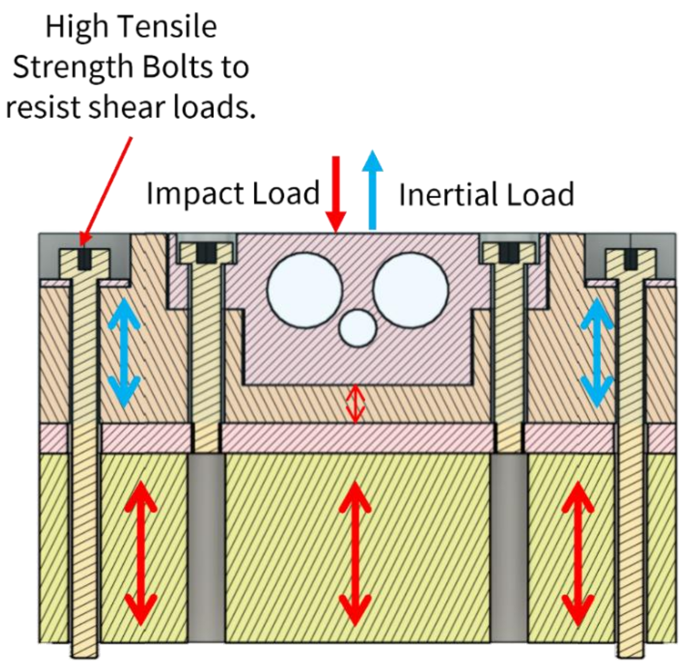

Figure 3.21 – Load paths within heater block during a tip strike

In the heater block design, there are no connected chains of metallic parts between the heater block and the load cell. This ensures that all heat will have to flow through the Syndanyo block, slowing the rate of heating at the load cell. Thermal simulations completed using Ansys Discovery (Figure 3.22) predict that it will take ~60 minutes for the load cell to reach 120°C, a result which was validated by heating the block while measuring its temperature using the FLIR A6750sc thermal camera. This provides sufficient time to heat the sample, ensure the sample has heated evenly, and to complete a 5 minute 0.02µm/pass test.

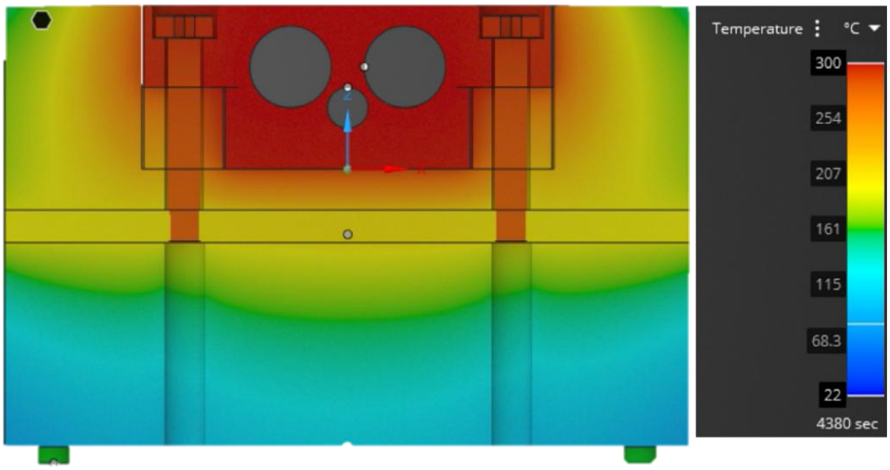

Figure 3.22 – A snapshot of the transient thermal analysis of the heater block, with a backplate temperature of 300°C after ~1 hour

The heater block mounts onto the LSR using the existing sample mounting plate (Figure 3.23). When mounting the block to the rig an additional thermocouple is added between the base of the heater block and the load cell assembly to ensure temperatures stay within working limits. While heating the sample a further thermocouple is mounted to the centre of the abradable sample surface, held in place with a steel mass.

To validate the strength of the block, and to ensure that additional mass of the heater did not have any adverse effects on the load cell, a series of tests were conducted at incursion rates from 0.02 – 2µm/pass on M601 at 55HR15y with the block unpowered. These tests did not lead to any structural issues or unexpected resonances within the system.

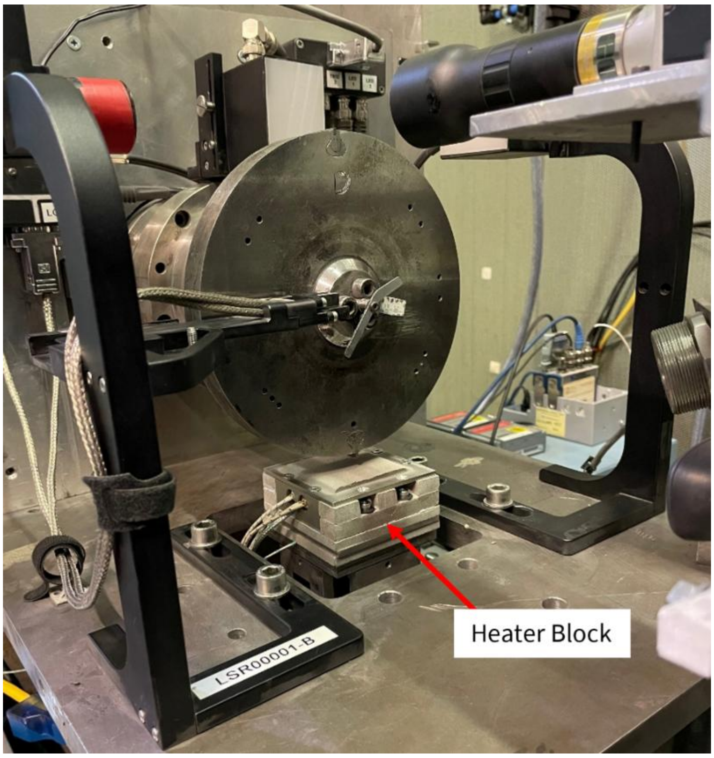

Figure 3.23 – An image of the heater block mounted to the Low-Speed rig

3.2 Blade and Abradable Sample Design

The AlSi based abradable samples used in this work were created by an atmospheric plasma spray process using a Oerlikon Metco plasma spray gun. They were sprayed onto a 2mm thick A2 Stainless Steel backing plate prepared following the surface preparation guidelines provided by Oerlikon Metco (105).

The plasma spray process works by passing a plasma gas, typically argon, nitrogen or hydrogen, between a pair of electrodes which are charged with a high DC voltage difference. This results in an arc forming between the electrodes, stripping the gas molecules of their electrons and forming a plasma. As the plasma ions recombine back to a gaseous state large amounts of thermal energy are released. The desired coating material is fed into this high energy gas in the form of a powder; this melts the powder and propels it towards the sample to be coated. This process is visualised in Figure 3.24.

In this thesis three AlSi based abradables are tested: M601, M320, and XPT268. To cover the full hardness range recommended by the material supplier samples have been sprayed at three target hardnesses. However, between samples there is some variation in the hardness. The resulting hardness bands are: 50 – 52, 60 – 63.2, 73 – 75.6. The actual hardness of each batch is measured before testing, with the hardness value of tested samples provided in the method of each chapter.

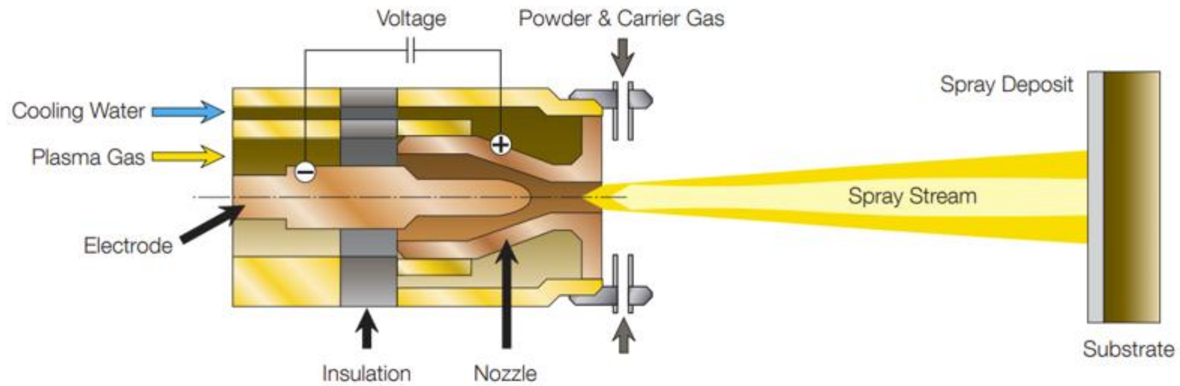

Figure 3.24 – Plasma spray gun schematic (106)

The hardness of the abradable can be varied by adjusting spray parameters such as powder flow rate, the current, and the distance between the gun and the backing plate (107). From each batch an abradable sample was tested against the Rockwell 15Y scale to validate that the coating is of the desired hardness.

A harder sample of an AlSi based abradable has a higher proportion of the larger AlSi particles than voids or dislocator. However, due to the higher temperatures and particle velocities involved in the spray process of harder samples the particles typically become more compacted on contact with the backing plate. Due to this there is no clear trend between the hardness and the roughness of the samples. The samples used in this work all had Sa values between 25 and 35 µm (Measured to ISO 11562, applying a linear planar, order 0 roughness filter in accordance with ISO 16610-61).

All samples are sprayed onto a standardized sample backing plate as shown in Figure 3.25, this geometry is shared between each of the spindle test rigs. The flat design simplifies the coating processes, allowing samples to be sprayed without the need for bespoke tooling. It also allows for multiple samples to be sprayed simultaneously, producing more consistent batches.

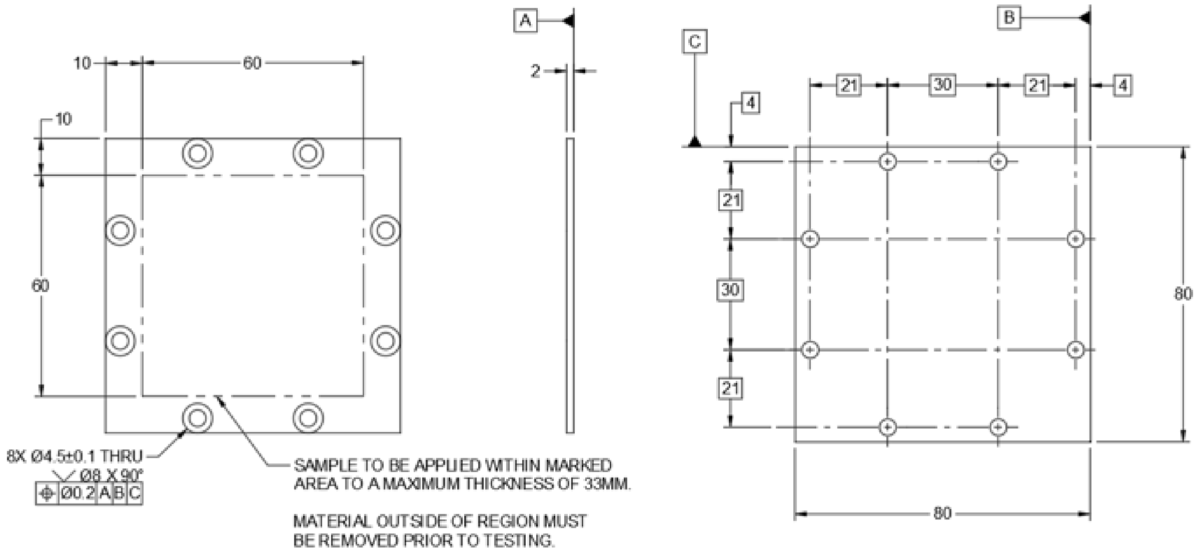

Figure 3.25 – Abradable sample geometry

The test blades are made of the same material as the blades within the engine (Grade 5 Titanium for this thesis), but the geometry has been simplified as shown in Figure 3.26. The flat geometry of the blades allows for them to be cut from a stock 2mm sheet, reducing the price per blade. A common blade design is used for both the High and Low speed spindle test rigs.

Examples of a blade and abradable sample made for this study are shown in Figure 3.27.

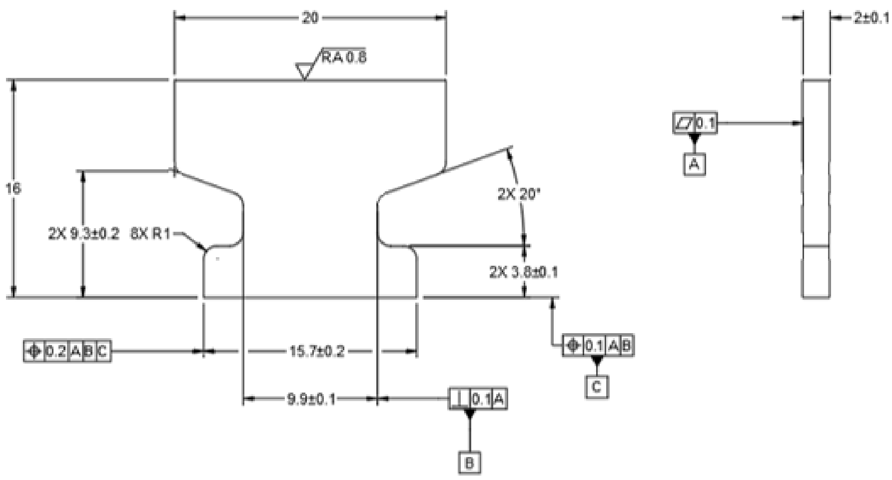

Figure 3.26 – Test blade geometry

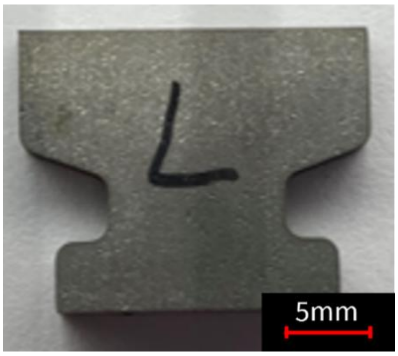

(a) Test Blade

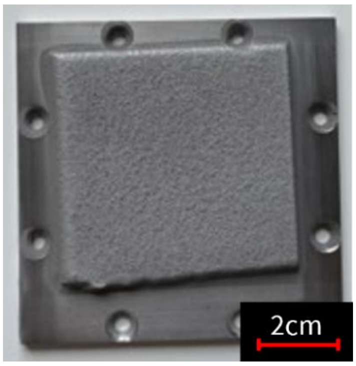

(b) Abradable Sample – M601

Figure 3.27 – Images of a test blade and abradable sample

3.3 Processing of Test Data

To process the data collected during each test a custom MATLAB program has been developed as part of this work. The program is centred on a core live script called *LowSpeedAnalysis.mlx* which includes graphical controls and plain text instruction, allowing the tools to be easily adopted by new users.

The live script is broken into sections which are run sequentially, each calling external functions as needed. The code is structured in this manner to minimize repeated code and to allow for easier comprehension. Figure 3.28 to Figure 3.31 show the structure of the code, with the live script shown on the left with data flowing down between sections. On the right the functions are shown, with the arrows showing where the functions are called and the direction of data flow.

The first stage in the data processing is the inputting of test parameters and the loading of test data. The code structure is shown in Figure 3.28, with the output of this section being a data structure detailing the test conditions, processed force and temperature data, and MATLAB representations of the thermal camera, spark, front and side cameras produced for further processing.

With the data processed, and images accessible, the next stage is the preprocessing of the data (shown in Figure 3.29). This stage collects a range of user inputs based on the thermal and visible camera data to ensure the footage is correctly aligned and generates the warp matrix for the abradable thermal footage. The output of this section is a data structure including all the required location data. As this data is a function of the rig set-up the data structure can be shared between any test completed during the test campaign.

With all data loaded, and the camera footage spatially and temporarily aligned, Figure 3.30 shows the structure of the code which produces the final processed output. The key output is a single, standardised, data structure which includes all force and temperature data against common time and rub length arrays. Alongside this data there are 2D arrays showing how the blade and abradable profiles and temperatures change at any location and time. These variables are all aligned with a common position array (horizontal axis), meaning any physical characteristics can be extracted for the same position and time by accessing the same index position in each array. This code section also produces a series of standard plots which can be directly compared between tests. All processed data is saved to a new processed data folder which can be directly loaded into the code, allowing data to be reviewed in the future without the need to reprocess.

To allow for easy visualization of the data an additional section of code (Figure 3.31) has been developed which will collate all the processed data and produce a video. These videos align the visible and thermal cameras, while also displaying the force data and highlighting adhesion and wear events (Figure 3.32), allowing for relationships to be observed. The addition of a visualisation of the abradable profile, alongside a quantified gap area between the blade and coating, can be used by engine manufacturers to visualise how the coatings will perform within the engine.

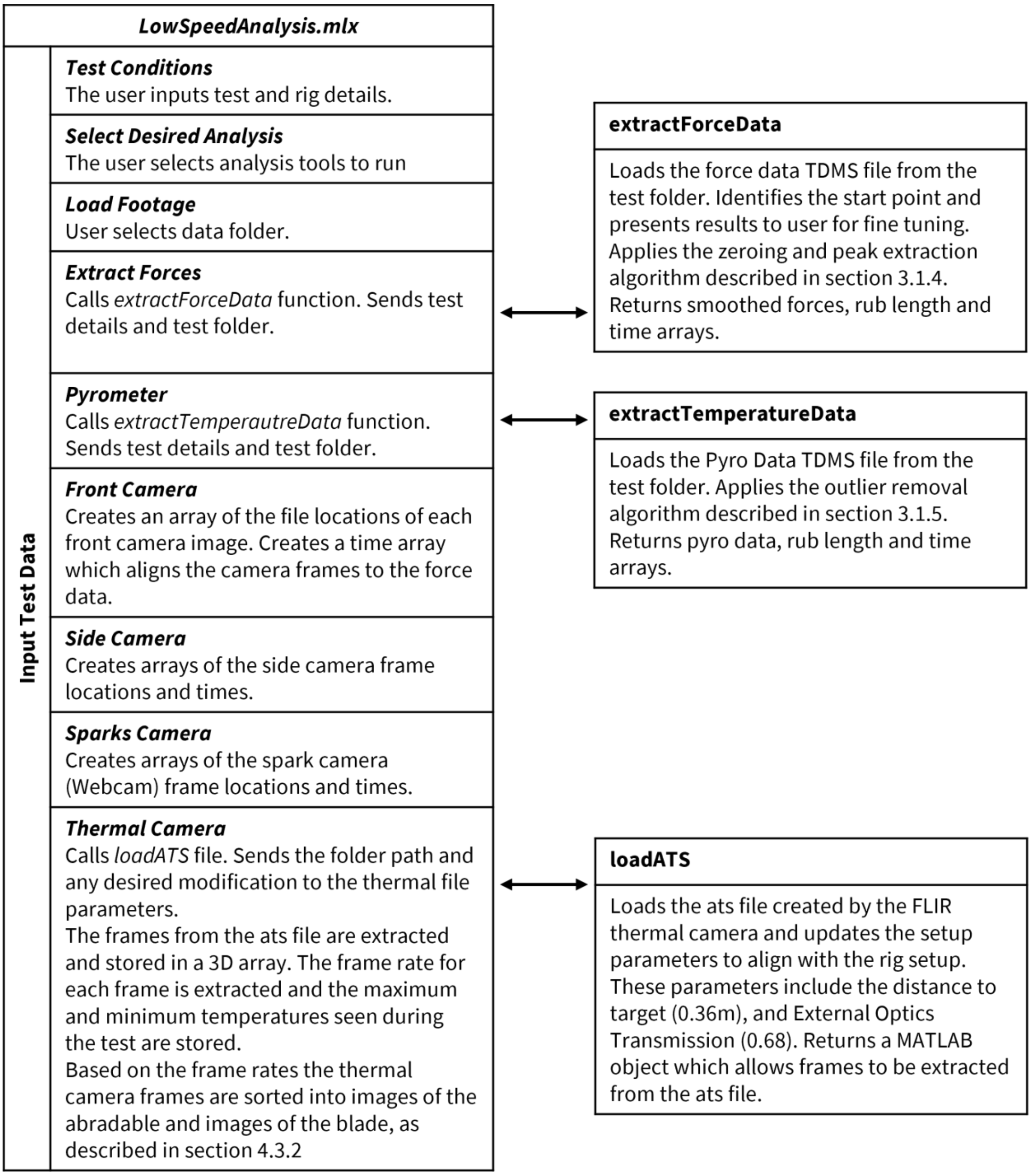

Figure 3.28 – Structure of the MATLAB code to read in test data

LowSpeedAnalysis.mlx

Preprocess Data

Generate Warp Map
The user selects the ats file containing the recording of the moving PCB template described in section 4.3.2. The file location is passed to the *loadATS* function.
Each frame in the ats file is passed to the *produceTransform* function. The returned matrix is appended to a 3D array.
The data stored in the 3D array is used to calculate the linear relationships which describe how each element of the transformation matrix varies with stage position.

Set Warp Height
The user enters a set of measurements of the stage position and abradable thickness taken before a test. The values are passed to the *polyTform* function, alongside the linear relationships previously calculated.

Rotate Blade Images
A graphical user interface (GUI) is presented to the user to allow the blade images to be adjusted to correct for any camera/blade misalignment.

Select Blade Corners
A GUI is presented to the user to allow the corners of the blades to be selected. This data is used to determine pixel size, and to form a foundation for further image analysis.

Detect Centre of Thermal Camera Footage
Composite images of the hottest pixels captured during the test for both the blade and abradable are created. These images are used to determine the location of the blade and abradable within the frame, and to set the scale of the images to align with the front camera footage.

Fine Tune Thermal Position
A GUI is presented to the user which displays the aligned front camera, abradable, and blade thermal images at any time during the test. Controls are provided to fine tune the scale and position of the thermal footage to better align with the front camera.

loadATS

Loads the ats file created by the FLIR thermal camera and updates the setup parameters to align with the rig setup. These parameters include the distance to target (0.36m), and External Optics Transmission (0.68). Returns a MATLAB object which allows frames to be extracted from the ats file.

produceTransform

Within the received frame the hole pattern is located, and the relationship between the hole pattern and the desired orientation is calculated. The result is returned as a transformation matrix.

polyTform

Based on the measurements taken the position of the abradable surface is calculated. Using the linear relationships a transformation matrix can be calculated for this abradable position. The result is returned.

Figure 3.29 – Structure of the MATLAB code to calculate variables needed for data processing

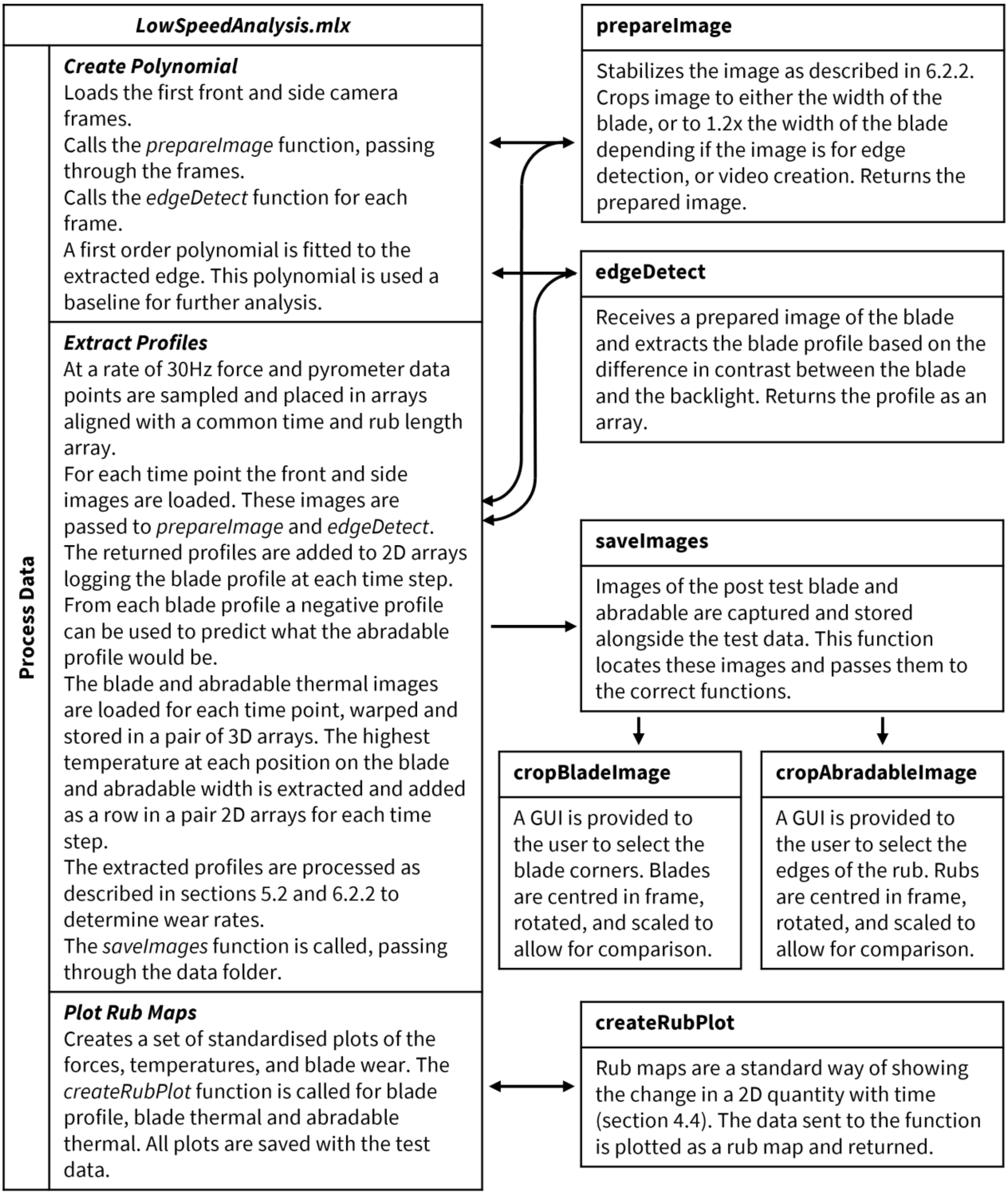

Figure 3.30 – Structure of the MATLAB code to process the test data

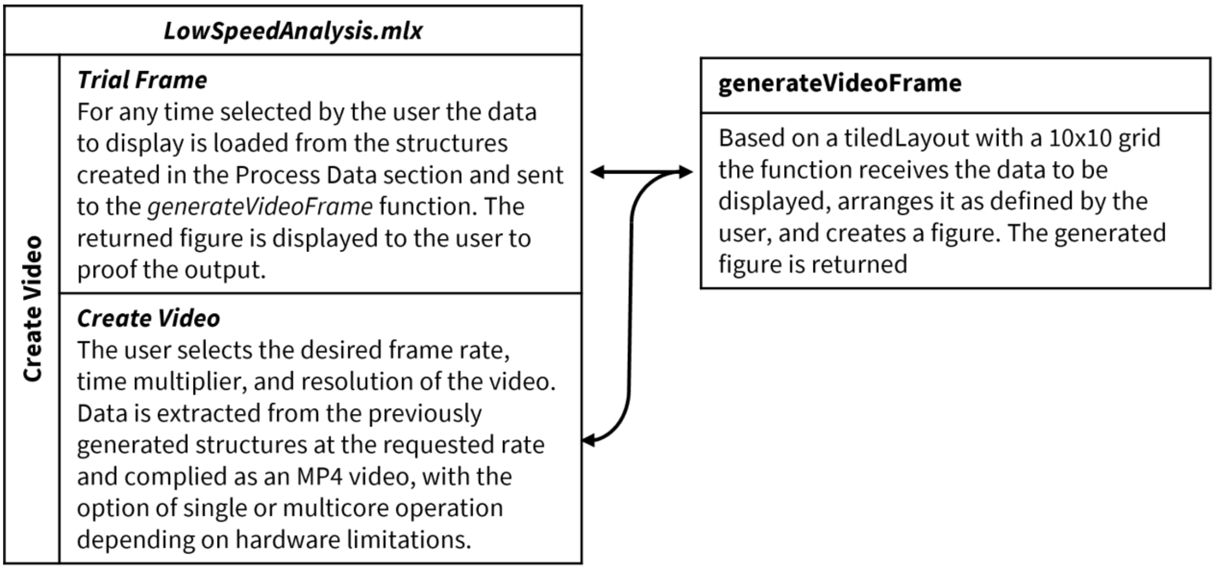

Figure 3.31 – Structure of the MATLAB code to create test videos

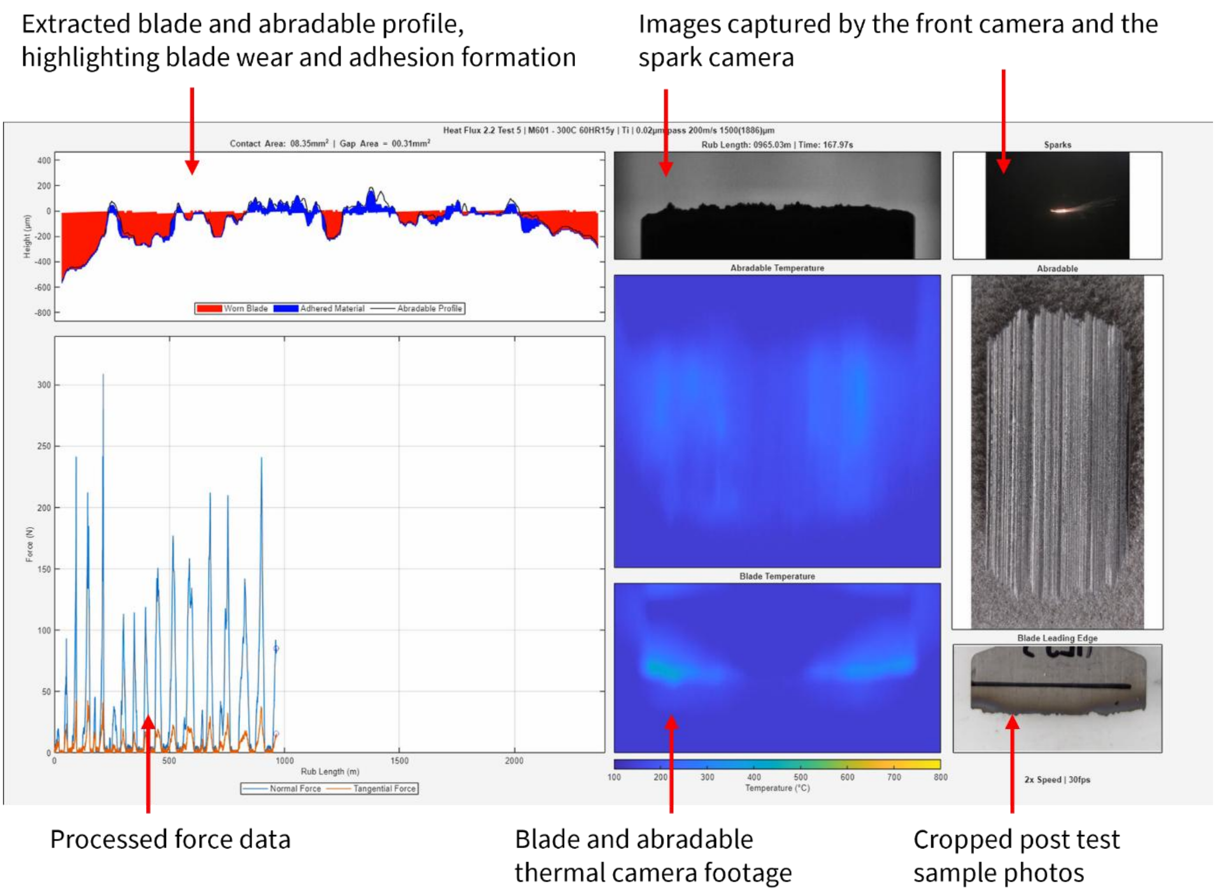

Figure 3.32 – An example frame taken from a video created for a 0.02µm/pass M601 test

3.4 Material Characterisation

While in-situ measurements allow for a visibility of how wear develops during a rub, it is important to be able to classify which wear mechanisms have occurred and to determine the state of the samples, both before and after the test.

This section describes the methods used to prepare tested samples for further inspection, and the tools used to measure key parameters such as roughness and hardness of test samples.

3.4.1 Alicona Profile Measurement

The Alicona InifiteFocusSL is a measuring system which combines optical microscopy with vertical scanning to produce a 3D topology map of the sample. From this 3D model it is possible to measure the form and roughness of the sample and provide high resolution microscopy images with a larger depth of field than traditional microscopes.

This tool was used to inspect the profile of the blades and abradables before and after the rub to measure sample roughness.

3.4.2 Sample Preparation and Optical Microscopy

To inspect the microstructure of the samples they must be sectioned and prepared. However, as the abradables materials can be soft, care must be taken not to compress or introduce cracks into the microstructure during cutting or polishing (108).

Samples are cut on an Abrasimet using an abrasive cutoff disk designed for use with soft materials (MetAbrase 11-4207-010). Samples are clamped via the steel backing plate to prevent damage to the abradable. Each section cut should is less than 20mm long to allow it to be mounted into a standard 32mm sample preparation cup.

The cut sections of the sample are then placed, in pairs, into a 32mm sample preparation cup and vacuum impregnated with an epoxy resin (EpoThin 2). By adding two samples to each cup the steel backing plates act as hard stops during the polishing process, preventing uneven wear of the softer abradable.

The mounted samples are then ground and polished using an Ecomet, starting with grinding papers of P240, progressing to P1200. The final polish is completed using a polishing cloth with 3µm and then 1µm diamond suspensions. The result is shown in Figure 3.33.

The polished samples can then be inspected using Light Optical Microscopy to inspect the microstructure, allowing for the compositions and any signs of compaction of subsurface damage to be observed.

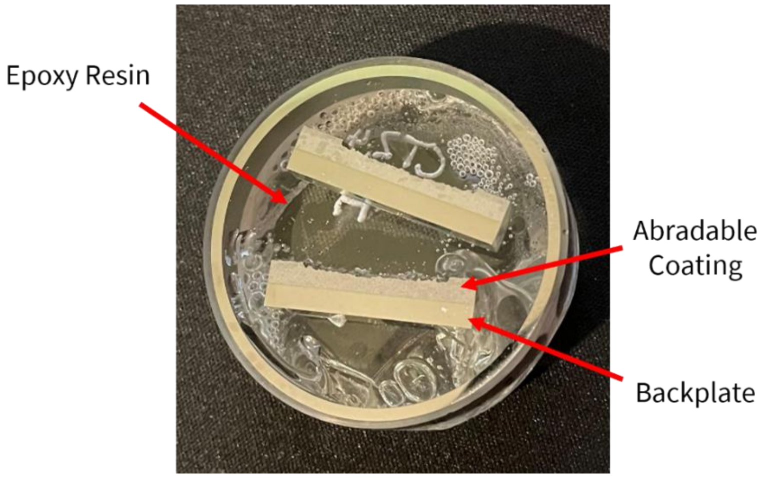

Figure 3.33 – Abradable samples prepared for optical inspection

3.4.3 Rockwell Hardness Measurement

The wear performance of an abradable varies significantly with its hardness (76), it is therefore vital to be able to accurately measure the hardness of the samples being tested.

The Superficial Rockwell 15Y scale is commonly used when measuring the hardness of abradable samples. This scale is ideal as the soft abradable will undergo measurable deformation at the low forces of this scale, and the large diameter of the ball indenter used will produce an average hardness over the contact patch, limiting the impact of subsurface variability.

The Rockwell scale is a displacement-based hardness measure, this means that after applying a predetermined load profile with a standardized indenter (1/2” Tungsten Carbide Ball for 15Y) a measurement of how deep the indenter has pressed into the material is taken and used to determine the hardness.

For the Rockwell 15Y scale the load and displacement curves are shown in Figure 3.34. In this test an initial load (F_0) is applied to ensure the indenter has contacted the surface and a position measurement is taken, a test load (F) is then applied and held for a dwell time (t_{TF}). After the dwell time the force is reduced back to F_0 and a second position measurement is taken. The difference between these two measurements (h), in mm, is used to determine the hardness using the relationship: $HR15Y = 100 - \frac{h}{0.001}$.

Table 3.2 – Test Parameters for the Rockwell Hardness 15Y Scale

Variable	Standard Range	Test Values
F_0 (N)	29.0	
F (N)	147.0	
v_a (mm/s)	2.5	1.0
t_{TA} (s)	1.0 – 8.0	4.0
t_{TF} (s)	2.0 – 6.0	4.0
t_R (s)	0.2 – 5.0	2.5

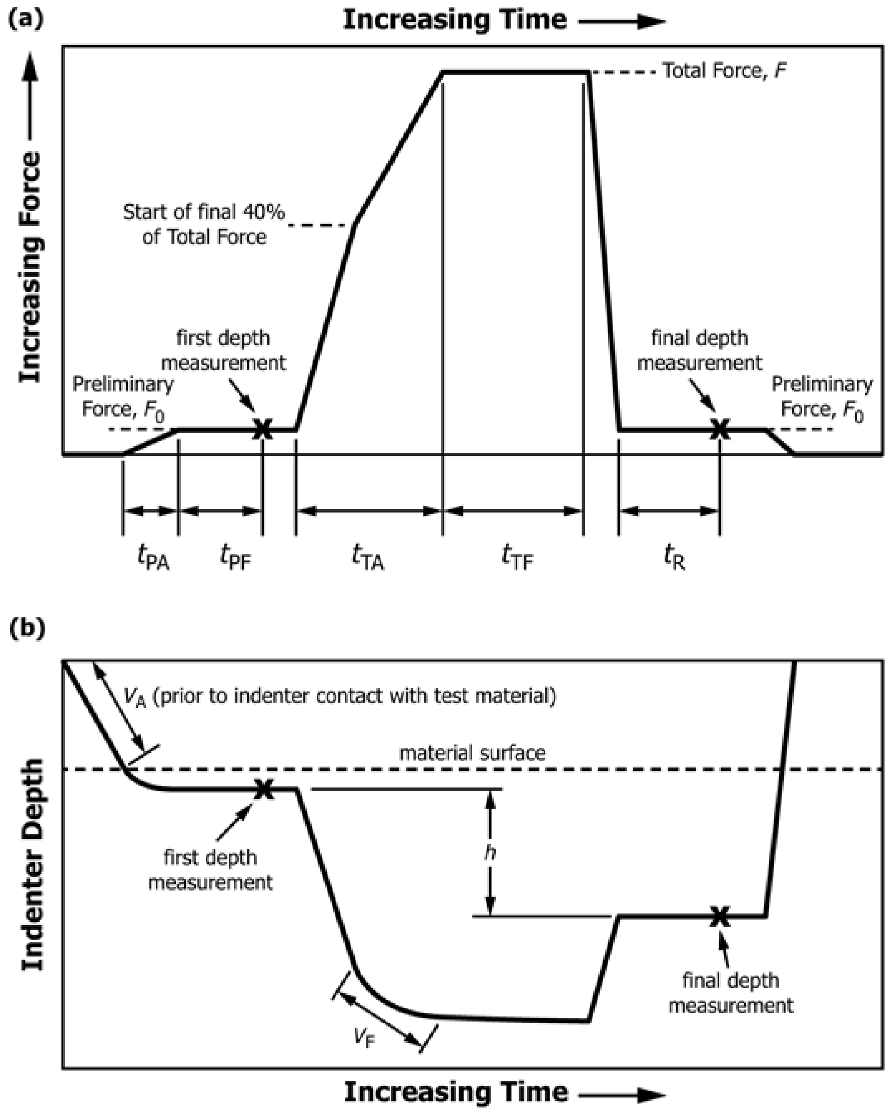

Figure 3.34 – Load (a) and displacement (b) profiles for a HR15Y test (109)

Hardness tests were completed using a Tinius Olsen Universal Testing Machine (UTM), with a load profile programmed to follow that shown in Figure 3.34a. The variables for test timings and speeds were chosen as the midpoint of the range given in the standards (Table 3.2).

To measure the displacement of the indenter relative to the sample the encoder within the UTM could not be used due to its low resolution and repeatability. Instead, a Laser Triangulation displacement sensor (optoNCDT 1220) was mounted to the indenter (Figure 3.35), minimising compliance between the measurement sensor and the contact point and providing a measurement repeatability of 1µm (110).

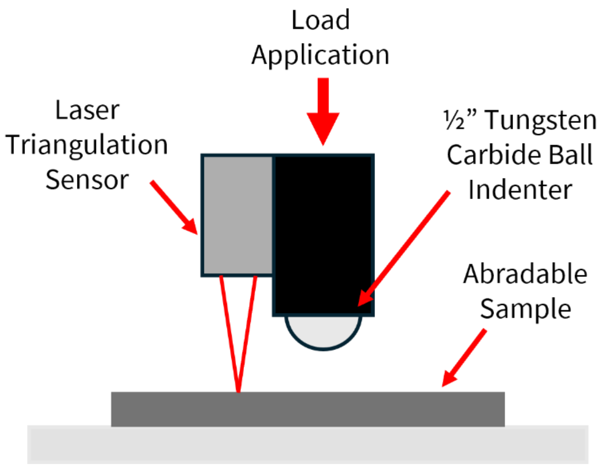

Figure 3.35 – Schematic of HR15Y hardness test setup

3.5 Conclusion

This method provides an overview of the common tools applied to all chapters within this thesis, detailing sample design, the test rigs and the basic data and sample processing. Through the course of this work further tools and techniques were developed, including novel in-situ measurements tools, data analysis techniques, and sample heater blocks. These are detailed in the method section of the relevant chapter.

4 In-Situ Measurements of Blade-Abradable Wear

4.1 Introduction

This thesis aims to fill gaps in current knowledge around the impact of thermal properties to wear mechanisms through the development of novel in-situ measurement tools. In this chapter stroboscopic imaging techniques have been applied to record blade profile, while using a thermal camera to record hotspots on the blade and the abradable. Together these will allow for the simultaneous monitoring of blade wear, blade temperature and abradable temperature. Observing how these variables interact and develop during a test will allow for a deeper understanding of how abradable wear mechanisms relate to thermal behaviours.

Previous research looking into how in-situ measurement techniques can be applied to abradability testing, such as the addition of cameras recording the blade (79) and dynamometers recording rub forces (78). These developments have shown how gathering data throughout the rub makes it possible to better understand how adhesions form, and how wear mechanics are dependent on events which have occurred previously. This new insight, alongside force measurement techniques, has provided a strong foundation to develop theories on why adhesions form. Further to this, in-situ thermal measurements tools employed by Agrapart et al. (100) have shown the importance of thermal management during a rub due to the large heat flux into the abradable. This work has been built on by Nyssen et al (111) showing the benefits of including thermal behaviours in mechanical models of blade rubs during vibration events.

Although thermal behaviour has been shown to be important, there is a gap in understanding of the thermal behaviour with respect to adhesion and wear mechanisms. Attempts to model the thermal behaviour of Metco 601 by Watson et al. resulted in poor correlations (74). It was theorised that this was to be due to nonlinearities and missed effects within the system, properties that the tools developed in this study have the potential to observe.

4.2 Requirements for In-situ Measurement tools on the Low-Speed Rig

Prior to this work the Low-Speed rig was equipped with a dynamometer to measure forces, a camera recording the side of the blade, a pyrometer for temperature measurement, and a thermal camera which was triggered by a laser pyro to recorded either the blade or the abradable during a test.

To allow for the visualisation of blade wear, and to relate this wear to any thermal behaviour, the full blade profile needs to be extracted during a test and the thermal footage must be collected for both blade and abradable in a manner where the output can be aligned spatially with the blade profile.

The side camera was limited as it could only record the highest point on the blade. As wear on the blade does not typically occur uniformly across the blade front a second camera was required pointing at the front of the blade. A front camera solution has been installed on the High-Speed rig and produced promising results. However, this solution struggled with image quality due to the uneven lighting of its strobe system, the camera and lens were too large to fit inside the Low-Speed rig enclosure, and the 3D printed camera and strobe mounts could not be adapted to mount onto the Low-Speed Rig. For this application a bespoke solution would be required which could improve on the image quality seen in the High-Speed implementation, while also being more compact so that it can fit within the Low-Speed rig.

The thermal camera implementation on the Low-Speed Rig allowed the camera to see into the enclosure and, using a laser tachometer, the camera could be triggered when either the blade, or the abradable was visible. This setup struggled with triggering reliability when the dust generated in a test obscured the laser. It was also not possible to extract the position of any recorded hotspots with respect to the abradable as there were no visible reference points resulting from a filter blocking anything colder than 150°C. To provide the output required in this work a novel triggering solution is required, which can reliably trigger for both the blade and abradable positions in the same test. A novel alignment process is also required so that the thermal and the front camera footage can be aligned temporarily and spatially.

4.3 Method

This work aimed to build on the existing capabilities of the low-speed spindle test rig to allow for the measurement of thermal and visible data simultaneously. This chapter details how these tools have been developed and how they can be used to better understand the fundamentals of abradable wear mechanics.

4.3.1 Front Camera Set-up

A camera has been installed into the rig which can record the front of the blade during the test. This set-up uses similar stroboscopic techniques to those employed by Rahimov et al. (79) on the High-Speed Rig. A bespoke solution has been developed for this application to allow for integration with the Low-Speed rig and to improve image quality.

Due to the limited space within the rig, a fixed focal length lens (Edmund Optics #59-870) and a small sensor camera (Allied Vision Alvium 1800 U-500c) have been used. This combination results in a narrow field of view, which the blade fills, while minimising the margin of error between features measured at the leading edge of the blade compared with those at the trailing edge (112).

Figure 4.1 shows how a feature of the same size (H) appears larger to the camera sensor if it is positioned at the leading edge of the blade (L_1) compared to if it were positioned at the trailing edge (L_2). The size of the feature on the camera sensor is a ratio of the lens focal length and the distance of the object from the focal point, the ratios for this set-up are given in Equations 1 and 2. For this test setup measurements of adhesion heights will have an error of up to 1.2% depending on their position on the blade (Equation 3).

$$\frac{L_1}{H} = \frac{16}{167} \tag{4.1}$$

$$\frac{L_2}{H} = \frac{16}{169} \tag{4.2}$$

$$\frac{L_1}{L_2} = \frac{169}{167} = 1.012 \tag{4.3}$$

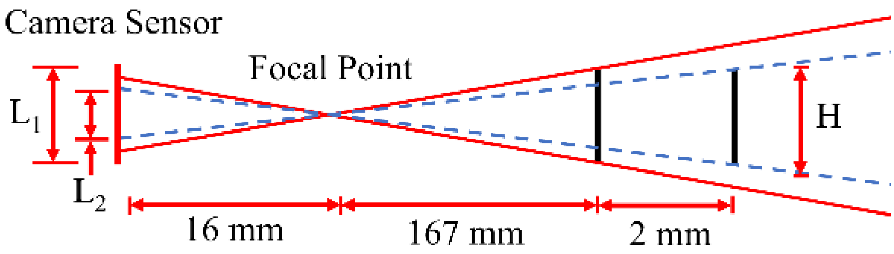

Figure 4.1 – Theoretical visualisation for the field of view of the Low-Speed Rig front camera

The stroboscopic set up by Rahimov et al. (79) made use of two separate LEDs to illuminate the blade. This resulted in a distinct lighting gradient with bright spots at the centre of each diode (Figure 4.2), this had to be corrected in post processing. To improve upon this for this application a light diffuser has been fitted in-front of the LEDs, smoothing the light gradient.

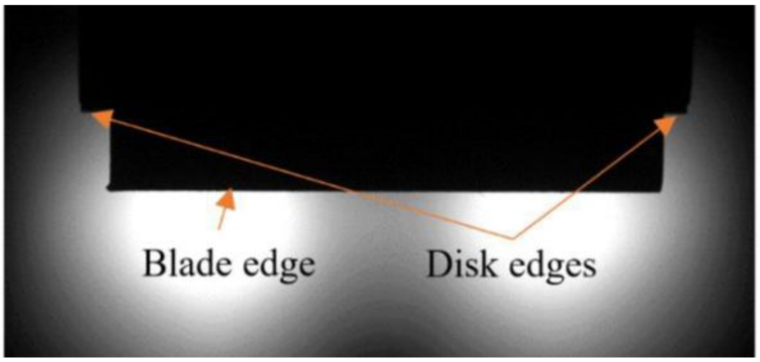

Figure 4.2 – Example image from the High-speed rig front camera system (79)

The camera is triggered by the light gate installed by Fois et al. (77) for the side camera. This light gate has been shown to have a very repeatable response time and is unaffected by dust produced during a test (73). This minimises the variation in blade position between images. Figure 4.3 shows the aligned front and side outputs for 0.02µm/pass tests for two different abradable materials.

(a) Metco 601

(b) Metco 320

Figure 4.3 – Example Front and side camera outputs from tests completed against (a) M601 and (b) M320 on the Low-Speed Rig

4.3.2 Thermal Camera Set-up

4.3.2.1 Recording Abradable Hot Spots

The FLIR A6750sc Thermal Camera was selected for this use case for its high frame rate, allowing for images to be captured for every pass of the blade. Due to the large form factor of this camera, it has been set-up outside of the protective enclosure, observing the abradable through a window of Zinc Sulphide, as shown in Figure 4.4. A lens extender (FLIR PN: 222-0006-05 REV-A) has been added to minimise the working distance.

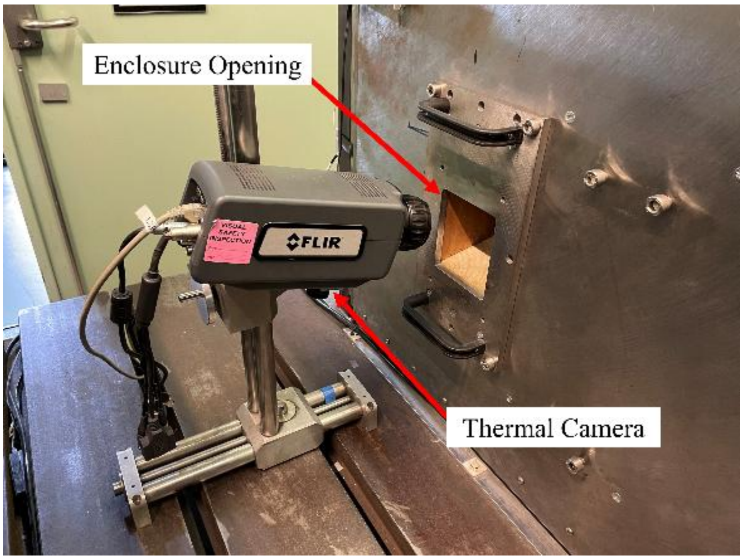

Figure 4.4 – Image of the thermal camera set-up on the Low-Speed Rig

This set-up results in a shallow camera angle which can view the abradable under the rotating disk. Whilst practical as a test set-up, this arrangement brings issues as the blade does block the view of the abradable once per revolution, and the abradable surface cools rapidly after each strike. As such, for the most consistent results, each image must be taken when the blade is not obstructing the camera view, with the same time delay after the rub event.

To synchronise the frame rate of the camera and the rotational speed of the spindle, the output of the light gate used for the strobes is connected to the SYNC IN pin of the cameras AUX Connector (Pin 10). A delay between triggering and capturing a frame is then set within the ReaserchIR software package provided by FLIR, this allows the captured images to be set to a point where the blade is out of view of the camera.

Due to the shallow angle of the camera the raw image is compressed, making it challenging to distinguish individual hot spots. Figure 4.5 shows the raw output of the thermal camera while recording the abradable during a rub. The red areas show the presence of surface hotspots on the rub surface. To improve the clarity of the output homography methods have been applied to warp the output so that it appears that the footage was taken normal to the surface.

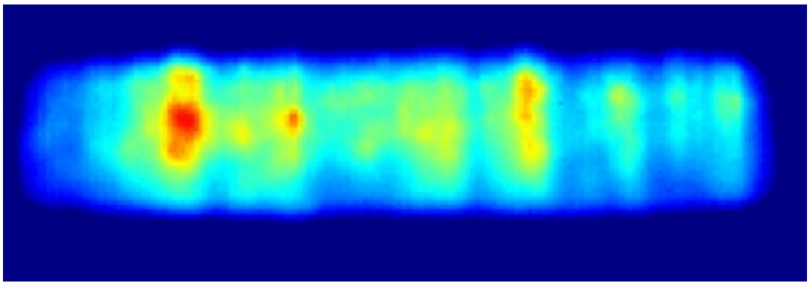

Figure 4.5 – An example of thermal camera raw output, showing an image of the abradable during a test

To create the required warp matrix, a PCB with a gold surface layer was used with a pattern of 9 holes drilled through the board, the gold surface was able to reflect the heat emitted from a flood light producing a clear image for the thermal camera (Figure 4.6A). The holes were all separated by 7.5mm and were aligned parallel to the direction of travel of the blade with the central hole aligned with the centre of the rub path.

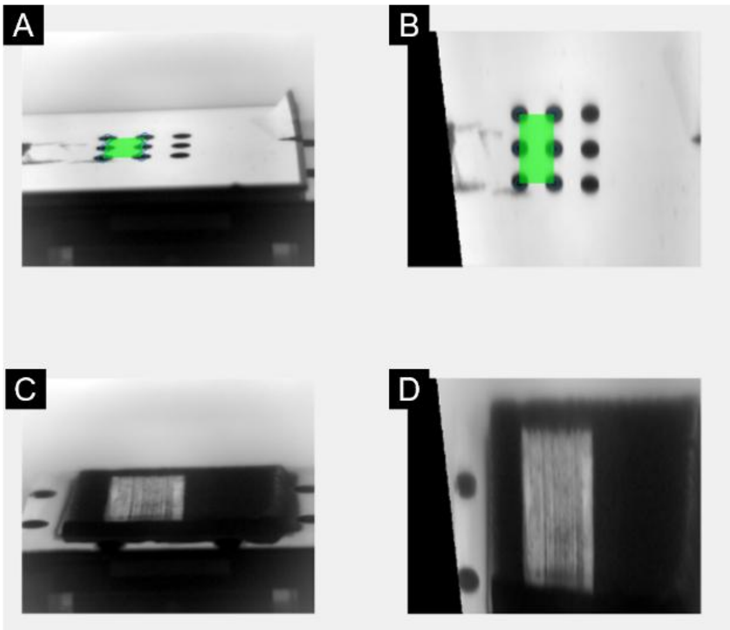

Figure 4.6 – Examples of the homography process run on the PCB with holes template (A, B), and then on a tested abradable sample (C, D)

Using MATLAB, the hole positions are detected using the *detectMSERFeatures* function. A projective transformation matrix is then created using the *fitgeotrans* function. This matrix can then be applied to any image taken with the same position relative to the camera using the *imwarp* function, outputting an image which appears to have been taken from directly above the abradable.

The required warp matrix will change for blades and abradables of different lengths and thicknesses. To generate the required warp matrix for a given test arrangement a video is taken of the stage moving with the template on top, and the matrix created at regular intervals as the stage moves. The elements of the 3x3 warp matrix vary linearly with stage position (Figure 4.7). Finally, knowing the gradient for each matrix element and the starting stage height for recording, it is possible in turn to extract a warp matrix for any stage height.

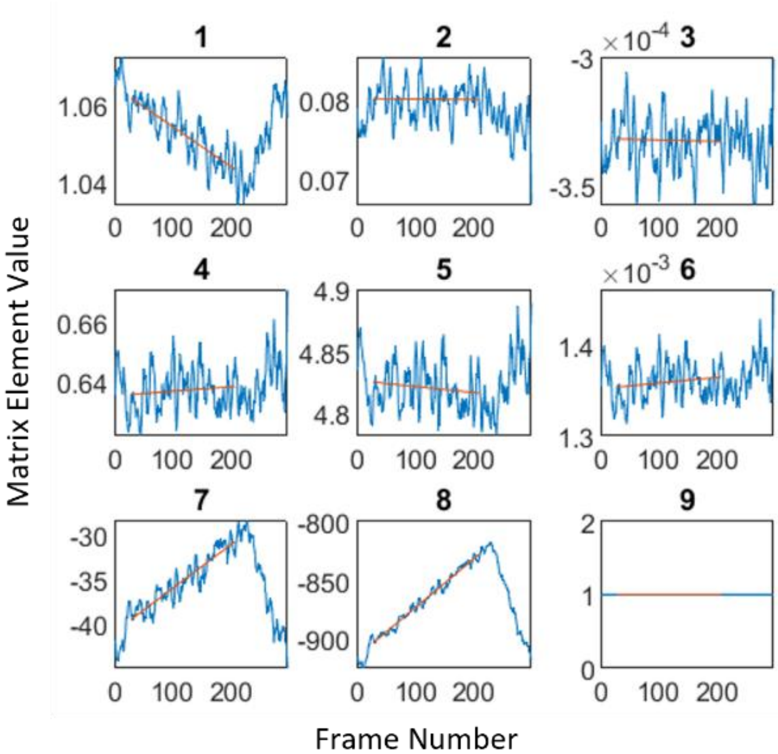

Figure 4.7 – Variation in the values of each element of the warp matric with increasing stage height

The output of the warped thermal image, alongside the front and side images, is shown in Figure 4.8.

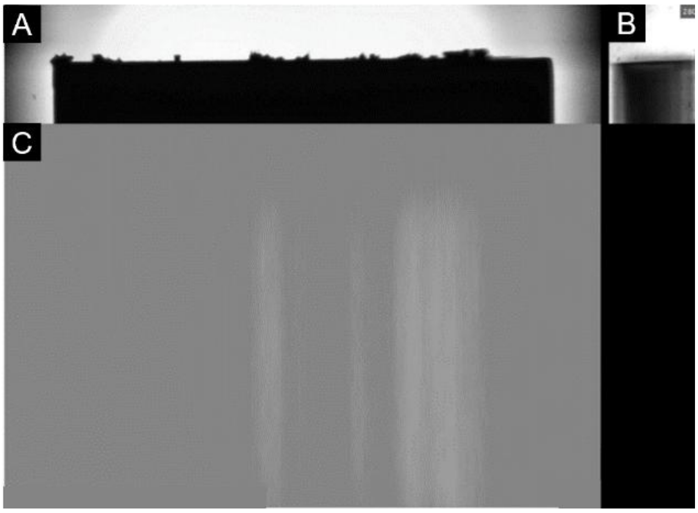

Figure 4.8 – An example output of the in-situ measurement tools for a 0.2µm/pass, M601 test from the A – Front camera. B – Side camera. C – Warped abradable thermal.

4.3.2.2 Recording Blade Hot Spots

To capture images of the blade and the abradable during the same rub a second light gate has been installed. This light gate is positioned 6mm closer to the axis of the disc and can therefore be triggered by a shorter trigger arm (Figure 4.9). By using the offset light gate as a trigger for the thermal camera images can be taken twice per revolution, once when the blade is visible, and once when the abradable is unobstructed.

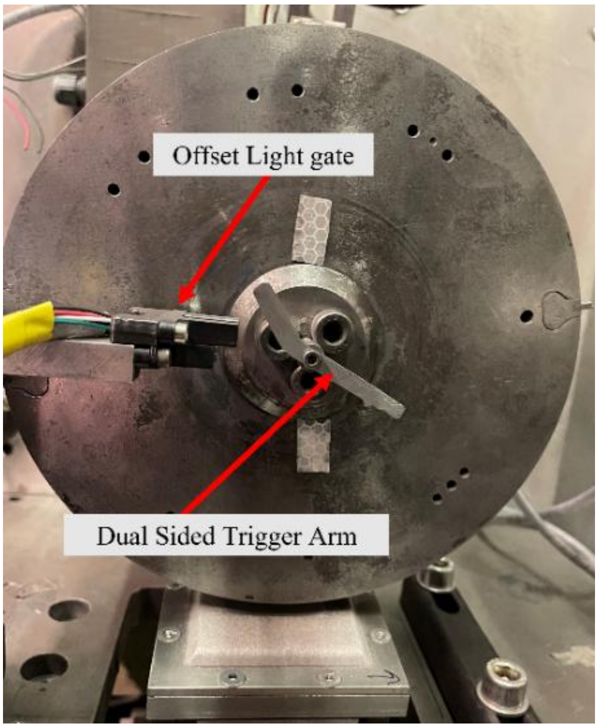

Figure 4.9 – Image of the dual light gate trigger set-up to allow capturing frames of both the blade and abradable

For tests with tip speeds less than 100ms^{-1} the thermal camera can capture two frames for each revolution. At higher speeds, the maximum frame rate of 400Hz makes it impossible to capture both blade and abradable within the same revolution. Increasing the delay between sync input and image capture by one rotational period reduces the rate of image capture to two images per three revolutions. This allows the tool to be used up to the maximum speed of the spindle test rig (200ms^{-1}).

To avoid the dummy blade from obstructing the abradable images the two trigger arms are separated by ≈160°. Due to the asymmetric positioning of the two trigger arms the time between frame captures differs for a blade image and an abradable image. The blade and abradable frames are therefore separated depending on the frame rate. At 200ms^{-1} blade images will have a frame rate of 230Hz while abradable images have a rate of 210Hz.

With the images captured and separated into two separate videos, they are lined up with each other and played alongside the front and side footage, as shown in Figure 4.10.

For these results the apparent temperatures of the blade and abradable have been extracted from the ResearchIR software package using the default emissivity of 0.92. This is sufficient to identify hot spots, but the error in any calculated temperature is a function of material and camera properties (113).

With these limitations the results from this rig can only be compared to other results made using this rig as the errors will be consistent. At this stage this is sufficient to answer the question of how wear mechanisms link to hot spots and provides a level of insight which has not previously been possible. If work using these tools shows that accurate temperature readings would be beneficial measurements of how the emissivity of the abradable varies throughout the test would be required. This could be achieved by heating abradable samples which have been tested to varying incursion depths to known temperatures. By recording these samples with the thermal camera, it will be possible to extract information on how emissivity varies with temperature and incident angle for each abradable material.

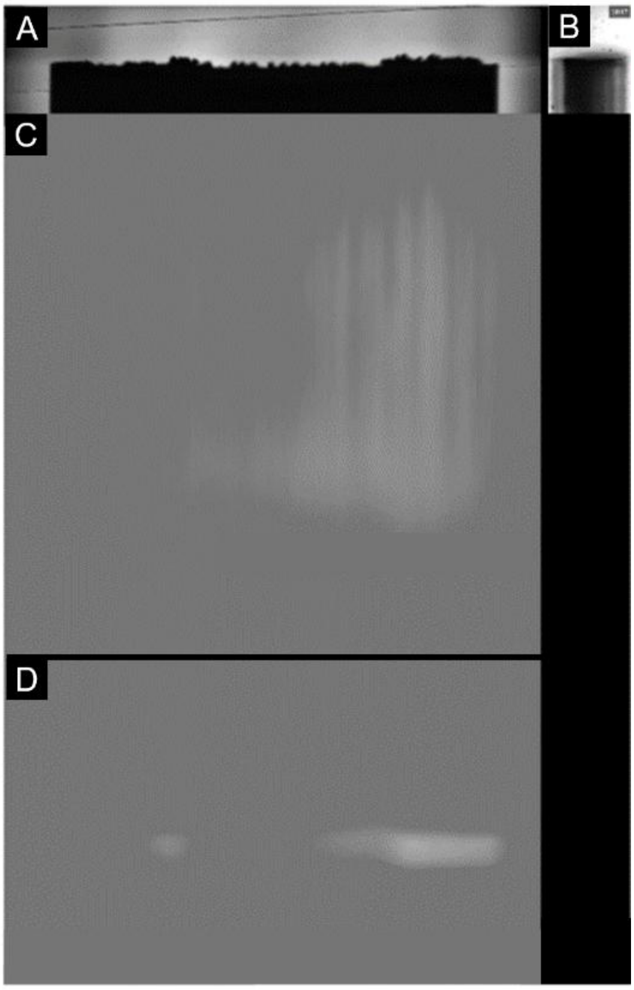

Figure 4.10 – An example output of the in-situ measurement tools for a 0.2µm/pass, M601 test from the A – Front camera. B – Side camera. C – Warped abradable thermal. D – Blade thermal

4.3.2.3 Temporal Alignment of Visible and Thermal Cameras

All cameras are triggered by the LabView code developed to control the spindle test rig, the footage from the two visible cameras is collected by LabView, with the alignment of these videos confirmed by observing events such as adhesions breaking off on both video feeds. The thermal camera is triggered through LabView using the cameras AUX Connector (Pin 8), the video is then recorded using the FLIR ReasearchIR software. This results in a delay between the thermal and visible cameras.

To align the cameras a separate test has been completed to measure the delay between them. This took the form of a protractor being rotated at a fixed angular velocity by a stepper motor with a needle pointing radially inwards at the protractor markings (Figure 4.11).

The front camera and thermal camera were both triggered to record the protractor, with the difference in angle recorded by both cameras used to measure the time delay (Figure 4.12).

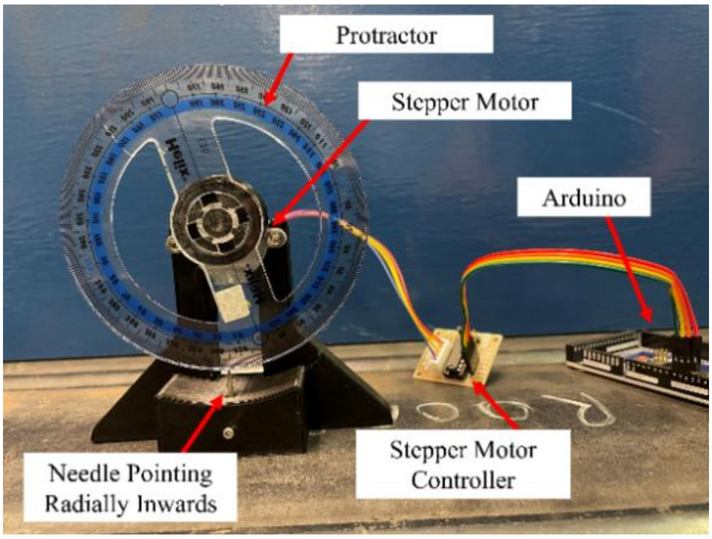

Figure 4.11 – Image of the delay measurement tool used to align the thermal and visible cameras

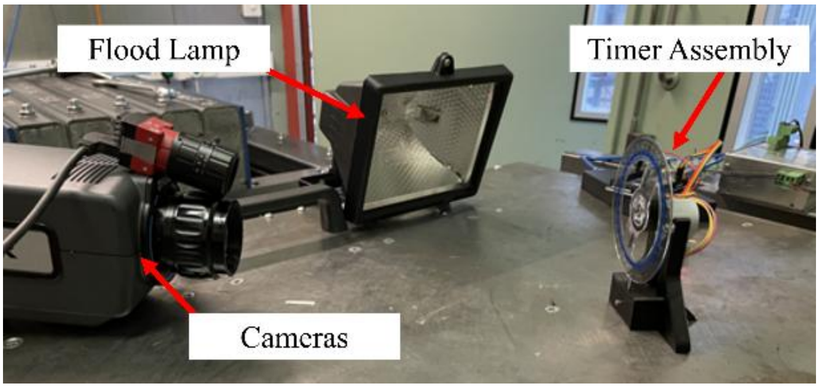

Figure 4.12 – Image of the set-up for the camera temporal alignment testing

As shown in Figure 4.13b, the black markings reflect more energy than the clear acrylic and therefore appear hotter (brighter in colour) in the thermal camera output. This allows the numbers and markings to be clearly seen.

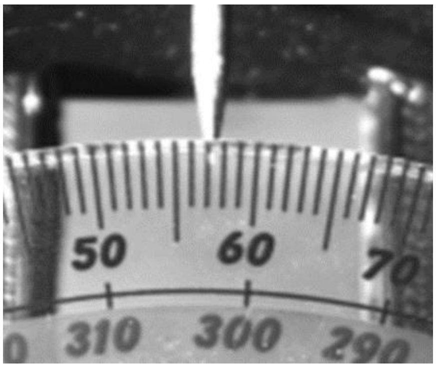

(a) Visible image

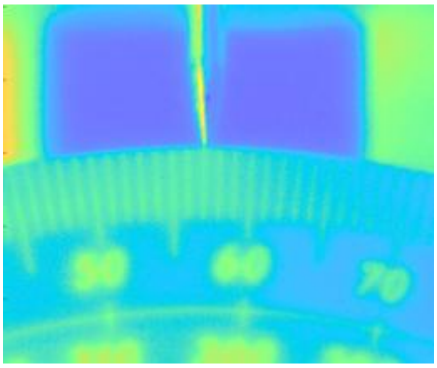

(b) Thermal image

Figure 4.13 – Example images of the delay timer captured by (a) the optical camera and (b) the thermal camera

To reduce parallax error the lenses of the two cameras were positioned on a plane passing parallel to the pin and normal to the protractor (Figure 4.14). The camera positions were fine-tuned until the angles measured by both cameras were within 1°.

(a) Front View

(b) Top View

Figure 4.14 – Images of the position of the optical and thermal cameras for the temporal alignment testing from the front (a) and the top (b)

To convert the measured degree difference into time delay the rotation period of the compass was measured. The period was measured 42 times using a laser tachometer (Figure 4.15). All measurements were between 4.09 - 4.11s, with this period one degree is traversed in 0.0114s.

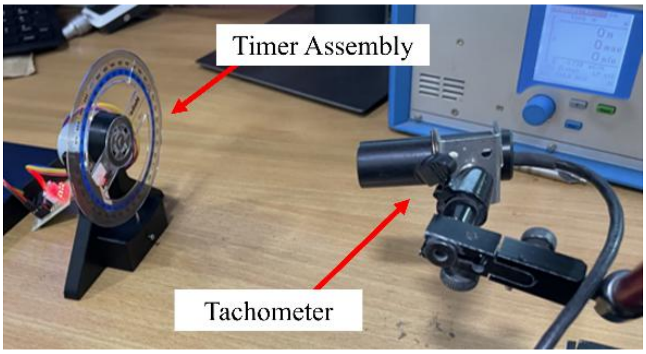

(a) Test set-up

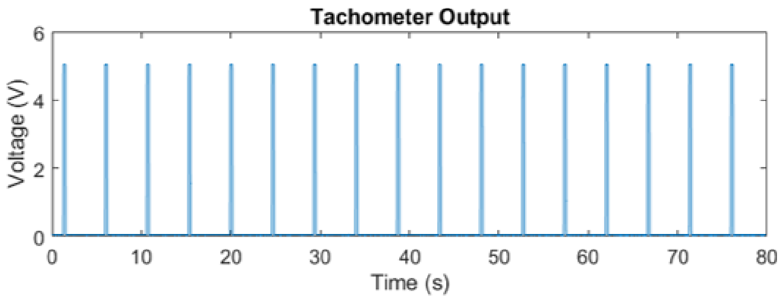

(b) Tachometer output

Figure 4.15 – Images of the setup for rotational period measurements (a) and an example of the collected results (b)

The delay between the visible and thermal cameras is primarily a function of the frame rates of the two cameras. For this investigation the frame rate of the visible camera was limited to 60Hz, and the thermal camera was set to 220Hz. These frame rates were selected to mimic those for a $200ms^{-1}$ test with both blade and abradable thermal capture. A total of 35 datapoints were collected.

These results fell within a normal distribution with an average delay of 0.252s between the two cameras, with the visible camera triggering before the thermal, and a standard deviation of 0.036s.

Thermal and visible footage can therefore be aligned by adding a 0.252s delay to the thermal video, at which point the alignment will be correct to within ±0.1s with a confidence interval of 99.5%.

4.3.3 Design of the Stroboscopic Imaging System

The design of the hardware required for the in-situ measurement of blade profile is built upon the lessons learned from the development of the High-Speed Rig implementation by Rahimov et al. (79) and the side camera setup by Fois et al. (77). The key issues faced in these setups were dust build up on the LEDs, leading to nonuniform lighting, and noise in the electrical signals which interfered with strobe timing and reliability.

To overcome the issues with signal noise all electrical interfaces and signal processing was placed within EMI rated aluminium enclosures which were all grounded (Figure 4.16), all connections between enclosures were done with shielded cables, connected with BNC connectors where possible. The addition of these EMI mitigation features reduced the noise within the light gate signals to levels which allowed for the thermal camera to be triggered by the same light gates which trigger the strobes.

Due to the limited range of voltages accepted by the thermal camera as a sync source, additional hardware was required. This hardware was included in the Light Gate Signal Conditioning enclosure and took the form of a voltage regulator to ensure a steady 5V input voltage was provided to the light gates, and a potential divider which was tuned to the light gates. This ensured that the high sync signal to the thermal camera stayed within the 3-5V range set by FLIR.

For the strobes, LEDs from the Cree XLamp range were used, the same as those used by Fois et al. (77). These LEDs are ideal for this application due to their consistent colour temperature, high efficiency, and integrated solder pads for ease of use. They do, however, have a rough protective layer over the diodes. This layer quickly becomes dusty during a test, reducing the amount of light which reaches the camera, it is also difficult to clean without damaging the LED.

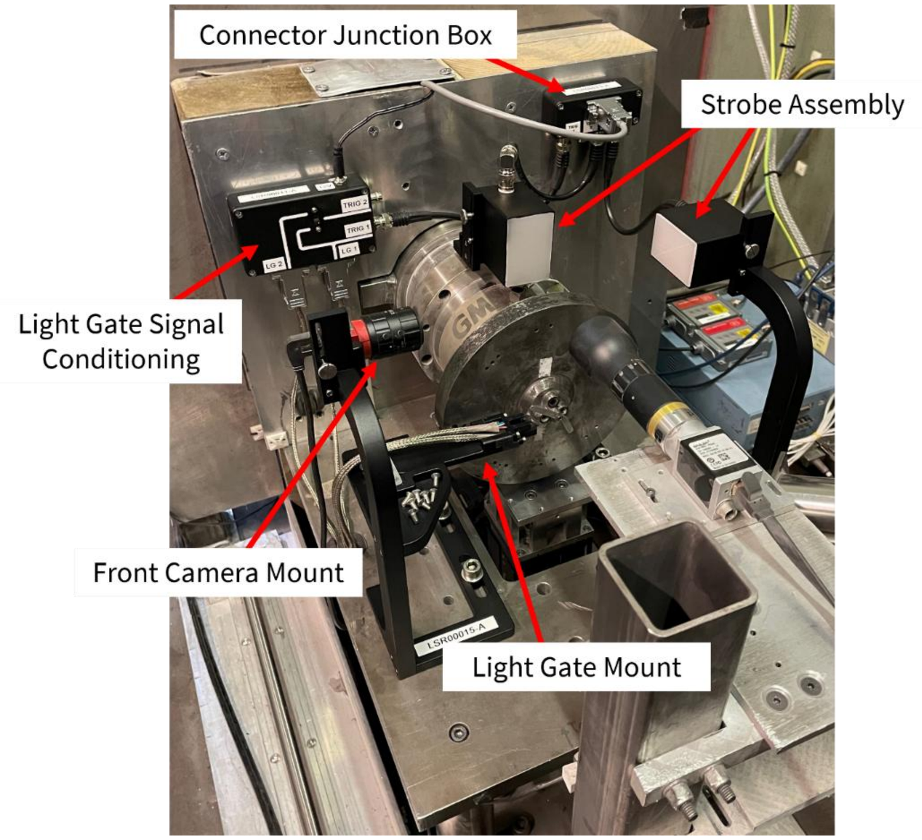

Figure 4.16 – Image of the Low-Speed rig modifications to allow for in-situ blade front monitoring.

To overcome this issue the LED array has been enclosed by a dust proof enclosure which includes a frosted acrylic diffuser screen (Figure 4.17). This arrangement allows for easy cleaning of the diffuser screen, while preventing any dust from reaching the LEDs. The aluminium enclosure and BNC connection also aid in reducing the electromagnetic interference due to the high frequency pulsing.

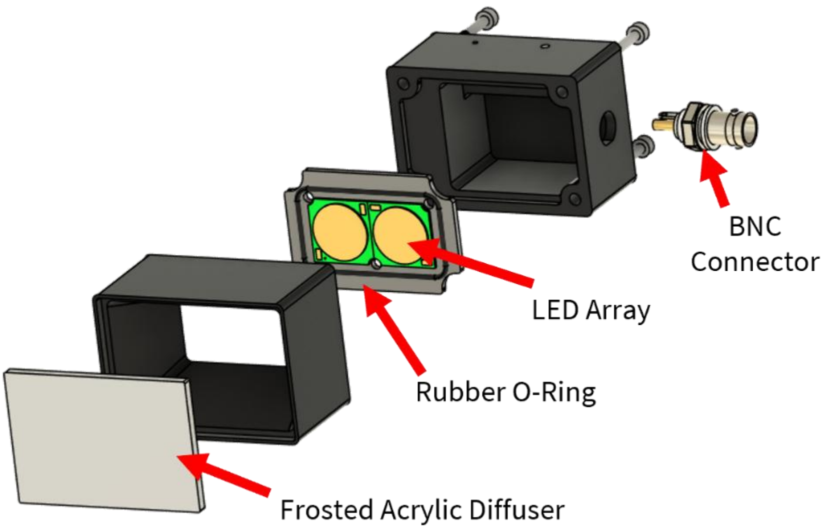

Figure 4.17 – Exploded view of the design for the LED strobe assembly

4.3.4 Test Matrix for the Application of In-situ Temperature and Blade Profile Measurements

To validate the new tools described in this chapter a set of rub tests have been completed. These tests have been completed using AlSi - Polyester Abradable (Metco 601) samples with a hardness range of 65.8 – 68.6 R15Y, the incursions have been completed with Titanium blades (An example of a blade and abradable sample is shown in Figure 3.27). These materials have been selected as the results should align with research completed by Rahimov et al. (79).

Tests have been completed at incursion rates of 2, 0.2 and 0.02µm/pass, with a minimum of six repeats of each condition (Table 4.1)52. The tests were all run with a blade speed of 200ms^{-1}. These tests should therefore make it possible to observe a range of behaviours, while repeats allow for the evaluation of repeatability of the tools.

Table 4.1 – Test matrix for tests to determine the impact of bulk temperature on wear mechanisms for M601

Hardness (HR15y)	Incursion Rate (µm/pass)	Tip Speed (m/s)	Incursion Depth (µm)	Blade Material	Number of Repeats
65.8 – 68.6	0.02	200	1500	Ti-6Al-4V	11
	0.20				6
	2.00				9

4.4 Results

All M601 tests exhibited the behaviours expected from previous research by Rahimov et al. (79), with a transition from mostly thermal blade wear at 0.02µm/pass to mostly adhesion at 2µm/pass (Figure 4.18).

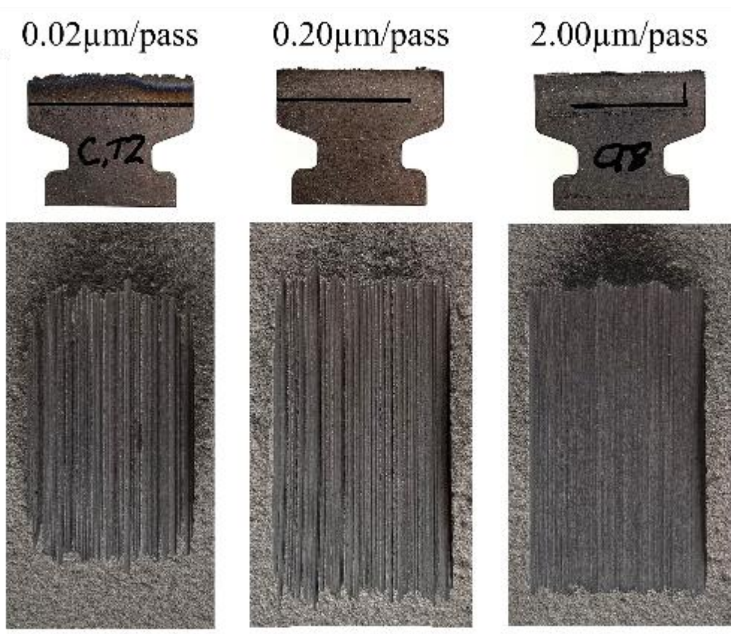

Figure 4.18 – Images showing examples of the cutting variability of 65.8HR15y M601 seen during tests at varying incursion rates

The transition from thermal blade wear to adhesion is echoed in the recorded thermal camera data, with a reduction in the maximum blade and abradable temperatures as incursion rates increase (Figure 4.19).

With the repeats at each condition producing similar levels of wear, it would be expected that at each test condition the temperatures measured would be similar. The maximum range in temperatures between repeats was ±13%, highlighting the repeatability of these tools.

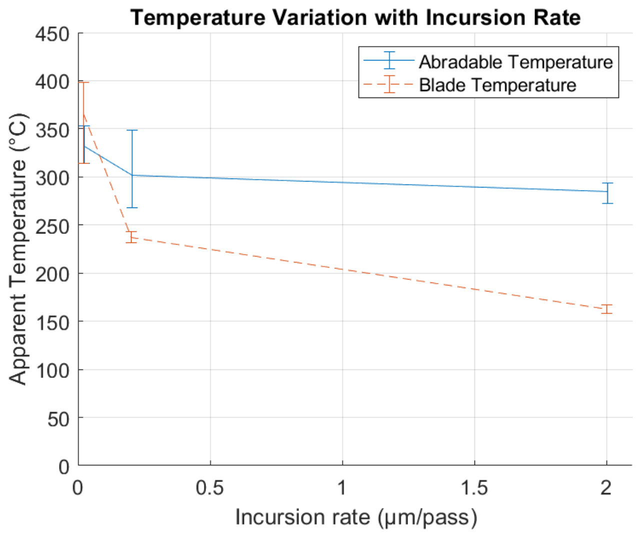

Figure 4.19 – Maximum blade and abradable temperatures measured during 65.8HR15y M601 tests.

The data from each test has been analysed through the use of rub maps, using the approach developed by Rahimov et al. (79). Each rub map presents how one of the measured attributes varies with rub length, where rub length is the cumulative distance that the blade has rubbed along the abradable surface during a test.

Figure 4.20 shows the rub maps for a 0.2µm/pass rub. Figure 4.20a and d show the blade height from the front and side respectively. Figure 4.20b and c show the blade and abradable thermal respectively. These conditions produced the largest quantity of blade adhesion/ fracture events, with minimal blade melting. As adhesions form on the blade, hot spots can be observed on the blade and the abradable, the time and location of these hotspots align with the adhesions positionally and temporally. This can be seen clearly with the set of three adhesion events which have been highlighted in Figure 4.20. It is notable that the side camera showed the adhesions forming at the trailing edge of the blade, with this true at all tested incursion rates.

The force and adhesion behaviours measured during this study replicate the results produced by Watson et al. (74) and Rahimov et al. (79), the new outputs presented here are the thermal behaviours. At different incursion rates the thermal behaviour of the abradable varies significantly. At 2µm/pass the maximum apparent temperatures observed were the lowest of all test conditions, these temperatures were however distributed more uniformly across the full width of the rub (Figure 4.21a). Unlike at 0.2µm/pass the blade temperatures did not follow the abradable hotspots, the blade temperature instead stayed predominately below measurable levels (Figure 4.21b).

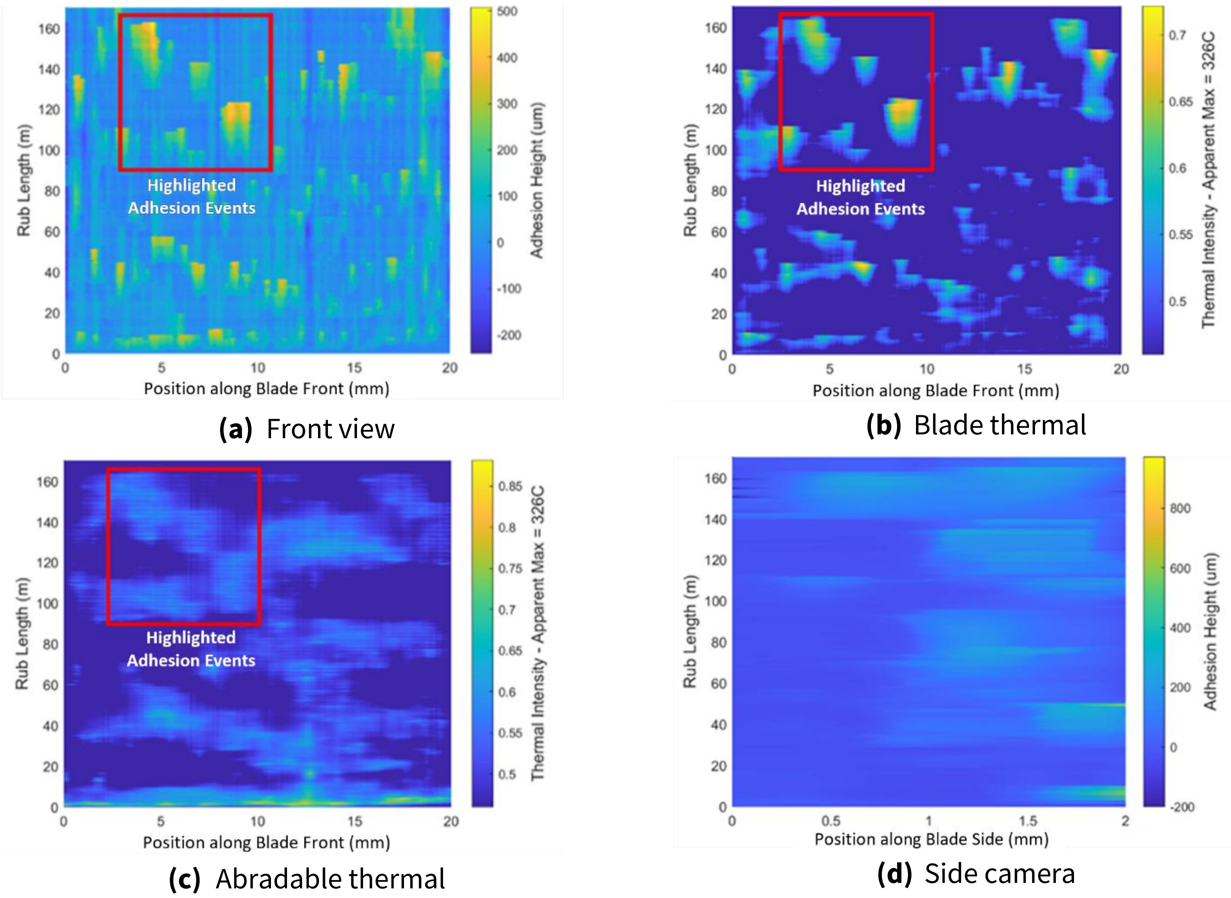

(a) Front view **(b)** Blade thermal

(c) Abradable thermal **(d)** Side camera

Figure 4.20 – Rub maps for a 0.2µm/pass test on 65.8HR15y M601

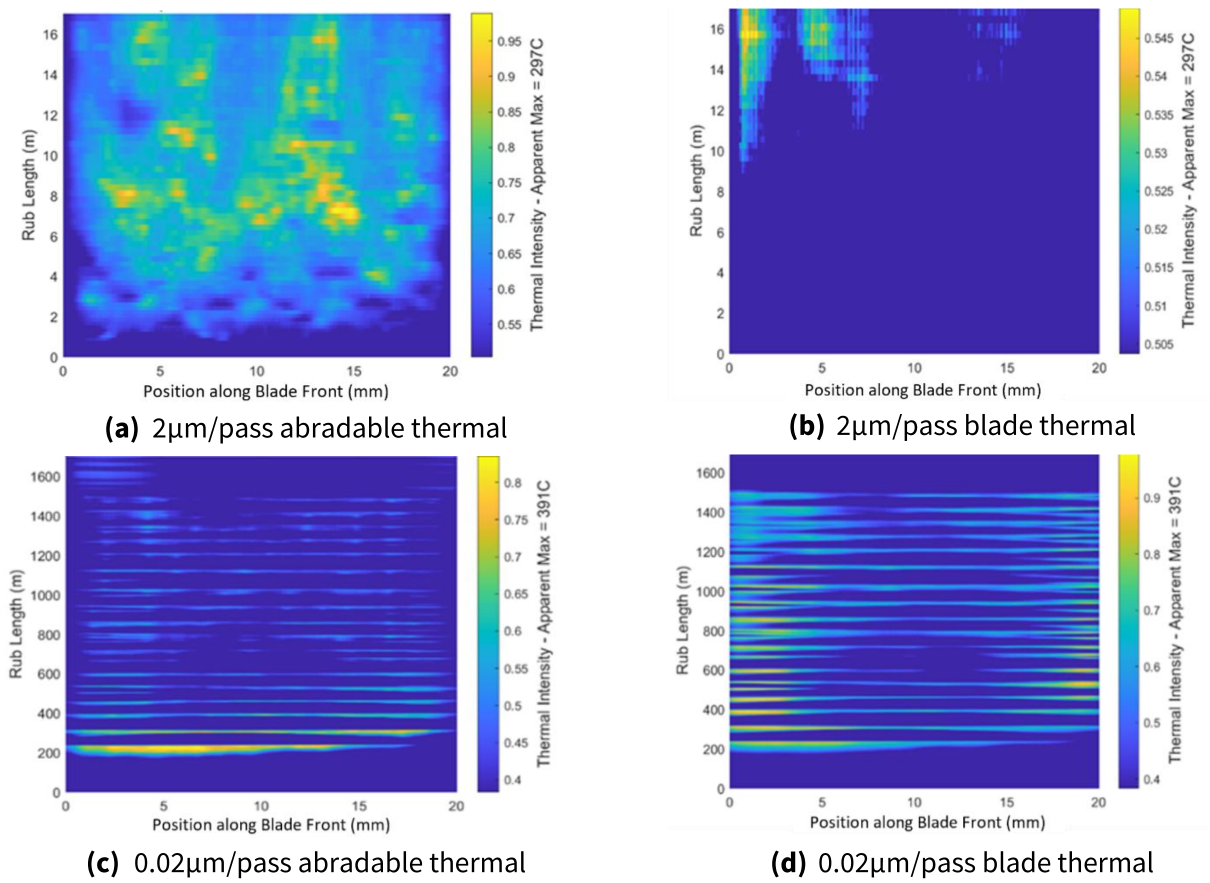

(a) 2µm/pass abradable thermal **(b)** 2µm/pass blade thermal

(c) 0.02µm/pass abradable thermal **(d)** 0.02µm/pass blade thermal

Figure 4.21 – Thermal rub maps for 2µm/pass and 0.02µm/pass tests on 65.8HR15y M601

At 0.02µm/pass the highest apparent temperatures were recorded, these temperatures were seen to form across the full rub width for both the blade and the abradable (Figure 4.21c/d). Unique to this test condition was the cyclic thermal loading which occurred for the full duration of the rub.

The cycling temperatures aligned with the measured force data. Both normal and tangential forces show cyclic behaviour which aligns with the temperature pulses (Figure 4.22). With each pulse of temperature, adhesion and melting events were observed forming across the entire width of the blade. The adhesions form in small chunks and were short lived, quickly breaking away from the blade.

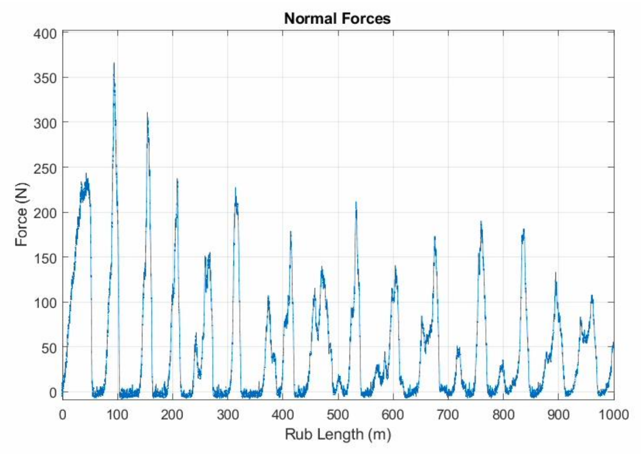

(a) Normal force

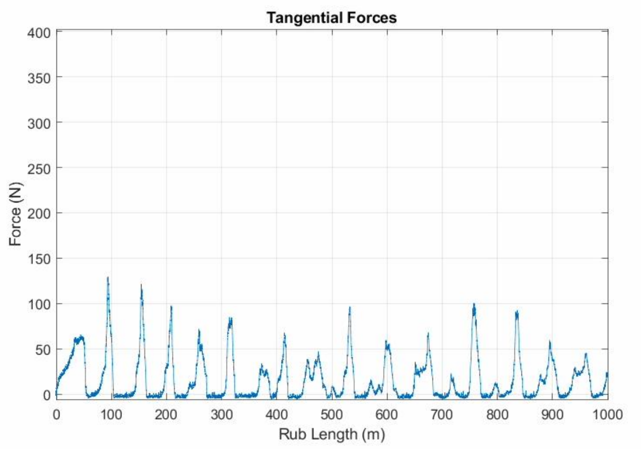

(c) Tangential force

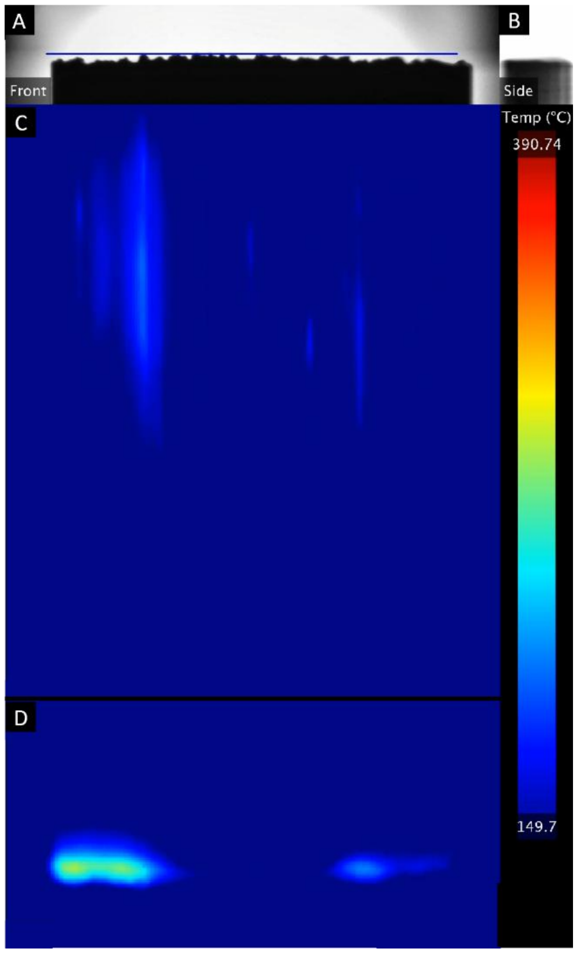

(b) Camera output at 1000m rub length. A – Front camera output. B – Side camera output. C – Warped abradable thermal. D – Blade thermal

Figure 4.22 – Force response and in-situ output for 0.02µm/pass test on 65.8HR15y M601

4.5 Discussion

The tools introduced in this chapter are intended to provide a deeper insight into how thermal and visible behaviours relate to one another, the power of these tools is exemplified by the 0.2µm/pass test results.

The aligned video shown in Figure 4.22 is an effective tool for visualising wear behaviour, making it clear to see when a blade is melting or when adhesions are forming. The created rub maps (Figure 4.20) abstract the problem and allow for easier extraction of time dependant patterns such as adhesions repeating at a single point.

To extract further information from these plots individual events can be identified and examined. For this test the event of an adhesion growing and breaking off has been selected (Figure 4.23). Focusing on this event in Figure 4.24 there is a clear event occurring both visibly and thermally, it can also be seen that not all events occur simultaneously. However, from this view the delays cannot be immediately resolved.

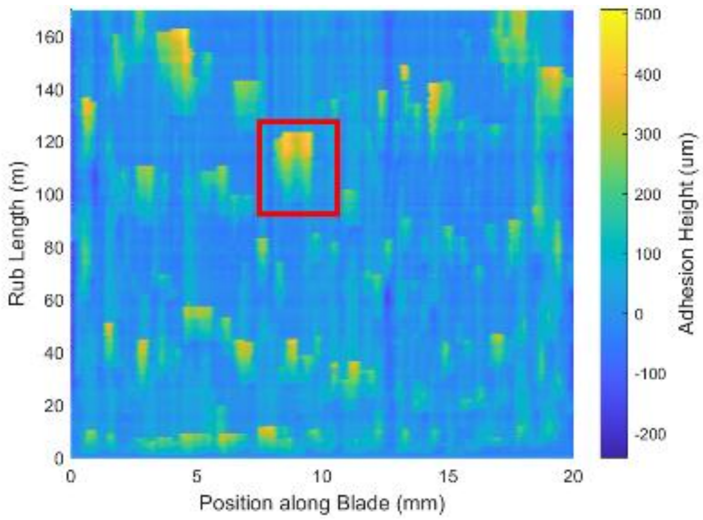

(a) Appearance on rub map

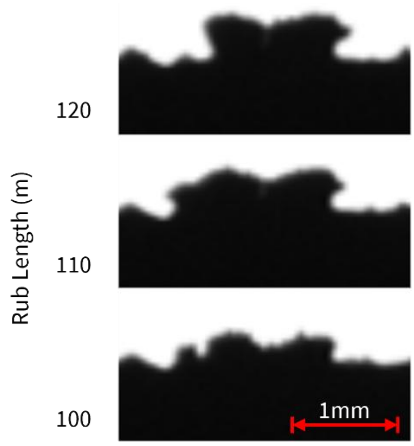

(b) Images of isolated adhesion extracted at increasing rub lengths

Figure 4.23 – Isolated adhesion event highlighted for a 0.2µm/pass test on 65.8HR15y M601

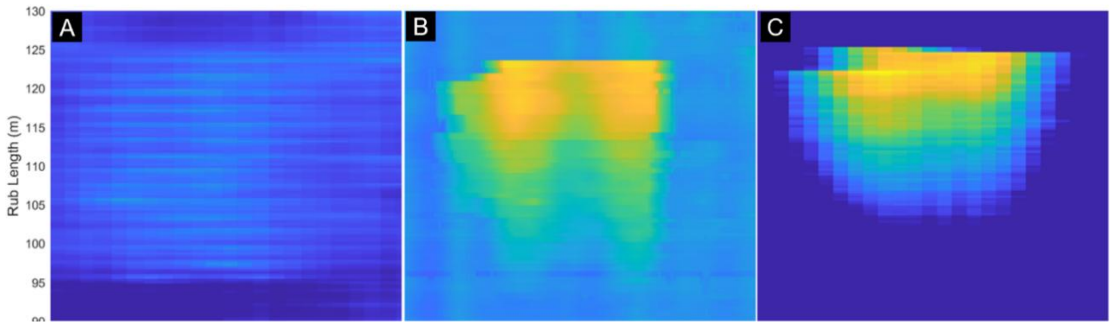

Figure 4.24 – Zoomed view of the adhesion event highlighted in Figure 4.23 showing the A – Abradable hotspot. B – Adhesion formation. C – Blade hotspot

However, by plotting the adhesion height, abradable and blade temperatures at a single position on the blade (Figure 4.25) on a single plot direct comparison of the different properties can be undertaken. From Figure 4.26 it can be seen that while blade temperature lags adhesion formation, abradable temperature consistently leads the adhesions. The adhesions also increase in size as the rub progresses. These results align with work completed by Rahimov et al. which showed how adhesions appear more likely to form in a position where an adhesion previously broke away from (79).

With these tools being applied in tests of different materials at a range of incursion rates it may be possible to relate different wear mechanisms to different time phasing and magnitudes of the thermal and wear properties, this insight will help when trying to determine the root cause of the wear mechanics and will become a focus in the following chapters.

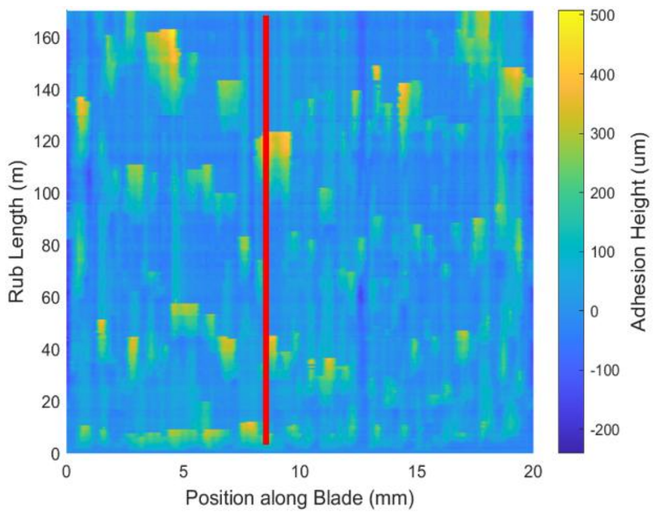

Figure 4.25 – A rub map for the blade profile for a 0.2µm/pass test on 65.8HR15y M601 with a line of extracted points highlighted

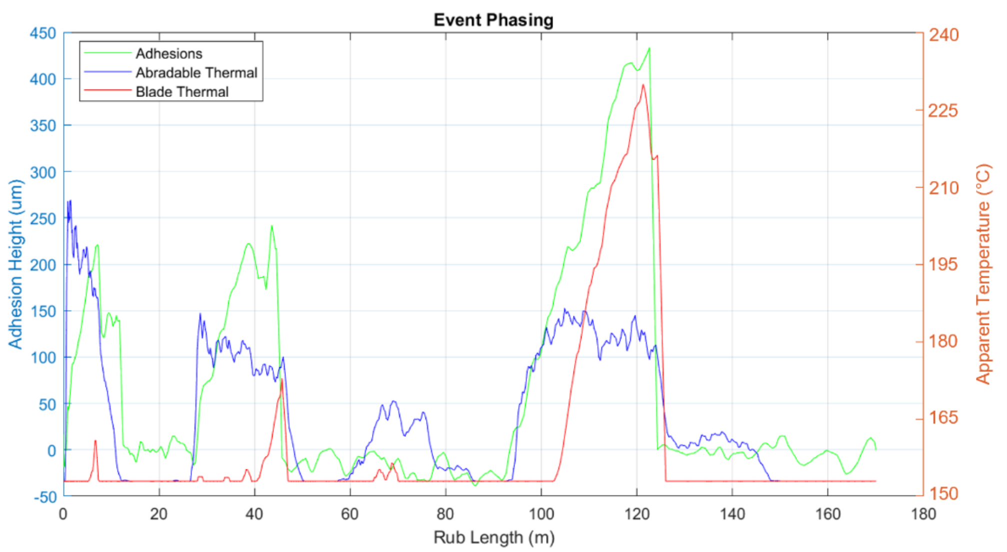

Figure 4.26 – The temperature and adhesion height time history from the line shown in Figure 4.25

The increased visibility that these tools can provide during a rub will be useful when trying to devise novel theories on wear mechanisms, or when trying to understand the shortcomings of existing theories. For example, the models created by Watson et al. (74) struggled to predict the temperatures generated during a rub of Titanium blades on M601, where this was suggested to be due to nonlinearities within the system. With these new tools it is now possible to observe the nonlinear behaviour which may occur, such as the cycling temperature behaviour identified in this study.

4.6 Conclusion

Research into the cutting behaviour of abradables has made significant jumps as new testing techniques and measurement tools have allowed for more information to be gathered. From initial rub tests which looked at how a blade changed before and after a rub, to more recent developments in in-situ measurements which have provided an insight into how wear mechanisms develop during the rub. The novel in-situ tools described in this chapter aim to take this further by allowing for the simultaneous recording of visible, thermal and force data during a test.

The addition of the blade side and front cameras have been shown in previous research to provide vital information when looking to characterise wear mechanics and when looking at how these develop during a rub (76)(79). By adding the thermal camera, alongside the front and side cameras, it is now possible to see how the temperature of the blade and abradable relates to adhesion growth.

Initial testing with these new tools has highlighted their ability to not only align hot spots with adhesions, but to also to observe how temperatures and adhesions develop over time. Results of tests with Metco 601 at 0.2µm/pass have shown clear, and repeatable, time phasing between the wear mechanics and hotspots on the blade and abradable.

These initial results are of a limited run of tests and are therefore insufficient to draw any conclusions on the general relationships between adhesions and temperatures. However, these results do show how these tools could be applied to multiple different abradables at different test conditions allowing for temperature-adhesion relationships to be extracted.

These tools can also be applied to provide evidence for existing theories, and to improve on limitations identified in previous work.

5 The Role of Thermal Properties in M601 Wear

5.1 Introduction

Metco 601 is an AlSi-Polyester abradable coating designed to be safe to use with Titanium Blades (89) but, in reality, the rub conditions can lead to significant variability in the abradable cutting performance.

The wear performance of M601 between 0.2 and 2µm/pass is predictable and follows Archard's wear relationship (97). This is beneficial for engine manufacturers as the initial run-in of the engine is completed in controlled conditions, allowing for some control over the incursion rates which will be witnessed by the abradable liner. However, during operation, tip – liner contacts mostly occur due to external factors such as turbulence. These conditions are more likely to produce incursion rates which are in the order of 0.02µm/pass. Testing has shown that at these incursion rates significant amounts of blade damage and abradable scoring occurs (23,74). Within the engine the increased tip clearance, and scored abradable profile, leads to efficiency loses as turbulent air can flow around the blades. The uncertainty around the wear behaviour of AlSi-Polyester at lower incursion rates is therefore a significant issue for engine manufacturers and hence has been a key area of focus for abradable research.

At low incursion rates Watson et al. observed a periodic behaviour in the abradable temperature during 0.02µm/pass testing, a behaviour unique to the low incursion rate tests (74), highlighting a potential relationship between temperature and the wear mechanisms. A further link between temperature and adhesive wear was subsequently observed in Chapter 4, with adhesion events on the blade aligning with hotspots on the abradable. However, this study did not provide a sufficient range of data to determine the nature of the relationship.

Building on these studies, this chapter looked to apply the in-situ measurement techniques developed in Chapter 4 to relate measured adhesion volumes with forces and rub lengths for a range of different test conditions to identify any deviations from Archard's relationship. The in-situ thermal measurement techniques will then be applied to develop an understanding of why these deviations occur.

5.2 Method

The data for this chapter is a combination of data collected on the Low-Speed spindle test rig, applying the in-situ tools developed in Chapter 4, and data collected by Rahimov on the High-Speed Spindle test rig which also included a front facing camera (82).

The data collected by Rahimov on the High-Speed Rig (Section 3.1.2) has been reprocessed with the tools developed in this study and included to maximise the data set. Additionally, with this rig being able to reach blade tip speeds of 280ms^{-1} (79), this data allows for the largest range of test conditions when looking for patterns in wear behaviour. However, this rig does not include any thermal measurement tools. To analyse the thermal behaviour, tests using in-situ thermal measurement techniques on the Low-Speed Rig (Section 3.1.1) have been completed. Both rigs test the same grade 5 titanium blades and abradable samples but the Low-Speed rig makes use of a smaller disk and less powerful motor, limiting blade tip speeds to 200ms^{-1} (73).

Although these rigs make use of different sized disks both have been able to produce similar, engine representative, wear results, with Rahimov comparing test results between the two rigs to show that at any given test condition a similar output is obtained from each (82).

Both rigs can measure the forces acting on the abradable during the rub using Kistler tri-axial piezoelectric force transducers fitted below the abradable sample. Both rigs are also fitted with a camera aimed at the leading edge of the blade. Both camera systems use stroboscopic imaging techniques as described in Chapter 4, with the captured blade images being aligned temporally with the normal and tangential forces. From the images of the leading edge the profile of the blade can be extracted, mapping how the blade profile changes for the duration of the test. Although it is not possible with this test setup to measure the profile of the abradable during the rub, Rahimov et al. (79) has shown that the profile of the abradable is the inverse of the highest points on the blade during the test. Measurement of just the blade alone is therefore sufficient to get a good view of the wear mechanisms occurring during the blade/abradable contact.

As this work is looking to relate back to the relationships put forward by Archard (97) the key characteristics which must be extracted are the volume of adhesive wear which occurs during the rub, the rub length during which adhesions formed, and the normal force during that process. As adhesions form and break off for the duration of the rub this cannot be measured post-test, instead is calculated from the in-situ blade profile measurements.

5.2.1 Calculating Blade Wear Volume

To calculate adhesion volume, in-situ images of the front of the blade are used. For each image the blade edge is detected, and the total area enclosed by that edge is measured and multiplied by the blade depth to calculate volume, the volume of the previous frame is then removed. This gives the change in volume of the blade between each image.

Figure 5.1 – An example image from the High-Speed rig front camera showing uneven illumination of blade.

This wear volume is over a blade with a width of 20mm, which is the standard size used within both test rigs. However, as can be seen in Figure 5.1, lighting gradients for some tests produced dark regions in the centre of the blade, reducing edge detection accuracy. To overcome this, tests with uneven backgrounds had 3mm from the centre of the blade excluded from the analysis. To ensure that the wear volumes for all tests are directly comparable, volumes for tests with the centres cropped have been multiplied by the width ratio of a full blade to a cropped blade. This means that all wear volumes used in this work here are mm^3 over a 20mm width.

To validate the accuracy and reliability of the blade profiles extracted from the stroboscopic images, the final blade profile extracted was compared with a profile map of the post-test blade captured with a Bruker Alicona InfinteFocusSL. An example of the results of this are shown in Figure 5.2, with Figure 5.2b showing the detected edge aligning with the profile from the Alicona. This process was repeated for each test batch to ensure that no errors were introduced into the stroboscopic system during setup.

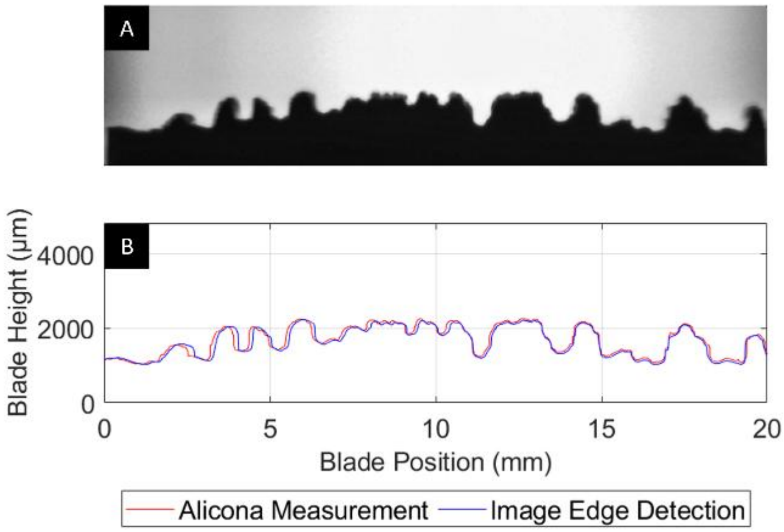

Figure 5.2 – Blade profile measurements from a test at 200m/s on a 77.5HR15y sample **A -** The stroboscopic image of the blade. **B –** Comparison of edge detection to Alicona profile measurements.

5.2.2 Calculating Rub Length

The rub length through the duration of the test does not vary linearly, this is due to the blade cutting a curved path into a flat abradable sample. To calculate the rub length which has occurred between two images the total rub length (L, m) at each image must be calculated from the current incursion depth (i, m), incursion rate (r, m/pass) and the disk radius (R, m).

From the current incursion depth, the number of passes which have occurred (N) can be calculated using $N = i/r$. Using this value Equation 5.1, derived by Rahimov et al. (79), can be used. The rub length per image is therefore the difference in total rub length calculated between two frames.

$$L = \sum_{n=1}^{N} 2R\cos^{-1}\left(\frac{R - in}{R}\right)$$

Equation 5.1 – Calculation of total rub length.

5.2.3 Sampling of Measured Normal Force Data

The capture rate from the load cell mounted beneath the abradable sample (100kHz) is much higher than the frame rate of the camera (30Hz). To extract the normal force which was present for each image the mean force is calculated between the current and previous frame.

When the wear volumes, rub lengths, and forces have been extracted for each image the frames which include adhesive wear can be isolated by removing any frames with a wear volume change ≤ 0 mm^3. The rub lengths and adhesion volumes can then be summed to give a total volume of adhesion and total rub length, similarly the force values can then be averaged to calculate the average normal force while adhesions were forming.

By running tests with AlSi-Polyester samples of varying hardness, at varying speeds and incursion rates, it is known from previous work by Borel et al. (23) and Watson et al. (74) that the volume of adhesions which will form on the blade will vary. With the additional information extracted from the in-situ measurement techniques, the volume of adhesion can be measured and related back to the relationship proposed by Archard (97). An overview of the tests completed for this study are detailed in Table 5.1. This table breaks down the completed tests into a matrix showing, for every combination of incursion rate and hardness, how many tests were completed at each tip speed (for example '1 x 280' = 1 test at 280ms^{-1}). Tests performed on the Low-Speed rig with the addition of the thermal camera as part of this study are also noted.

Table 5.1 – Test matrix for tests used to evaluate relationships between adhesion rates, normal force and hardness

		Hardness (HR15y)		
		Low (53.5 – 55.0)	Medium (60.5 - 68.6)	High (70.0 - 77.5)
Incursion Rate (µm/pass)	0.02	1 x 100	1 x 100	1 x 100
		1 x 200	1 x 200	1 x 200
		1 x 280	1 x 280	1 x 280
		1 x 200*		1 x 200*
	0.20	1 x 100	1 x 100	1 x 100
		1 x 200	1 x 200	1 x 200
		1 x 280	1 x 280	1 x 280
				1 x 200*
	1.00	1 x 100*	1 x 100*	1 x 100*
		1 x 200*	1 x 200*	1 x 200*
	2.00	1 x 100	1 x 100	1 x 100
		1 x 200	1 x 200	1 x 200
		1 x 280	1 x 280	1 x 280
				1 x 200*

* Data collected on the Low-Speed Rig

It is expected from work by Watson et al. (22) that the data collected at 0.02µm/pass will follow a different pattern to the data collected at higher incursion rates. To investigate the wear in more detail the tests completed on the Low-Speed rig as part of this study will be processed further using the in-situ thermal analysis techniques developed in Chapter 4 at a range of incursion rates.

Using these tools, it is possible to look at individual points on the abradable and to observe how the temperature varies during the test. It is also possible to identify individual adhesion events on the blade and extract the temperature of the abradable and the blade at this location.

By applying these tools to tests completed at a range of different incursion rates it will be possible to observe how the blade and abradable temperatures differ at different test conditions.

5.3 Results

The initial rub maps produced by testing samples of AlSi-Polyester of the same hardness and speed but with different incursion rates align well with the results presented by Borel et al. (23). For example, at a blade tip speed of 100m/s and an abradable hardness of 69HR15y, Figure 5.3 shows high levels of adhesion at 2µm/pass with the volume of adhesions reducing at lower incursion rates. At 0.02µm/pass there is a significant amount of blade damage.

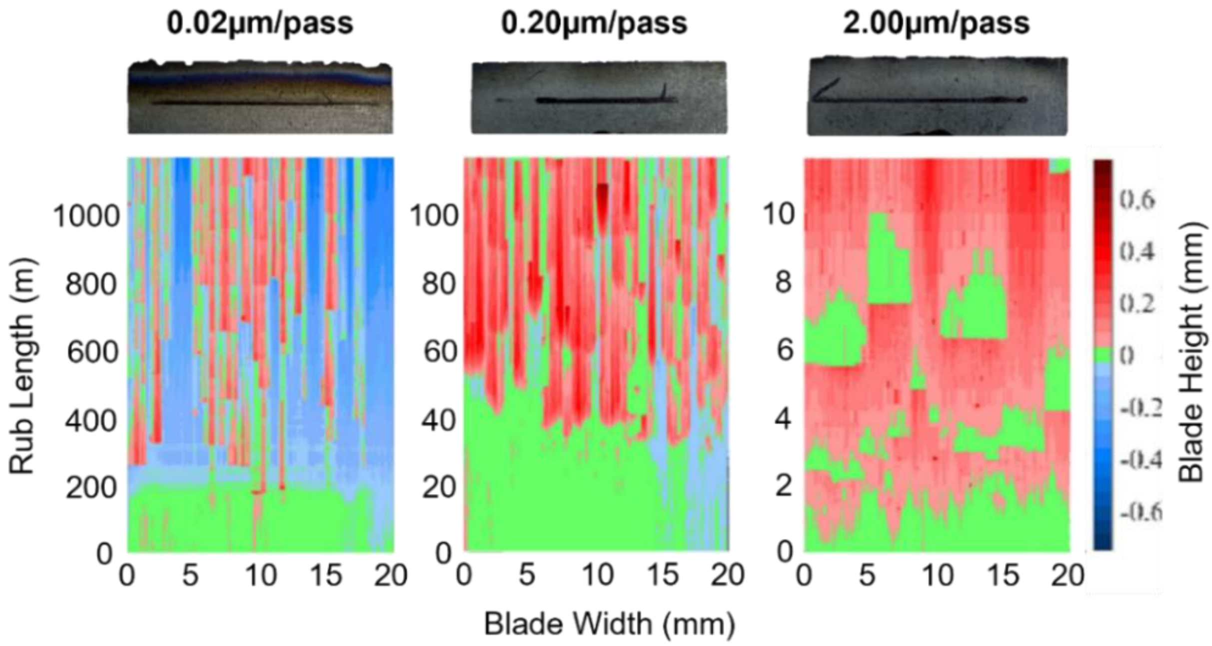

Figure 5.3 – Rub maps at different incursion rates for abradables of hardness 69HR15y at a tip speed of 100m/s

Using the in-situ data analysis methods described above, each test has been analysed, and the results have been plotted in Figure 5.4. The results have been plotted in a manner which relates to Archard's relationship (Equation 5.2). This relationship states that the ratio of adhesion volume (*A*) to rub length (*l*) should be proportional to the ratio of normal force (*F*) to hardness (*H*).

$$\frac{A}{l} \propto \frac{F}{H}$$

Equation 5.2 – Archard's Relationship

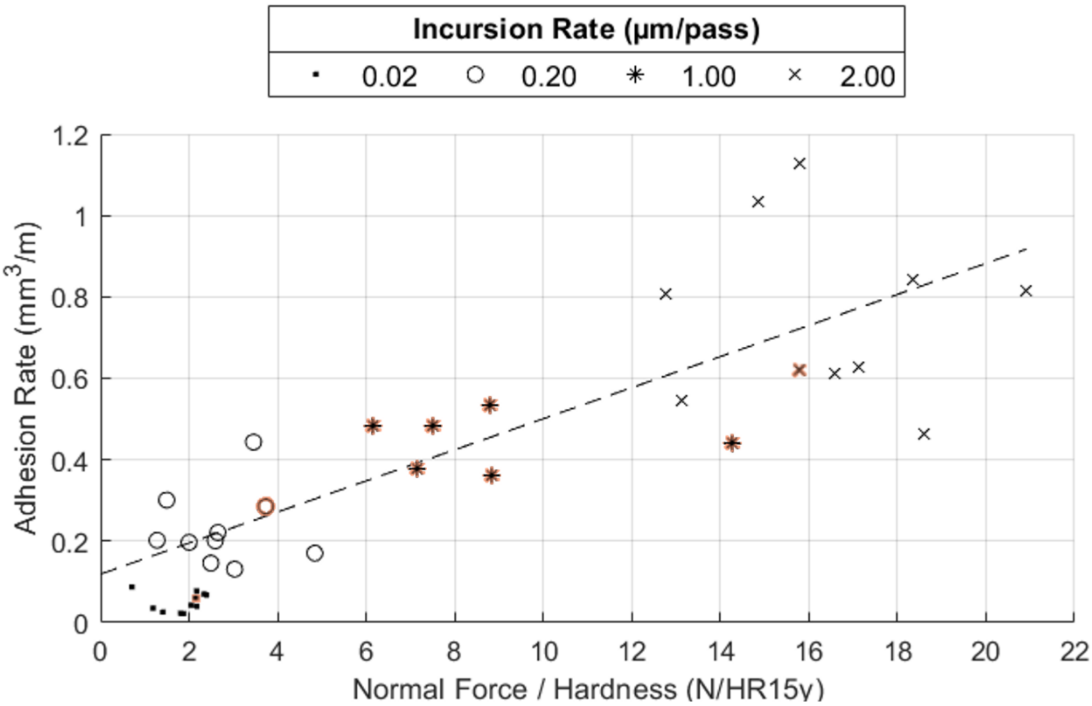

Figure 5.4 – Adhesion Rates against Force/Hardness. The data collected on the Low-Speed Rig is highlighted in red

Between 0.2 and 2µm/pass a line of best fit can be plotted with a Pearson correlation coefficient of 0.80, showing that there is a strong relationship between adhesion rate and the force to hardness ratio, aligning with Archard's relationship. This plot also shows how the spread of data increases with increasing incursion rate, which is due to the reduced test time at higher incursion rates limiting how much data can be collected. However, even with the increased spread at the higher incursion rates the mean value for each incursion rate sits on the line.

If this relationship were to hold at 0.02µm/pass the mean value of the 0.02µm/pass data would also sit on the line. To test this a single sample T-Test has can be completed with the null hypothesis that the mean of the residuals from the 0.02µm/pass data about the linear relationship is zero. With a sample mean of -0.140, a sample standard deviation of 0.031, and 10 degrees of freedom it is possible to reject this null hypothesis at a confidence level of 99%. This shows that there is a statistically significant difference between the mean at 0.02µm/pass and the linear relationship.

While Figure 5.4 shows the deviation from the linear relationship at a global level, these differences can also be seen when directly comparing data from individual tests. For example, Figure 5.5 shows how adhesion formation varies between three 0.02µm/pass tests at 100m/s with varying hardnesses. The ratio of average normal force to hardness for each of these tests remained consistent at 2.07±0.16 N/HR15y, and therefore from Archard's relationship the adhesion rates are also expected to remain consistent. However, it can be seen that as the hardness reduces adhesion formation becomes more favourable.

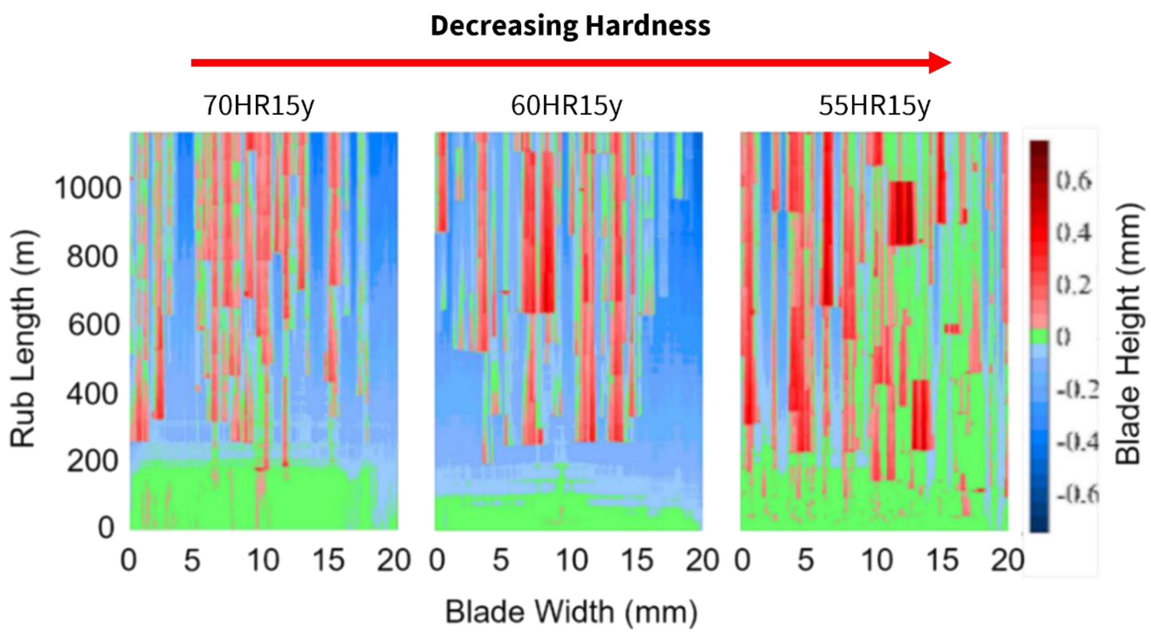

Figure 5.5 – Rub Maps for 0.02µm/pass tests with decreasing hardness at a tip speed of 100m/s

These results show that, although existing relationships are able to make reliable predictions for the volume of adhesions expected at high incursion rates, at low incursion rates there are additional factors at play which influence adhesion formation with AlSi-Polyester.

To determine what these factors could be, differences between the different incursion rate tests can be investigated from the in-situ data collected.

A significant difference between the different incursion rates is the duration of the tests, and the rate at which the normal load increases. The time duration for each test is proportional to the incursion rate. For 2 and 0.2µm/pass a 2000µm incursion at 200m/s lasts for 3s and 30s respectively whereas a 0.02µm/pass incursion will last for 300s (5 minutes). With the increased test length, while the peak and average forces experienced at 0.2 and 0.02µm/pass may be similar, the rate of increase in force is lower at the lower incursion rate. An example of this is shown in Figure 5.6, which shows the first 3.5 seconds of 200m/s tests of abradable samples with a hardness of 77.5HR15y at varying incursion rates.

Further differences are visible in the thermal camera footage showing how the abradable surface heats up. For example, Figure 5.7 shows snapshots of the blade front and the abradable temperature for two 200m/s tests on 77.5HR15y samples. Each snapshot is selected at a time when there are hot spots visible on the abradable surface. Figure 5.7a, b shows how at 0.2µm/pass hotspots occur at isolated regions on the abradable at positions which align with adhesion formations on the blade. At 0.02µm/pass Figure 5.7c, d shows how the blade heats up more uniformly with adhesions being distributed evenly along the blade edge.

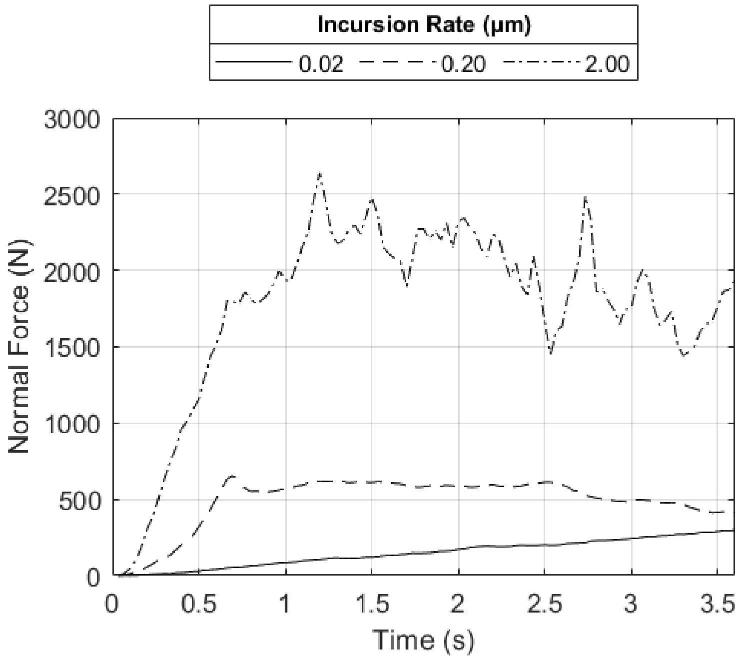

Figure 5.6 – Force application rate at varying incursion rates for samples of hardness 77.5HR15y at 200m/s

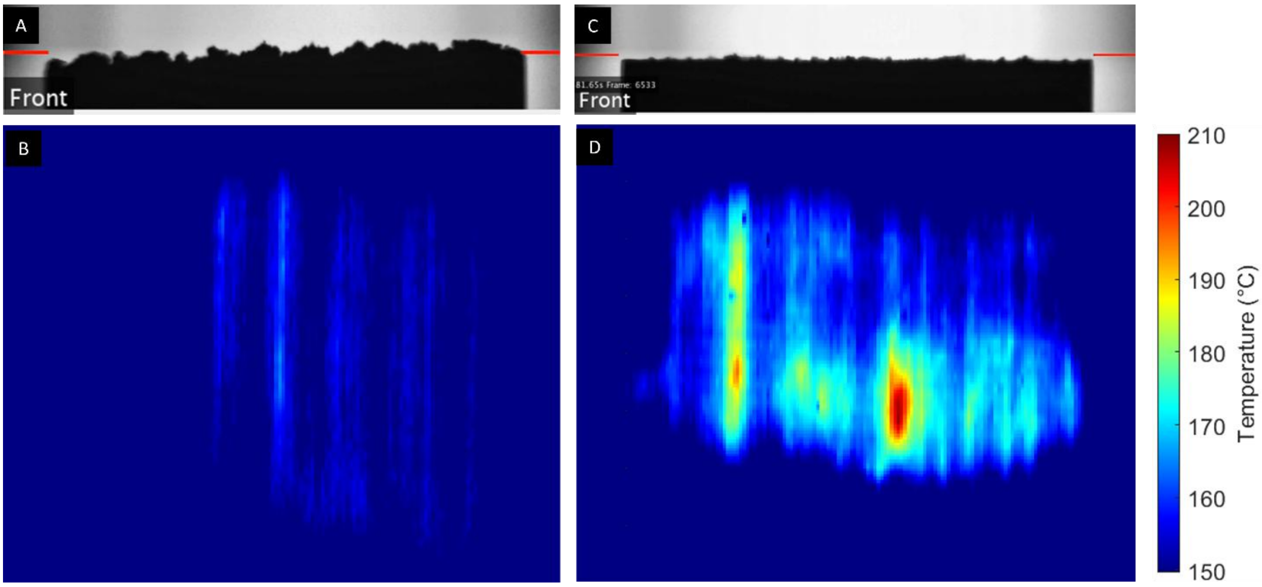

Figure 5.7 – Snapshots showing hotspots from tests at 200m/s of 77.5HR15y samples. **A –** The blade front at 0.2µm/pass. **B –** The abradable temperature at 0.2µm/pass. **C –** The blade front at 0.02µm/pass. **D –** The abradable temperature at 0.02µm/pass.

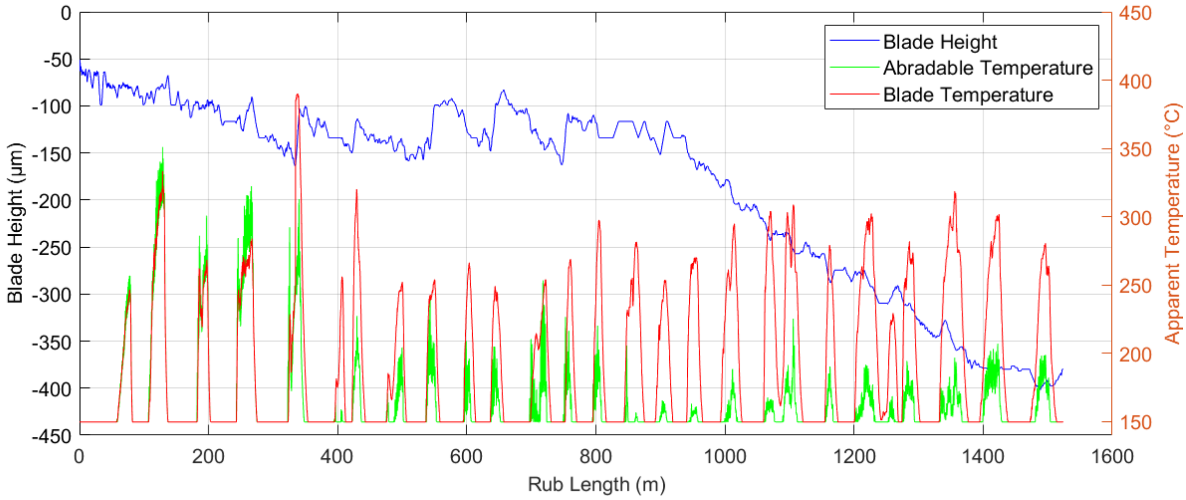

Figure 5.8 – Blade and abradable temperatures alongside blade height at a single point on the blade for a 0.02µm/pass test at 200m/s, 65.8HR15y

This more even wear distribution leads to periodic drops in contact area as large-scale fracture events occur. This explains the cyclic force behaviour observed by Watson et al. (74). The cyclic behaviour is also observed in the blade and abradable temperatures, an example of this is shown in Figure 5.8 for a 200m/s rub at 65.8HR15y. This figure shows the blade temperature, abradable temperature and blade height at a single location on the blade for a 0.02µm/pass test. From this plot the temperature peaks can be seen to align with wear events, but what can also be observed is the transition from adhesion formation and fracture events early in the rub, to blade wear as the rub progresses.

A piece of work which helps to draw these observations together was completed by Watson et al. (22) which showed how reducing the hardness of AlSi-Polyester also led to a reduction in its thermal conductivity, highlighting a potential link between adhesion rate and thermal management within the abradable.

Considering first the overall difference in heating seen between high and low incursion rates, it is notable that at different incursion rates there is also a difference in the thermal input into the abradable during the rub. Larger incursions lead to larger flash temperatures (114), and the more gradual increase in normal force at 0.02µm/pass leads to a gentler increase in the rate of frictional heating (115). The combination of differing thermal input and the ability of the abradable to manage that heat can explain the differences observed with the thermal camera.

At higher incursion rates with high rates of frictional heating the irregularity of the thermal properties within a single abradable (as shown by Watson et al. (22)) lead to local hotspots, and localised wear events. At 0.02µm/pass the heat flow rate is lower allowing the heat to flow throughout the surface, this makes the heating less dependent on irregularities within the abradable and allows for an increase in the abradable bulk temperature. At these test conditions the further differences between the wear behaviours observed at different abradable hardnesses highlight the abradables ability to manage this heat as a potential factor determining its wear performance.

Moving to the transition from adhesion to blade wear seen at lower incursion rates, if the temperature of the abradable is a significant factor in the formation of adhesions, with higher temperatures being more favourable to adhesion formation, a reduction in surface temperature would be expected as the rub progresses in order to explain the transition from adhesion formation to blade wear shown in Figure 5.8. To better understand how the abradable manages heat, and how that varies throughout a rub, a thermal model can be used.

5.4 Thermal Model of Heat Flow Through an Abradable

To go beyond the surface and investigate the heat flowing through the abradable a simplified thermal model was created using the PDE Toolkit within MATLAB (116). This model took the form of a 2D cross section of the abradable with a circular arc removed with a radius equal to the disk of the low-speed spindle test rig used in this study. This was created within the PDE Toolkit using the *geometryFromEdges* function. Thermal properties of the abradable were set to those measured by Watson et al. (22) and assumed isotropic. This model is able to run steady state and transient analysis using the *createpde("thermal","steadystate")* and *createpde("thermal","transient")* functions respectively. This allows for visibility of how heat flows through the abradable to the backplate (Figure 5.9).

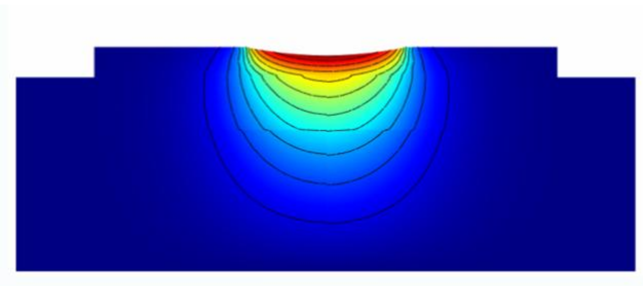

Figure 5.9 – An example output of the abradable thermal model

A transient analysis with this model highlights the importance of test duration to thermal management within the abradable. Figure 5.10 shows how the temperature at the abradable surface compares to the temperature at the backing plate of the sample. The analysis was completed for a 3mm thick sample with an incursion depth of 500µm, applying a constant heat flux of 1W to the rub surface. Due to the poor thermal diffusivity of AlSi-Polyester (2670m^2/s for 55HR15Y (22)) the time required to reach a steady state thermal condition across the abradable is large compared with the durations of the 2 and 0.2µm/pass tests. These results align well with the observations that show during the longer duration tests thermal energy was able to spread across the surface, while for the shorter tests hotspots were more localised as there was insufficient time for the heat to spread before wear occurred.

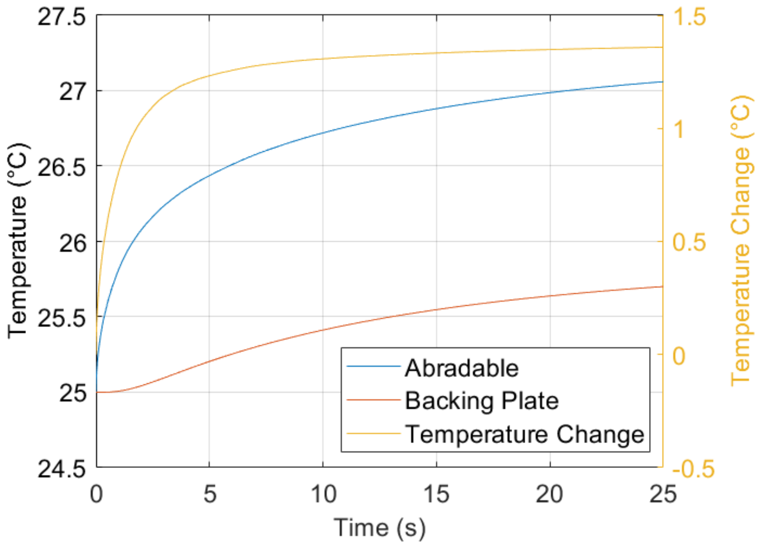

Figure 5.10 – Transient analysis of temperature distribution across abradable for a 1W thermal load at a 500µm incursion

However, these results also point to a difference in the effectiveness of thermal conductivity as a mechanism for thermal energy removal from the abradable via the back plate. At 0.02µm/pass the temperature distribution across the abradable will be near steady state and therefore heat flux through the abradable will be at its maximum. For 0.2 and 2µm/pass tests the temperature across the abradable will be transient and therefore there will be a lower heat flux through the backplate while more energy is being stored within the abradable.

For a test with a 200m/s blade speed, a 2µm/pass test will produce a 0.66mm incursion in 1 second and a 0.2µm/pass test would produce a 0.066mm incursion. The abradable material removed will either adhere to the blade or will come away as chips, taking with it any thermal energy stored within it. Figure 5.11 shows the simulated heat distribution through the abradable after 1s of applying a thermal load of 50°C to the rub surface with a 25°C starting temperature. The vertical lines in this plot show how much material is removed in that same time period at each incursion rate. At 2µm/pass it can be seen that a significant amount of high temperature material is removed, removing energy from the system, and revealing a layer of lower temperature abradable. Conversely, at 0.2µm/pass some high temperature material is removed, but the effect is not as significant as volumes are more reserved. At 0.02µm/pass only 0.0066mm of material is removed per second, and at these rates the material revealed after the removal is of similar temperature to the previous layer, and therefore thermal energy removed through material removal is far less effective at these lower incursion rates.

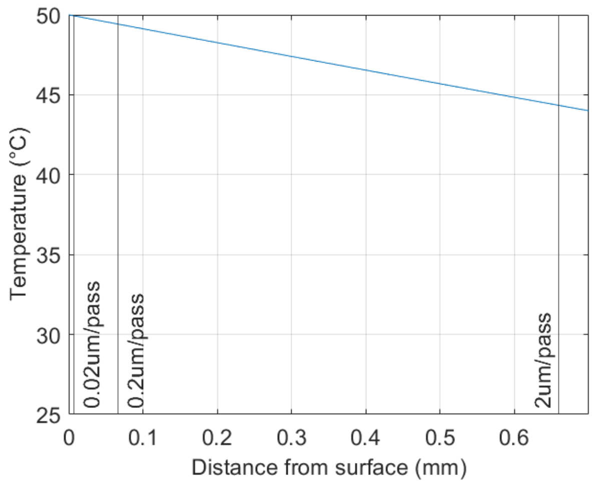

Figure 5.11 – Temperature distribution through abradable 1s after a 50°C thermal load is applied

This analysis suggests that the primary mechanisms for removing thermal energy differ between high and low incursion rate tests. At incursion rates higher than 0.2µm/pass the energy removal through conduction is limited as the temperature distribution within the abradable is still transient. However, there is a high rate of material removal from the abradable, taking heat away through chips. At 0.02µm/pass the rate of material removal is far lower and therefore less energy is removed from the system through this mechanism. Instead, the large timescales for this test lead to a near steady state temperature distribution through the abradable and therefore maximise conductive heat transfer out of the backplate.

If conduction through the abradable is a leading mechanism for thermal energy removal during a 0.02µm/pass test, it would be expected that the temperature of the abradable surface would reduce as the test continues. This is because, as shown in Figure 5.12, the thickness of the abradable reduces as the test progresses and the length of the rub track also increases. The increase in surface area and reduction in thickness will lead to a reduction in thermal resistance through the abradable. In Figure 5.12, *r* is the radius of the circular path taken by the test blade, *d* is the incursion depth, and *t* is the initial thickness of the abradable sample.

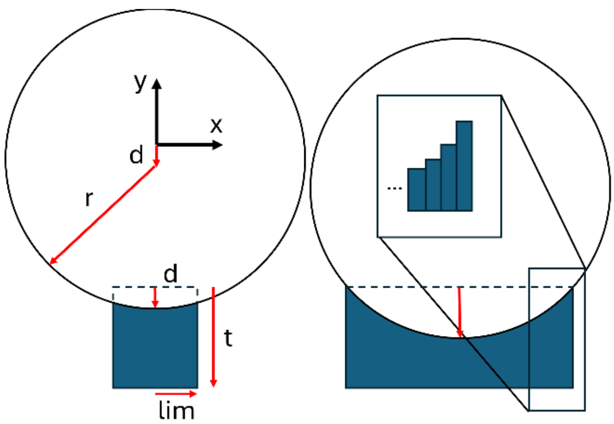

Figure 5.12 – Simplified abradable geometry used to generate the analytical solution for thermal resistance

The change in thermal resistance as the test progresses can be extracted from the thermal model using a quasi-steady analysis with 1W of heat flux being applied to the rub surface. The temperature difference between the rub surface and the backplate is the thermal resistance of the abradable. To validate the model an analytical solution can be derived from the simplified geometry shown in Figure 5.12. This geometry can be broken up into a series of vertical rectangles of width dx and height equal to the thickness of the abradable at that location. By treating these rectangles as a series of parallel thermal resistors, each with a thermal conductivity of *k* and a depth *W*, it is possible to integrate along the rub length to find the total resistance of the abradable. The integral to do this is shown in Equation 5.3, with limits (*lim*) being calculated as the width of the abradable under the rub track.

$$1/R = kW \int_{-lim}^{lim} \frac{1}{r - d + t - \sqrt{r^2 - x^2}} dx$$

$$lim = \pm\sqrt{d(2r - d)}$$

Equation 5.3 – Analytical solution for thermal resistance

The results of the simulation and analytical solution are shown in Figure 5.13. Both solutions predict similar thermal resistances through the abradable, with the rate of change in resistance reducing as the test goes on. This is expected as the rate of increase in rub length is not linear.

Finally, it should be noted that the analytical solution predicts a larger resistance than the model, this is because the simplified geometry only includes the material directly below the rub whereas the computational model includes the entire abradable at all rub depths. That said, this simplified model is more than sufficient to validate the numerical model and establish the relationship required for this work.

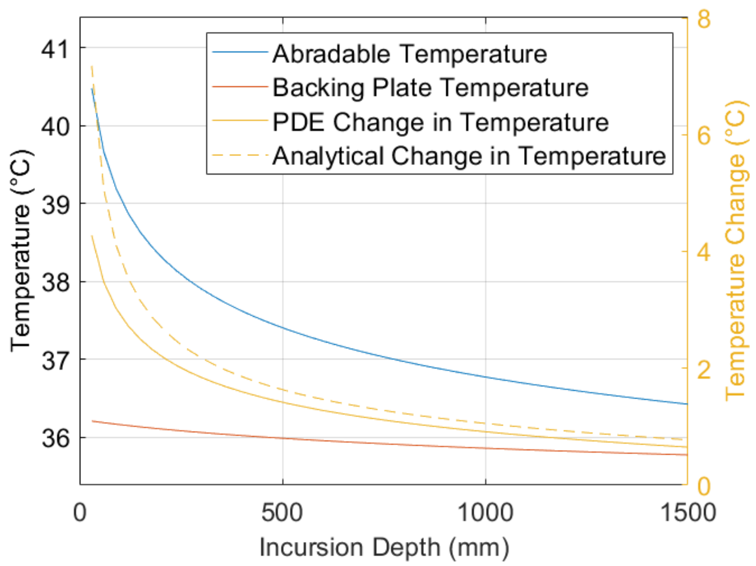

Figure 5.13 – Predicted thermal resistance of the abradable at varying incursion depths

5.5 Discussion

The experimental results can be combined with those from the thermal model to further understand the wear mechanisms present.

Taking the temperature at a point on the abradable from the 0.02μm/pass test shown in Figure 5.8 and extracting only the peak values of the blade and abradable temperature the trend in temperature with rub depth can be seen (Figure 5.14). While the blade temperature remains fairly constant throughout the rub, the abradable temperature reduces as the rub progresses, with a pattern which mimics that predicted in the analysis in Figure 5.13.

These results align with the theory that at the lower incursion rates conduction is a leading mechanism for thermal energy removal, and as the rub progresses the abradable becomes better at conducting heat to the backplate, reducing the surface temperature.

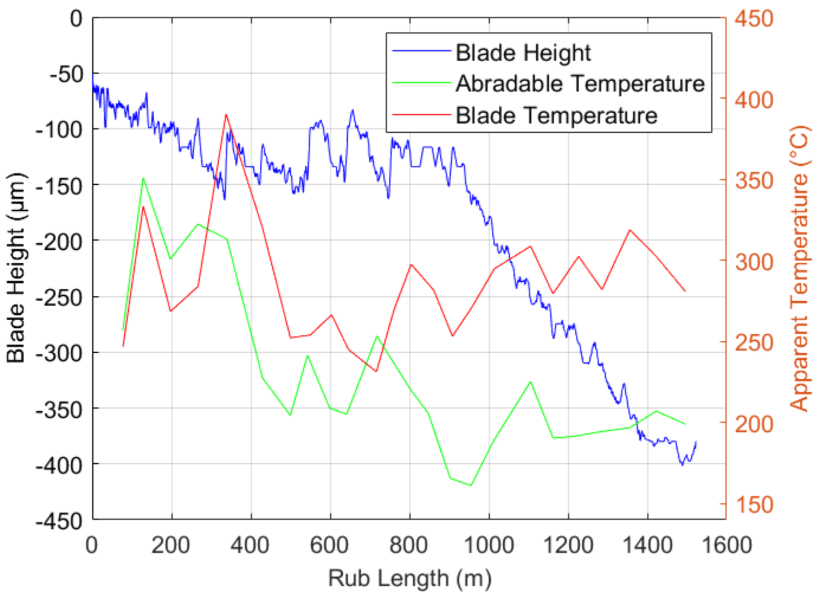

Figure 5.14 – Peak blade and abradable temperatures from the data shown in Figure 5.8 alongside blade height

Evidence in support of this conclusion can also be found by comparing individual heating cycles from the beginning of a rub and from the end of the rub. Figure 5.15a shows an enlarged view of three heating cycles taken early in the rub, during a period where adhesions were forming readily on the blade. Looking at the time phasing of the blade and the abradable heating it can be seen that both bodies heat up at similar rates and times, and also that the adhesion formation on the blade aligns with the peaks in the abradable temperature.

Figure 5.15b shows the same data but taken towards the end of the rub. For these thermal cycles the rate of heating of the blade remains similar to what was observed early in the test. However, the rate of heating of the abradable is noticeably less. At this stage in the test there are fewer adhesions forming and instead the blade is wearing, with the wear events aligning with the peaks in blade temperature.

As the peaks in blade temperature do not show a significant reduction during the rub, but there is a clear transition from adhesions to blade wear, these results also show how the adhesions act as a sacrificial layer during the early stages of the test. This is evident in Figure 5.15a where the blade length is seen to increase at abradable hotspots before subsequently reducing again at blade hotspots. As the test continues the abradable temperature does not increase as rapidly and the blade wears before adhesions are able to form.

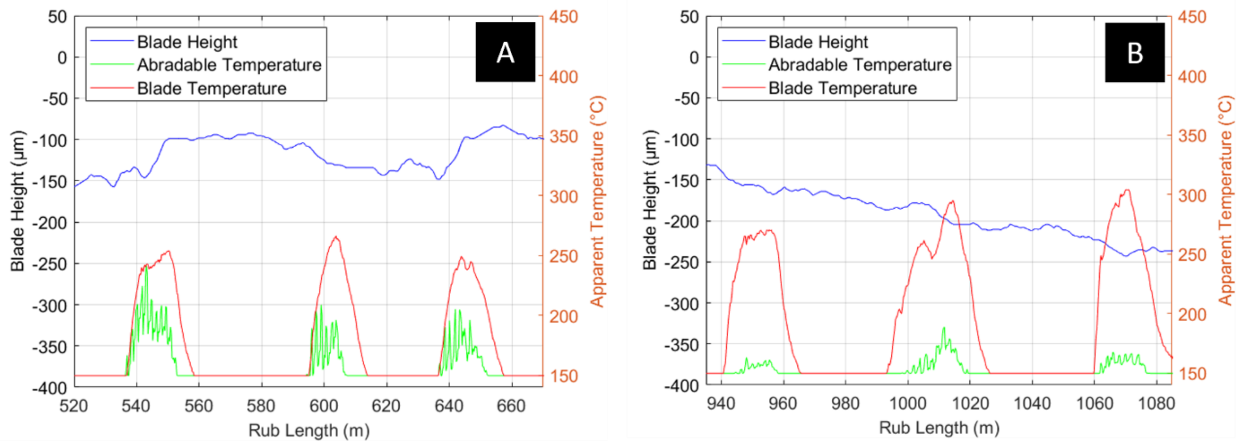

Figure 5.15 – Plots from a 0.02µm/pass test showing the abradable and blade temperatures alongside blade height from three cycles extracting from **A –** early in the rub **B –** late in the rub

With the application of these results an explanation can now be put forward to answer why the wear behaviour of AlSi-Polyester at 0.02µm/pass differs from that of higher incursion rates, and why the force response exhibits a unique cyclic profile.

At high incursion rates local hotspots due to the high frictional heating produce sporadic adhesion events. At the lower incursion rates the lower force application rate produces a smaller heat flux over a larger time period, allowing the heat to dissipate more uniformly across the surface. The more uniform surface temperature leads to an even distribution of wear events over the surface, and hence periodic large-scale adhesion and fracture events are established which lead to a significant reduction in contact area, and hence load. These periods of reduced loading also allow for the abradable to cool. This cooling, along with the improved thermal conductivity through the abradable, allows for lower bulk temperatures and hence leads to a shift from a primarily adhesive wear mechanism to one of blade wear. This agrees with work by Gåård et al. (98,99) which show that adhesive wear is more prevalent at increased bulk temperatures. These theories are further supported by a transition from adhesion formation to blade wear which aligns with a reduction in abradable surface temperature.

These additional insights into how the bulk temperature of the abradable can impact the adhesion rates of AlSi-Polyester provide an additional tool to engine manufactures when trying to produce more predictable operational wear conditions. However, they also highlight a significant difference between the tests completed here and the real-world applications.

In operation AlSi-Polyester will typically be found in the low-pressure compressor of the engine. Although this is one of the cooler parts of the engine, temperatures can be in the region of 300°C.

The impact on the abradable is elevated further by the fact that the casing can also be at similar temperatures. With the high temperature of the abradable and casing the abradable will not be able to dissipate heat from the rub as readily, in fact the abradable will be held at temperatures which have been observed during adhesion formations in testing. This could make AlSi-Polyester applied to a real engine far more susceptible to adhesive wear than when testing in an unheated test rig. This deviation from a real-world application could be compensated for through the use of heating plates fitted under the abradable. By applying heat to the abradable backing, it will be possible to better control the heat flux through the abradable during a test. With this additional control it would be possible to extract a more detailed relationship between temperature, force and adhesion rates, providing engine designers with tools which will allow them to better predict the wear behaviour of AlSi-Polyester within an engine.

5.6 Conclusion

At incursion rates higher than 0.2µm/pass the wear performance of Metco 601 follows Archard's relationship (97). At 0.02µm/pass wear mechanisms are harder to predict with fewer adhesions and more blade wear being observed, even though forces measured are comparable with those measured at 0.2µm/pass.

This work makes use of in-situ measurement techniques to measure the adhesions during rubs of differing test conditions to show that there is a statistically significant difference in wear behaviour at lower incursion rates. The use of in-situ thermal measurement combined with thermal analysis tools can then explain these differences by showing how the thermal energy added to the abradable at lower incursion rates can be conducted more effectively through the abradable.

Further work could be done to address limitations between testing completed here and real operation by investigating the impact of the elevated starting temperatures and backplate temperatures found in an engine.

6 Varying M601 Wear Mechanisms Through the Control of Bulk Temperature

6.1 Introduction

The wear mechanisms which occur during a tip rub between a Titanium blade and a M601 abradable liner have been shown to vary significantly with incursion rate and with abradable hardness (23). At incursion rates above 0.2µm/pass the wear behaviour is well understood and follows the well-established wear law put forward by Archard (97). At rates below this, as discussed in Chapter 5, these laws are no longer followed. Instead, the way that the abradable is able to manage the thermal energy during a rub can have a significant impact on what wear mechanisms are observed.

When thermal energy is removed from the abradable through effective conduction out of the backplate, the surface of the abradable will heat at a rate lower than that of the blade, this results in the blade wearing before adhesions begin to form. However, if the abradable cannot dissipate the energy its surface increases in temperature, leading to conditions more favourable to adhesion formation (98,99). As adhesions form on the tip of the blade they can act as a sacrificial layer, protecting the blade from wear.

Although these mechanisms have been observed during the tests completed in Chapter 5, they have only been seen as a result of heat being generated by the rub itself. This differs to coatings within a gas turbine which can operate in ambient, and backplate temperatures as high as 325°C (89).

This chapter aims to develop the understanding of the impact of bulk temperature on M601 wear by testing M601 samples of varying hardnesses at a range of bulk temperatures. This will provide further understanding of how the varying material properties and change in thermal energy management within the sample impact the wear mechanisms seen during a rub.

6.2 Method

Testing for this chapter has been completed on the Low-Speed Spindle Test rig (LSR) described in Section 3.1.1. Working with the LSR allows for large amounts of in-situ data to be collected using the methods developed in Chapter 4.

6.2.1 Controlling Bulk Temperature during a Test

To allow for the control of abradable bulk temperature a heater block was produced which can be installed on top of the LSR load cell, this heater was described in section 3.1.7 and has been utilized to collect the data in this chapter.

To ensure the results for each test are comparable, each test was started when the surface of the abradable reached a set temperature. This temperature was set at the point where the surface temperature of the abradable was increasing at a rate of less than 1°C/minute for a soft (52HR15y) sample. The soft samples were chosen to set the start temperature as they have the lowest thermal conductivity and therefore will take longer to heat than the harder samples (22). The starting temperatures determined for each backplate temperature are shown in Table 6.1.

Table 6.1 – Surface temperature of sample before starting test using the abradable heater block

Backplate Temperature (°C)	Surface Temperature (°C)
100	80
200	150
300	210

6.2.2 Extracting Rates of Adhesion and Blade Wear

By leveraging the data from the front camera to measure the adhesion and wear rates of the blade during a rub in Section 5.2.1 it was possible to quantify how the wear mechanisms vary between tests. The method developed for this worked by measuring the total area of the blade and calculating the change in area between successive frames, if the area increased the frame was considered adhesive. This area-based approach was able to detect global trends in the wear mechanisms which occur during a test. However, during an actual test both adhesion formation and wear occur simultaneously, this results in some events being missed by an area-based approach. Although this method can provide a global view of adhesion and wear formation, as changes in this study are expected to be smaller than those seen in Chapter 5, a higher resolution approach is required.

For this work a pixel-based approach has been developed (Figure 6.1). This approach looks at the difference between the height of the blade for each individual pixel of the image, grouping pixels into adhesive and abrasive pixels. By applying this approach more data can be collected per test, which will allow any differences in wear rates to be more distinct. As differences in the wear at different temperatures measured by Martinet et al. (60) were subtle a higher resolution approach in this study is favourable.

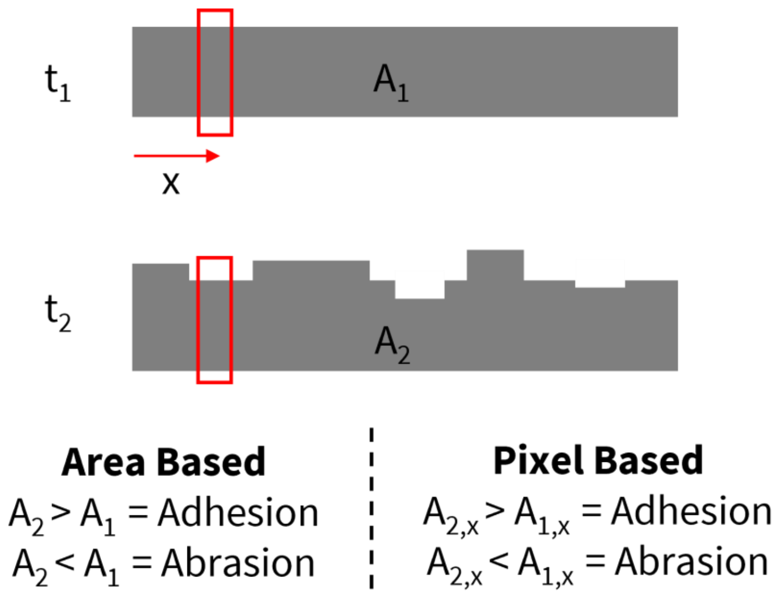

Figure 6.1 – Visualization of Area vs pixel-based wear measurement

Although the pixel-based approach can provide higher data resolution, it also introduces additional errors which must be accounted for. These errors are produced by vibrations in the rig leading to camera shake. As the camera shakes the blade appears to move within the camera frame, this results in false adhesions being measured.

During a test, the blade position in the images varies horizontally, because of this when measuring the blade height at a single point neighbouring pixels will move in and out of the measurement point. This pixel motion is measured as adhesion formation and wear, as visualised in Figure 6.2.

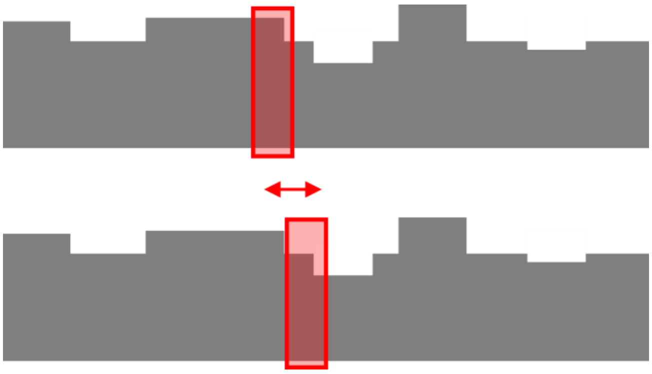

Figure 6.2 – Visualization of horizontal shake induced error

To correct for the horizontal shake, the blade images are centred during the post processing of the data. The stabilization is completed by isolating a region on each side of the blade, as shown in Figure 6.3. For each side image an edge detection algorithm is run, based on the methods applied by Rahimov et al. (79), these edge positions are used to centre the blade in the image.

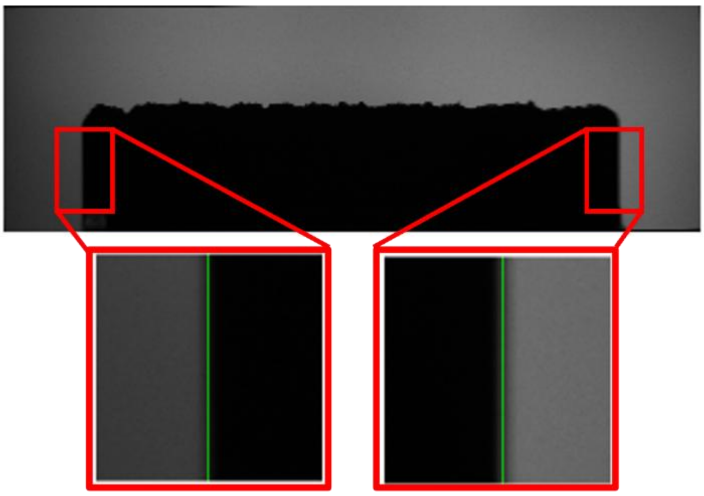

Figure 6.3 – Stabilizing blade images through side profile detection

The impact of stabilizing the blade horizontally can be seen in the cumulative sum of the adhesions which have formed during a test. An example of this is shown in Figure 6.4 which shows the cumulative adhesion formation for a trial test with and without blade stabilization. The reduction in the gradient of the line demonstrates how stabilization removes the gain error introduced by the horizontal shake.

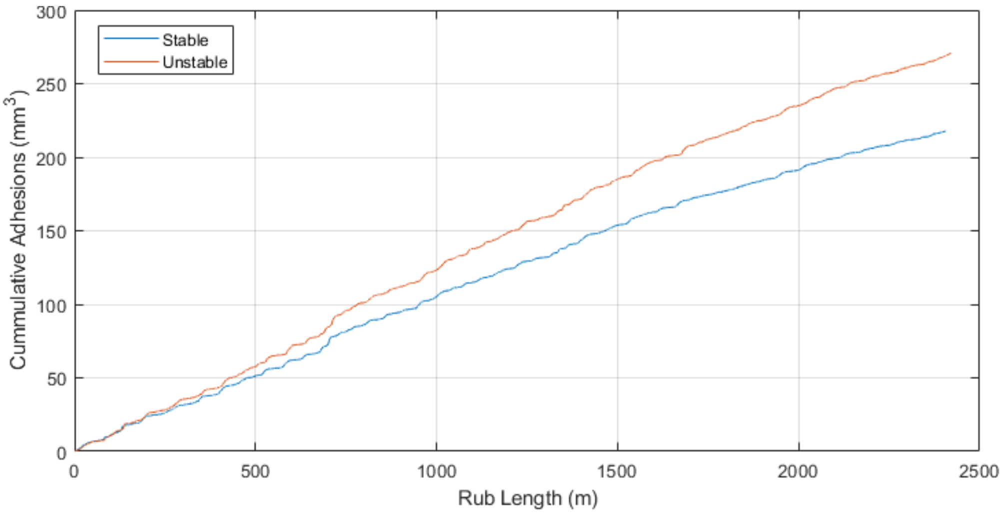

Figure 6.4 – Impact of blade stabilization on measured wear rates

During a test the vibrations are not only limited to horizontal motion, but also in the vertical direction. Vertical vibrations can also introduce errors into the wear measurement as the blade tip moves up and down, appearing to be adhesions forming and fracturing along the entire blade width (Figure 6.5). To correct for this error, it is not possible to stabilize the image as there are no visible datum points in the vertical axis, instead this error has been quantified so that it can be removed from the final data.

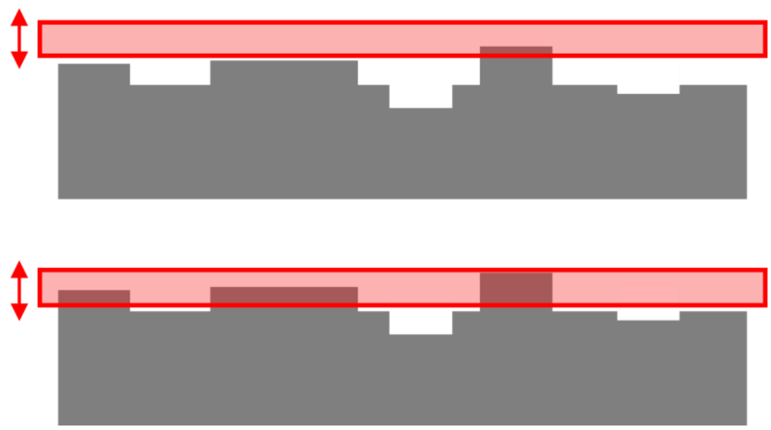

Figure 6.5 – Visualization of vertical shake induced error

To measure the error introduced by vertical oscillations data was collected during a 10s window before the blade contacted the sample, while the disk was spinning at test speeds. The profile of the blade was then extracted for each frame; an example of how the apparent blade height varies from a trial test is shown in Figure 6.6. The variations seen were in the order of ±15µm (~1 pixel), resulting in erroneous measurements of adhesion formation and wear.

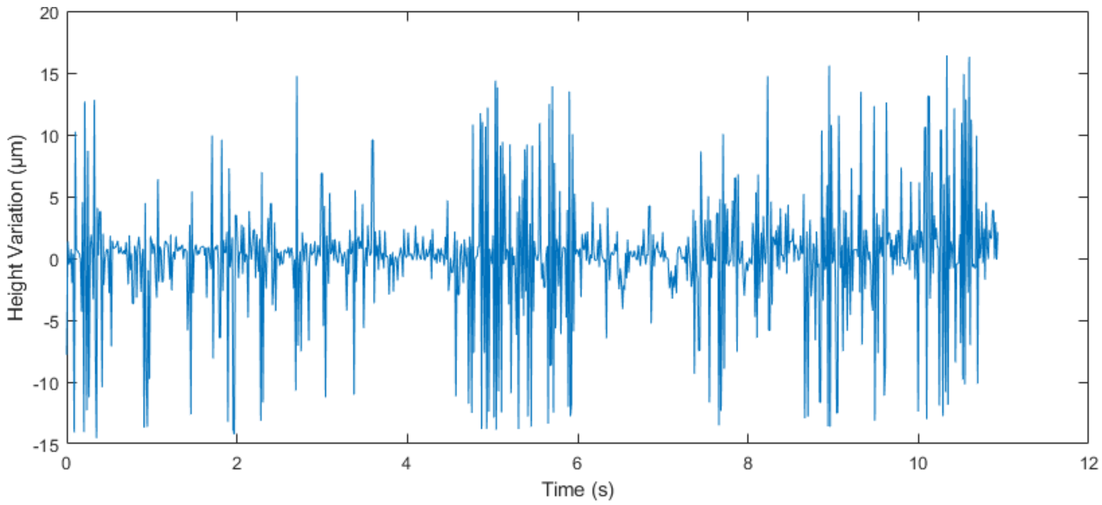

Figure 6.6 – Measured blade height variation before contact

To help visualize how the vertical oscillation is recorded as false adhesions and wear, Figure 6.7 show a simplified case where the blade is oscillating vertically following a 331Hz sinusoidal wave, with a magnitude of 15µm. When the blade appears to move above its correct position, to the processing code it appears that the blade is growing – adhesions are forming, quantified by the blue area. As the blade then moves down it appears to get smaller – the blade is wearing, quantified by the orange area. In reality the blade has not changed size but just moved relative to the camera. The resulting adhesions and wear are thus false and must be removed.

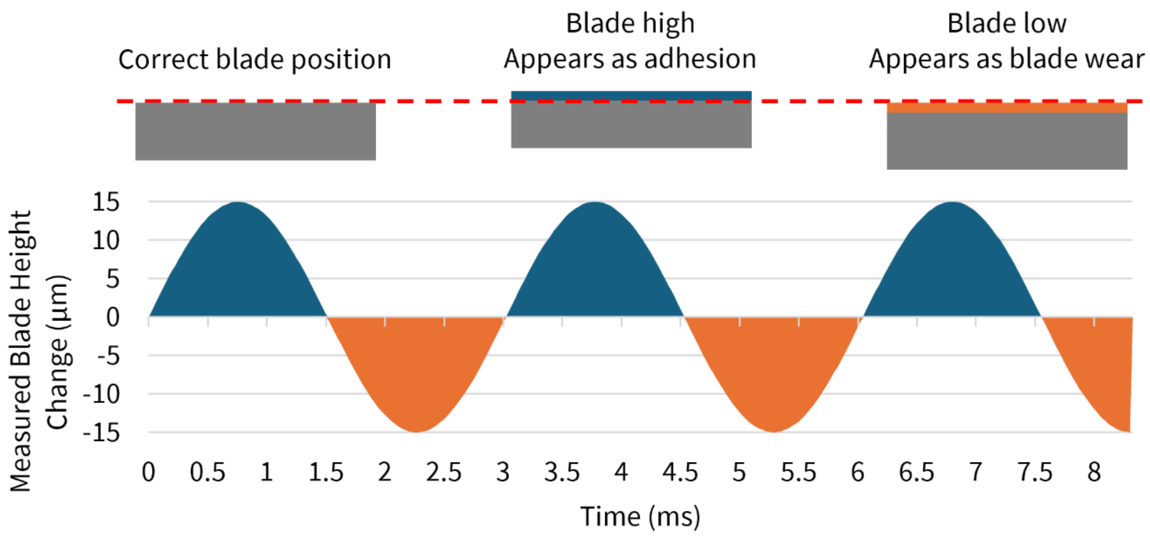

Figure 6.7 – Simplified representation of how vertical oscillation of the blade is recorded as false adhesions or blade wear

Applying the pixel-based wear measurement techniques to the extracted frames allows for the error in wear and adhesion rates to be quantified, the rates extracted for the trial test are shown in Figure 6.8.

The image shake is caused by the vibrations within the rig during a test. These vibrations are primarily due to an unbalance within the disk of the spindle test rig, and therefore are consistent during, and between, tests. The total error introduced by vertical shake is directly proportional to time and can therefore be subtracted from the extracted wear rates.

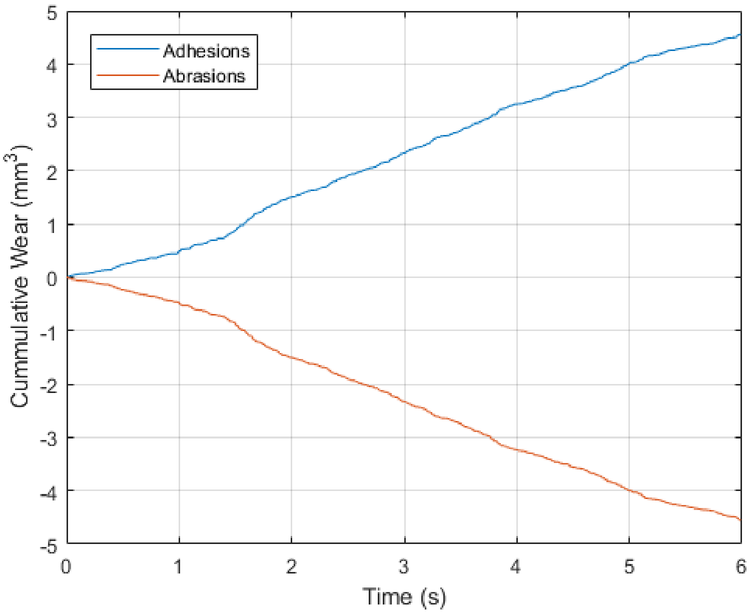

Figure 6.8 – Wear measurement error due to vertical shake

The false wear was measured for the period before blade contact for each test completed in this chapter and line of best fit through the data plotted against time was extracted, with the gradient of this line being the false wear rate.

Partway through this test campaign the spindle test rig underwent maintenance, and a new disk was installed and balanced. The balance on the new disk was superior to that of the original disk; this reduced the amount of vibration seen during a test and therefore reduced the blade shake observed by the camera. Although it is possible to compensate for the changes in the shake through the measurement of the separate false wear rates, in this study only tests completed with the new disk have been used for wear rate measurement. This has been done to ensure the data is consistent. The average false wear value for all tests completed on the new disk has been calculated with the results shown in Table 6.2.

Table 6.2 – Magnitude of false wear volume due to vertical shake

Average false wear (mm^3/s)	Spread of false wear (mm^3/s)	Number of tests sampled
0.1115	+0.0208/-0.0229	20

For each test the false wear rate can be removed from the data, an example of this from the trail test can be seen in Figure 6.9. The result of this is a drop in the total measured adhesion volume, and adhesion rates which fall close to zero during the period of zero force which occur due to the periodic nature of M601 wear at low incursion rates.

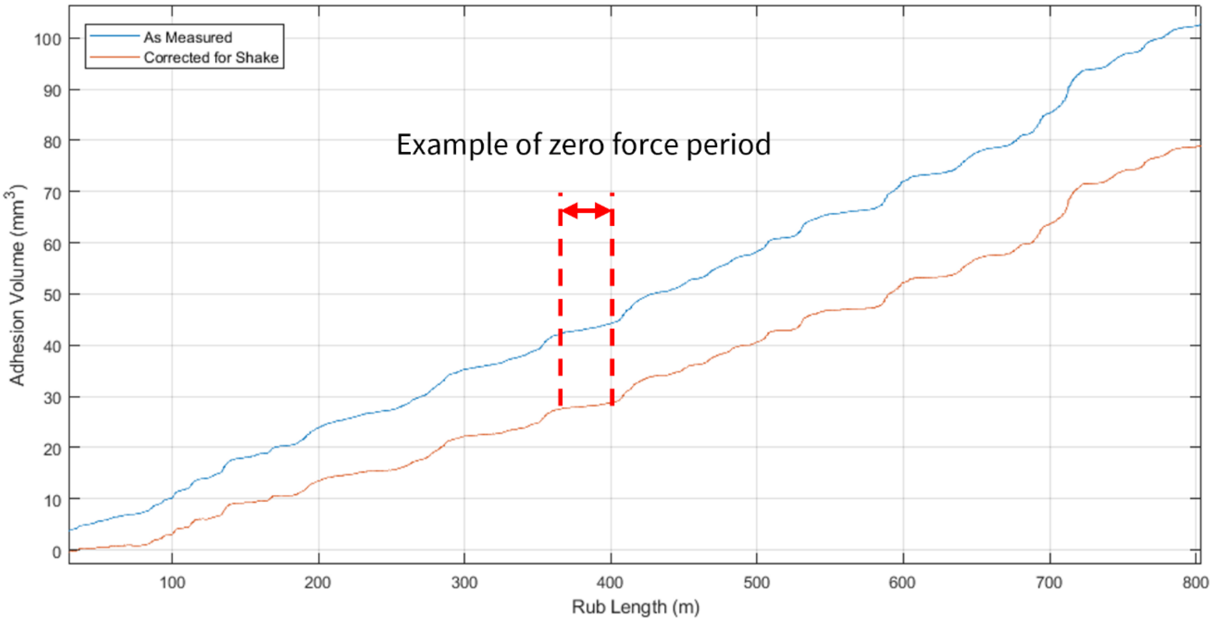

Figure 6.9 – Wear measurements corrected for vertical shake

A further benefit of the pixel-based analysis is the ability to separate wear of the blade from wear of adhesions. To process the adhesion and blade wear the height of adhesions at each pixel is recorded. Stepping through each frame, any increases in height are added to the adhesion height and reductions are removed. If a reduction in height is calculated at a point on the blade where the adhesion height is zero this is recorded as blade wear.

By separating the adhesions from the blade, it allows for easier visualization of how the wear develops during a test (Figure 6.10) and allows the wear rate of the blade to be separated from the wear rate of adhesions.

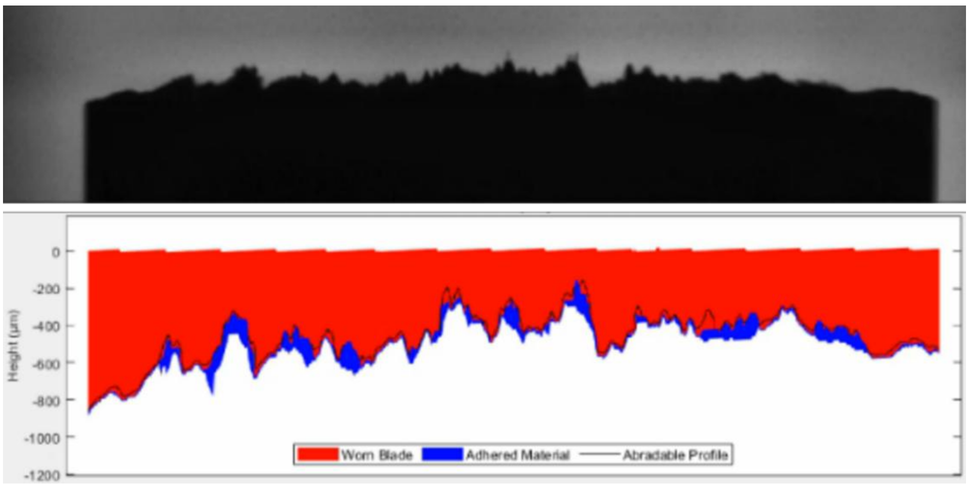

Figure 6.10 – Separation of adhesion wear and blade wear extracted from a front camera image

6.2.3 Test Matrix to Determine the Impact of Bulk Temperature on Wear Mechanisms

To maximise the output of tests completed in this study, the test conditions have been targeted to maximise the impact of controlling bulk temperature. In Chapter 5 it was shown that the thermal properties of the abradable had the greatest impact on wear performance at low incursion rates (0.02µm/pass), with wear at higher incursion rates (0.2 – 2µm/pass) following Archard's wear law. Testing has therefore been completed at 0.02µm/pass.

The hardness and temperature range has been selected to cover the full operating limits of the material within an engine. Three hardnesses have been selected: 52, 60, and 73HR15y, representing a Soft, Medium and Hard abradable respectively.

Three temperatures have been selected: 100, 200, and 300°C, spanning the operational range of M601. During these tests the heater block will be set to maintain the target temperature for the duration of the rub. For this reason, a room temperature test has been omitted. To maintain the backplate at room temperature a cooler block would be required to remove the energy generated during the rub.

As M601 is designed to be used with Titanium blades, these tests have therefore been completed using Ti-6Al-4V blades in the design detailed in Section 3.2. All abradable samples have been manufactured as detailed in Section 3.2.

For each test, force data, thermal camera data and the front stroboscopic imaging data has been collected. During some tests dust build up on the cameras and strobe prevented the extraction of wear data. Table 6.3 details all the tests which have been completed, separating tests completed on the old and new disks, and detailing how many tests allowed for wear rate measurement.

Table 6.3 – Test matrix for tests to determine the impact of bulk temperature on wear mechanisms for M601

Disk	Hardness (HR15y)	Backplate Temperature (°C)	Incursion Rate (µm/pass)	Number of Tests	Tests with Blade Wear Data
Old Disk	52 - Soft	300	0.02	1	0
	60 - Medium	100	0.02	1	0
		200	0.02	1	0
		300	0.02	1	0
	73 - Hard	100	0.02	1	0
		200	0.02	1	0
		300	0.02	1	0
New Disk	52 - Soft	100	0.02	3	2
		200	0.02	3	2
		300	0.02	2	2
	60 - Medium	100	0.02	2	2
		200	0.02	2	2
		300	0.02	2	2
	73 - Hard	100	0.02	2	2
		200	0.02	2	2
		300	0.02	2	2

6.3 Results

As work investigating the mechanical properties of M601 at differing bulk temperatures showed small changes relative to the impact of changing hardness, the trends seen between hardnesses should be dominated by the hardness rather than the bulk temperature (46,47,60). Therefore, by plotting the average peak forces for each test against hardness, the data can be compared with existing studies to ensure the additional mass of the heater block does not influence the recorded force values (Figure 6.11). These results show peak normal forces in the range of 50-350N, aligning with results seen in Chapter 4 and in work completed by Rahimov (82). These forces also follow the trend observed by Rahimov of decreasing with hardness from soft to medium, before increasing at higher hardnesses.

Although the global trend of forces follows existing research, there is a significant spread in the force values as visualized by the error bars in Figure 6.11. This spread is introduced because of the varying bulk temperature, generated by heating the backplate to temperatures of 100, 200, and 300°C. The resulting error bars can be seen to vary depending on backplate temperatures. Additionally, the wear seen in the post test sample images shown in Figure 6.14 shows variation between different backplate temperatures, most notably for the hard abradable samples.

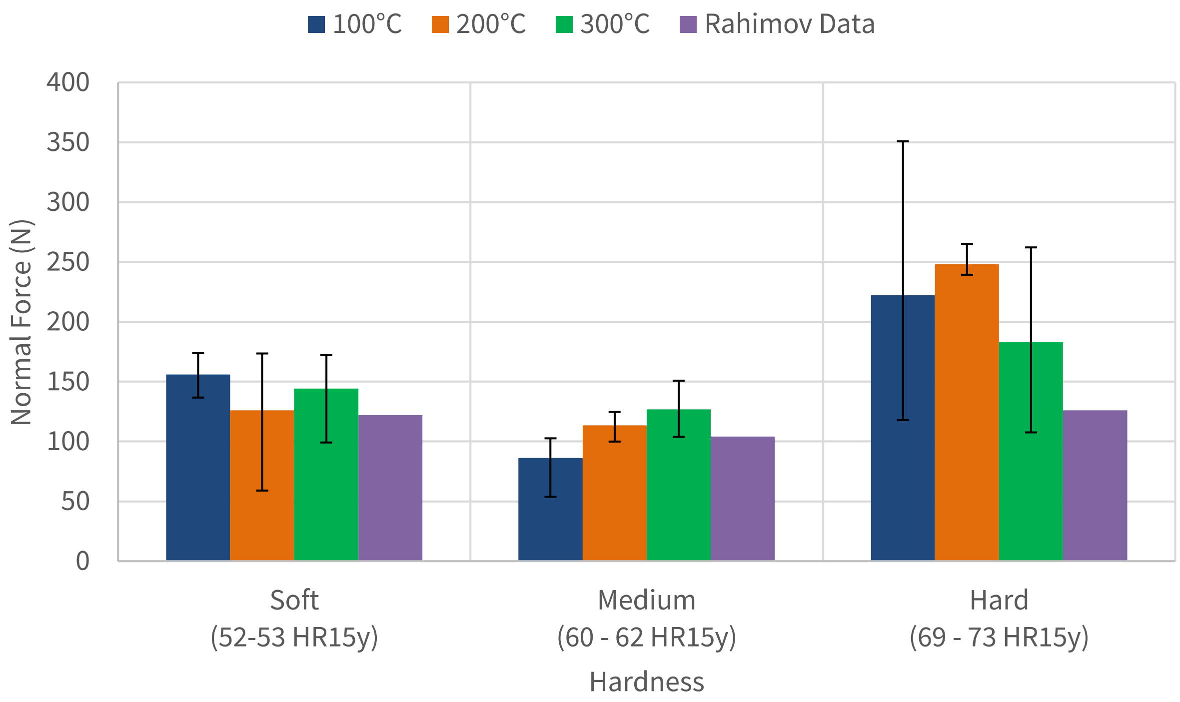

Figure 6.11 – The influence of hardness on peak normal loads for M601 tests at 0.02µm/pass. Data has been separated by backplate temperature, alongside room temperature tests completed by Rahimov (82)

For all test conditions the resulting abradable wear surface shows significant grooving, caused by wear and adhesion formation on the blade tips. For the soft and medium hardnesses there are clear signs of multimodal wear on the blade tips, with areas of thermal damage and blade wear, alongside adhesions (Figure 6.12). For the hard samples there is more blade wear, and due to the volume of wear it is not clear if there are any adhesions present from visual inspection alone.

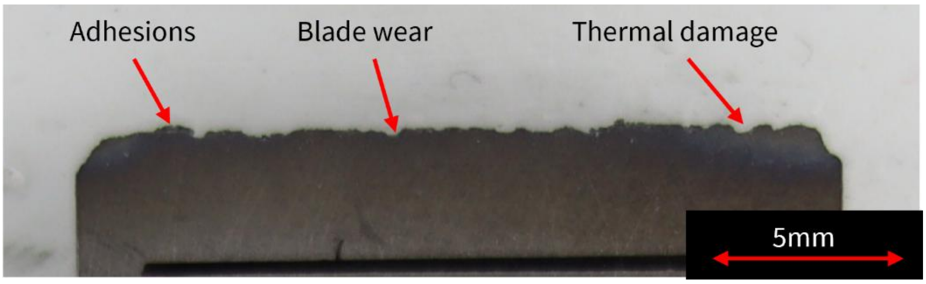

Figure 6.12 – Image of a tested blade from a 0.02µm/pass, 52HR15y M601 test showing multimodal wear

To better visualize the development of adhesions and blade wear for each condition, rub maps - like those used in Chapter 5 - have been created for each test displayed in Figure 6.14. These are shown in Figure 6.15. These rub maps show how the blade profile varies during a rub, with the colour indicating blade height (yellow indicating adhesions, blue indicating blade wear). The x-axis shows the position along the blade front, and the y-axis is the increasing rub length as the test progresses. From these rub maps both adhesion formation and blade wear can be seen to occur at all sample hardnesses regardless of temperature, with the ratio of adhesion formation to blade wear decreasing as hardness increases, aligning with the results shown in section 5.3.

Using the data presented in the wear tracks (Figure 6.14) and rub maps (Figure 6.15) examples of the impact of bulk temperature on the wear mechanisms can be highlighted.

From the rub maps of the medium hardness samples there is a noticeable increase in the uniformity of adhesion formation across the blade front with increasing backplate temperature, with a more consistent adhesion height and fewer regions of blade wear. This is visible in the rub maps from the more consistent colour on the map, with more, larger, yellow regions (adhesions) at 300°C compared with the 100°C test which has fewer, smaller, yellow regions interspersed with the blue and green areas (blade wear). The impact of this can also be seen on the post-test images which have been enlarged in Figure 6.13. At 100°C there are many small adhesions visible on the blade tip, aligning with the small yellow regions on the rub maps. There are also large areas of blade wear, aligning with the blue on the rub map. At 300°C the blade front no longer shows the multiple small adhesions, but instead has fewer, wider adhesions, aligning with the larger yellow regions on the rub map. There is also less wear on the blade tip, relating back to the rub map showing less green and blue that at the lower backplate temperatures.

From the blade images a tendency for wear to occur at the corners of the blade can be observed. This behaviour relates back to observations made by Rahimov (82) who noted that blade wear typically occurs first at the corners of the blade and works inwards as the test progresses. This is due to the blade corners contacting the abradable on two faces, the tip and the side, leading to higher local temperatures and therefore more blade wear than at the centre where there is only contact at the tip.

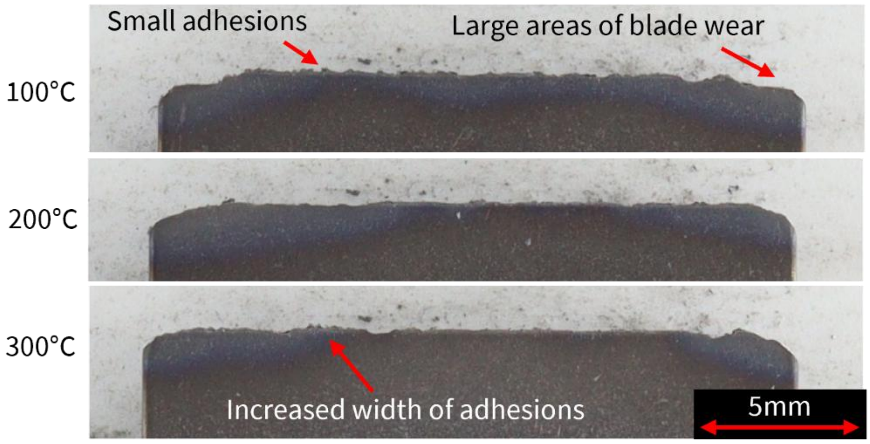

Figure 6.13 – Images of blades tested against 60HR15y M601 at 0.02µm/pass with various backplate temperatures

For the soft abradable samples there are also differences visible in the rub maps at different back plate temperatures, but the trend does not follow that seen for the medium hardness samples. Adhesions were most common at 100°C, with the large regions of orange and yellow on the rub map highlighting adhesion growth, and very little blue showing blade wear. As temperatures increase to 200°C the regions of yellow become smaller, and there in an increase in green and blue areas signifying a transition from adhesion formation to blade wear. The size and quantity of yellow regions then increase again at 300°, showing more adhesion formation. At the higher temperatures there was however an increase in the amount of blade wear, with large blue areas seen at the corners of the blade at 300°C.

From the examples shown in Figure 6.14 and Figure 6.15 it appears that the hard samples follow the same trend as the medium samples, with an increase in adhesion formation (increased yellow and orange areas on the rub maps) and reduction in blade wear at increasing backplate temperatures (reduced blue area). However, the actual performance of the abradable was more varied. The level of blade wear observed between repeats varied significantly at 100°C and 300°C, meaning no clear trend can be immediately observed.

Although it is possible to observe differences between tests completed on materials of the same hardness but with different backplate temperatures, there were no step changes in the performance of the abradable across its working temperature range. This means that while the bulk temperature of the abradable does impact the wear mechanisms, testing completed at room temperature does still produce results with are representative of an abradable being used at elevated temperatures.

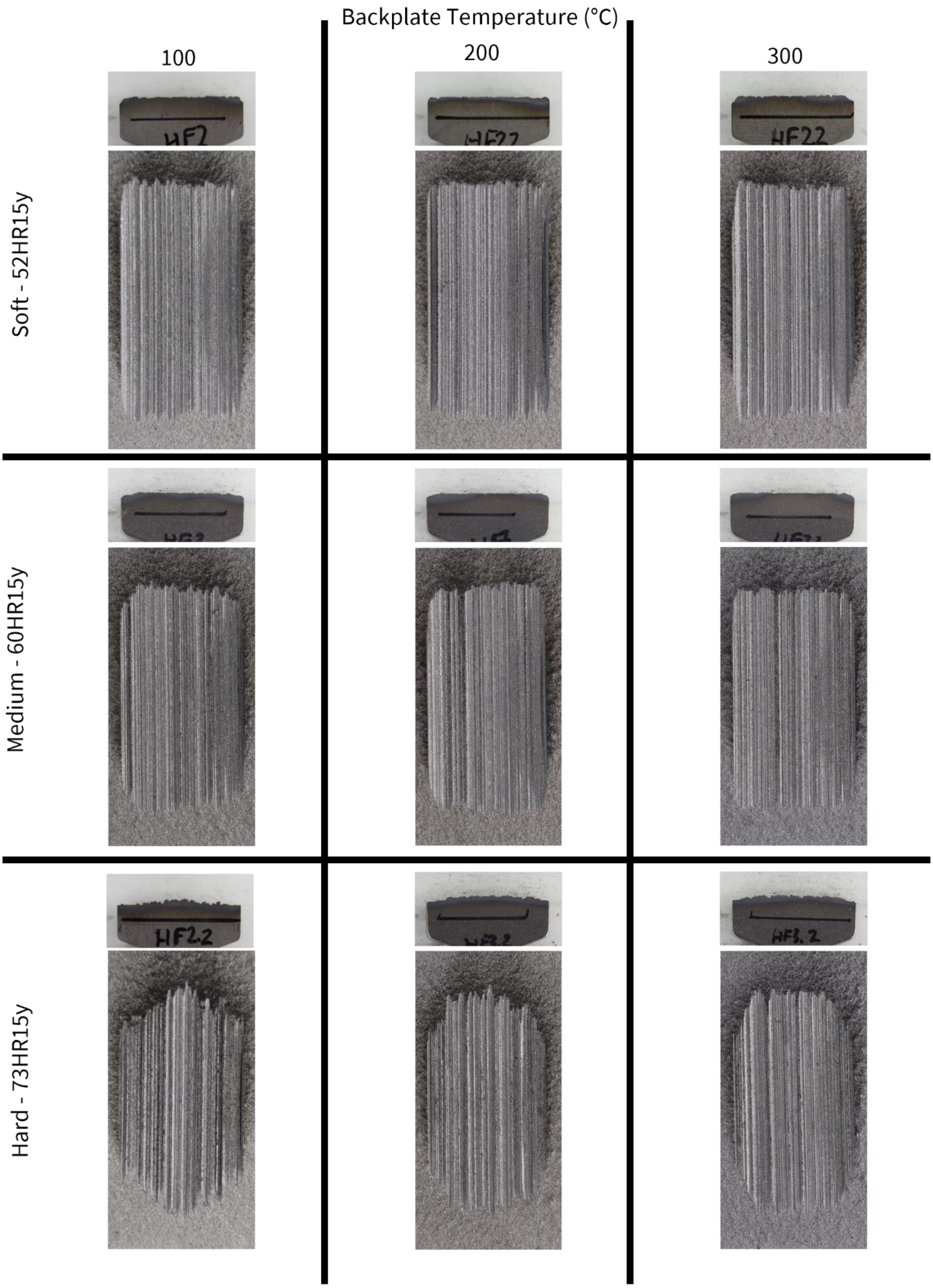

Figure 6.14 – Examples of the wear track and blade profile of M601 samples with varying hardness and temperature

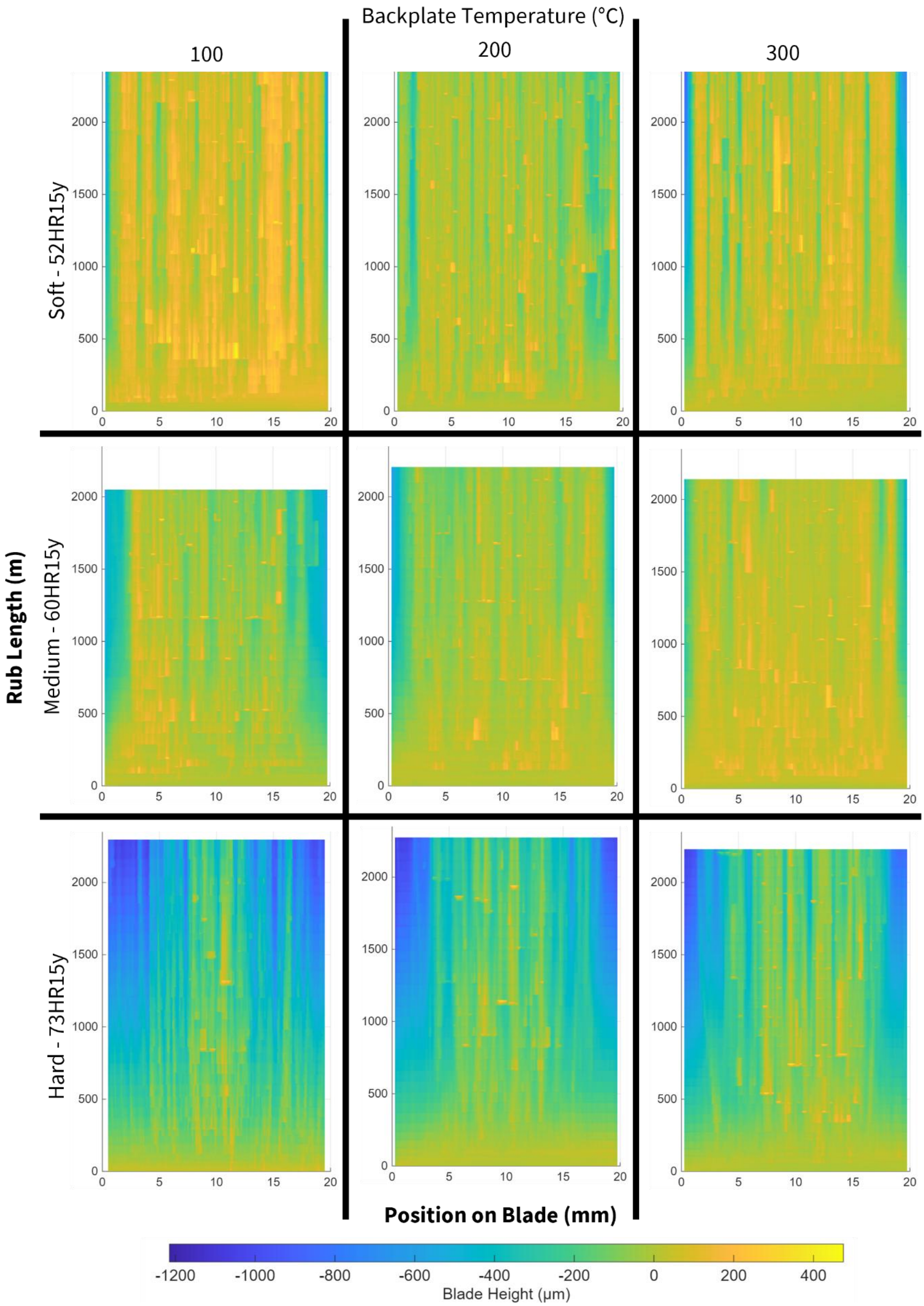

Figure 6.15 – Examples of the rub maps from M601 samples with varying hardness and temperatures

6.3.1 Impact of Bulk Temperature on Forces

Visual inspection of the wear scars and rub maps allow for qualitative results to be drawn, but to allow for a quantitative comparison between the tests at differing backplate temperatures the force data can be used. Force data has been selected as it is a key parameter in both heating and wear relationships.

The normal forces produced during the 0.02µm/pass tests all showed periodic behaviour, as seen in Figure 6.16. This periodic behaviour was observed in Chapter 5 and was seen to be due to large scale wear events occurring across the blade front simultaneously. These events reduce the area of contact between the blade and abradable and therefore lead to a reduction in force. As most of the wear during a 0.02µm/pass test occurs at the peaks in force, to allow for easier comparison between tests, these peaks have been extracted. An example of this process is shown in Figure 6.16.

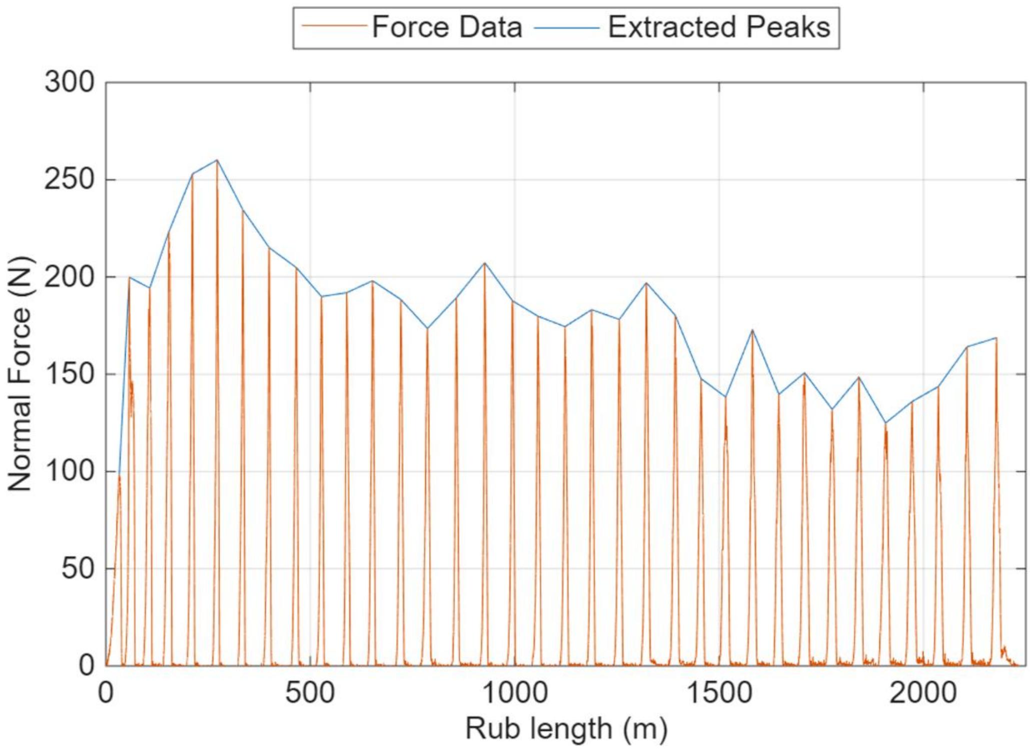

Figure 6.16 – Example of peak force extraction from a 300°C, 73HR15y test

For each test the peaks in the force data have been extracted and an average value has been calculated. These results have then been grouped by hardness and backplate temperature, with the average of each group plotted in Figure 6.17.

The trend in peak force with changing backplate temperature differs between the different hardness levels. The medium hardness samples follow a steady trend, with peak normal forces increasing with backplate temperature - echoing the steady increase in adhesion uniformity with temperature observed in Figure 6.15.

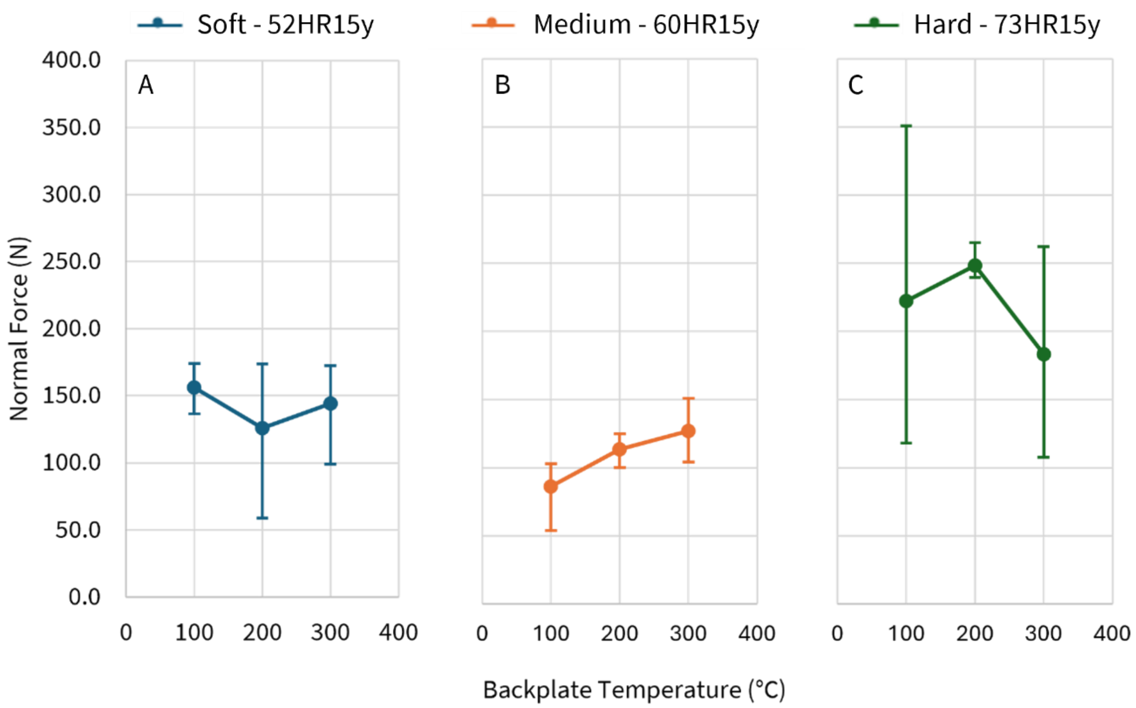

Figure 6.17 – Impact of temperature and hardness on peak normal forces for soft (A), medium (B), and hard (C) M601 tested at 0.02µm/pass

The hard samples initially follow the same trend from 100 to 200°C but then forces reduce as the temperature increases further to 300°C. Significant levels of variation in the peak forces are also seen at 100 and 300°C, relating back to the variation in wear scars seen at these conditions.

The soft samples once again follow a different pattern, with peak forces at a minimum at 200°C, increasing as temperatures increase and decrease from that point. However, this does further relate back to the observations made using the rub maps, with adhesion prominence aligning with the peak force values.

With the large variation in peak force values seen for the hard and soft samples there is insufficient information from the force data alone to make any definitive statements on the impact of bulk temperature on the wear behaviour. Instead, the in-situ data collected for each test individually must be studied to identify the root cause of the variability and to gain a better understanding of any behaviours and trends.

6.4 Discussion

The results produced in this study allow for trends in the force data and wear mechanisms to be identified, these trends can then be used to bring together existing literature to provide a cohesive understanding of the response of M601 to bulk temperature during blade tip – liner interactions. As the force and wear response of M601 differs with hardness each hardness will be discussed individually.

6.4.1 The Impact of Bulk Temperature for Medium Hardness Abradables

With a hardness of 60HR15y, the medium hardness samples produced a consistent response with temperature for both wear and peak normal forces. The increase in normal loads with temperature initially seems at odds with the work completed by Martinet et al. (60), which showed that during a single pass of an abradable at elevated temperatures there was an increase in wear depth for a given temperature.

However, this work differs from that completed by Martinet et al. as, rather than a single pass, this work was completed on a spindle test rig which completes multiple passes during a single test. Tests completed on spindle test rigs by Zhang et al. (75) have demonstrated that over successive rubs an AlSi abradable will compact, leading to a progressive increase in the normal load.

As the temperature increases the Aluminium phase within the abradable softens and its failure mode becomes increasingly ductile, with an increase in its strain to failure (103). This allows for further compaction to occur before the abradable factures, increasing the peak normal loads.

At these test conditions the force results at each backplate temperature have shown little variation (Figure 6.17B), highlighting the stability of this relationship and leading to repeatable wear of the blade and abradable.

6.4.2 The Impact of Bulk Temperature for Low Hardness Abradables

At a low hardness of 52HR15y the force trend differs significantly, with an initial peak force higher than that of the 60HR15y samples at 100°C but then reducing as the temperature increases (Figure 6.17A). To understand this response, models of how stress flows within an abradable sample during a rub can be applied.

M601 is formed of an irregular structure of AlSi and Polyester, this results in some local regions of thin AlSi branches and struts. As the AlSi phase acts as the load bearer within the microstructure this leads to stress hotspots at the thin struts within the AlSi, and material failure initiating with failure of these struts (Figure 6.18) (54). As hardness reduces there is an increase in the ratio of polyester to AlSi, leading to fewer AlSi struts, and larger continuous regions of polyester. Simulations of this completed by Cheng et al. (54) predict a significant increase in the ductility of M601 at lower hardnesses, with the polyester phase bearing more of the stress within the microstructure.

With fewer AlSi struts and larger continuous polyester regions the polyester phase will begin to dominate the material properties of soft M601. This accounts for the increase in peak normal loads seen for soft hardness M601 compared with medium samples, as the polyester phase will allow for more compaction and has fewer AlSi structs to act as fracture points. As the temperature increases to 100°C this difference becomes more pronounced due the polyester being held close to its glass transition temperature of 138°C, the point where the polyester phase transitions to an amorphous, rubbery state (47). In this state the polyester is increasingly ductile, allowing for further compaction and normal loads.

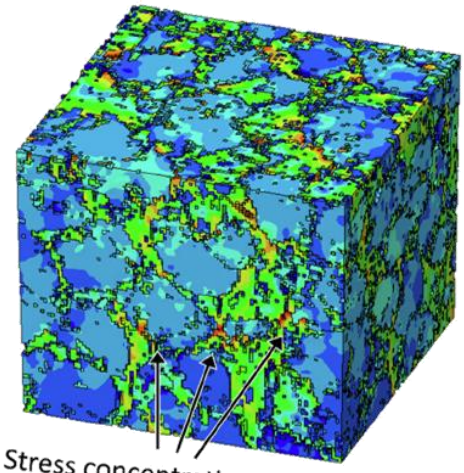

Figure 6.18 – Modelled stress distribution within M601 under compression (54)

As the backplate temperature increases to 200°C the peak normal forces reduce. With the mechanical properties of soft M601 being dominated by the polyester phase this reduction in force can be explained using work completed by Lye et al. (47). Lye et al. investigated the crystallization of the Polyester phase within a M601 sample and using differential scanning calorimetry was able to measure the cold crystallization temperature of the polyester phase within a M601 sample (Figure 6.19). This temperature was measured at 194°C.

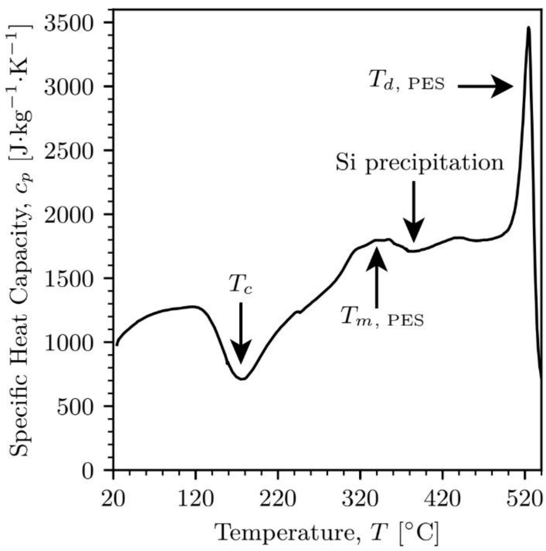

Figure 6.19 – Heat flow plot for M601 (47)

In their work they showed that for M601 as sprayed the polyester phase is amorphous due to the pronounced T_c peak. After aging the sample at 200°C Nano-Hardness testing showed a measurable increase of the mean reduced modulus of the polyester phase from 5.1 to 8.2 GPa. The impact of this with a rub test is that as the polyester phase within the M601 crystallizes the material becomes increasingly brittle, with an increased Youngs modulus and reduced strain to failure. With the material transitioning to a brittle failure mode the amount of compaction is reduced, therefore reducing the peak normal force.

However, it can be seen from the error bars in Figure 6.17A that at this temperature there is a large spread in the results. This spread is likely due to the time dependant nature of crystallization (117). As the tests completed in this study were begun when a predefined abradable surface temperature was reached, the time spent heating and heating rates were not controlled and vary between tests.

Finally, as the backplate temperature increases to 300°C the polyester phase is heated close to its melting point. At this temperature, the material will return to an amorphous state, leading to an increase in ductility and allowing for more abradable compaction.

6.4.3 The Impact of Bulk Temperature for High Hardness Abradables

The hard abradable samples (72HR15y) have a composition of more than 40% AlSi (22), and it is therefore expected that the mechanical response of the material will be dominated by the AlSi phase, as was seen for the medium hardness samples. This appears to hold true from 100 to 200°C, but as the temperature increases further the peak normal forces fall (Figure 6.17C).

There is also a wide range of force and wear results which occur at both 100 and 300°C. To investigate the variation at 100°C, the blade profiles measured in-situ have been used.

Figure 6.20 shows the rub maps and post-test sample images for two tests completed with a backplate temperature of 100°C, one of which produced high peak normal forces and one with low normal forces. The high normal force test shows initial adhesion formation across the entire blade, these adhesions then fracture, but smaller scale adhesions continue to form and fracture at that point, preventing blade wear from occurring. The low force test sees fewer adhesions early in the test and as a result suffers more severe blade wear, limiting the potential abradable compaction and the peak normal loads. The difference in wear behaviour of two tests of the same condition highlights that there is variability in the wear mechanisms which can occur.

This variability was identified by Bounazef et al. and Fois in the creation of wear maps for different abradables systems, where it was found that there was not a clean transition in wear mechanism as test conditions change, instead there would be a region where either mechanism could occur (87,94). Rahimov took this further by showing that transition of wear mechanism for abradable systems is probabilistic (80), meaning that at boundaries between different wear conditions it is only possible to predict the likelihood of each mechanism, rather than make a definitive statement about which will occur. This behaviour was found to be due to subtle changes introduced into each abradable sample due to the plasma spraying process.

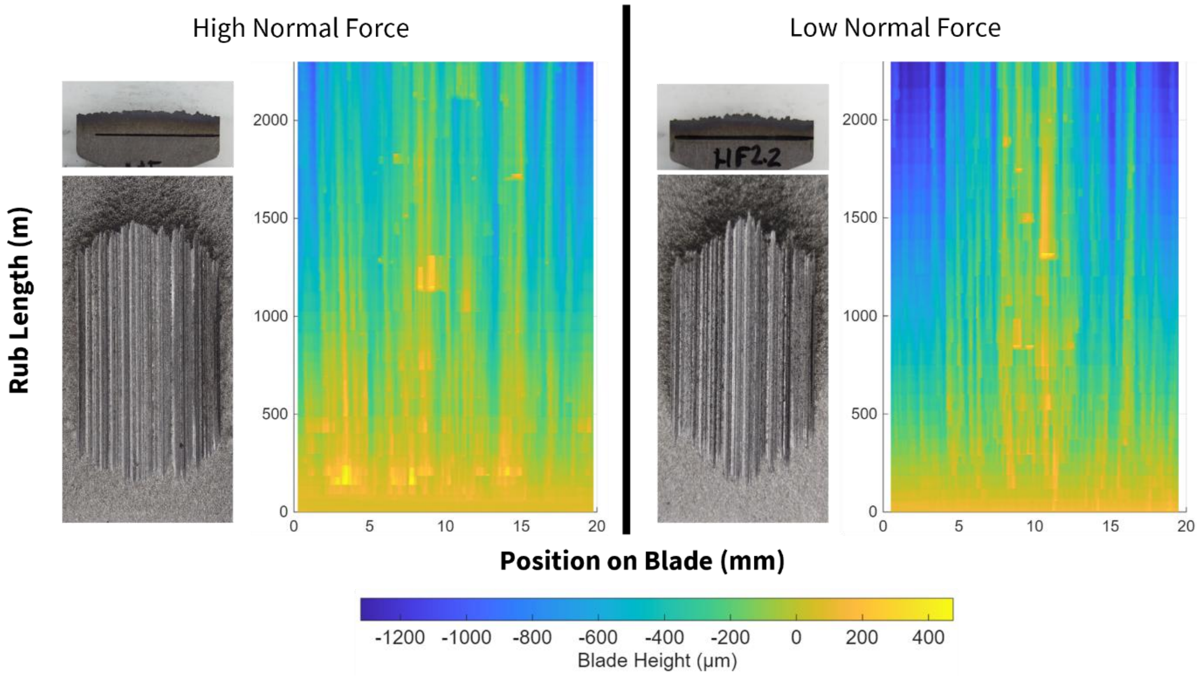

Figure 6.20 – Rub maps and sample images for hard M601 tests at 100°C with varying wear performance

For samples of high hardness M601, previous testing at 0.02µm/pass by Rahimov and Watson showed high levels of blade wear with little adhesion formation (40,82). By increasing the temperature of the abradable the material will become more ductile, leading to higher normal forces, and at the elevated temperatures provide a favourable environment for adhesion formation (Chapter 5). As these tests were completed with conditions known to lead to severe blade wear, the probabilistic nature of the adhesion formation would lead to some tests forming adhesions early in the test, providing a foundation for future protective adhesions to form, and some tests where adhesions do not form early on and the blade is left unprotected from wear.

This probabilistic theory can be applied further when looking at the results of the tests completed with a backplate temperature of 200°C. The peak normal forces seen during these tests were higher than at 100°C, due to the increased ductility and compaction of the abradable, and were also a lot more consistent with a smaller error bar (Figure 6.17C). The repeatability of the tests can also be seen in the post test images for each repeat at these test conditions shown in Figure 6.21. Each blade shows similar levels of blade wear, leaving a consistent rub track on each abradable sample.

The tests completed at 100°C appear to be at a boundary point in the backplate temperature, where the increased ductility and temperature of the abradable makes adhesions more favourable, but the variability in the abradables can result in each test producing different levels of wear.

Increasing the temperature to 200°C has further increased the normal load and abradable temperature, creating a more favourable environment for adhesion formation. This has pushed the conditions further from the boundary of severe wear and mixed modal, leading to more repeatable results.

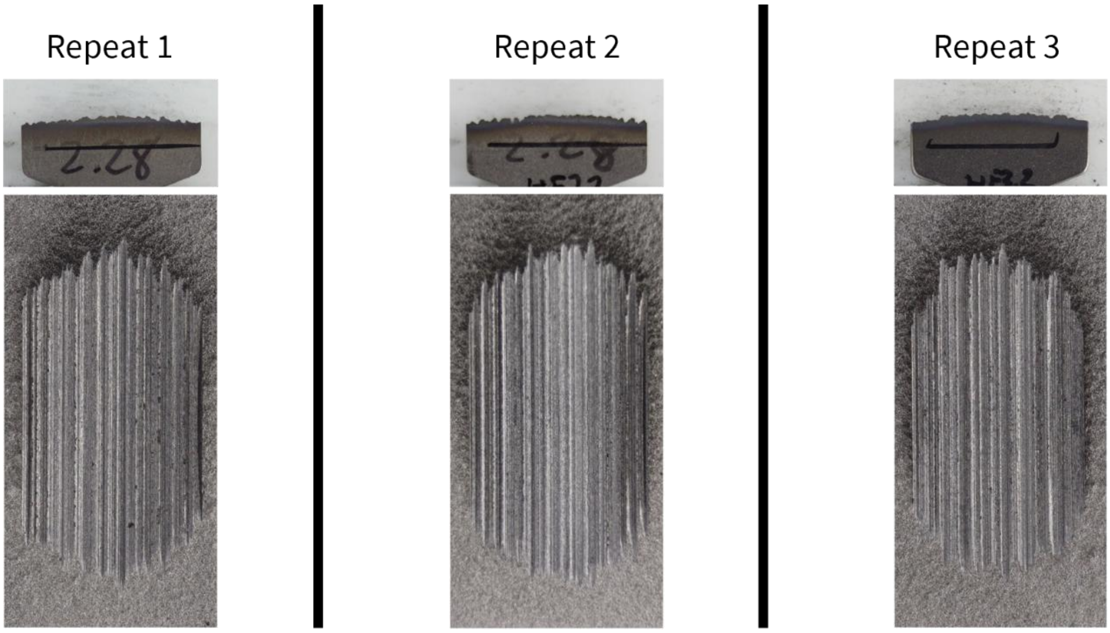

Figure 6.21 – Sample images for each test completed on 72HR15y (hard) M601 at 200°C

At 300°C it would be expected for this trend to continue, with the elevated temperatures leading to higher forces and a more favourable environment for adhesion formation. However, the force and wear results instead became highly variable. To investigate this variability a wear map has been produced for one test which generated high normal loads, and one which generated low loads. These rub maps have been plotted in Figure 6.22 alongside images of the post test samples. From these plots there is a distinct difference in the wear mechanism from each test, with the high load test generating more adhesions and showing less blade wear than the test which produced low loads. Although it is typically expected that under lower normal loads the rate of wear would be less (97), it was demonstrated in Chapter 5 that adhesions can form a protective layer on the blade, protecting it from wear. This behaviour can be seen in Figure 6.23 where the rate of adhesion formation has been plotted against the blade wear rate for each test. These plots show that the test which produced higher normal forces also produced the higher adhesion rates, while its rate of blade wear reduced. This demonstrates the ability of the adhesions to protect the blade, with the adhesions forming on the blade surface and acting as a sacrificial layer to reduce blade wear. In the case of the low force test there is a lower rate of adhesions, meaning there is not as much of a protective layer and therefore more blade wear is recorded.

During a test which shows high levels of blade wear the total depth incurred into the abradable is reduced, limiting the potential compaction and reducing the peak forces. If the blade is protected it can compact the abradable to the point where abradable rupture can occur.

These tests demonstrate how the formation of adhesions on the blade surface can form a protective layer which prevents blade wear, but from these plots alone it is not immediately clear why the samples behaved differently.

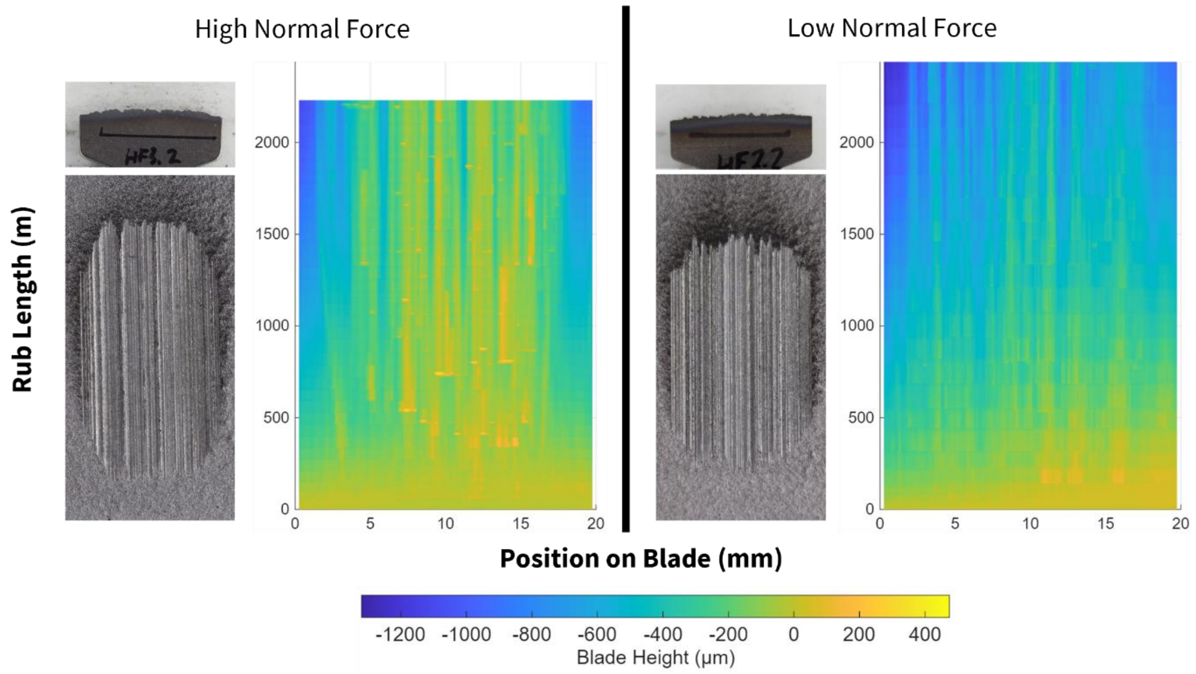

Figure 6.22 – Rub maps and sample images for hard M601 tests at 300°C with varying wear performance

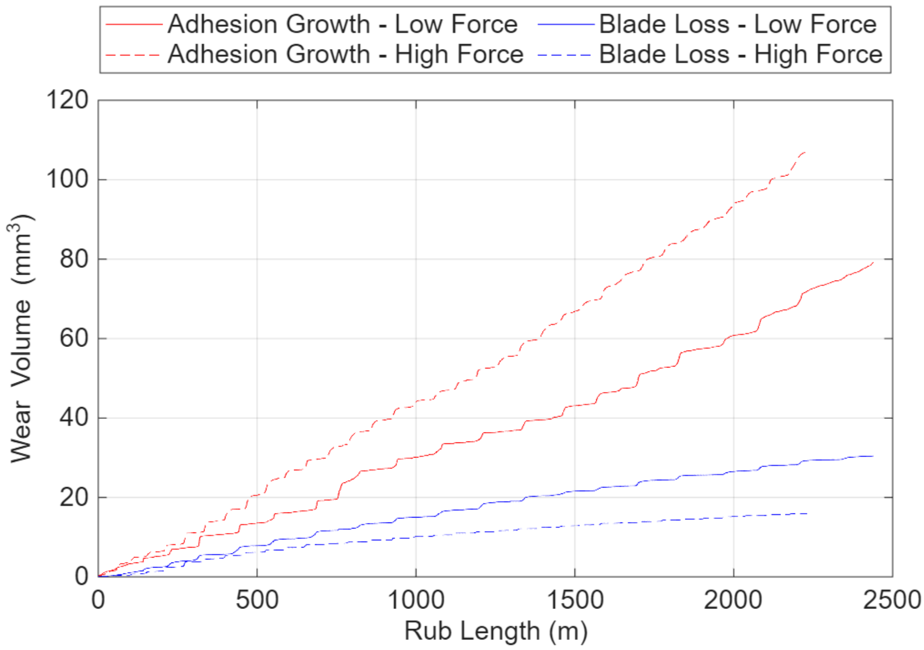

Figure 6.23 – Comparison of adhesion formation and blade wear rates for two hard M601 tests at 300°C

Reviewing the footage from the front camera before the rub began reveals that the orientation of the blade which experienced high wear rates was not square to the abradable surface (Figure 6.24). This would result in the left corner of the blade contacting the abradable surface before the rest of the blade.

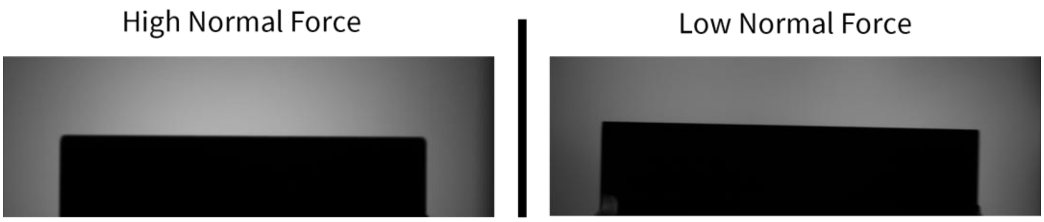

Figure 6.24 – Difference in blade orientation between two hard M601 tests at 300°C with varying wear performance

The impact of the non-uniform contact can be seen in the thermal camera footage of the blade and abradable. This data is shown in the form of rub maps for both the high and low force tests in Figure 6.25, with the data shown only for the first 500m of each rub.

For the sample which produced high normal loads there were short periods of high temperature across the entire blade and abradable, interspersed with cooler periods. This is symbolic of the periodic behaviour caused by large scale wear events seen in Chapter 6. In the low force test the temperature distribution is less uniform, and the high temperature events are longer in duration. This is most evident in the region A marked in Figure 6.25.

Region A highlights the corner of the blade which first contacts the abradable. The small area of contact leads to localized heating of the blade, with a gradual increase in the contact area. The gradual increase in contact area means there cannot be large scale simultaneous wear events as seen in the high force case, resulting in a prolonged period of heating. During this time region B highlights how the abradable can maintain a cooler temperature, likely due to the uncontacted material around the rub where heat can be dissipated. This results in a blade which heats up at a much higher rate than the abradable, and as described in section 5.5, will lead to blade wear.

With the blade wearing early in the test adhesions cannot form, this means that as the test progresses adhesions are less likely to form, as Rahimov et al. showed that adhesions form more readily on areas of the blade where an existing adhesion has broken off (79). This leaves the blade unprotected and more susceptible to blade wear.

The identification of adhesions as protective features on the blade, with an adhesion present early in the test having a lasting impact on the wear performance, presents the idea of pre-treating the blade tips with a layer of M601 to act as a nucleation site for further adhesion formation. The potential benefit of this was shown by Rahimov, who demonstrated that by running a 2µm/pass rub on a blade adhesion would form across the surface. Testing this blade again at 0.02µm/pass would then result in less blade wear than when testing with an untested blade (82).

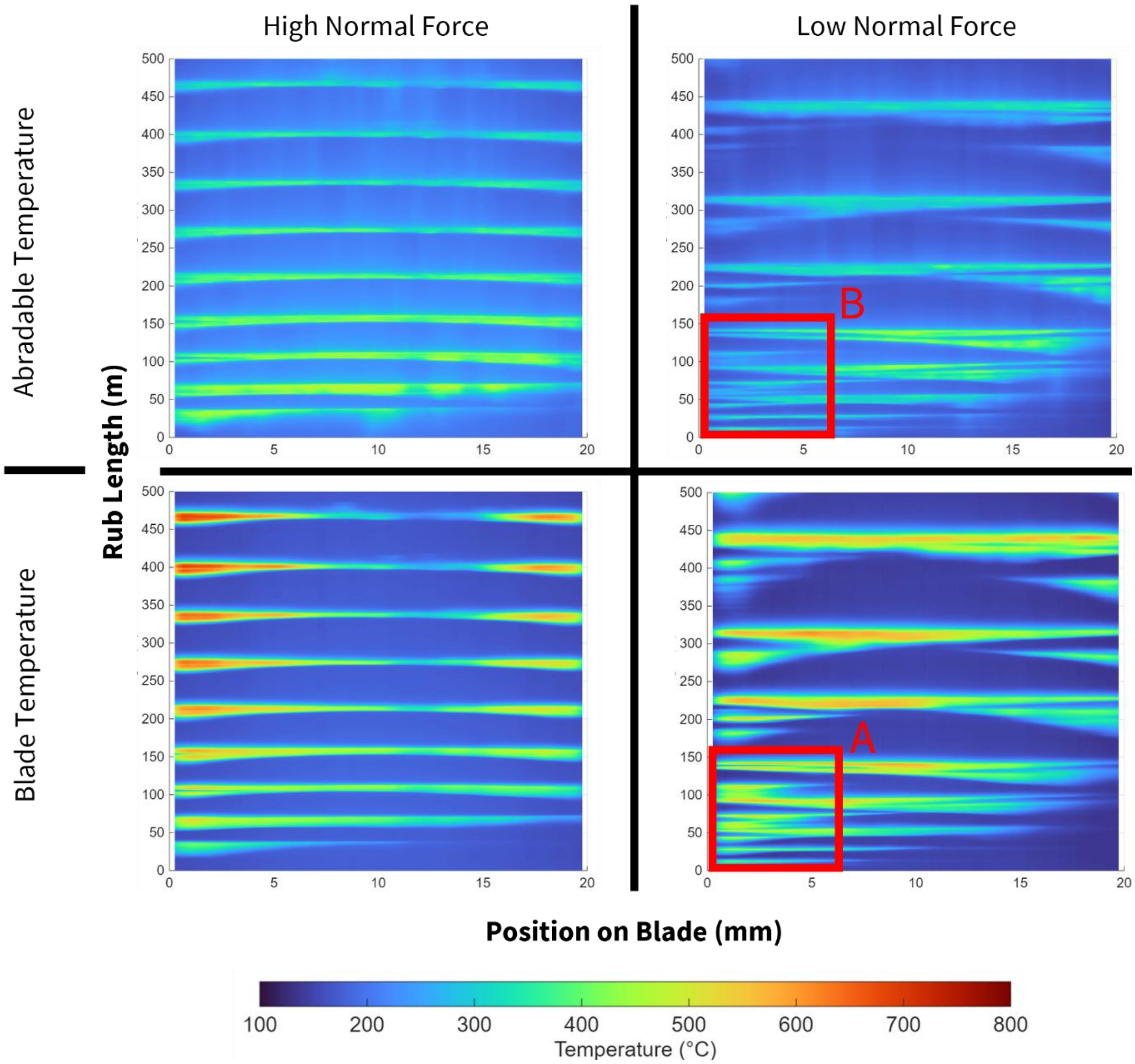

Figure 6.25 – Rub maps for Abradable and Blade temperatures, highlighting the impact of changes in blade orientation

6.5 Conclusion

The importance of thermal properties in the wear of M601 has been shown through analysis of thermal data collected during testing in Chapter 5, and the impact of bulk temperature on mechanical and wear properties has been demonstrated in published works (47,60,101).

This work builds upon these findings by completing rub tests using a spindle test rig fitted with a heater block below the abradable to control backplate temperature. These results show how at low hardnesses the polyester phase dominates the mechanical properties of M601 and how it reacts to changes in bulk temperature, with polyester glass transition and crystallization resulting in changes in the wear response of M601.

At medium and high hardnesses the AlSi becomes the dominant contributor to the mechanical properties, with the increased ductility at elevated temperatures leading to increasing levels of abradable compaction and therefore higher normal loads. For the hard samples the blade began to wear faster than adhesions could form, leading to reduced abradable compaction and lower forces at elevated temperatures. However, the wear behaviour at these conditions was not consistent and varied significantly if adhesions formed early in the rub, providing a protective layer for the blade.

7 Evaluating if M601 Adhesion Relationships Apply to M320 and XPT268

7.1 Introduction

Through the application of novel in-situ measurement techniques, and the development of a sample heater block, it has been possible to visualize the impact of temperature on adhesion formation and blade wear in a manner that was not previously possible. This has allowed for the development of a better understanding of how adhesions form on the blade, building upon existing research to form a more detailed set of relationships to better predict adhesion behaviours. These relationships are:

- The rate of adhesion formation increases with increasing normal loads (97).
- Adhesions form more readily at elevated temperatures (Chapter 5).
- Adhesions can provide a protective layer on the blade (Chapter 6).
- If the blade heats up faster than the abradable it is likely to wear before adhesions can form (Chapter 4).
- New adhesion formation is more likely at the site of a previously fractured adhesion (79).

These criteria have been developed and observed in testing completed on M601, an abradable material made from AlSi and polyester, but this is not the only AlSi based abradable system.

At elevated temperatures, the polyester phase will begin to burn out, limiting the maximum operating temperature of M601 to 325°C (89). In hotter regions of the engine a different AlSi abradable, M320, is applied. This material replaces the polyester phase with hexagonal boron nitride (hBN) which increases the material friability and acts as a solid lubricant, the resulting materials exhibits a vastly different wear response than M601 (90).

During a rub test with M601 the key parameters which impact the wear response are incursion rate and material hardness. At low incursion rates (0.02µm/pass) the blade will wear, with some adhesion formation, as incursion rates increase the amount of adhesion formation increases and blade wear decreases, until at 2µm/pass the wear is primarily adhesion formation. The volume of adhesion formation is also impacted by the abradable hardness, with softer abradables producing more adhesions (Chapter 5).

The wear response of M320 is also dependent on incursion rate, but unlike M601, adhesions do not form at high incursion rates. Between 0.2 and 2µm/pass M320 will produce an efficient cut, leading to a smooth wear scar and minor wear on the blade, this behaviour is independent of material hardness. The performance of the abradable begins to worsen at low incursion rates (0.02µm/pass), with highly variable wear, with the blade either wearing against soft abradables or adhesions forming against hard abradables (76,78).

The change in mechanism was shown by Fois et al. to be due to a change in the mechanism of material removal, with a transition from cutting at high incursion rates to compaction of the abradable at lower incursion rates (76). The evidence for this can be seen in Figure 7.1 which shows how the pores and hBN under the rub surface of a 0.02µm/pass test have become compacted. The compaction leads to an increase in the normal force and introduces more heat to the contact area due to frictional heating.

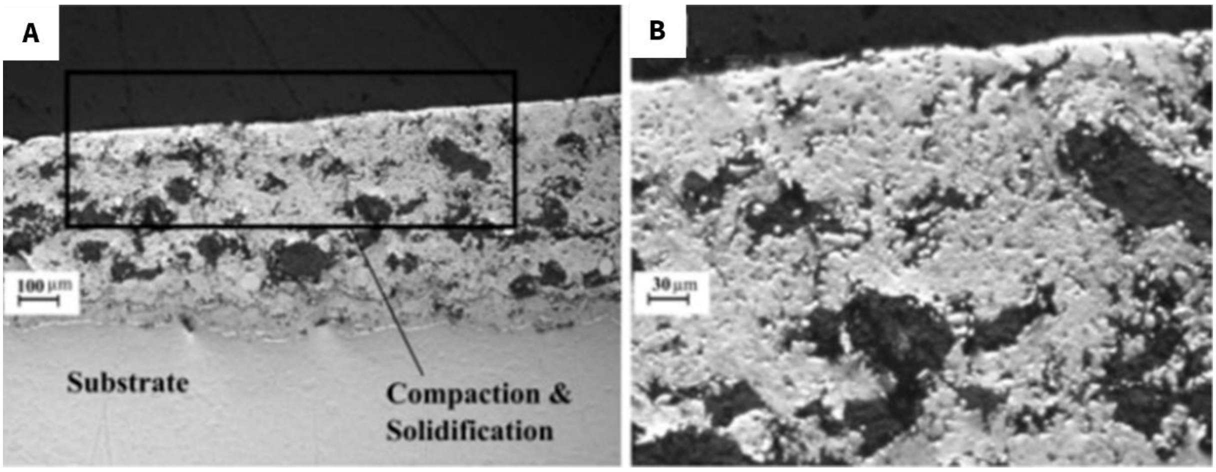

Figure 7.1 – Images of M320 microstructure after a 0.02µm/pass test, with the region of compaction highlighted in A, and magnified in B (78)

To understand how the thermal energy passes through the abradable thermal models have been created by researchers such at Bolot et al. (51) and Watson et al. (22), allowing the heat flux through abradables to be predicted from microstructure images. These techniques were then applied by Fois et al. to M320 (76). They found that the hBN within the abradable was not uniformly distributed but formed in clumps, and that there was a high thermal resistance across the boundary between the hBN and the AlSi. The results of the thermal simulations (Figure 7.2) show that hBN clumps under the surface of the abradable act to block the heat flow, creating hotspots on the surface.

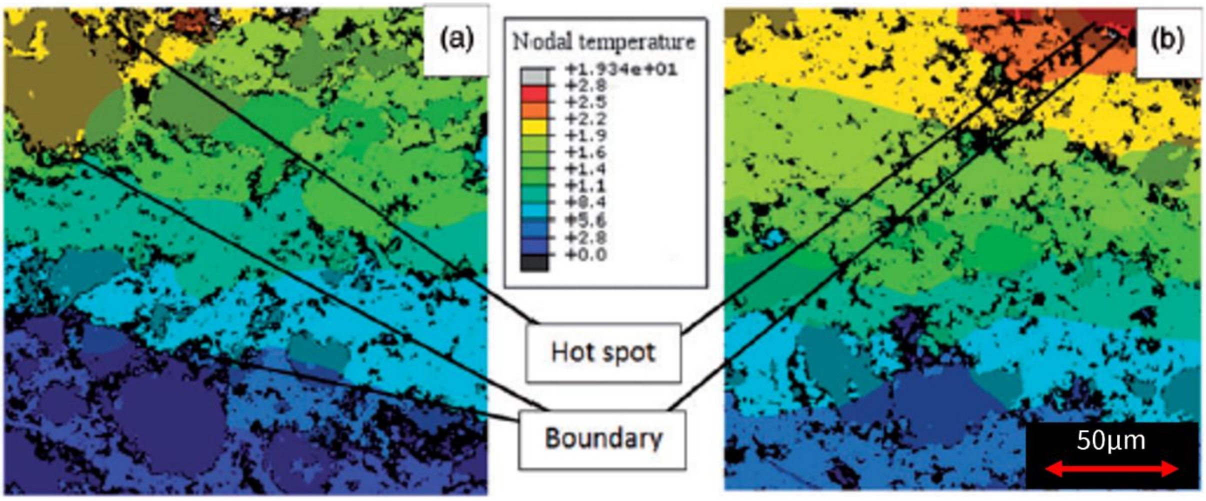

Figure 7.2 – Results of a thermal model showing the hotspots produced by clumps of hBN in M320 of hardness 55HR15y (a) and 73HR15y (b) (76)

The prevalence of these hBN clumps is influenced heavily by the hardness of the abradable. Figure 7.3 shows how the microstructure changes for each of the AlSi based abradables with varying hardness. As the hardness of M320 reduces the number and size of the hBN clumps increases, the amount of porosity also increases leading to the AlSi branches being broken. As the heat primarily flows through the AlSi, this leads to a global reduction in the thermal conductivity, as well as an increase in hotspots due to hBN clumps. This was measured by Fois et al. for M320 of two hardnesses across a range of temperatures (Figure 7.4) (76). They found that the average thermal conductivity of M320 reduced from 21.79 W/(mK) at 72.37 HR15Y to 14.12 W/(mK) at 54.6 HR15Y.

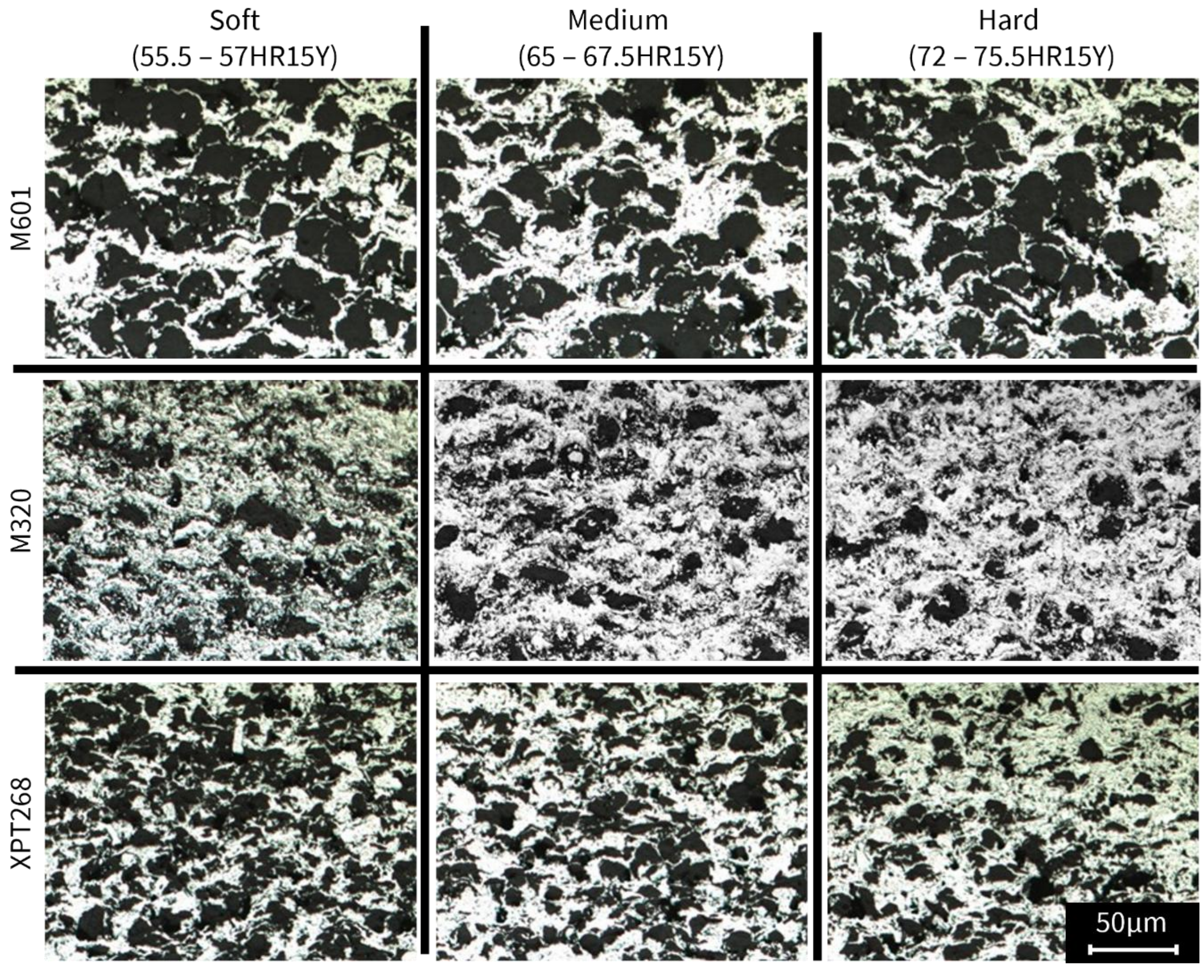

Figure 7.3 – Variation in the microstructure of M601, M320 and XPT268 for a range of hardnesses. Samples prepared by Turbine Surface Technologies, Nottingham

Fois et al. proposed that the at low hardnesses the low thermal conductivity and hBN clumps would produce hotspots on the abradable surface, causing the blade to undergo thermal damage and wear. At higher incursion rates the heat would flow thought the abradable, protecting the blade.

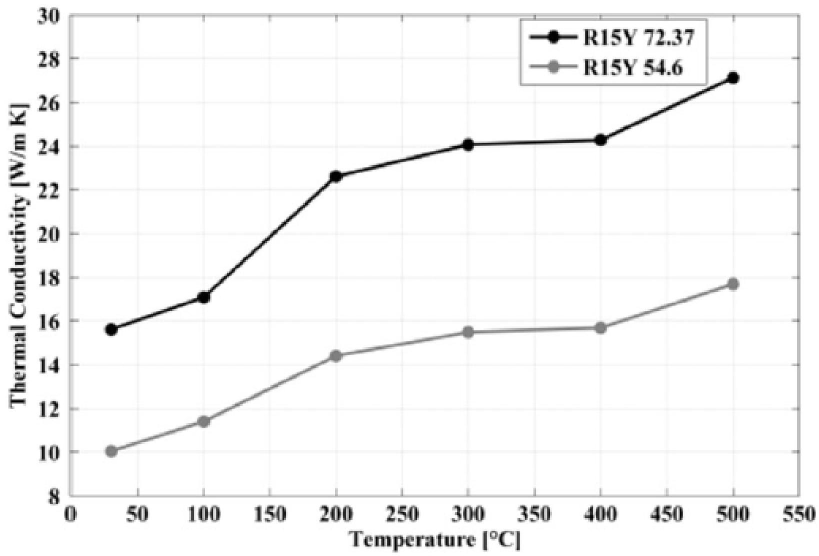

Figure 7.4 – Changes in thermal conductivity of M320 at varying temperatures for two hardnesses (76)

A second, more recent addition to the AlSi abradable family, is XPT268. This material aims to add the high incursion rate performance of M320 to M601 by adding both polyester and hBN to the AlSi matrix. The hBN added to the material powder is smaller than that in M320, this results in hBN platelets of reduced size within the microstructure rather than the clumps seen in M320. Although there is no mention of changes to the size of the polyester powder from the manufacturer (89), inspection of the microstructure (Figure 7.3) shows that the polyester phase is better distributed and is in smaller chunks. This appears to have increased the ratio of AlSi to dislocator when compared to M601 of the same hardness (Figure 7.5), although it should be noted that only a single data point is currently available in published literature (44).

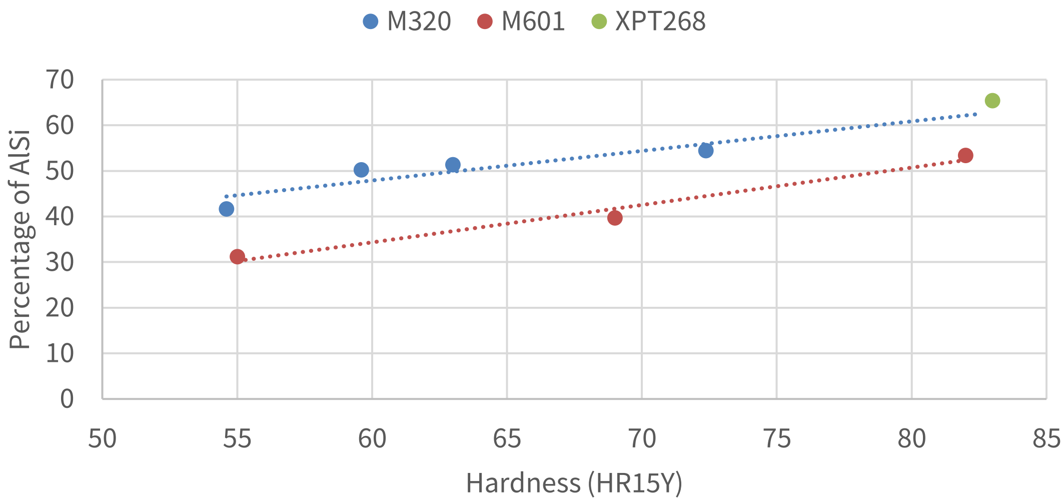

Figure 7.5 – The volume fraction of AlSi in M601, M320 and XPT268 at different hardnesses (22,44,94)

The abradability of XPT268 is currently not well understood, with published data limited to a single study completed by Bertuol et al. which included a back-to-back comparison between XPT268 and M601 (44). This work included tests on a spindle test rig, incurring titanium test blades into the abradable coatings at a 50m/s tip speed with an incursion rate of 50µm/s (0.83µm/pass), these tests produced higher forces and temperatures for the XPT268 samples, as well as more adhesions (Figure 7.6). However, these tests were completed with samples of different hardness, with XPT268 being harder than M601. It is therefore not possible to determine if the increase in force and adhesion was due to the material or the hardness.

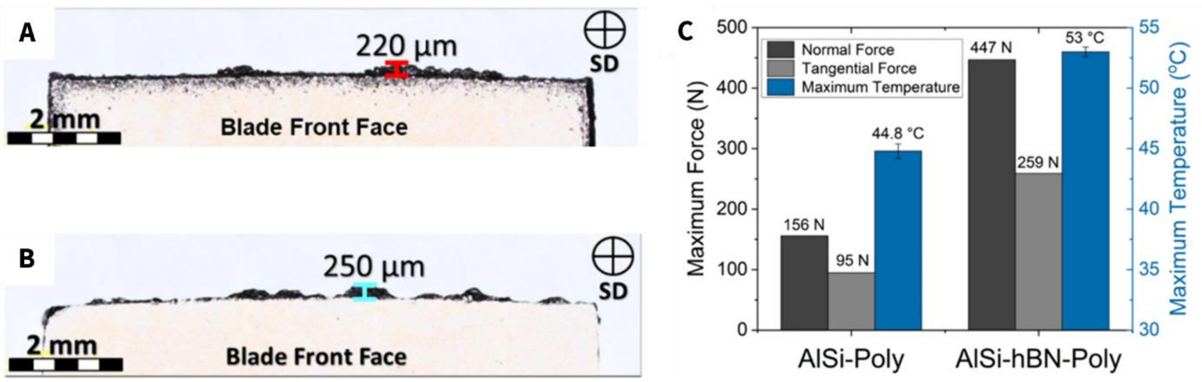

Figure 7.6 – Blade profile images collected for M601 (A), XPT268 (B) after a 50m/s, 50µm/s test with force and temperature results provided in C (44)

This chapter looks to apply the adhesion criteria developed previously in this thesis to M320 and XPT268, AlSi based abradables with wear performance which differs from that of M601. This will demonstrate if these criteria are specific to M601, and to identify any knowledge gaps which require further research to fully explain the adhesion performance of AlSi abradable systems in general.

7.2 Method

The abradability of M320 at high incursion rates (0.2 – 2µm/pass) is well understood, with efficient cutting leading to minimal adhesion formation. However, at low incursion rates (0.02µm/pass) the wear is more variable with both adhesions and wear occurring depending on the hardness. In this chapter 0.02µm/pass tests will be run on the Low-Speed spindle test rig with M320 of varying hardnesses. The in-situ thermal and blade profile monitoring tools developed in Chapter 4 being used to observe the wear, allowing the results to be compared back to the adhesion criteria developed.

In Chapter 6 it was seen that the adhesion behaviour of M601 at low incursion rates (0.02µm/pass) was also impacted by the abradable bulk temperature using a heater block. This heater block was also used in this study to produce a wider range of results.

The hardnesses and backplate temperatures are selected to match those used with M601 in Chapter 6, this allows for direct comparison between results. Data was also collected for XPT268 at the same conditions, allowing for comparison with M601.

Table 7.1 – Test matrix for tests to determine the impact of bulk temperature on the wear of M320 and XPT268

Material	Hardness (HR15y)	Backplate Temperature (°C)	Number of Tests	Tests with Blade Profile Monitoring
M320	50.8 - Soft	100	1	1
		200	2	1
		300	1	1
	62 - Medium	100	1	1
		200	1	1
		300	1	1
	74.3 - Hard	100	1	1
		200	1	1
		300	1	1
XPT268	51.1 - Soft	100	1	1
		200	1	1
		300	1	1
	63.2 - Medium	100	1	1
		200	1	1
		300	1	1
	75.6 - Hard	100	1	1
		200	2	1
		300	1	1

Table 7.1 shows the test matrix completed in this study. For each condition, a single test has been completed, with repeats only completed for tests which suffered hardware issues with the front facing camera – resulting in force and temperature measurements, but no blade profile monitoring.

Repeats have not been included in this work, as this is a qualitative study taking a detailed look within individual tests, identifying wear events, and applying the adhesion criteria developed in this thesis. As this study is applying the in-situ measurement tools to investigate individual adhesion events each single test contains multiple opportunities for data to be extracted.

Tests in this study have been completed with abradable samples made to the geometry, and in the manner described in section 3.2 with grade 5 titanium blades. Similarly employed, the heater block was operated as described in section 6.2.1, with the tests started when the abradable surface reached the temperatures defined in Table 6.1. All tests were completed with a blade tip speed of 200m/s to a depth of 1500µm to allow for direct comparison with the results from Chapter 6.

Data from these tests were extracted and processed into rub maps to allow for easy visualisation of how the wear develops. Further tools produced during this thesis, such as the monitoring the time phasing of the force, blade and abradable temperatures, as well as the monitoring of blade wear and adhesion formation were used to understand how the wear developed and related back to the proposed adhesion criteria.

7.3 Results

The data collected in this study has been processed to extract the forces, temperatures, and blade profiles. These have been used to create a set of rub maps for each material. The blade and abradable post-test have also been imaged to observe any differences in the wear scars.

7.3.1 The Impact of Bulk Temperature on M320

While M601 exhibits a periodic force response, the force response of M320 is less uniform comprising of periods of progressive and cyclic loading. An example of this is shown in Figure 7.7 where examples of each loading type are highlighted.

The periodic behaviour of M601 is due to the uniform heat distribution across the surface, which leads to large scale adhesion and wear events. The periods of progressive loading indicate that the wear over that period is not uniform across the blade, relating to the findings of Fois et al. that the hBN clumps lead to local hotspots (76).

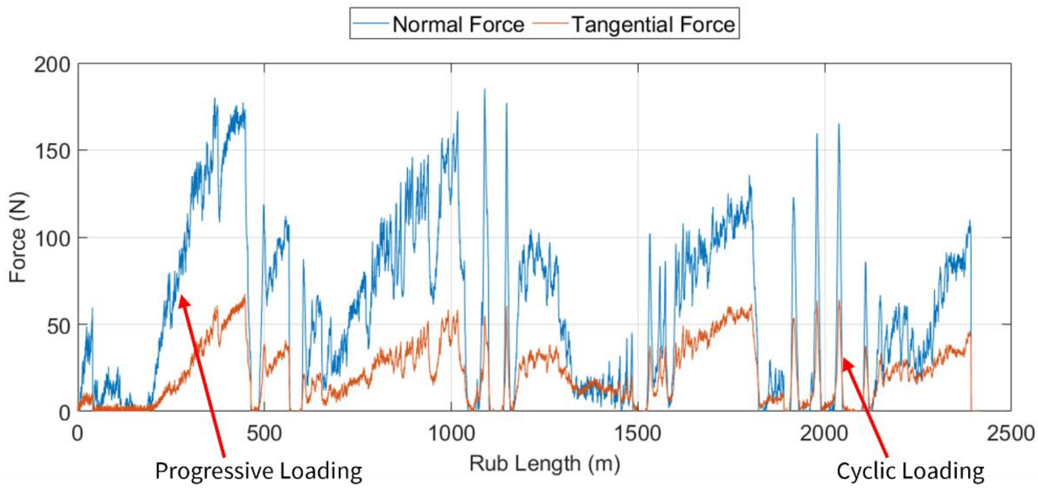

Figure 7.7 – Example of the force response for a Soft (50.8HR15y) M320 test with a 200°C backplate

As the forces are not periodic, the average peak extraction methods applied to the force data for M601 in Chapter 6 cannot be used. Instead, the maximum force value has been extracted, with the results plotted in Figure 7.8. As the effect of backplate temperature is expected to be less than the impact of hardness, the plot shows the trend of hardness on normal force, with the error bars showing the impact of backplate temperature.

While the hard samples produced higher normal forces than the soft samples, the medium hardness samples see a reduction in the normal load. The spread of data with temperature is also largest at the highest hardness, indicating that backplate temperature has the biggest contribution when the abradable is in this state.

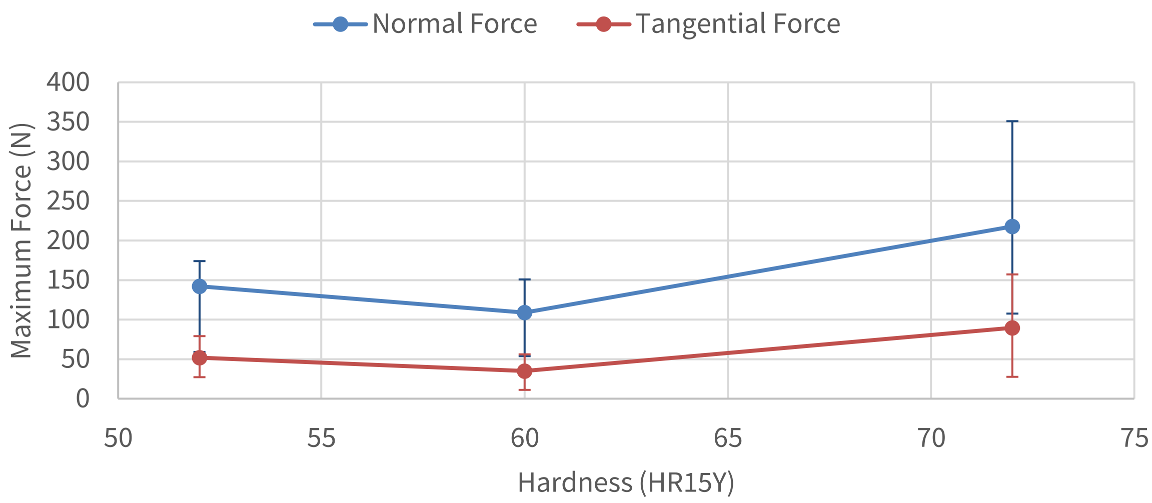

Figure 7.8 – Trend of maximum forces for M320 samples with varying hardnesses for all backplate temperatures combined

From existing literature, it was expected that for a soft abradable sample the blade would have worn, while for a hard sample adhesions would form. From the post-test images shown in Figure 7.13 the opposite behaviour has occurred for these tests with elevated bulk temperatures.

For the soft abradable samples, the blades all show evidence of adhesion formation, with limited blade wear – even though there is significant decolouration on the tips, showing that they reached elevated temperatures during the rub (Figure 7.9). From the rub maps shown in Figure 7.14 these adhesions are seen to form throughout the test, with the higher temperature sample producing the largest adhesions (brightest yellow on the rub maps). Pitting is also visible on the abradable surface, evidence of pull out from the surface (Figure 7.10).

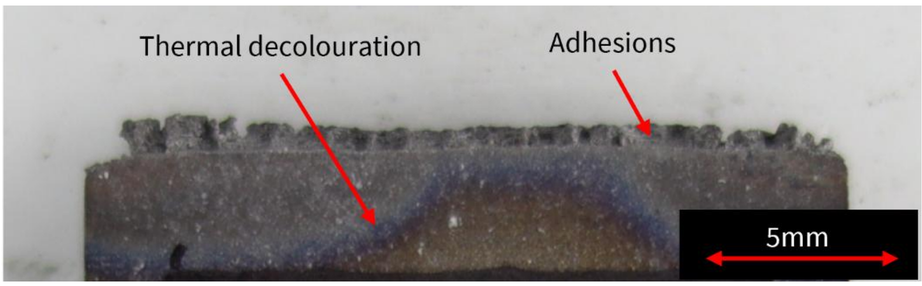

Figure 7.9 – Image of blade after a M320 50.8HR15y, 0.02µm/pass test with a 100°C backplate

The post-test images of the medium hardness samples show rougher abradable surfaces, evidence of mixed modal wear (Figure 7.11). The blade images also show localised regions of wear, but few adhesions are visible on the post-test blades. The rub maps however show that large adhesions formed on the tip for all backplate temperatures, but these adhesions all fractured before the end of the test.

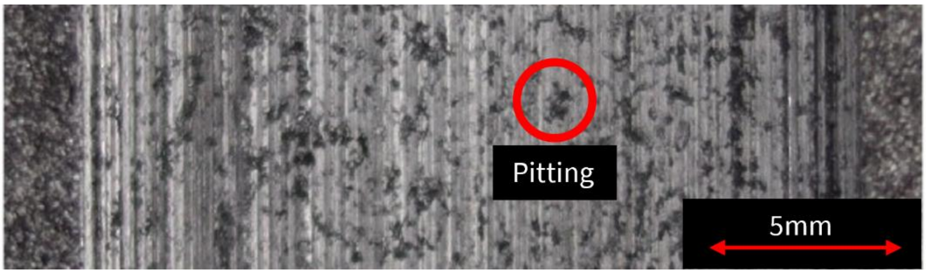

Figure 7.10 – Section of M320 50.8HR15y rub track showing pitting after 0.02µm/pass test with a 100°C backplate

Figure 7.11 – Image of mixed modal wear on a blade tested against M320 62HR15y, 0.02µm/pass with 200°C backplate

The hard abradable samples show the largest variation with backplate temperature, with the tests at 100°C and 200°C showing a mixture of adhesion formation and smearing (Figure 7.12), while the 300°C test produced significant blade damage with titanium transfer to the abradable surface.

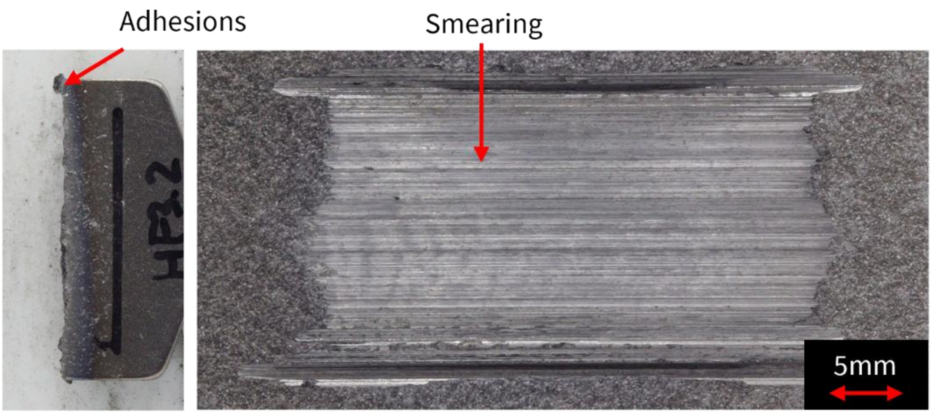

Figure 7.12 – Image of blade and M320 74.3HR15y abradable after a 0.02µm/pass test with a 200°C backplate

It should be noted that, although the target test depth was 1500µm, the actual test depth can vary by ±200µm due to the tolerance in the initial position zeroing process during setup. As this study is looking primarily at data collected during the test, rather than just the post-test images, the variations in rub depth do not impact these results. This variation can be seen in the rub maps as variations in maximum rub length.

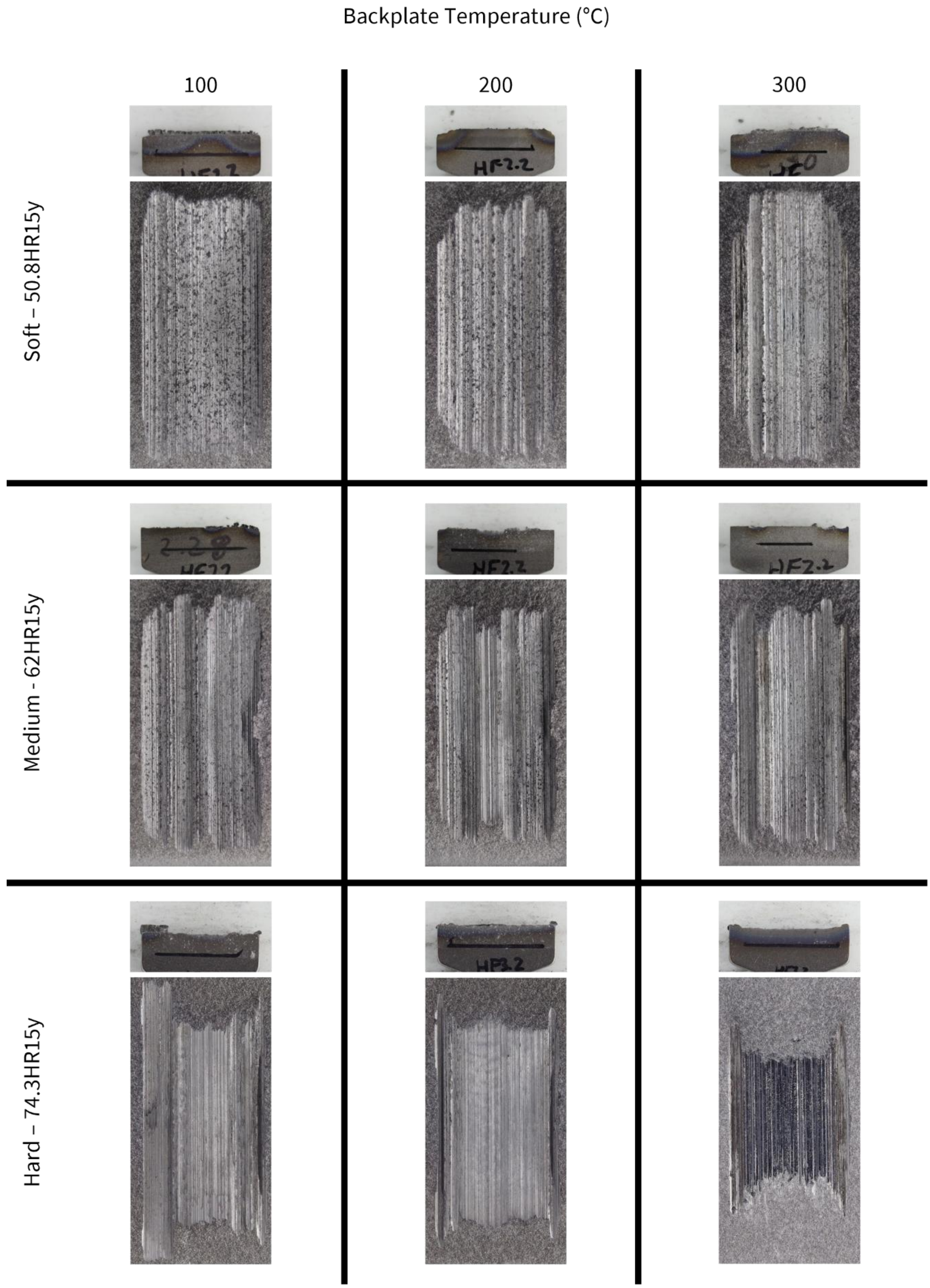

Figure 7.13 – Images of the wear track and blade profiles of M320 samples with varying hardnesses and temperature

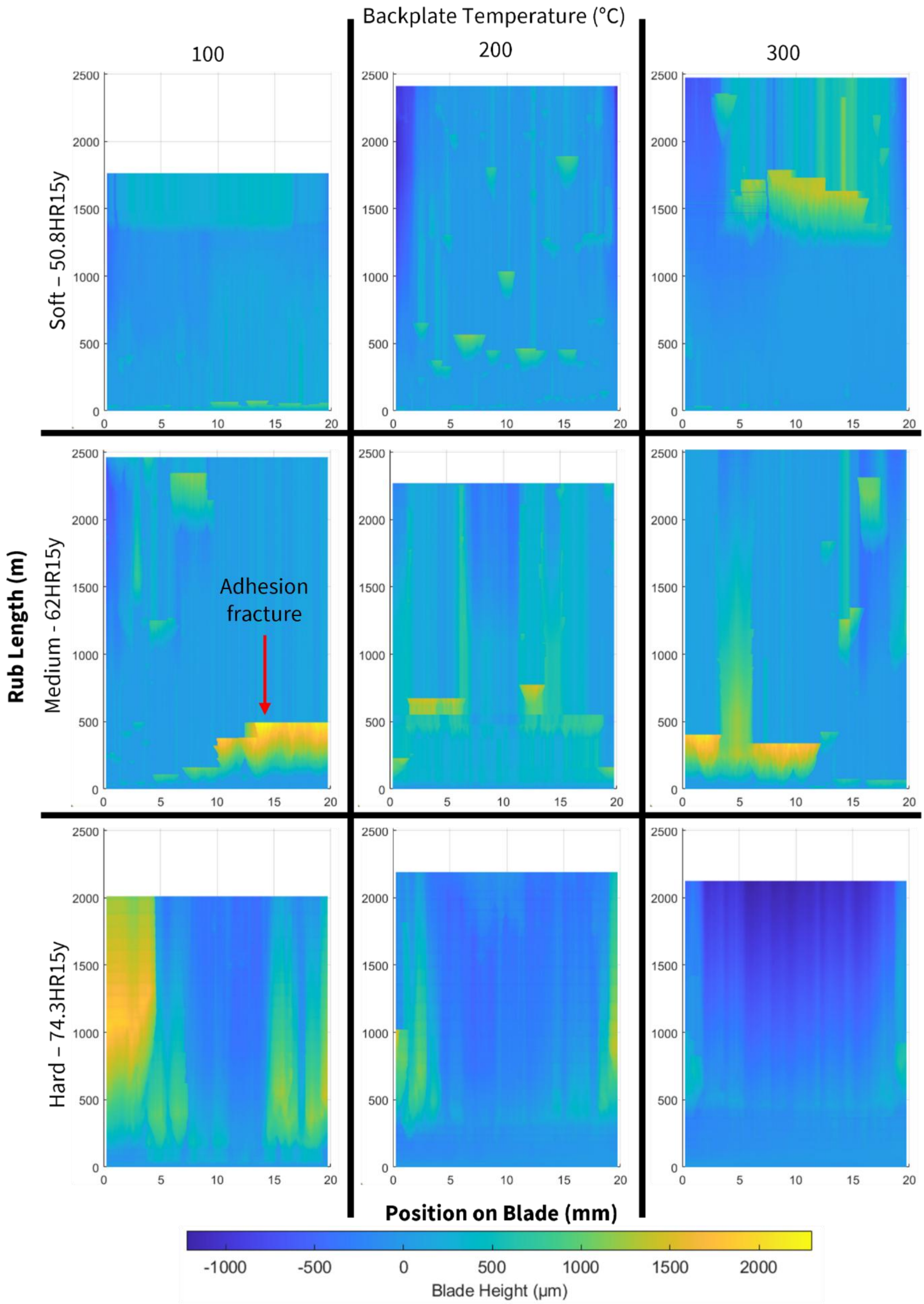

Figure 7.14 – Rub maps from M320 samples with varying hardnesses and temperatures

7.3.2 The Impact of Bulk Temperature on XPT268

As XPT268 is a new material there is no published work on how its abradability is impacted by its hardness. However, from the microstructure images (Figure 7.3), XPT268 closely resembles M601, with the additional hBN being well distributed throughout the abradable. With the uniform microstructure it would be expected that the wear across the abradable surface would be more consistent. This can be seen in the force response of the material which, like M601, shows a periodic response (Figure 7.15), symbolic of large-scale wear events.

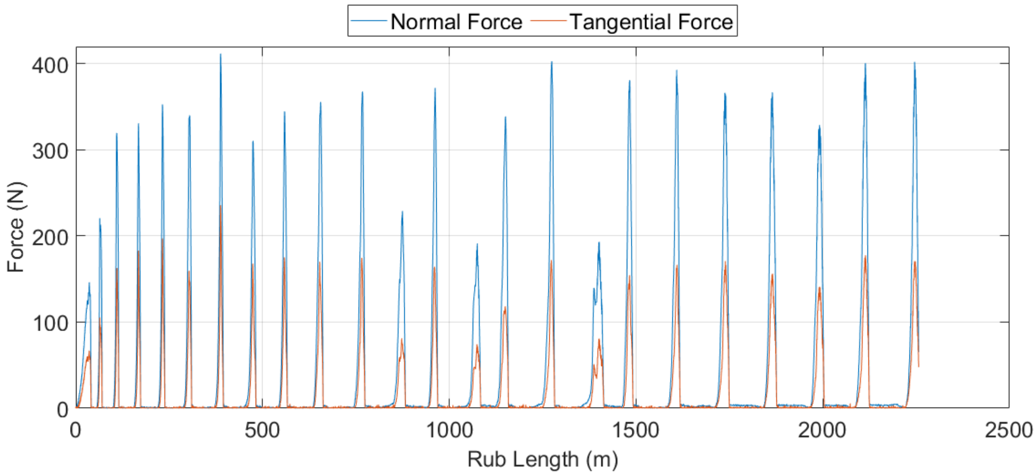

Figure 7.15 – Example of the force response from a hard (75.6HR15y) XPT268 sample at 200°C

With a periodic force response the average peak extraction method applied in Chapter 6 can be applied, with the results shown in Figure 7.16. From this data a linear relationship can be seen between hardness and peak forces, with the impact of bulk temperature (the error bars) increasing with hardness.

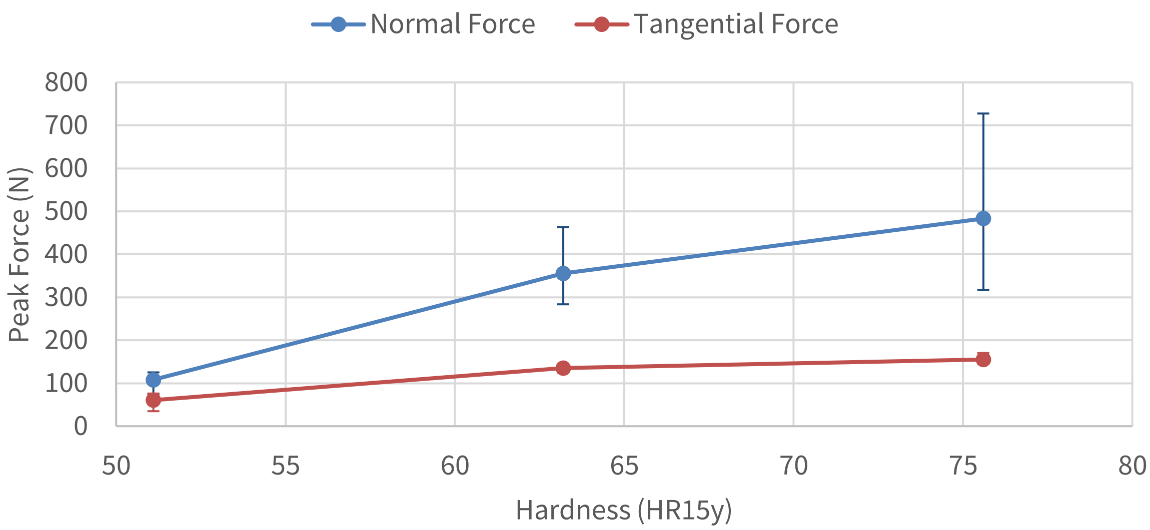

Figure 7.16 – Trend of peak forces for XPT268 tests with varying hardnesses for all backplate temperatures combined

In general, XPT268 demonstrates good abradability at these test conditions, but the wear does show a dependence on the hardness of the coating.

For the soft samples, the images in Figure 7.18 show minor damage to the blades, with the abradable showing a scored surface. From the rub maps in Figure 7.19 this scoring can be seen to be due to a cycle of adhesions growing (appearing as yellow on the rub map) and then fracturing (returning to green) which occurs for the full test duration. As the backplate temperatures increase there is not a notable change in the behaviour observed.

With the medium hardness samples there is evidence of more blade wear (appearing as blue on the rub maps), primarily visible at the corners of the blades. The abradable does have less scoring, with a more uniform profile and from the rub maps it can be seen that adhesions are forming more uniformly across the blade (large regions of yellow). The increase in adhesions is accompanied by visible pitting on the surface, highlighting potential pullout (Figure 7.17). The quantity of these adhesions also increases with the backplate temperature (larger, brighter regions of yellow).

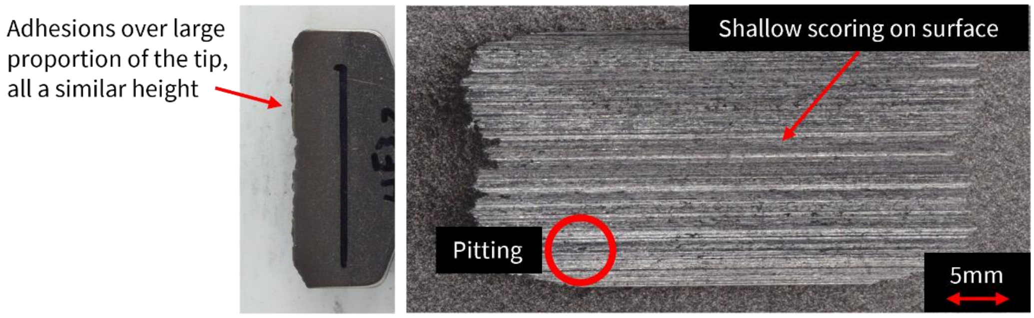

Figure 7.17 – Image of blade and XPT268 63.2HR15y abradable after a 0.02µm/pass test with a 200°C backplate

Moving to the hard samples there is a notable transition away from primarily adhesion formation to blade wear (large regions of blue on the rub maps). This behaviour is however highly dependent on backplate temperature, with the higher temperature samples showing an increase in adhesion formation (increasing amounts of green and yellow) on the rub maps and an equivalent reduction in blade wear (less blue).

The wear observed for XPT268 shares many similarities with that seen for M601, with the grooved abradable surface, and the transition to blade wear at high hardnesses. However, there are some key differences between the responses of each material.

M601 sees a reduction in the peak normal force when the hardness increases from soft to medium samples, this was explained as due to the transition from the polyester phase to the metal phase as the key contributor to the mechanical properties. For XPT268 the force and adhesions quantities increase linearly with hardness from soft to medium samples.

The wear response of M601 in a hard state was also highly variable, with changes in the test setup at high backplate temperatures leading to significant changes in the wear rates. The XPT268 results have produced a steadier trend, with increasing temperatures producing more adhesions and less blade wear. These results are however limited to a single test in each condition.

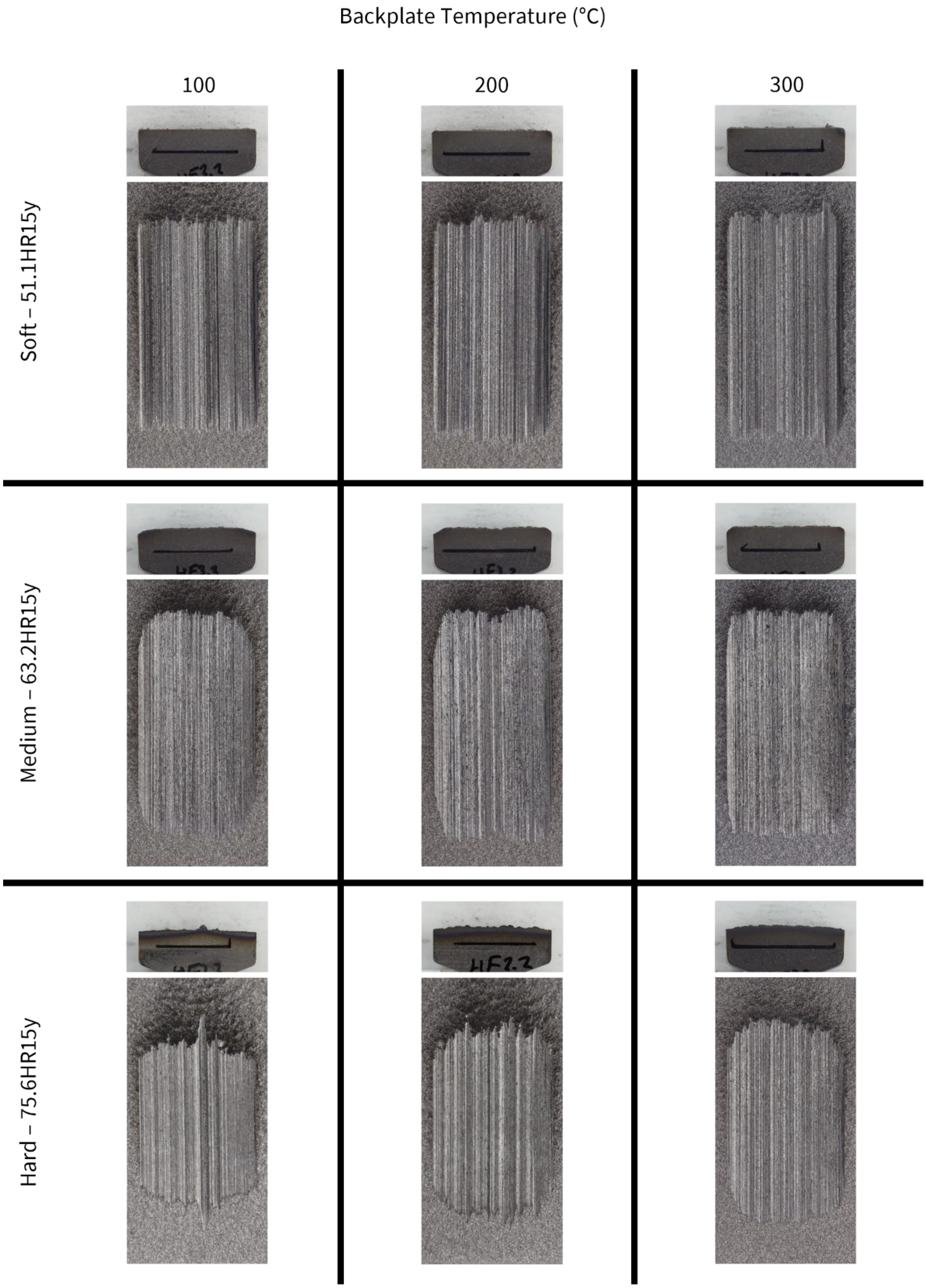

Figure 7.18 – Images of the wear track and blade profiles of XPT268 samples with varying hardness and temperatures

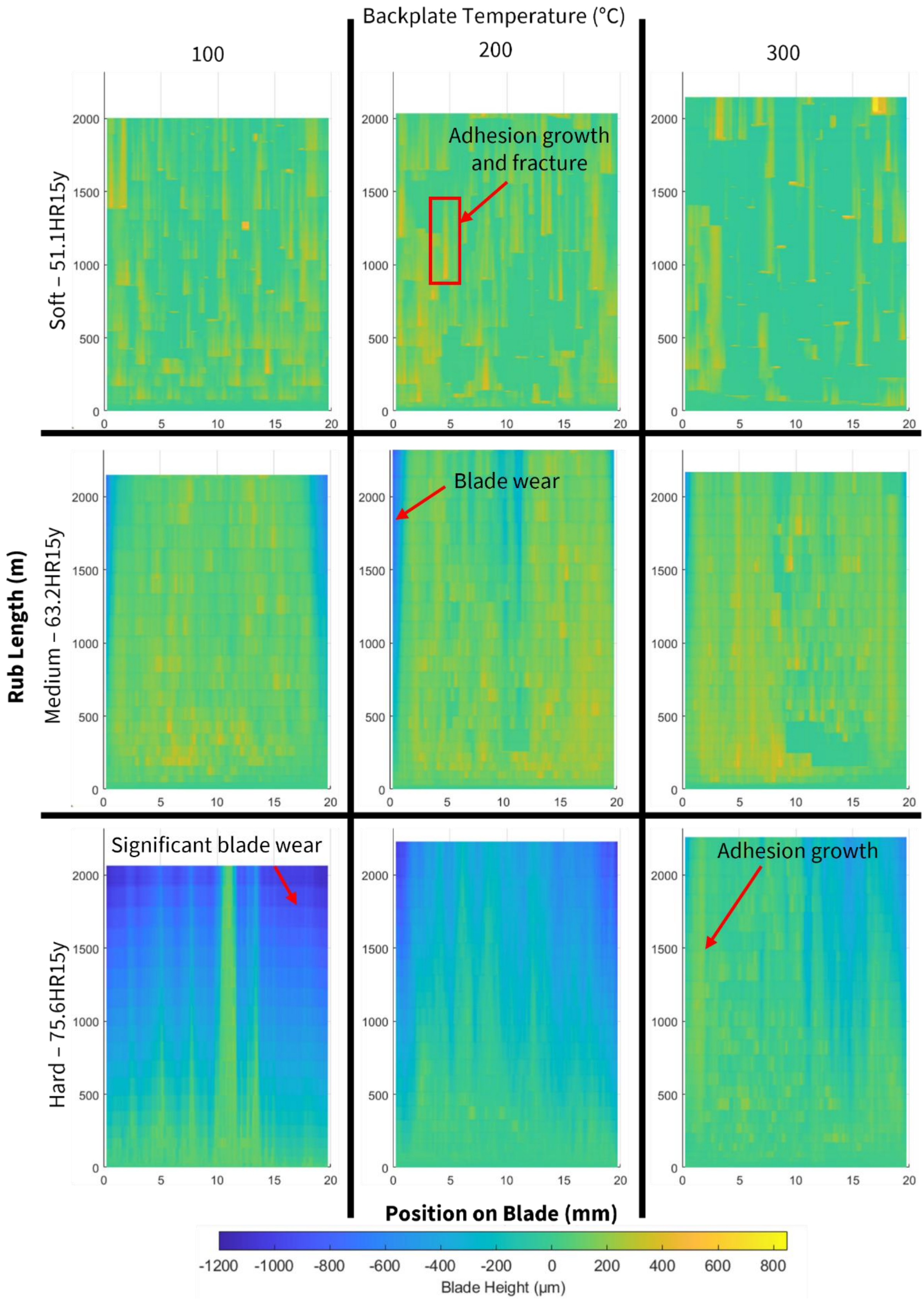

Figure 7.19 – Rub maps from XPT268 samples with varying hardness and temperatures

7.4 Discussion

The results for both M320 and XPT268 demonstrate that the hardness and the backplate temperature of the sample impacts the wear response during a test. Additionally, the wear response of M320 at the elevated temperatures does not align with test results completed at room temperature where blade wear was previously reported.

By further analysing the blade profile and temperature data collected during these tests the adhesion criteria can be applied to explain the results observed.

7.4.1 Analysis of Results from M320 Bulk Temperature Testing

Fois et al. completed tests on M320 samples of 55HR15Y at 0.02µm/pass and observed significant blade wear, while samples with a hardness of 73HR15Y produced adhesions. They proposed that this was due to the larger, more numerous hBN clumps in the soft samples leading to surface hotspots.

While it must be taken into consideration that the samples sprayed within their testing, although of the same hardness, may have had a different distribution of hBN, the conclusion that the hotspots alone lead to blade wear does not align with the results seen in this work. In this study samples with a hardness of 50.8HR15Y, held at elevated temperatures produced more adhesions and did not wear, while the samples at higher hardnesses did. There is however evidence in this work that hotspots caused by hBN do contribute to the wear mechanisms.

This discussion works though each material hardness, extracting the force, temperature, and blade profile data at key wear events to explain what wear has occurred, and provides justification for why these results differ from previous testing.

7.4.1.1 The Impact of Bulk Temperature on Low Hardness M320

To visualise the wear which has occurred during the rub the tools developed in Chapter 4 have been applied, allowing the force data to be aligned with the blade temperature, abradable temperature and blade height at a single point on the blade. From this data is possible to see the time phasing of the data, getting a better idea of the causality of the wear events.

Figure 7.20 shows how the forces (B) vary during a test at 100°C with a soft abradable sample. The temperatures and blade height have also been plotted (C), extracted along the red dashed line shown on the rub map (A).

From this data three distinct regions within the rub can be identified, and have been marked on Figure 7.20C.

After first contact with the abradable there is an initial period of adhesion formation. This is due to the entire blade width contacting the abradable at once, producing large normal forces. There will also be a contribution due to the roughness of the surface leading to local regions of high pressure, aligning with work completed by Khan et al. who showed how wear rates are higher against rougher surfaces (118). Before this interaction, the blade is also cold, while the abradable is at an elevated starting temperature meaning adhesion formation is more likely to occur than blade wear.

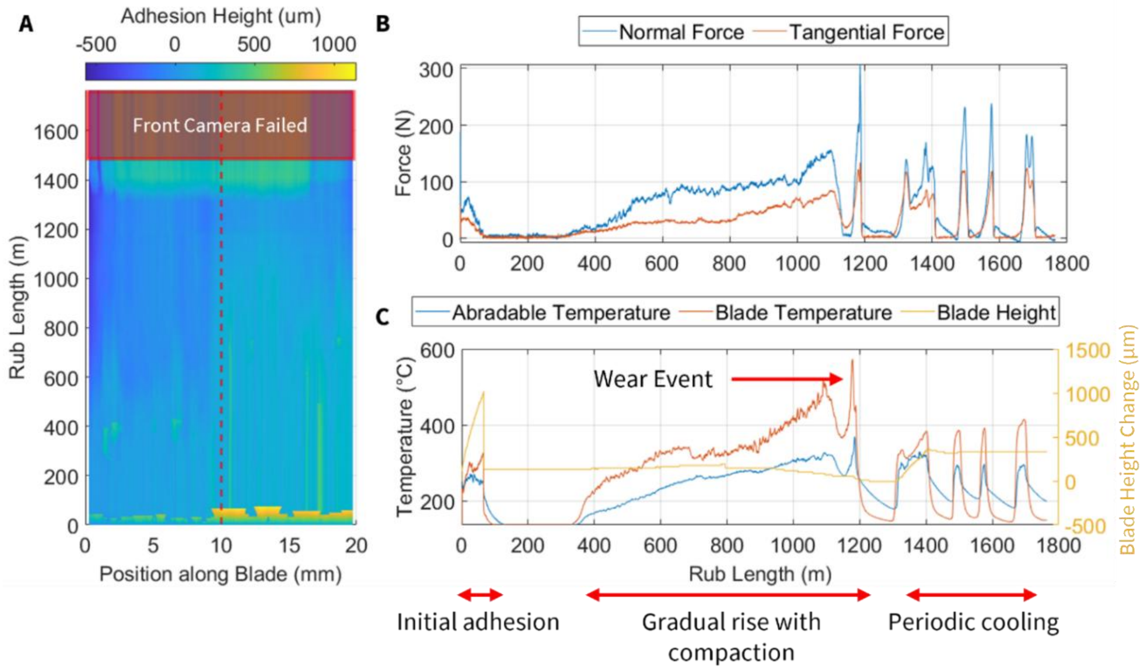

Figure 7.20 – For a 51.1HR15Y M320 test at 100°C: **B –** The force plots. **A –** The rub map, with a data line highlighted. **C –** The temperatures and blade height along the data line

These initial adhesions fracture from the surface, but as the adhesions did not grow uniformly the abradable surface will be stepped. This produces a more gradual rise in the normal loads during the second contact as the contacting area between the blade and abradable gradually rises. The abradable surface will also compact, further increasing the normal load (as demonstrated by Fois et al. (78) in Figure 7.1). With the gradual increase in the forces both the blade and abradable can be seen to increase in temperature, with the rate of increase of blade temperature exceeding that of the abradable. At a rub length of ~800m the elevated forces and blade temperatures result in the adhesions present on the blade beginning to wear.

At a rub length of ~1200m a significant wear event occurred leading to a rapid drop in the blade height. Although, it is not clear from this data the exact mechanism for this event the result was a sudden drop in the normal load, allowing both the blade and abradable to cool. From the temperature data recorded it can be seen that the rate of cooling of the blade exceeded that of the abradable, meaning that during the next contact the abradable was at a higher base temperature and alongside the high normal forces was able to form adhesion more readily, protecting the blade from further wear.

If the reduced cooling rate of the abradable during the periodic cooling rate did in fact lead to the formation of further adhesions, rather than blade wear, it would be expected that at elevated back plate temperatures this effect would be more pronounced. To investigate this the force, temperature, and blade profile data for point halfway along the blade have been extracted for a test with a soft abradable a 300°C. This data is shown in Figure 7.21.

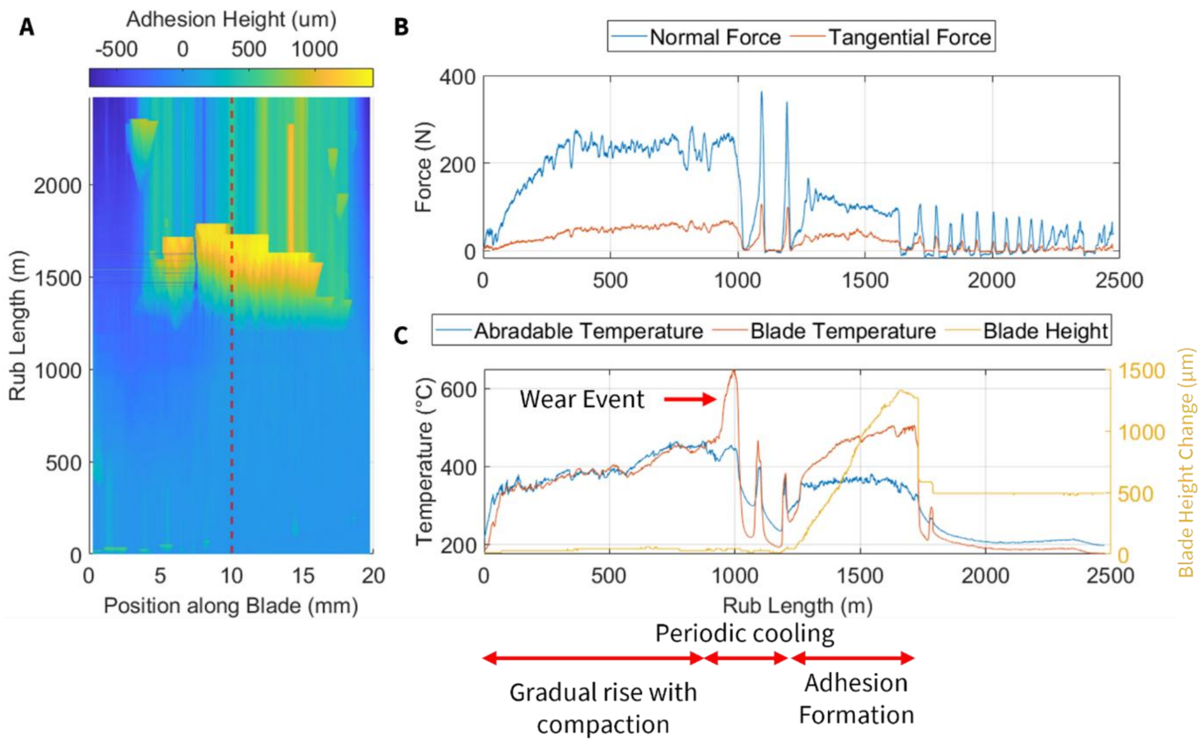

Figure 7.21 – For a 51.1HR15Y M320 test at 300°C: **B –** The force plots. **A –** The rub map, with a data line highlighted. **C –** The temperatures and blade height along the data line

For this test, the initial rate of force application was lower, potentially due to the increased ductility of AlSi at elevated temperatures. The more gradual force application rate meant that the adhesions did not form during the initial contact, but instead the abradable began to compact, as also seen by Fois et al. (76) and Zhang et al. (75), leading to a gradual increase in force. Unlike the test at 100°C the abradable and blade temperatures increased at the same rate, showing that the abradable was unable to conduct heat away from the surface as well as it could previously. With the blade and the abradable heating together, instead of blade wear occurring, adhesions began to form on the surface - protecting the blade. This can be seen from the blade height change data in Figure 7.21C which shows a steady increase in the blade height from 0 to 100µm over the first 1000m of rub.

At a rub length of ~1000m there is a further large-scale wear event. This event was visible on the front camera and spark camera, with significant sparking and glowing of on the blade tip. The result was a sudden drop in normal loads, allowing the blade and abradable to cool.

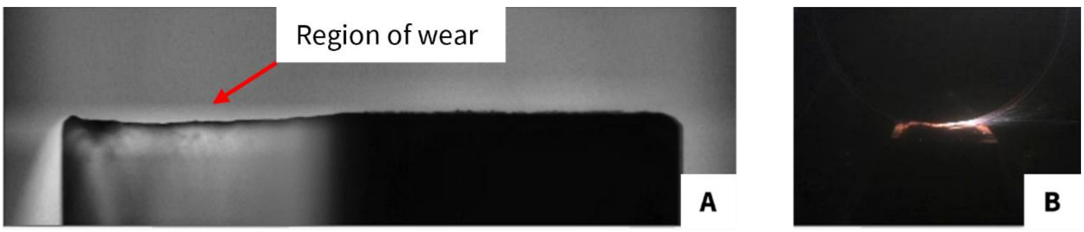

Figure 7.22 – Footage captured of the blade front (A) and sparks (B) during a sudden wear event highlighted in Figure 7.21

Once again, the blade was able to cool faster than the abradable meaning that in subsequent contact the abradable, at elevated temperature and under sufficient loading was able to form adhesions. In the case of this test the adhesions rapidly grew to a height of ~1.3mm, outpacing the incursion rate.

From these results it becomes apparent that with the low hardness samples the rate of increase of the normal loads due to compaction is sufficiently low that the abradable can efficiently dissipate the thermal energy. With the addition of the heater block the abradable could not conduct as much heat away from the surface, meaning adhesions formed more readily.

In the case of the testing by Fois et al. the abradable backplate was uncontrolled, allowing for heat to conduct through. This meant that as the load increases the blade will heat faster than the abradable and, as can be seen between 800 – 1200m in Figure 7.20C, the blade will wear.

7.4.1.2 The Impact of Bulk Temperature on Medium Hardness M320

Following the argument that the low loads created by the soft abradable generated heat at a rate manageable by the abradable, it would be expected for a harder abradable to produce higher forces and hence more heat.

Although the maximum test forces displayed in Figure 7.8 show a reduction in force going from soft to medium hardness, the force plot in Figure 7.23B shows the initial forces for a 100°C medium hardness test increasing at a high rate. With the high load application rate adhesions can be seen to form rapidly, at a rate far exceeding the incursion rate.

The adhesion which formed during this test is shown in Figure 7.24A and was more than 2mm tall. When this adhesion fractured the region of blade revealed never regained contact with the abradable, reducing the contact area – and normal load – for the rest of the test.

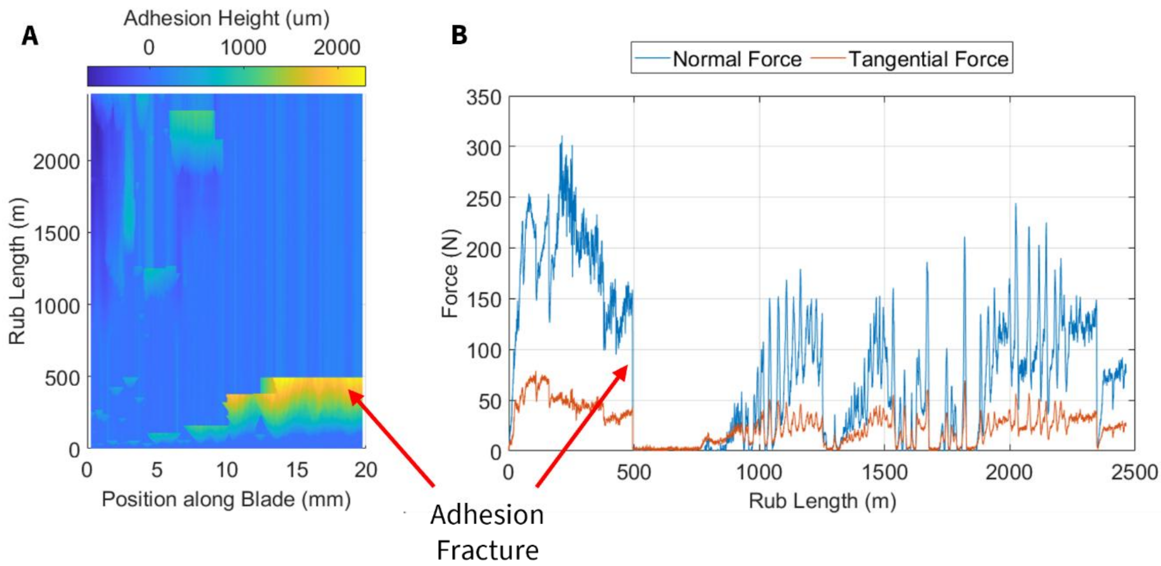

Figure 7.23 – For a 63.2HR15Y M320 test at 100°C: **B –** The force plots. **A –** The rub map, with the adhesion fracture event highlighted

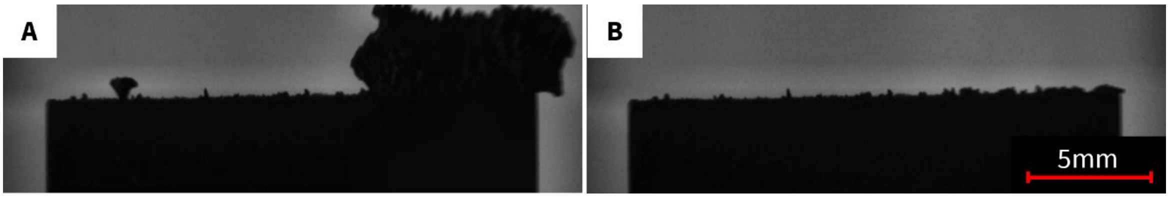

Figure 7.24 – Blade front images captured just before (A) and after (B) the adhesion fracture event highlighted in Figure 7.23

The rapid force application leads to an increase in the abradable temperature as the heat flux due to conduction is not sufficient to remove the energy. With high loads and abradable temperatures, the formation of adhesions is more likely. However, the size and robustness of the adhesions formed with M320 far exceeds that seen with M601 under similar conditions. From the data collected in this study it is not possible to determine why M320 adhesions are so much larger. To fully understand this behaviour further research would be required.

7.4.1.3 The Impact of Bulk Temperature on High Hardness M320

With the increasing hardness of the abradable the maximum normal loads are seen to increase, which should increase the possibility of adhesion formation. However, alongside the increase in normal loads, the thermal conductivity of the abradable also increases, improving the ability of the abradable to manage that excess heat and acting against adhesion formation. This results in a mixed modal wear response, an example of this can be seen in the rub map for a test at 100°C with a hard sample in Figure 7.25A .

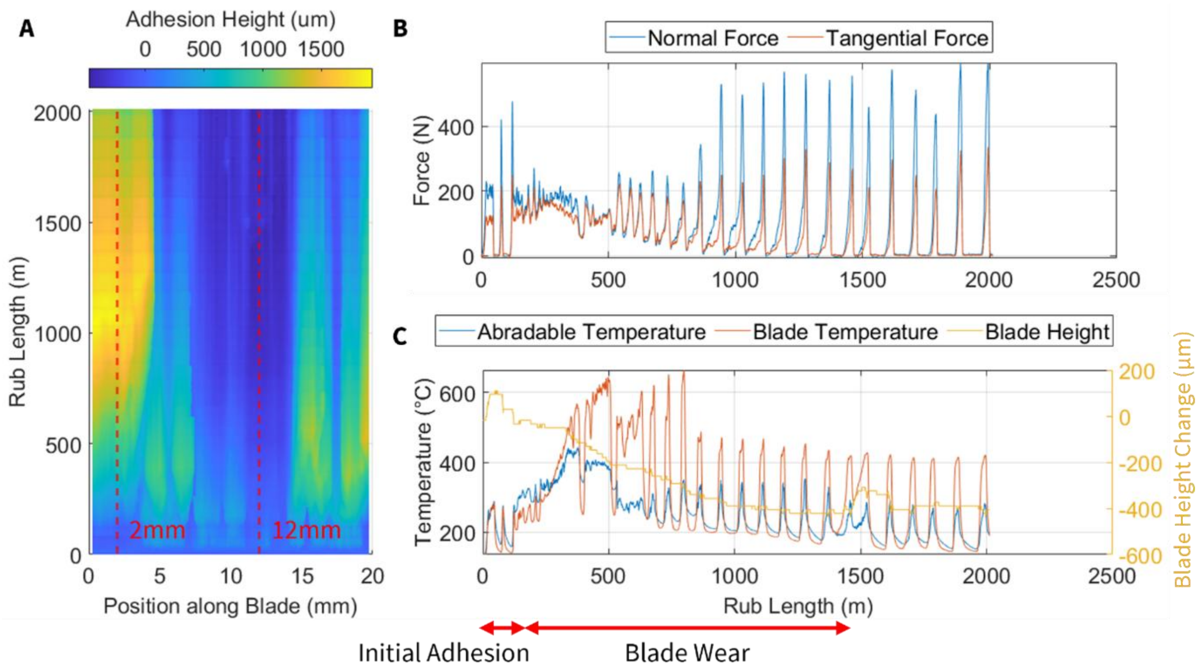

Figure 7.25 – For a 75.6HR15Y M320 test at 100°C: **B –** The force plots. **A –** The rub map, with two data lines highlighted. **C –** The temperatures and blade height along the 12mm data line

On this rub map two data lines have been highlighted, one at 2mm which shows large adhesion growth and a second at 12mm, a point which underwent blade wear.

From the force plot in Figure 7.25B there is an initial high force peak, aligning with early adhesions forming along the 12mm line. The temperatures and blade height at this point are shown in Figure 7.25C, and while adhesions can be seen to form early in the test, beyond this the rate of increase in blade temperature outpaces the abradable temperature, leading to blade wear.

Along the 2mm line however the temperature and blade profiles (Figure 7.26) are very different, this is mostly likely due to a hotspot caused by a hBN clump as modelled by Fois et al. (76). At this position there is a high rate of temperature increase, leading to adhesion formation. Between 100 – 300m the temperature of both blade and abradable climb at the same rate, resulting in a constant rate of adhesion growth (Rate 1). Between 300 – 1000m the blade temperature remains steady, but the abradable begins to cool. This could be a result of the hBN clump being cleared and leads to the temperature difference between the blade and abradable increasing. The reduction in abradable temperature is accompanied by a reduction in the rate of adhesion growth (Rate 2), further highlighting the relationship between abradable temperature and adhesion formation.

By 1000m the adhesion has grown to ~1.8mm, and the abradable has moved up by ~0.75mm meaning that the abradable thickness at this point will be less than 0.5mm. The thermal resistance to the backplate will therefore be much lower than at the start of the test, as shown in Chapter 5. This results in a steady reduction in the temperature of the abradable, as more energy can be conducted to the backplate. As the abradable begins to cool the adhesions begin to wear.

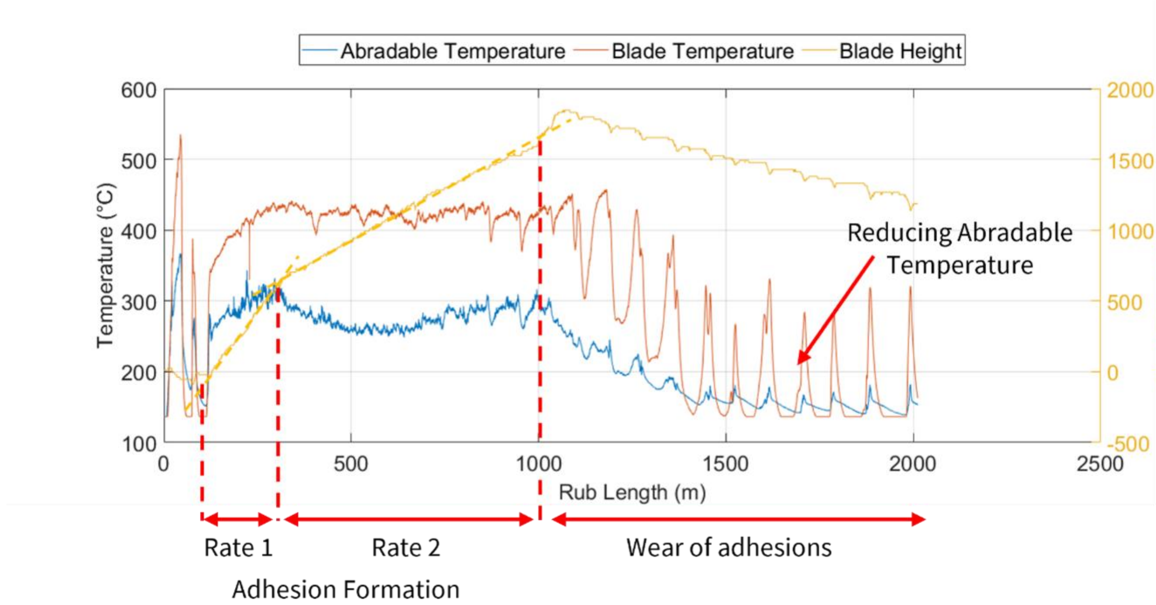

Figure 7.26 – The temperatures and blade profile data extracted along the 2mm data line highlighted in Figure 7.25A

Whilst combining these results with those of Fois et al. suggests that at low backplate temperatures the clumps of hBN result in local hotspots and create adhesion favourable conditions. At higher backplate temperatures these conditions should be less reliant on hBN clumps, as conduction through the abradable is no longer a viable method of cooling.

In the rub map created for a hard abradable tested at 300°C (Figure 7.27A), this is shown to be true, with uniform wear performance across the entire surface. However, the uniform wear across the surface also results in a periodic force response (Figure 7.27B).

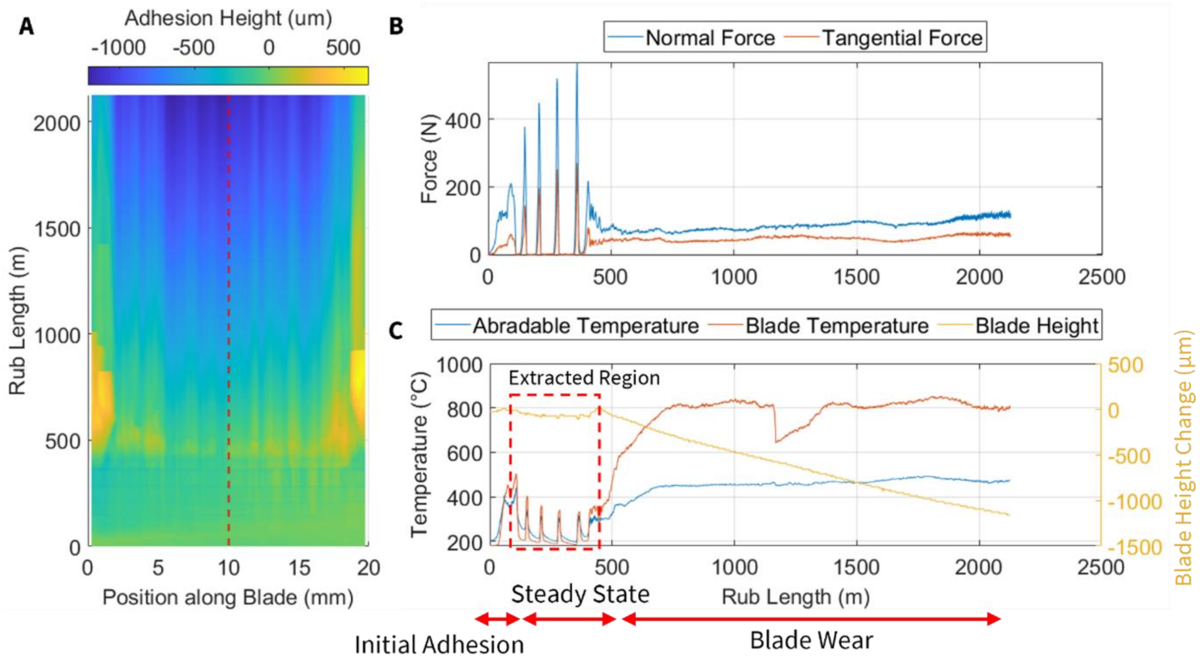

Figure 7.27 – For a 75.6HR15Y M320 test at 300°C: **B –** The force plots. **A –** The rub map, with a data line highlighted. **C –** The temperatures and blade height along the data line

With the periodic forces, the temperatures of the blade and the abradable also enter a cyclic pattern, leading to a steady state of blade wear and adhesion growth. In Figure 7.28 the temperatures and blade profile extracted from the highlighted region in Figure 7.27C are shown. These plots show how in the steady state region as the blade heats faster than the abradable blade wear occurs, but as the temperatures decrease the blade stays hotter for longer, allowing for adhesions to form as the blade has now cooled and resists the wear. During this time there is limited change in the blade height.

At 400m the period between contacts reduces, meaning that the abradable is still hot from the previous rub and adhesions form, rather than the wear seen during steady state. With the uniform surface temperature these adhesions form across the entire blade width, and result in increased contact time between the blade and abradable over a large contact area. The rapid increase in blade temperature leads to a shift in the wear mechanism to steady blade wear, with a reduction in normal loads as the abradable is no longer being compacted.

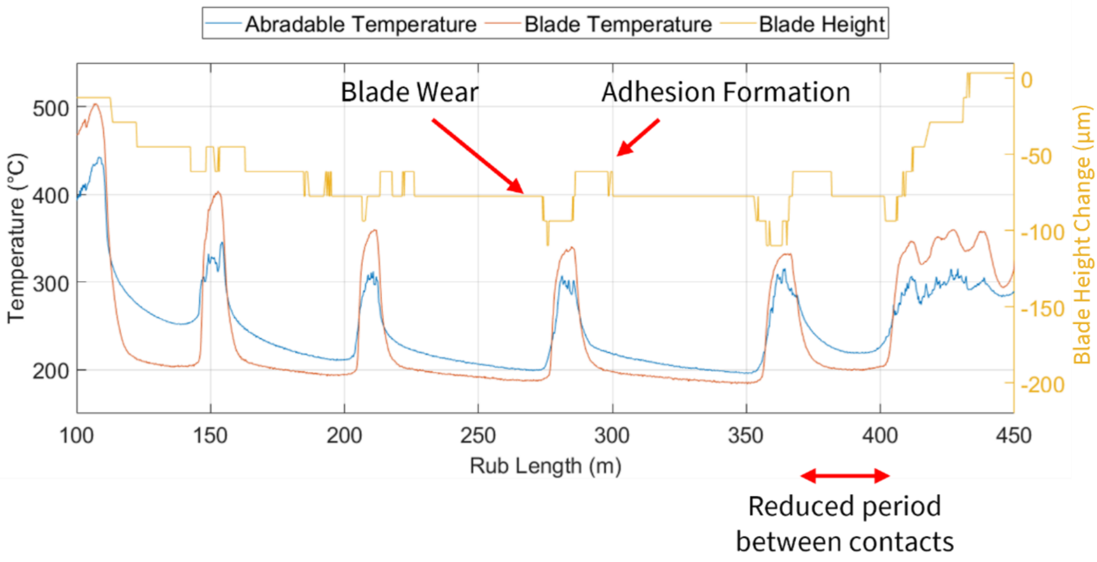

Figure 7.28 – The temperature and blade profile data from the extracted region in Figure 7.27C

With a high backplate temperature the wear across the surface becomes increasingly uniform, as without conduction as a mechanism for heat removal the clusters of hBN have less of an impact. But for tests with an uncontrolled backplate temperature, such as those completed by Fois et al., the wear will become multimodal, with adhesions forming at local hotspots.

The tests completed with M320 as part of this study have shown that, although Fois et al. were correct in predicting hotspots on the abradable surface, the theory that this would lead to blade wear has not aligned with test data. Instead, by applying the adhesion criteria developed in the previous chapters of this thesis the changes in wear with backplate temperature could be explained – with surface hotspots leading to adhesion formation, and effective conduction through the abradable leading to blade wear.

7.4.2 Analysis of Results from XPT268 Bulk Temperature Testing

Due to the lack of published work on XPT268 there are no wear studies or theories to compare to the results collected here. However, as this material is designed to be applied in place of M601, a direct comparison of abradability would provide a novel insight.

The peak normal forces observed during testing with XPT268 increased linearly with hardness, and apart from for the soft abradable, were higher than those seen for M601 (Figure 7.29). This aligns with observations from the microstructure that XPT268 has smaller sized polyester chunks, and more AlSi branches. In M601 the soft sample's mechanical properties are dominated by its polyester phase, with this shifting to the AlSi for harder samples. With more AlSi branches in XPT268 at low hardnesses the dependence on the polyester phase is reduced, explaining why there is not a reduction in normal load between soft and medium abradables.

With higher normal loads more adhesions are also seen to form on the blade, with a comparison of the adhesion volume during two tests of medium hardness XPT268 and M601 at 200°C shown in

Figure 7.30. However, the adhesion rate for XPT268 is also greater than M601 at low hardnesses when the normal loads are similar. This implies that the addition of hBN has aided in the formation of adhesions, potentially leading to hotspots on the surface as seen in M320.

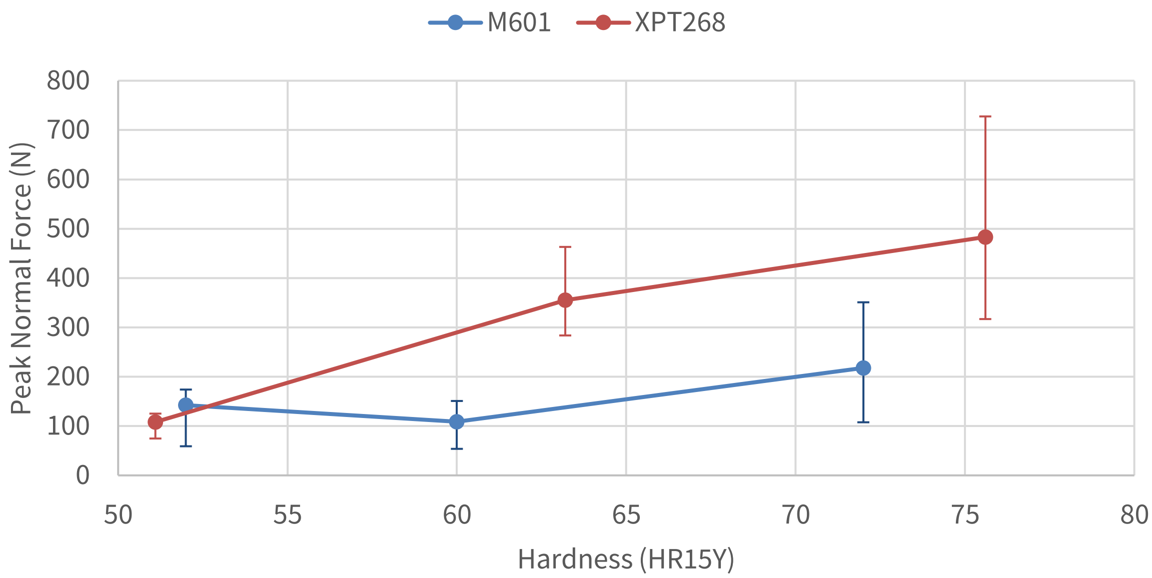

Figure 7.29 – Comparison of the peak normal forces at varying hardnesses between M601 and XPT268 for all backplate temperatures combined

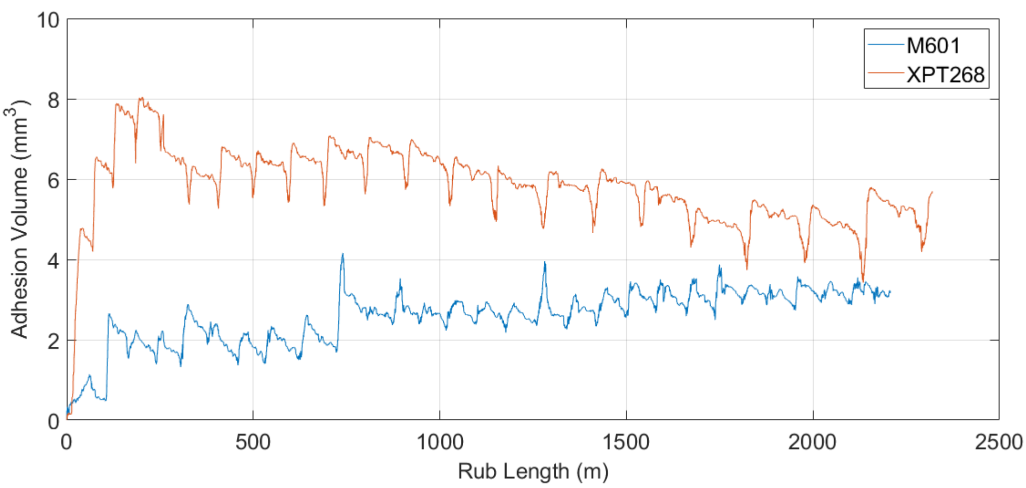

Figure 7.30 – The total volume of adhesions measured during test of 60HR15Y M601 and 63.2HR15Y XPT268 at 200°C

Although it appears that the added hBN has made XPT268 more adhesive than M601, unlike M320 the adhesions which form with XPT268 do not grow at a rate faster than the incursion rate. This allows them to form a protective layer on the blade, without creating large scars in the abradable surface. The potential benefit of this is shown in Table 7.2 which shows the blade wear rates for XPT268 and M601, and the change when moving over to XPT268.

For soft and medium hardness abradables there was a wear reduction across all back plate temperatures. The harder samples did produce more wear at low backplate temperatures, but as temperature increased to 300°C the rate of adhesion formation increased to a level greater than that of the blade wear.

Table 7.2 – The extracted blade wear rates for M601 and XPT268 at varying hardnesses and temperatures

Hardness	Backplate Temperature (°C)	Blade Wear Rate (mm^3/m)		Percentage Change
		XPT268	M601	
Soft (51.1 – 52)	100	0.00037	0.00126	-71%
	200	0.00010	0.00158	-94%
	300	0.00094	0.00157	-40%
Medium (60 – 63.2)	100	0.00126	0.00386	-67%
	200	0.00115	0.00274	-58%
	300	0.00042	0.00280	-85%
Hard (72 – 75.6)	100	0.01624	0.01183	37%
	200	0.00971	0.00939	3%
	300	0.00366	0.01034	-65%

From these results it appears that XPT268 is an improvement over M601 at low incursion rates. However, this goes against initial reports from engine manufacturers that the coating led to significant blade wear against titanium blades. Further work is therefore required to fully understand the behaviour of XPT268 across the full range of incursion rates, as well as further studies to better quantify its fundamental properties such as thermal conductivity and composition as a function of hardness.

Without an understanding of the thermal properties of XPT268 it is not possible to fully apply the adhesion criteria developed in this thesis, but from the data collected during these tests the results to appear to align. As the normal force increases with hardness, and as the backplate temperatures increase the rate of adhesion increases highlighting the importance of both thermal properties and normal force. There is also a cyclic adhesion wear and growth pattern as the blade and abradable heat and cool at different rates, as has been observed with M601 and M320.

7.5 Conclusion

M320 at low incursion rates has previously been shown to cause blade wear at low hardnesses, and mixed mode adhesion and wear at high hardnesses. Testing completed in this study produced differing results.

With the application of the in-situ tools and analysis techniques created in this thesis, the criteria for adhesion formation developed with M601 could be used to explain the differences. The differences in wear were shown to be a function of heat flow rate into the sample and how well the abradable can manage that heat. Increasing the backplate temperature, as with M601, reduced the abradables ability to manage that heat, varying the wear. Following the wear trends with increasing backplate temperatures relate the wear seen in this study with that observed in previous work.

XPT268 when compared to M601 produced higher normal forces, and therefore more adhesions. It was also apparent that the increased adhesion rate was not only a function of normal force, but also as a consequence of adding hBN. The mechanisms behind this require further research.

The behaviour of M320 at low incursion differs significantly from its behaviour at high incursion rates, the mechanisms behind this shift are not well understood. The results collected using the in-situ tools developed here have provided a novel insight into this problem, and through the application of theories developed for M601 the changes in wear with changing hardness and backplate temperature could be explained. This provides confidence that the adhesion criteria can be applied to AlSi abradable systems in general, not just to M601. However, further work to determine the thermal properties of XPT268 should be completed to ensure that the data collected for that coating aligns beyond what can currently be observed.

8 Discussion

With the addition of in-situ thermal-mechanical measurement tools to the Low-Speed rig it is now possible to observe how temperatures and wear develop throughout a test, and how these properties relate to each other.

When these tools were applied to M601 samples at 0.2µm/pass it could be seen that the adhesions aligned with hotspots on the abradable, highlighting a relationship between abradable temperature and adhesion formation. Data analysis techniques were also developed for extracting the time phasing between blade height, temperature and abradable temperature, providing tools to further investigate the causality of adhesion and wear events. From these results it can be observed that adhesion growth occurs alongside increases in abradable temperature, while in instances where the blade heated first the blade would wear before adhesions could form.

These tools also provided better visualisation of the wear behaviour through the temporal and spatial alignment of all data streams in the form of a video – an example frame is shown in Figure 8.1. Viewing data in this form allows for relationships between the different parameters to be observed, for example that peaks in the periodic forces seen during 0.02µm/pass tests align with high blade and abradables temperatures. These tools also provided the insight that adhesion growth and blade wear events occur simultaneously across the blade, contrary to the previous belief that a single mechanism dominated at any one time.

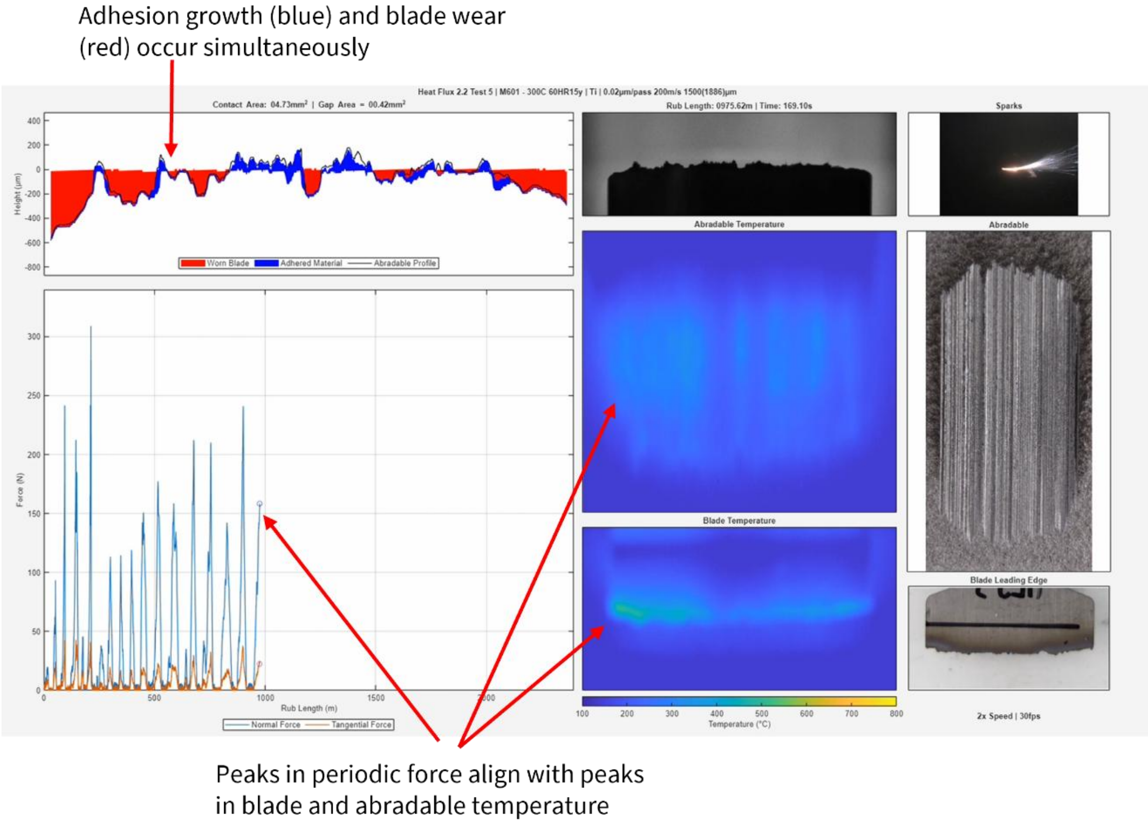

Figure 8.1 – An extracted video frame from a 60HR15y M601 test completed at 0.02µm/pass

A key gap in the understanding of the wear mechanism of M601 is why the wear mechanisms at low incursion rates (0.02µm/pass) do not follow the same trends as those observed at higher incursion rates (0.2 - 2µm/pass). Through the application of the novel in-situ measurement this knowledge gap could be further investigated.

By recording the blade profile and forces during tests at varying incursion rates, tip speeds and hardnesses it was possible to plot the wear rates against the normal force to hardness ratio. From this data it could be confirmed that for incursion rates between 0.2 – 2µm/pass Archard's wear law was followed but at 0.02µm/pass this law could no longer be applied. To explain this deviation the in-situ thermal monitoring tools were applied to observe how the blade and abradable temperatures developed alongside the blade wear. It was observed that rate of heating of the abradable relative to the blade has a significant impact on the wear mechanism, with the blade wearing if the blade heats significantly faster than the abradable. At low incursion rates the heat flux into the abradable was sufficiently low that the heat could be conducted to the backplate, leading to blade wear. Further evidence for this could be proposed by applying thermal models to the test data, demonstrating how as the test progresses the thermal resistance of the sample reduces. This aligned with a reduction in the temperature at the surface of the abradable, and a transition from adhesion formation to blade wear.

These results highlighted that the transition in wear mechanism from adhesion formation to blade wear is highly dependent on the relationship between blade and abradable heating rate. The change in wear mechanism at lower incursion rates can therefore be shown to be due to the change in heat flux into the abradable and blade and how these components manage that energy.

With the importance of thermal management demonstrated further insight into the scale of the impact could be extracted through control of the abradable bulk temperature during a test. This had the additional benefit of better replicating the conditions within the engine, where these samples will be held at elevated temperatures prior to any wear events occurring. A sample heater capable of heating the abradable backplate to 300°C was therefore developed.

By changing the backplate temperature it was possible to vary the wear mechanisms, with changes which could be explained by applying the findings of the previous chapters, that the adhesions are a function of both temperature and normal force, and that the ability of the abradable to manage the heat created during the rub relative to the blade will determine if the blade wears, or if adhesions form. Changes were also seen due to the changes in the coatings mechanical properties at elevated bulk temperatures, these results aligned with existing literature.

The results of these tests also demonstrated that adhesions could act as a sacrificial layer on the blade, protecting it from wear. Adhesions were also seen to form more readily on existing adhesions, or at the point of a previous adhesion fracture. This demonstrates that adhesion formation early in the test can provide a long-lasting impact on the wear mechanisms, preventing blade wear by encouraging adhesion formation.

Although these results have shown that bulk temperature does have an impact on wear, the impact was smaller than the impact of changing incursion rates or material hardnesses. Results completed at room temperature are still therefore valid for engine applications.

The testing and analysis completed in this thesis has provided a deeper insight into the factors which influence the formation of adhesions for blade-liner contacts with M601. These insights have allowed for the wear behaviour at low incursion rates to be explained, building on the existing understanding of adhesion formation at higher incursion rates.

The key novel findings from this work on M601 are a set of relationships between temperature, normal loads and wear mechanism which, when combined with pre-existing relationships, can explain the behaviour of M601 at low incursion rates. These relationships are:

- The rate of adhesion formation increases with increasing normal loads (97).
- Adhesions form more readily at elevated temperatures (Chapter 5).
- Adhesions can provide a protective layer on the blade (Chapter 6).
- If the blade heats up faster than the abradable it is likely to wear before adhesions can form (Chapter 4).
- New adhesion formation is more likely at the site of a previously fractured adhesion (79).

However, M601 is not the only AlSi based abradable which is applied within a jet engine. M320 is another commonly applied coating and, as with M601, the wear response at low incursion rates is not well understood. At low incursion rates the response is highly variable with either severe blade wear, or mixed modal large-scale adhesion and blade wear. The response at 0.02µm/pass was found to be dependent on the material hardness and was proposed to be due to the thermal properties of the material.

By applying the heater block and the in-situ tools developed to tests of M320 at 0.02µm/pass at varying hardnesses the full spectrum of wear could be observed, varying with both backplate temperature and abradable hardness.

The results of these tests showed that M320 follows the same relationships which were identified with M601. For M320 the impact of thermal properties was a significant factor to the wear mechanism as the addition of hBN was found to impact the thermal properties and hence wear of the abradable.

Although it was possible to relate the wear mechanisms observed back to the thermal properties of the material, the adhesions which were formed during a test with M320 were larger and more robust that those observed during M601 tests. Figure 8.2 shows an example of such an adhesion, with the adhesion height (~1.5mm) exceeding the depth of the rub. When these adhesions fracture a large gap is left between the blade tip and the abradable, which would lead to significant efficiency losses within the engine. From this work it was not possible to determine why the addition of hBN would result in larger adhesions.

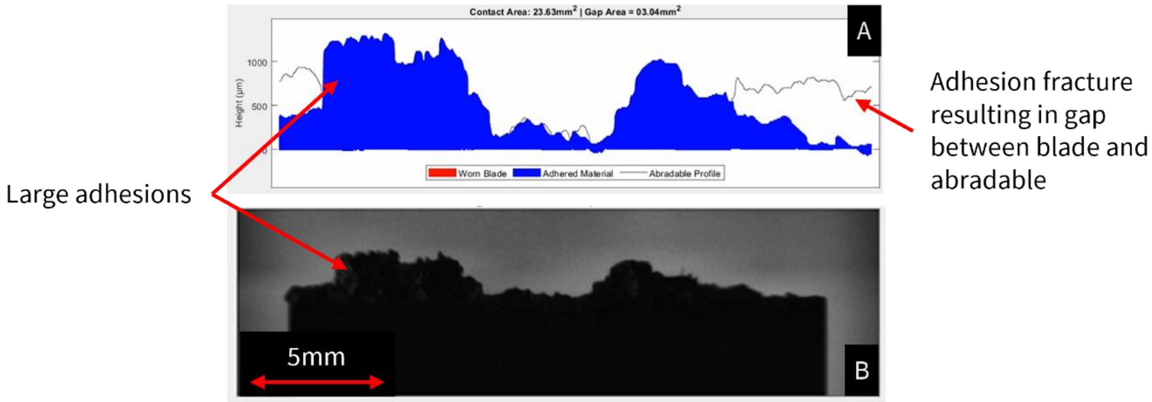

Figure 8.2 – The extracted blade profile (A) and front camera image (B) showing adhesion formation during a 62HR15y M320 test at 0.02µm/pass

Further testing of XPT268 produced wear results which also aligned with the relationships observed for M601, with the addition of hBN appearing to have a positive impact on the wear performance at 0.02µm/pass by promoting adhesions which protect the blade from wear.

Through this thesis novel in-situ measurement tools and analysis techniques have been applied to identify, and explain, the adhesion mechanics at rub conditions which did not align with existing adhesion theory. This work was developed with M601 but has been applied to both M320 and XPT268, demonstrating that the findings can be applied to AlSi based abradables in general.

9 Conclusion

9.1 Conclusions

The potential efficiency and environmental benefits of the use of abradables within jet engines has prompted the development of bespoke abradability testing rigs, spread over many research groups. These rigs have been able to test abradable coatings at a range of test conditions, producing engine representative wear and allowing relationships to be formed between the wear mechanisms and tip speed, incursion rate, and material hardness. This data is often presented in the form of wear maps, allowing engine manufacturers to target more favourable regions. These maps were initially formed through observations made post-test. More recent work has looked at applying in-situ measurement tools to monitor the wear during a test, allowing information to be gathered not only on what wear has occurred, but also how it formed.

Commonly within the low and intermediate pressure compressors of the engine AlSi based abradables are used. However, AlSi alone does not abrade well, leading to the addition of a secondary dislocator phase. This has resulted in materials such as M601 (AlSi – Polyester), M320 (AlSi– hBN), and XPT268 (AlSi – Polyester – hBN). M601 and M320 have been shown produce results which vary with incursion rate and hardness, these results align with fundamental tribological relationships at high incursion rates (0.2 – 2µm/pass), but at low incursion rates (0.02µm/pass) the behaviour is less well understood. XPT268 is a new material with little published work, but initial studies have shown that it performs similarly to M601.

A key issue with the use of AlSi based abradables is the formation of adhesions on the blade tips. These adhesions produce a scored abradable surface, increasing airflow around the blade tips and introducing inefficiencies to the engines. This thesis aims to provide a better understanding of the mechanisms behind the formation of adhesions, knowledge that engine and coating manufacturers could apply to avoid adhesion formation and improve engine efficiency.

The objectives of this work were to develop a set of novel in-situ measurement tools and analysis techniques to identify the key material and test parameters which affect adhesion behaviour, to determine how modifying these impact wear behaviours, and then to further apply this to AlSi abradable systems in general.

This work has met these objectives through the development and use of in-situ blade profile monitoring, alongside blade and abradable thermal imaging to identify that the management of thermal energy during a rub is a key driver on which wear mechanisms will occur. This improved understanding can fill previous gaps in the understanding of why M601 behaves differently at low incursion rates (0.02µm/pass), to the more predicable behaviours at higher rates (0.2 - 2µm/pass). Testing with a bespoke sample heater has allowed for further understanding of how the bulk temperature impacts the wear, building on research looking into how temperature can impact the mechanical properties of the abradable, and applying it to abradability testing.

Further testing on M320 and XPT268 demonstrates that these findings are not unique to M601 but can be applied to AlSi abradables systems in general. However, this work did highlight that the impact of hBN to the abradables goes beyond a purely thermal effect, and instead can produce larger, more robust adhesions which cannot be explained in this work.

This work can be applied directly by engine manufacturers. The improved knowledge on the drivers of different wear mechanism, especially at lower incursion rates, will allow for better understanding of the root cause of wear observed within operational engines. This improved understanding will allow for design improvements which can target different wear mechanisms – this could take the form of coatings on the blades to improve the thermal resistance of the blade, or targeted cooling to change the heating rates between blade tip and abradable.

9.2 Future Work

This work provides a qualitative explanation of the mechanisms behind adhesion formation and has been used to explain the wear behaviour across the full range of incursion rates, hardnesses and backplate temperatures. It does not however allow for qualitative predictions within the engine to be made. Previous attempts to create statistical models for the wear of M601, such as that created by Watson et al. (74), had difficulty in predicting the wear which occurs at low incursion rates. As a result of work completed in this thesis the key parameters which influence the wear mechanism, such as the relationship between blade heating and abradable heating rates, have been identified. By including these parameters in the model, it should be possible to create better predictions at low incursion rates.

While this work has identified the parameters which impact the wear rates and has discussed the impact each of these has on adhesion rates, the actual tribo-chemical interaction which leads to the adhesion formation has not been explored. This is most evident with the significant difference in the properties of adhesions formed with M320 when compared to M601. Further work aimed at understanding what initially causes adhesions to form, and what influences their material properties would provide a better understanding of how they can be controlled.

This work has also demonstrated that XPT268 has the potential to outperform M601 at low incursion rates, but the lack of knowledge on the material and its mechanical properties limited the discussion. These findings also go against the reports by engine manufacturers that this material leads to significant blade wear. Further testing at a range of incursion rates is therefore required. Following additional work to develop an understanding of how the microstructure and thermal properties vary with hardness, the in-situ tools and theories developed in this paper could be further applied to this material to explain its wear performance.

References

1. Airports Council International (ACI). State of the Industry and Outlook for Airport Traffic [Internet]. 2025 [cited 2026 Apr 21]. Available from: https://www.icao.int/sites/default/files/Meetings/a42/Documents/WP/wp_556_en.pdf

2. Darecki M, Edelstenne C, Enders T, Fernandez E, Hartman P, Herteman JP, et al. Flightpath 2050 Europe's vision for aviation. European Commission; 2012. doi:10.2777/50266

3. IATA. CORSIA Fact Sheet [Internet]. 2025 [cited 2026 Apr 21]. Available from: https://www.iata.org/en/iata-repository/pressroom/fact-sheets/fact-sheet-corsia/

4. The University of Sheffield [Internet]. 2025 [cited 2026 Apr 21]. Knowledge Exchange and Impact Awards. Available from: https://sheffield.ac.uk/collaborate/research-and-innovation/university-sheffield-knowledge-exchange-and-impact-awards

5. Wei K. Turbofan and turbojet engines: Working process and future development. Theoretical and Natural Science. 2023;12(1):114–9. doi:10.54254/2753-8818/12/20230447

6. Faradiba F, Yuniarti E. Thermodynamic Concepts on Efficiency of Aircraft Engines. Physical Science International Journal. 2021;1–7. doi:10.9734/psij/2021/v25i130231

7. Schmid RK. New high temperature abradables for gas turbines [Thesis]. Swiss Federal Institute of Technology Zurich; 1997. doi:10.3929/ethz-a-001809249

8. Storer JA, Cumpsty NA. Tip Leakage Flow in Axial Compressors. J Turbomach. 1991;113(2):252–9. doi:10.1115/1.2929095

9. Salvat N, Batailly A, Legrand M. Modelling of Abradable Coating Removal in Aircraft Engines Through Delay Differential Equations. J Eng Gas Turbine Power. 2013;135(10). doi:10.1115/1.4024959

10. Lattime SB, Steinetz BM. Turbine Engine Clearance Control Systems: Current Practices and Future Directions [Internet]. 2002 [cited 2026 Apr 21]. Available from: www.sti.nasa.gov

11. Chupp R, Ghasripoor F, Moore G. Applying Abradable Seals to Industrial Gas Turbines. In: 38th AIAA/ASME/SAE/ASEE Joint Propulsion Conference. Reston, Virigina: American Institute of Aeronautics and Astronautics; 2002. doi:10.2514/6.2002-3795

12. Rolls Royce. Rolls Royce Image Repository [Internet]. 2025 [cited 2025 Nov 14]. Available from: https://www.flickr.com/photos/rolls-royceplc/

13. Wilson S. Thermally Sprayed Abradable Coating Technology for Sealing in Gas Turbines. In: The Future of Gas Turbine Technology, 6th International Conference. Brussels; 2012.

14. Final Report A330-300, Registration 9V-SSF Dual Engine Surge [Internet]. 2015 [cited 2026 Apr 21]. Available from: https://asn.flightsafety.org/reports/2013/20130422_A333_9V-STO.pdf

15. Uihlein T, Schlegel H. Titanium Fire in Jet Engines. In: Proceedings AGARD-CP-587. Munich; 1997.

16. Sundberg D, Dennis R, Hurst L. Abradable Compressor and Turbine Seals [Internet]. Washington, DC; 1979 [cited 2026 Apr 21]. Available from: https://ntrs.nasa.gov/api/citations/19800005978/downloads/19800005978.pdf

17. Schmid RK, Ghasripoor F, Dorfman M, Wei X. An Overview of Compressor Abradables. In: Thermal Spray 2000: Proceedings from the International Thermal Spray Conference. 2000. p. 1087–93. doi:10.31399/asm.cp.itsc2000p1087

18. Oerlikon Metco. Improve efficiency and reduce emissions with high pressure turbine abradable coatings for industrial gas turbines - SF-0015.1 [Internet]. 2014 [cited 2026 Apr 21]. Available from: https://downloads.oerlikon.com/EN

19. Ma X, Matthews A. Investigation of abradable seal coating performance using scratch testing. Surf Coat Technol. 2007;202:1214–20. doi:10.1016/j.surfcoat.2007.07.076ï

20. Oelikon Metco. Material Product Data Sheet Nickel Chromium Aluminum / Bentonite Abradable Powders [Internet]. 2012 [cited 2026 Apr 21]. Available from: https://downloads.oerlikon.com/EN

21. Bolot R, Seichepine JL, Vucko F, Coddet C, Sporer D, Fiala P, et al. Thermal Conductivity of AlSi/Polyester Abradable Coatings. In: International Thermal Spray Conference Proceedings. 2008. p. 1056–61. doi:10.31399/asm.cp.itsc2008p1056

22. Watson M, Marshall M. A Novel Image Segmentation Approach for Microstructure Modelling. Coatings. 2017;7(10):166. doi:10.3390/coatings7100166

23. Borel MO, Nicoll AR, Schläpfer HW, Schmid RK. The wear mechanisms occurring in abradable seals of gas turbines. Surf Coat Technol. 1989. doi:10.1016/0257-8972(89)90046-7

24. Novinski ER. The Selection and Performance of Thermal Sprayed Abradable Seal Coatings for Gas Turbine Engines. Journal of Aerospace [Internet]. 1989 [cited 2026 Apr 21];98:60–3. Available from: https://www.jstor.org/stable/44471607

25. Sharsar S, Bhagat R, Kapoor N. Evaluation of Erosion Wear of HVOF Sprayed Al-Si Polyester Abradable Coating by Taguchi Method. International Journal of Research in Mechanical Engineering & Technology. 2014;4.

26. Raj A, Malik A, Atray B. Erosion Wear Behaviour Analysis of HYOF Sprayed Al-Si-Polyester Abradable Coating at High Temperature. The IUP Journal of Mechanical Engineering. 2014.

27. Malvi B, Roy M. Elevated Temperature Erosion of Abradable Seal Coating. Journal of Electrochemical Science and Engineering. 2022. doi:10.5599/jese.1388

28. Maozhong Y, Baiyun H, Jiawen H. Erosion Wear Behaviour and Model of Abradable Seal Coating. Wear. 2002. doi:10.1016/S0043-1648(01)00681-0

29. Steinke T, Mauer G, Vaßen R, Stöver D, Roth-Fagaraseanu D, Hancock M. Process Design and Monitoring for Plasma Sprayed Abradable Coatings. Journal of Thermal Spray Technology. 2010;19(4):756–64. doi:10.1007/s11666-010-9468-1

30. Ji GC, Li CJ, Wang YY, Li WY. Erosion Performance of HVOF-Sprayed Cr 3C 2-NiCr Coatings. Journal of Thermal Spray Technology. 2007;16(4):557–65. doi:10.1007/s11666-007-9052-5

31. Irissou E, Dadouche A, Lima RS. Tribological Characterization of Plasma-Sprayed Conicraly-BN Abradable Coatings. Journal of Thermal Spray Technology. 2014;23(1–2):252–61. doi:10.1007/s11666-013-9998-4

32. ASTM International. Test Method for Adhesion or Cohesion Strength of Thermal Spray Coatings. West Conshohocken, PA; 2021. doi:10.1520/C0633-13R21

33. Dorfman MR, Fiala P, Hajmrle K, Wilson S. Future Abradable Requirements Needed by Aerospace OEM's and Their Material and Equipment Suppliers. In: Volume 5: Turbo Expo. 2007. p. 17–24. doi:10.1115/GT2007-27059

34. Chupp RE, Lau YC, Ghasripoor F, Baldwin DJ, Ng C, McGovern T, et al. Development of Higher Temperature Abradable Seals for Gas Turbine Applications. In: Volume 4: Turbo Expo. 2004. p. 221–9. doi:10.1115/GT2004-53029

35. Batailly A, Agrapart Q, Millecamps A, Brunel JF. Experimental and Numerical Simulation of a Rotor/Stator Interaction Event Localized on a Single Blade within an Industrial High-Pressure Compressor. J Sound Vib. 2016;375:308–31. doi:10.1016/j.jsv.2016.03.016

36. Batailly A, Legrand M, Millecamps A, Garcin F. Numerical-Experimental Comparison in the Simulation of Rotor/Stator Interaction Through Blade-Tip/Abradable Coating Contact. J Eng Gas Turbine Power. 2012;134(8). doi:10.1115/1.4006446

37. Legrand M, Batailly A, Magnain B, Cartraud P, Pierre C. Full Three-Dimensional Investigation of Structural Contact Interactions in Turbomachines. J Sound Vib. 2012;331(11):2578–601. doi:10.1016/j.jsv.2012.01.017

38. Batailly A, Legrand M. Unilateral Contact Induced Blade/Casing Vibratory Interactions in Impellers: Analysis for Flexible Casings with Friction and Abradable Coating. J Sound Vib. 2015;348:344–64. doi:10.1016/j.jsv.2015.03.027

39. Nyssen F, Batailly A. Sensitivity Analysis of Rotor/Stator Interactions Accounting for Wear and Thermal Effects within Low- and High-Pressure Compressor Stages. Coatings. 2020;10(1):74. doi:10.3390/coatings10010074

40. Watson M. Modifications of Blade Tips in Abradable Contacts [Thesis]. The University of Sheffield; 2017.

41. Liang YN, Li S. Evaluation of Abradability of Porous Seal Materials in a Single-Pendulum Scratch Device. Wear. 1994;177:167–73.

42. Ma X, Matthews A. Evaluation of Abradable Seal Coating Mechanical Properties. Wear. 2009;267(9–10):1501–10. doi:10.1016/j.wear.2009.03.044

43. Tang JJ, Liu K, Yang QZ, Wang YH, Zhang P, Wang Y, et al. The Influence of Size and Distribution of Graphite on the Friction and Wear Behaviour of Ni–Graphite Coatings. Surf Coat Technol. 2014;252:48–55. doi:10.1016/J.SURFCOAT.2014.04.063

44. Bertuol K, Rivadeneira F, Nair RB, Barnett B, Moreau C, Stoyanov P. Influence of hBN on the Abradable Performance of AlSi-Based Coatings: Bridging the Gap Between Tribological Assessment and Abradability Testing. Surf Coat Technol. 2024;489. doi:10.1016/j.surfcoat.2024.131060

45. Bertuol K, Rivadeneira F, Arendarchuck B, Nair RB, Barnett B, Moreau C, et al. Effect of Mo and Cr on Abradability and Tribological Performance of AlSi-Based Abradable Coatings. Wear. 2025;571. doi:10.1016/j.wear.2025.205837

46. Pellegrino A, Perez-Martin MJ, Dragnevski K, Zumpano G, Petrinic N. Temperature and Strain Rate Dependent Mechanical Response of Metco 601 Aluminium-Polyester Abradable Seal Coating. In: EPJ Web of Conferences. 2018. p. 04012. doi:10.1051/epjconf/201818304012

47. Lye R, Pellegrino A, Bennett C, Rouse J, Agyakwa P, Zumpano G. Influence of Temperature, Strain Rate, and Condition on the Mechanical Response of an AlSi-PES Abradable. Exp Mech. 2025. doi:10.1007/s11340-025-01211-z

48. Wang H. Criteria for Analysis of Abradable Coatings. Surf Coat Technol. 1996;79:71–5.

49. Berthoul B, Batailly A, Legrand M, Stainier L, Cartraud P. Abradable Coating Removal in Turbomachines: A Macroscopic Approach Accounting for Several Wear Mechanisms. In: ASME Turbo Expo. 2015. doi:10.1115/GT2015-42500

50. Bolot R, Aussavy D, Montavon G. Application of FEM to Estimate Thermo-mechanical Properties of Plasma Sprayed Composite Coatings. Coatings. 2017;7(7). doi:10.3390/coatings7070091

51. Bolot R, Seichepine JL, Qiao JH, Coddet C. Predicting the Thermal Conductivity of AlSi/polyester Abradable Coatings: Effects of the Numerical Method. Journal of Thermal Spray Technology. 2011;20(1–2):39–47. doi:10.1007/s11666-010-9592-y

52. Faraoun HI, Seichepine JL, Coddet C, Aourag H, Zwick J, Hopkins N, et al. Modelling Route for Abradable Coatings. Surf Coat Technol. 2006;200(22–23):6578–82. doi:10.1016/j.surfcoat.2005.11.105

53. Faraoun HI, Grosdidier T, Seichepine JL, Goran D, Aourag H, Coddet C, et al. Improvement of Thermally Sprayed Abradable Coating by Microstructure Control. Surf Coat Technol. 2006;201(6):2303–12. doi:10.1016/j.surfcoat.2006.03.047

54. Cheng J, Hu X, Lancaster D, Sun X, Joost W. Modelling Deformation and Failure in AlSi-polyester Abradable Sealcoating Material using Microstructure-based Finite Element Simulation. Mater Des. 2022;219. doi:10.1016/j.matdes.2022.110791

55. Pychynski T, Hofler C, Bauer HJ. Experimental Study on the Friction Contact between a Labyrinth Seal Fin and a Honeycomb Stator. J Eng Gas Turbine Power. 2016;138(6). doi:10.1115/1.4031791

56. Delebarre C, Wagner V, Paris JY, Dessein G, Denape J, Gurt-Santanach J. An Experimental Study of the High Speed Interaction Between a Labyrinth Seal and an Abradable Coating in a Turbo-engine Application. Wear. 2014;316(1–2):109–18. doi:10.1016/j.wear.2014.04.023

57. Thévenot M, Wagner V, Paris JY, Dessein G, Denape J, Harzallah M, et al. Thermomechanical Phenomena and Wear Flow Mechanisms during High Speed Contact of Abradable Materials. Wear. 2019;426–427:1102–9. doi:10.1016/j.wear.2019.01.094

58. Sutter G, Philippon S, Garcin F. Dynamic Analysis of the Interaction Between an Abradable Material and a Titanium Alloy. Wear. 2006;261(5–6):686–92. doi:10.1016/j.wear.2006.01.030

59. Vincent J, Philippon S, Cappella A, Meriaux J, Selezneff S. Enhancement of an Experimental Method to Measure Accurately the Evolution of Forces During Short-lived Interactions: Application to Blade-abradable Material Contacts in Turbomachines. Measurement. 2017;98:167–78. doi:10.1016/j.measurement.2016.11.034

60. Martinet B, Cappella A, Philippon S, Montebello C. Effect of Temperature on Wear Mechanisms of an Aluminium - Based Abradable Coating for Aircraft Engines after a Dynamic Interaction with a Ti6Al4A Blade. Wear. 2020;446–447. doi:10.1016/j.wear.2020.203202

61. Wollmann T, Lye R, Ebert C, Becker B, Bennett C, Rouse J, et al. Investigation into the Effects of Abradable Evolution and Ovalisation during Blade-casing Interactions. Tribol Int. 2023;189. doi:10.1016/j.triboint.2023.108900

62. Nitschke S, Wollmann T, Ebert C, Behnisch T, Langkamp A, Lang T, et al. An Advanced Experimental Method and Test Rig Concept for Investigating the Dynamic Blade-tip/casing Interactions under Engine-like Mechanical Conditions. Wear. 2019. doi:10.1016/j.wear.2018.12.072

63. Mandard R, Witz JF, Boidin X, Fabis J, Desplanques Y, Meriaux J. Interacting Force Estimation during Blade/seal Rubs. Tribol Int. 2015;82(PB):504–13. doi:10.1016/j.triboint.2014.01.026

64. Mandard R, Desplanques Y, Hauss G, Fabis J, Witz JF, Meriaux J. Mechanisms of Incursion Accommodation during Interaction Between a Vibrating Blade and an Abradable Coating. Wear. 2015;330–331:406–18. doi:10.1016/j.wear.2015.01.014

65. Mandard R, Witz JF, Desplanques Y, Fabis J, Meriaux J. Wavelet Analysis of Experimental Blade Vibrations during Interaction with an Abradable Coating. J Tribol. 2014;136(3). doi:10.1115/1.4027438

66. Oerlikon Metco. Rapid Validation of Turbomachinery Abradable Systems Using Oerlikon Metco's Rub-Test Facility - SF-0029.0 [Internet]. 2020 [cited 2026 Apr 21]. Available from: https://downloads.oerlikon.com/EN

67. Dadouche A, Conlon MJ, Dmochowski W, Liko B, Bédard JP. Experimental Evaluation of Abradable Seal Performance at High Temperature. In: ASME Turbo Expo. 2008. doi:10.1115/gt2008-51228

68. Zhang N, Shen J, Xuan H, Hu Y, Hong W. Evaluation of an AlSi-polyester Abradable Seal Coating Performance using High-temperature and High-velocity Abrasion Tests. Proceedings of the Institution of Mechanical Engineers, Part J: Journal of Engineering Tribology. 2016;230(7):842–51. doi:10.1177/1350650115619150

69. Xuan H, Zhang N, Lu B, Cheng L, Hong W. Investigation of High-speed Abrasion Behaviour of an Abradable Seal Rubber in Aero-engine Fan Application. Chinese Journal of Aeronautics. 2017;30(4):1615–23. doi:10.1016/j.cja.2017.02.019

70. Liu J, Yu Y, Liu T, Cheng X, Shen J, Li C. The Influence of Composition and Microstructure on the Abradability of Aluminum-Based Abradable Coatings. Journal of Thermal Spray Technology. 2017;26(6):1095–103. doi:10.1007/s11666-017-0526-9

71. Liu T, Yu YG, Shen J, Liu JM, Lu QY. Study on Wear Mechanism of an AlSi–Hexagonal Boron Nitride Abradable Seal Coating. Adv Mat Res. 2015;1095:655–61. doi:10.4028/www.scientific.net/amr.1095.655

72. Emery AF, Wolak J, Etemad S, Choi SR. An Experimental Investigation of Temperatures Due to Rubbing at the Blade-seal Interface in an Aircraft Compressor. Wear. 1983. doi:10.1016/0043-1648(83)90248-x

73. Stringer J, Marshall M. High Speed Wear Testing of an Abradable Coating. Wear. 2012. doi:10.1016/j.wear.2012.07.009

74. Watson M, Marshall M. Wear Mechanisms at the Blade Tip Seal Interface. Wear. 2018;404–405:176–93. doi:10.1016/j.wear.2018.03.009

75. Zhang B, Marshall M. Investigating Material Removal Mechanism of Al-Si Base Abradable Coating in Labyrinth Seal System. Wear. 2019;426–427:239–49. doi:10.1016/j.wear.2019.01.034

76. Fois N, Watson M, Marshall M. The Influence of Material Properties on the Wear of Abradable Materials. Proceedings of the Institution of Mechanical Engineers, Part J: Journal of Engineering Tribology. 2017;231(2):240–53. doi:10.1177/1350650116649528

77. Fois N, Stringer J, Marshall MB. Adhesive Transfer in Aero-engine Abradable Linings Contact. Wear. 2013;304(1–2):202–10. doi:10.1016/J.WEAR.2013.04.033

78. Fois N, Watson M, Stringer J, Marshall M. An Investigation of the Relationship Between Wear and Contact Force for Abradable Materials. Proceedings of the Institution of Mechanical Engineers, Part J: Journal of Engineering Tribology. 2015. doi:10.1177/1350650114545139

79. Rahimov E, Watson M, Hadjisoteriou A, Marshall M. Investigation of Wear Mechanisms in AlSi-polyester Abradable - Ti(6Al4V) Blade Contacts Using Stroboscopic Imaging. Wear. 2022;494–495:204207. doi:10.1016/j.wear.2021.204207

80. Rahimov E, Baillieu A, Liu A, Marshall M. An Investigation of the Contact Mechanisms between Inconel 718 Blades and a NiCrAl-bentonite Abradable System. Wear. 2024;556–557:205465. doi:10.1016/j.wear.2024.205465

81. Baillieu A, Parody A, Rahimov E, Garcia Panizo J, Marshall M. In Situ Measurements of Thermal-mechanical Wear in Blade-abradable Liner Contacts. Proc Inst Mech Eng C J Mech Eng Sci. 2023. doi:10.1177/09544062231187204

82. Rahimov E. Investigation of Wear Mechanisms in Abradable-Blade Contacts [Thesis]. The University of Sheffield; 2022.

83. Gao S, Xue W, Duan D, Li S. Tribological Behaviours of Turbofan Seal Couples from Friction Heat Perspective under High-speed Rubbing Condition. Friction. 2016;4(2):176–90. doi:10.1007/s40544-016-0114-x

84. Xue W, Gao S, Duan D, Wang L, Liu Y, Liu Y, et al. Study on the High-Speed Rubbing Wear Behavior Between Ti6Al4V Blade and Nickel–Graphite Abradable Seal Coating. Journal of Tribology-transactions of The ASME. 2017. doi:10.1115/1.4033454

85. Taylor TA, Thompson BW, Aton W. High Speed Rub Wear Mechanism in IN-718 vs. NiCrAl–Bentonite. Surf Coat Technol. 2007. doi:10.1016/j.surfcoat.2007.05.054

86. Zhang J, Xue W, Duan D, Jiang S, Song J, Gao S, et al. Effect of the Corrosion of Seal Coatings Used in Aero Engines on Their High-Speed Wear Behaviour. Journal of Thermal Spray Technology. 2020;29(8):1958–67. doi:10.1007/s11666-020-01116-4

87. Bounazef M, Guessasma S, Saadi BA. The Wear, Deterioration and Transformation Phenomena of Abradable Coating BN–SiAl–Bounding Organic Element, Caused by the Friction between the Blades and the Turbine Casing. Mater Lett. 2004;58(27–28):3375–80. doi:10.1016/J.MATLET.2004.02.049

88. Sporer D, Wilson S, Giovannetti I, Refke A, Giannozi M. On the Potential of Metal and Ceramic Based Abradables in Turbine Seal Applications. In. Proceedings of the Thirty-Sixth Turbomachinery Symposium; 2007.

89. Oerlikon Metco. Material Product Data Sheet Aluminum Silicon Polymer Thermal Spray Powders [Internet]. 2021 [cited 2026 Apr 21]. Available from: https://downloads.oerlikon.com/EN

90. Ghasripoor F, Schmid RK, Dorfman MR, Russo L. A Review of Clearance Control Wear Mechanisms for Low Temperature Aluminium Silicon Alloys. In: International Thermal Spray Conference. 1998. p. 139–44. doi:10.31399/asm.cp.itsc1998p0139

91. Chupp RE, Ghasripoor F, Turnquist NA, Demiroglu M, Aksit MF. Advanced Seals for Industrial Turbine Applications: Dynamic Seal Development. J Propuls Power. 2002;18(6):1260–6. doi:10.2514/2.6061

92. Hadjisoteriou A. Investigation of the Material Removal Mechanism and Thermal Response of Compressor Abradable Materials [Thesis]. The University of Sheffield; 2021.

93. Oerlikon Metco. Material Product Data Sheet - Aluminium Silicone Graphite Abradable Powders - DSMTS-0020.6 [Internet]. 2015 [cited 2026 Apr 21]. Available from: https://downloads.oerlikon.com/EN

94. Fois N. Investigation and Characterisation of the Wear Mechanisms of Abradable Compressor Linings [Thesis]. The University of Sheffield; 2015.

95. Liu T, Yu Y, Liu J, Cheng X, Zhang D, Yang S. Influence of Spray Process Parameters on Microstructure and Properties of AlSi–Hexagonal Boron Nitride Abradable Seal Coating. In: International Thermal Spray Conference. 2018. p. 69–74. doi:10.31399/asm.cp.itsc2018p0069

96. Oerlikon Metco. Material Product Data Sheet Aluminum Silicon Hexagonal Boron Nitride Abradable [Internet]. 2020 [cited 2026 Apr 21]. Available from: https://downloads.oerlikon.com/EN

97. Archard JF. Contact and Rubbing of Flat Surfaces. J Appl Phys. 1953;24(8):981–8. doi:10.1063/1.1721448

98. Gåård A, Hallbäck N, Krakhmalev P, Bergström J. Temperature Effects on Adhesive Wear in Dry Sliding Contacts. Wear. 2010;268(7–8):968–75. doi:10.1016/j.wear.2009.12.007

99. Gåård A, Krakhmalev P, Bergström J, Hirvonen Grytzelius J, Zhang HM. Experimental Study of the Relationship between Temperature and Adhesive Forces for Low-alloyed Steel, Stainless Steel, and Titanium Using Atomic Force Microscopy in Ultrahigh Vacuum. J Appl Phys. 2008;103(12). doi:10.1063/1.2938844

100. Agrapart Q, Brunel JF, Desplanques Y, Dufrenoy P, Mandard R, Millecamps A. An Energy Balance of Blade-casing Interaction. In: 16th International Symposium on Transport Phenomena and Dynamics of Rotating Machinery. 2016.

101. Skiba S, Chevrier B, Faure L, Philippon S. Thermoelastoviscoplastic Bilinear Compressive Constitutive Law of an AlSi-PE Abradable Material Based on Experimental Investigations. Journal of Dynamic Behavior of Materials. 2021;7(3):499–508. doi:10.1007/s40870-021-00294-8

102. Liu C, Mao Z, Xu X. The Influence of Heat Treatment on AlSi-polymer Abradable Coating. In: Journal of Physics: Conference Series. 2024. doi:10.1088/1742-6596/2842/1/012060

103. Summers PT, Chen Y, Rippe CM, Allen B, Mouritz AP, Case SW, et al. Overview of Aluminum Alloy Mechanical Properties During and After Fires. Fire Sci Rev. 2015;4(1). doi:10.1186/s40038-015-0007-5

104. Garcia Panizo J. Investigating the Tribological Behaviours of a Jet Engine's Abrasive Rotor and Stator Vane Contact [Thesis]. The University of Sheffield; 2022.

105. Bomford S. Oerlikon Metco [Internet]. 2025 [cited 2025 Oct 30]. Surface preparation. Available from: https://www.oerlikon.com/metco/en/solutions-technologies/what-is-thermal-spray/surface-preparation-thermal-spray-process/

106. Oerlikon Metco. Atmospheric Plasma Spray Solutions - BRO-0006.7 [Internet]. 2022 [cited 2026 Apr 21]. Available from: https://downloads.oerlikon.com/EN

107. Jech D, Čelko L, Komarov P, Ziegelheim J, Česánek Z, Schubert J. The Role of Different Atmospheric Plasma Spray Parameters on Microstructure of Abradable AlSi-Polyester Coatings. Solid State Phenomena. 2017;270:224–9. doi:10.4028/www.scientific.net/SSP.270.224

108. Struers. Thermal Spray Coatings - Proven Materialographic Knowledge [Internet]. 2014 [cited 2026 Apr 21]. Available from: https://www.struers.com/en/knowledge/materials/thermal-spray-coatings

109. ASTM International. Test Methods for Rockwell Hardness of Metallic Materials - E18-15. West Conshohocken, PA: ASTM International; 2015. doi:10.1520/E0018-15

110. Micro-Epsilon. optoNCDT Laser Displacement Sensors [Internet]. [cited 2026 Apr 21]. Available from: https://www.micro-epsilon.co.uk/distance-sensors/laser-sensors/optoncdt-1220/

111. Nyssen F, Batailly A. Thermo-Mechanical Modeling of Abradable Coating Wear in Aircraft Engines. J Eng Gas Turbine Power. 2019;141(2). doi:10.1115/1.4041647

112. Keyence. Image Processing Useful Tips [Internet]. 2018 [cited 2026 Apr 21]. Available from: https://www.keyence.com/products/vision/vision-sys/resources/vision-sys-resources/fundamentals-of-image-processing-filters.jsp

113. Ohman C. Measurement in Thermography. 5th ed. Buchgeister C, Danjoux R, Hallin H, editors. Taby: FLIR Systems and the Infrared Training Center; 2014.

114. Wu Z, Zhang Y, Xu Y, Jie D, Jackson RL. Modeling of Flash Temperature for Elastic Sliding Contact of Single Micro-Asperity Pair. J Tribol. 2024;146(1). doi:10.1115/1.4063334

115. Liu Y, Xu R, Wang J, Wan S, Bai L. Atomistic Insight into Flash Temperature during Friction. International Communications in Heat and Mass Transfer. 2022;138. doi:10.1016/j.icheatmasstransfer.2022.106317

116. The MathWorks Inc. MATLAB Partial Differential Equation Toolbox [Internet]. 2024 [cited 2026 Apr 21]. Available from: https://uk.mathworks.com/products/pde.html

117. Zuo P, Tcharkhtchi A, Shirinbayan M, Fitoussi J, Bakir F. Effect of Thermal Aging on Crystallization Behaviors and Dynamic Mechanical Properties of Glass Fiber Reinforced Polyphenylene Sulfide (PPS/GF) Composites. Journal of Polymer Research. 2020. doi:10.1007/s10965-020-02051-2/Published

118. Khan SA, Oliveira J, Ferreira F, Emami N, Ramalho A. Surface Roughness Influence on Tribological Behavior of HiPIMS DLC Coatings. Tribology Transactions. 2023;66(3):565–75. doi:10.1080/10402004.2023.2197472

A. Record of Completed Tests

All tests completed as part of this work have been detailed in Table A.1. For each test the rub conditions and instrumentation used have been recorded. Tests with a backplate temp of "RT" were completed at room temperature.

For each test batch the chapter where the results have been applied is recorded. The tests which have been assigned to "Chapter 0" were completed as part of the design and development of the Low-Speed rig front camera and the in in-situ thermal camera monitoring tools. No data collected during this stage has been presented in this thesis.

The raw data collected for all tests has been collated and stored in the physical data repository managed by the Abradable Research Group. Processed data has been stored for the tests completed for Chapters 4-7. All data is organized by Chapter and Test Batch within the repository.

Table A.1 – Tests completed as part of this work

Chapter	Test Batch	Number	Material	Hardness (HR15y)	Inc/Rate (µm/pass)	Tip Speed (m/s)	Depth (µm)	Backplate Temp (°C)	Forces	Front Cam	Side Cam	Spark Cam	Pyro	Thermal Camera	Heater Block
0	601 vs 320	1	M601	70.00	2.00	200	2000	RT	-	✓	✓	-	-	-	-
		2	M601	70.00	0.20	200	2000	RT	-	✓	✓	-	-	-	-
		5	M601	70.00	0.02	200	2000	RT	-	✓	✓	-	-	-	-
		6	M320	65.00	2.00	200	2000	RT	-	✓	✓	-	-	-	-
		7	M320	65.00	0.20	200	2000	RT	-	✓	✓	-	-	-	-
		8	M320	65.00	0.02	200	2000	RT	-	✓	✓	-	-	-	-
		9	M320	65.00	0.02	200	2000	RT	-	✓	✓	-	-	-	-
		10	M601	70.00	0.02	200	2000	RT	-	✓	✓	-	-	-	-
	601_320 Adhesion	1	M601	70.00	0.20	200	2000	RT	-	✓	✓	-	-	-	-
		2	M601	70.00	0.20	200	2000	RT	-	✓	✓	-	-	-	-

		3	M601	70.00	0.20	200	2000	RT	-	✓	✓	-	-	-	-
		4	M601	70.00	2.00	200	2000	RT	-	✓	✓	-	-	-	-
		6	M601	70.00	0.02	200	2000	RT	-	✓	✓	-	-	-	-
		7	M320	65.00	2.00	200	2000	RT	-	✓	✓	-	-	-	-
		8	M320	65.00	0.20	200	2000	RT	-	✓	✓	-	-	-	-
		9	M320	65.00	0.02	200	2000	RT	-	✓	✓	-	-	-	-
		10	M320	65.00	0.02	200	2000	RT	-	✓	✓	-	-	-	-
		11	M601	70.00	0.02	200	2000	RT	-	✓	✓	-	-	-	-
	XPT	1	XPT268	73.00	0.20	200	1500	RT	✓	✓	✓	-	-	-	-
		2	XPT268	73.00	0.20	200	1500	RT	✓	✓	✓	-	-	-	-
		3	XPT268	73.00	0.20	200	1500	RT	✓	✓	✓	-	-	-	-
		4	XPT268	73.00	0.02	200	1500	RT	✓	✓	✓	-	-	-	-
	dualLightGate	1	M320	68.00	2.00	200	1500	RT	✓	✓	✓	-	-	✓	-
		2	M320	73.00	2.00	200	1500	RT	✓	✓	✓	-	-	✓	-
	Thermal Dual Capture	1	M320	68.00	0.20	200	1500	RT	✓	✓	✓	-	-	✓	-
		2	XPT268	73.00	0.20	200	2000	RT	✓	✓	✓	-	-	✓	-
		3	M601	65.80	0.20	200	1500	RT	✓	✓	✓	-	-	✓	-
		4	M601	65.80	0.20	200	1500	RT	✓	✓	✓	-	-	✓	-
		5	M601	65.80	0.02	200	2000	RT	✓	✓	✓	-	-	✓	-
	Thermal Dual Capture 2	2	XPT268	73.00	0.20	200	2000	RT	✓	✓	✓	-	-	✓	-
		3	M601	65.80	0.20	200	1500	RT	✓	✓	✓	-	-	✓	-
		4	M601	65.80	0.20	200	1500	RT	✓	✓	✓	-	-	✓	-
		5	M601	65.80	0.02	200	1500	RT	✓	✓	✓	-	-	✓	-
		6	XPT268	73.00	2.00	200	1500	RT	✓	✓	✓	-	-	✓	-
		7	XPT268	73.00	0.20	200	1500	RT	✓	✓	✓	-	-	✓	-
		8	XPT268	73.00	0.02	200	1500	RT	✓	✓	✓	-	-	✓	-
		9	XPT268	73.00	2.00	200	1500	RT	✓	✓	✓	-	-	✓	-
		10	XPT268	73.00	0.20	200	1500	RT	✓	✓	✓	-	-	✓	-
	Comp	1	M320	68.00	2.00	200	1500	RT	✓	✓	✓	-	-	✓	-

		2	M320	68.00	2.00	200	1500	RT	√	√	√	-	-	√	-
		3	M320	68.00	2.00	200	1500	RT	√	√	√	-	-	√	-
		4	M320	68.00	2.00	200	1500	RT	√	√	√	-	-	√	-
		5	M320	68.00	0.20	200	1500	RT	√	√	√	-	-	√	-
		10	M320	68.00	0.02	200	1500	RT	√	√	√	-	-	√	-
		11	M601	69.00	2.00	200	1500	RT	√	√	√	-	-	√	-
		12	M601	69.00	2.00	200	1500	RT	√	√	√	-	-	√	-
		13	M601	69.00	2.00	200	1500	RT	√	√	√	-	-	√	-
		14	XPT268	73.00	2.00	200	1500	RT	√	√	√	-	-	√	-
		15	XPT268	73.00	2.00	200	1500	RT	√	√	√	-	-	√	-
		16	XPT268	73.00	2.00	200	1500	RT	√	√	√	-	-	√	-
		17	XPT268	73.00	2.00	200	1500	RT	√	√	√	-	-	√	-
		18	XPT268	73.00	2.00	200	1500	RT	√	√	√	-	-	√	-
		19	XPT268	73.00	0.20	200	1500	RT	√	√	√	-	-	√	-
		20	XPT268	73.00	0.20	200	1500	RT	√	√	√	-	-	√	-
		21	XPT268	73.00	0.02	200	1500	RT	√	√	√	-	-	√	-
		22	XPT268	73.00	0.02	200	1500	RT	√	√	√	-	-	√	-
	Thermal Testing	1	M320	65.00	0.20	200	2000	RT	√	√	√	-	-	√	-
		2	M320	65.00	0.20	200	2000	RT	√	√	√	-	-	√	-
		3	M601	60.00	0.20	200	2000	RT	√	√	√	-	-	√	-
		4	M320	65.00	0.20	200	2000	RT	√	√	√	-	-	√	-
		5	M601	60.00	0.20	200	1500	RT	√	√	√	-	-	√	-
		6	M320	65.00	0.20	200	1500	RT	√	√	√	-	-	√	-
4	Thermal Properties	1	M601	68.60	0.20	200	1500	RT	√	√	√	-	√	√	-
		2	M601	68.60	0.02	200	1500	RT	√	√	√	-	√	√	-
		3	M601	68.60	2.00	200	1500	RT	√	√	√	-	√	√	-
		4	M601	68.60	0.20	200	1500	RT	√	√	√	-	√	√	-
		5	M601	68.60	0.02	200	1500	RT	√	√	√	-	√	√	-
		6	M601	68.60	2.00	200	1500	RT	√	√	√	-	√	√	-

		7	M601	68.60	0.20	200	1500	RT	√	√	√	-	√	√	-
		8	M601	68.60	0.02	200	1500	RT	√	√	√	-	√	√	-
		9	M601	68.60	2.00	200	1500	RT	√	√	√	-	√	√	-
		10	M601	68.60	0.02	200	1500	RT	√	√	√	-	√	√	-
		11	M601	68.60	0.02	200	1500	RT	√	√	√	-	√	√	-
		12	M601	68.60	0.02	200	1500	RT	√	√	√	-	√	√	-
	Confirmation	1	M601	65.80	0.20	200	1500	RT	√	√	√	-	-	√	-
		2	M601	65.80	0.02	200	1500	RT	√	√	√	-	-	√	-
		3	M601	65.80	2.00	200	1500	RT	√	√	√	-	-	√	-
		4	M601	65.80	0.20	200	1500	RT	√	√	√	-	-	√	-
		5	M601	65.80	0.20	200	1500	RT	√	√	√	-	-	√	-
		6	M601	65.80	0.02	200	1500	RT	√	√	√	-	-	√	-
		7	M601	65.80	0.02	200	1500	RT	√	√	√	-	-	√	-
		8	M601	65.80	2.00	200	1500	RT	√	√	√	-	-	√	-
		9	M601	65.80	2.00	200	1500	RT	√	√	√	-	-	√	-
		10	M601	65.80	2.00	200	1500	RT	√	√	√	-	-	√	-
	Confirmation2	1	M601	65.80	0.02	200	1500	RT	√	√	√	-	-	√	-
		2	M601	65.80	2.00	200	1500	RT	√	√	√	-	-	√	-
		3	M601	65.80	2.00	200	1500	RT	√	√	√	-	-	√	-
		4	M601	65.80	0.02	200	1500	RT	√	√	√	-	-	√	-
5	601_VaryingHard 1umpass	1	M601	55.00	1.00	200	2000	RT	√	√	√	-	√	√	-
		2	M601	55.00	1.00	200	2000	RT	√	√	√	-	√	√	-
		3	M601	77.00	1.00	200	1500	RT	√	√	√	-	√	√	-
		4	M601	68.60	1.00	200	1500	RT	√	√	√	-	√	√	-
	ThermalPaper Repeats	1	M601	55.00	0.02	200	2000	RT	√	√	√	-	√	√	-
		2	M601	77.50	0.02	200	2000	RT	√	√	√	-	√	√	-
		3	M601	77.50	0.20	200	2000	RT	√	√	√	-	√	√	-
		4	M601	77.50	2.00	200	2000	RT	√	√	√	-	√	√	-
		5	M601	53.50	1.00	200	1500	RT	√	√	√	-	√	√	-

		6	M601	68.60	1.00	200	1500	RT	√	√	√	-	√	√	-
		7	M601	77.50	1.00	200	1500	RT	√	√	√	-	√	√	-
		8	M601	53.50	1.00	100	1500	RT	√	√	√	-	√	√	-
		9	M601	68.60	1.00	100	1500	RT	√	√	√	-	√	√	-
		10	M601	77.50	1.00	100	1500	RT	√	√	√	-	√	√	-
6	HeaterBlock_T1	1	M601	55.00	0.20	200	1500	RT	√	√	√	-	√	√	√
		2	M601	55.00	2.00	200	1500	RT	√	√	√	-	√	√	√
		3	M601	55.00	0.02	200	1500	RT	√	√	√	-	√	√	√
		4	M601	55.00	0.20	200	1500	100	√	√	√	-	√	√	√
		5	M601	55.00	0.02	200	1500	100	√	√	√	-	√	√	√
		6	M601	55.00	0.02	200	1500	200	√	√	√	-	√	√	√
	HeatFlux	1	M601	55.00	0.02	200	2000	300	√	√	√	-	√	√	√
		2	M601	55.00	0.02	200	2000	300	√	√	√	-	√	√	√
		3	M601	61.00	0.02	200	1500	RT	√	√	√	-	√	√	√
		4	M601	61.00	0.02	200	1500	100	√	√	√	-	√	√	√
		5	M601	61.00	0.02	200	2000	200	√	√	√	-	√	√	√
		6	M601	61.00	0.02	200	2000	300	√	√	√	-	√	√	√
		7	M601	75.00	0.02	200	2000	RT	√	√	√	-	√	√	√
		8	M601	75.00	0.02	200	2000	100	√	√	√	-	√	√	√
		9	M601	75.00	0.02	200	2000	200	√	√	√	-	√	√	√
		10	M601	75.00	0.02	200	2000	300	√	√	√	-	√	√	√
	HeatFlux_2	1	M601	52.00	0.02	200	1500	100	√	√	-	√	√	√	√
		2	M601	52.00	0.02	200	1500	200	√	√	-	√	√	√	√
	HeatFlux_2_2	1	M601	52.00	0.02	200	1500	200	√	√	-	√	√	√	√
		2	M601	52.00	0.02	200	1500	300	√	√	-	√	√	√	√
		3	M601	60.00	0.02	200	1500	100	√	√	-	√	√	√	√
		4	M601	60.00	0.02	200	1500	200	√	√	-	√	√	√	√
		5	M601	60.00	0.02	200	1500	300	√	√	-	√	√	√	√
		6	M601	73.40	0.02	200	1500	100	√	√	-	√	√	√	√

		7	M601	73.40	0.02	200	1500	200	√	√	-	√	√	√	√
		8	M601	73.40	0.02	200	1500	300	√	√	-	√	√	√	√
	HeatFlux 3	1	M601	52.00	0.02	200	1500	150	√	√	-	√	√	√	√
		2	M601	52.00	0.02	200	1500	100	√	√	-	√	√	√	√
		3	M601	52.00	0.02	200	1500	200	√	√	-	√	√	√	√
		4	M601	52.00	0.02	200	1500	300	√	√	-	√	√	√	√
		5	M601	59.70	0.02	200	1500	100	√	√	-	√	√	√	√
		6	M601	59.70	0.02	200	1500	200	√	√	-	√	√	√	√
	HeatFlux_3_2	1	M601	59.70	0.02	200	1500	300	√	√	-	√	√	√	√
		2	M601	73.40	0.02	200	1500	100	√	√	-	√	√	√	√
		3	M601	73.40	0.02	200	1500	200	√	√	-	√	√	√	√
		4	M601	73.40	0.02	200	1500	300	√	√	-	√	√	√	√
		5	M601	52.00	0.02	200	1500	100	√	√	-	√	√	√	√
7	HeatFlux_2_2	9	M320	50.81	0.02	200	1500	100	√	√	-	√	√	√	√
		10	M320	50.81	0.02	200	1500	200	√	√	-	√	√	√	√
		11	M320	50.81	0.02	200	1500	300	√	√	-	√	√	√	√
		12	M320	50.81	0.02	200	1500	200	√	√	-	√	√	√	√
		13	M320	50.81	0.02	200	1500	300	√	√	-	√	√	√	√
		14	M320	62.00	0.02	200	1500	100	√	√	-	√	√	√	√
		15	M320	62.00	0.02	200	1500	200	√	√	-	√	√	√	√
		16	M320	62.00	0.02	200	1500	300	√	√	-	√	√	√	√
		17	XPT268	75.60	0.02	200	1500	100	√	√	-	√	√	√	√
		18	XPT268	75.60	0.02	200	1500	200	√	√	-	√	√	√	√
	HeatFlux_3_2	5	XPT268	75.60	0.02	200	1500	200	√	√	-	√	√	√	√
		6	M320	74.30	0.02	200	1500	100	√	√	-	√	√	√	√
		7	M320	74.30	0.02	200	1500	200	√	√	-	√	√	√	√
		8	M320	74.30	0.02	200	1500	300	√	√	-	√	√	√	√
		9	XPT268	51.10	0.02	200	1500	100	√	√	-	√	√	√	√
		10	XPT268	51.10	0.02	200	1500	200	√	√	-	√	√	√	√

		11	XPT268	51.10	0.02	200	1500	300	√	√	-	√	√	√	√
		12	XPT268	63.20	0.02	200	1500	100	√	√	-	√	√	√	√
		13	XPT268	63.20	0.02	200	1500	200	√	√	-	√	√	√	√
		14	XPT268	63.20	0.02	200	1500	300	√	√	-	√	√	√	√
		15	XPT268	75.60	0.02	200	1500	300	√	√	-	√	√	√	√
		16	XPT268	75.60	0.02	200	1500	200	√	√	-	√	√	√	√